H24/3171

MONASH UNIVERSITY
THESIS ACCEPTED IN SATISFACTION OF THE
REQUIREMENTS FOR THE DEGREE OF
DOCTOR OF PHILOSOPHY
ON.....3 May 2002.....
.....[redacted].....
Sec. Research Graduate School Committee

MICROSTRUCTURAL DEVELOPMENT AND CONTROL OF CERAMICS IN THE Ca-Si-Al-O-N SYSTEM

Christopher Andrew Wood

B.Sc. (Hons.) (Mat. Sci.)

A Thesis Submitted for the Degree of Doctor of Philosophy

School of Physics and Materials Engineering

Monash University

Victoria, 3800

Australia

October 2001

Table of Contents

Declaration

This thesis contains no material that has been accepted previously for the award of any other degree or diploma in any University or other institution. To the best of my knowledge and belief, it contains no material published previously or written by any other person, except where due reference is made in the text.

Christopher Andrew Wood

October 2001

Acknowledgements

I would like to gratefully acknowledge and thank the following people for their support and contributions towards the production of this thesis:

- My supervisor, Dr. Yi-Bing Cheng, for his enthusiastic support, advice and direction throughout the duration of this project. I would also like to acknowledge and thank him for the FEGSEM work he conducted on several of my samples whilst on sabbatical in Japan.

- Dr. Hong Zhao, of the Monash University School of Physics and Materials Engineering, for training me in many of the processing techniques used in my research, and for general discussions and advice.

- All of the technical, support and academic staff in the School of Physics and Materials Engineering at Monash University.

- Mr. Steve Swenser, of the Monash University School of Physics and Materials Engineering, for giving his time to train me in transmission electron microscopy.

- All of my friends, especially Alex, Sally, Yu, and everyone at Richmond Christian Fellowship.

- My Mum and Dad, for all of their support over the years, and to Steve, for being a real brother.

- A special thank you to my wonderful wife Kylie, whose endless support and encouragement has helped make this possible, and to our little man Joshua, for coming along and making life a lot more entertaining.

Abstract

Since their discovery in the early 1970's, α-sialon materials have undergone considerable development. However, until the 1990's, studies of Ca-stabilised α-sialons were limited. The discovery of anisotropic Ca α-sialon grain growth has raised considerable interest in the possibility of developing high hardness, Ca α-sialon materials that exhibit the good fracture toughness and reliability properties often associated with elongated grain morphologies. Little is presently known about anisotropic α-sialon grain growth in the Ca-Si-Al-O-N system. Thus, this study seeks to develop a better knowledge of the factors that can promote and control anisotropic Ca α-sialon grain growth under pressureless sintering conditions.

Three Ca-Si-Al-O-N compositions adjacent to the α-sialon forming region were examined at temperatures ranging from 1400°C to 1800°C. Some intermediate phases were detected over the compositional range investigated. The behaviour of the intermediate phases was found to be critical to the densification kinetics during pressureless sintering. All three compositions attained >99% of maximum density after 4 hours at 1700°C and/or 1800°C. α-Sialon was observed with an elongated morphology in all three compositions. The three compositions also contained varying proportions of AlN/AlN-polytypoid phases and intergranular glass phase. Fracture toughness and R-curve analyses determined that the elongated α-sialon grains improved the fracture toughness of some of the densified materials.

The phase assemblages and grain morphologies of Ca and Al-rich Ca-Si-Al-O-N compositions were investigated by examining eight previously unstudied, high m and n-value, Ca-Si-Al-O-N compositions. These samples contained significant amounts of AlN/AlN-polytypoid phases and intergranular glass. AlN was observed with equiaxed grain morphologies. The AlN-polytypoid phases displayed large plate morphologies. Ca α-Sialon was observed with an elongated morphology in the seven samples that contained the phase. Fracture surfaces of samples dominated by AlN/AlN-polytypoid phases and glass phase presented few features indicative of microstructural toughening

mechanisms. Small nano-precipitates observed in some AlN grains during TEM analysis were determined to originate in the AlN starting powder.

The effects of varying processing parameters on the densification and microstructural development of Ca-Si-Al-O-N compositions were investigated. An examination of different isothermal hold times found that basic reactions to form α-sialon completed at 1550°C. α-Sialon grain growth at this temperature was minimal. Both grain growth and densification were found to proceed rapidly at 1800°C. The intergranular liquid phase was believed to be an important factor in anisotropic α-sialon grain growth. An investigation into substituting β-Si_3N_4 powder in place of α-Si_3N_4 powder in Ca-Si-Al-O-N compositions found little effect when half of the α-Si_3N_4 was replaced with β-Si_3N_4. The complete substitution of α-Si_3N_4 with β-Si_3N_4 was found to significantly hinder densification. It also promoted α-sialon grain growth at low temperatures. This was determined to be a result of the α-sialon nucleation mechanism, and the higher thermodynamic stability of β-Si_3N_4 over α-Si_3N_4 at elevated temperatures. An investigation into furnace heating rates found that in low m-value samples, slow heating rates could suppress anisotropic α-sialon grain growth. It was determined that this was related to the kinetics of α-sialon nucleation and growth.

Chapter 1

Introduction

The use of ceramic materials in society has it foundations in the world's earliest civilisations. Today, ceramic materials have an essential role in the successful operation of a wide range of industries (Kingery et al. 1976). These industries span a diverse range of fields, from mining and mineral processing, through to the electronic, optical and medical fields.

For much of their history, ceramic materials have been based upon the silicates. However, the more recent need for a range of materials that possess better properties than traditional silicate ceramics has led to the development of new, or advanced, ceramic materials, that exhibit unique or outstanding properties. Among the advanced ceramics, silicon nitride (Si_3N_4) and its related solid solutions, the sialons, have shown great promise. The superior thermal and mechanical properties of this family of materials make them ideal for use at elevated temperatures in a variety of applications. The work presented in this thesis concerns the study of one particular sialon system, namely the Ca-Si-Al-O-N system.

Silicon nitride has undergone development as an engineering material since the 1950's (Jack 1987). The highly covalent nature of the bonding in silicon nitride makes densification of the material difficult. This was overcome in the 1960's when Si_3N_4 powder was hot-pressed with an oxide additive (Deeley et al. 1961). The additive reacts with the silica layer present on Si_3N_4 powder to form a liquid phase that facilitates densification. The resultant material possesses improved strength. However, the retained amorphous intergranular phase is deleterious to high temperature properties.

In the early 1970's, researchers in Japan and England independently discovered that aluminium and oxygen could form a solid solution in Si_3N_4 (Oyama and Kamigaito 1971; Jack and Wilson 1972). The phases in this new Si-Al-O-N system were termed sialons, an acronym based on the four elemental constituents. The development of

sialons held great promise. Like Si_3N_4, sialons require a liquid phase to attain full density. However, unlike Si_3N_4, the potential exists to incorporate some or all of the transient liquid phase into the crystalline sialon structure.

Silicon nitride exists in two different but related structures, α and β. Both types form sialons, termed α-sialon (α′) and β-sialon (β′) respectively. β-Sialon is formed by simultaneous equivalent substitution of aluminium and oxygen for silicon and nitrogen respectively in the β-Si_3N_4 structure. α-Sialon is formed by the simultaneous equivalent substitution of aluminium and oxygen or aluminium and nitrogen for silicon and nitrogen in the α-Si_3N_4 structure. The charge imbalance created by the substitution of Al-N bonds in place of Si-N bonds is compensated for by the incorporation of metal cations into interstitial sites that exist within the α-Si_3N_4 unit cell.

A range of metal cations have been used to stabilise the α-sialon structure. They include Li, Mg, Ca, Y, and the rare-earth metals except La, Ce, Pr and Eu. Most research has concentrated on the Y and rare-earth systems. This has largely been a result of the refractory grain boundary phases that are formed in these materials, which makes them well suited to medium and high temperature applications (Ekström 1996).

β-Sialon readily forms microstructures exhibiting elongated grain morphologies. This imparts good fracture toughness and reliability properties to the materials. Contrasting this, the significantly harder α-sialon typically exhibits equiaxed grains, giving bulk α-sialon poor fracture toughness. β-Sialon is also processed more easily than α-sialon. Because of these factors, β-sialon has undergone the most development for commercial applications. α-Sialon typically finds use only as a minor phase in α-/β-sialon composites, where the hardness of the α-sialon phase supplements the toughness of the β-sialon phase.

Until recently, the Ca-Si-Al-O-N system had experienced only limited development. This has mostly been a result of the better high temperature properties of other α-sialon systems. The first rudimentary phase behaviour diagram of the Ca α-sialon plane was proposed in 1983 (Jack 1983). It was not until the 1990's that a detailed account of phase relationships on the Ca α-sialon plane was established by Hewett and co-workers

(Hewett et al. 1998a). Now, as the many attractive characteristics of Ca α-sialon are becoming better understood, interest in the Ca-Si-Al-O-N system is increasing.

The calcium required in Ca-Si-Al-O-N compositions can be sourced from calcium carbonate ($CaCO_3$), a cheap and abundant mineral. This makes Ca α-sialon significantly cheaper to produce than α-sialons that require expensive yttrium and rare-earth oxides as additives. Calcium has the highest observed solubility in the α-sialon lattice, which can greatly assist in reducing volumes of intergranular phase in densified materials (Jack 1983). Ca α-sialon is found to be more thermally stable than Y and rare-earth α-sialons, undergoing little $\alpha' \rightarrow \beta'$ transformation at temperatures between 1100°C and 1500°C (Hewett et al. 1998b; Seeber and Cheng 1998). The low-temperature CaO-Al_2O_3-SiO_2 eutectic formed in Ca-Si-Al-O-N compositions means that these materials can be densified at lower temperatures than their Y and rare-earth counterparts (van Rutten et al. 1995). The low temperature eutectic also has negative implications, as softening of the intergranular glass phase occurs at a relatively low temperature, limiting the use of the material at high temperatures.

In addition to this range of attractive properties, Ca α-sialon is notable for its ability to display anisotropic grain growth during sintering. This phenomenon was first observed in hot-pressed samples by Wang et al. (1996b). Subsequent work has shown that elongated Ca α-sialon grains readily develop during the pressureless sintering of some Ca-Si-Al-O-N compositions (Hewett et al. 1998a; Zhao et al. 1998). This is an exciting development in α-sialon research, as there clearly exists the potential to create high hardness, monolithic, Ca α-sialon materials that possess the good fracture toughness and reliability normally associated with β-Si_3N_4 and β-sialons.

At present, little is known about the development of elongated microstructures in Ca-Si-Al-O-N materials. A comprehensive investigation of the many facets of elongated grain growth in these materials is yet to be undertaken. The range of Ca-Si-Al-O-N compositions that develop elongated grains has not yet been established, and there is a lack of knowledge concerning factors that influence anisotropic grain growth. To fully exploit the potential benefits of this phenomenon, this knowledge is required. Consequently, a comprehensive study of these areas is warranted.

The purpose of the present investigation was to study anisotropic grain growth in pressureless sintered Ca-Si-Al-O-N compositions. By doing this, a better understanding of Ca α-sialon could be obtained, thus allowing it to be further developed into a useful structural material. The investigation examined a range of compositional and processing parameters to establish their effect on the development of Ca α-sialon materials. The structure of the study presented in this thesis is as follows:

Chapter 2 comprises a literature review that provides a background to the areas of work relevant to this investigation. Included is a more complete history of the development of silicon nitride and the sialons, and an introduction to the graphical representations of the phases in the Me-Si-Al-O-N system and the α-sialon plane. A background to the microstructural toughening of ceramics is outlined, and a review of grain growth in silicon nitride based ceramics is presented.

Chapter 3 outlines the experimental procedures relevant to the work undertaken. The techniques and parameters used in the preparation of compositions, the formation of green bodies and their subsequent sintering are fully described. Techniques and equipment operational parameters relevant to the characterisation of samples are also outlined.

Chapter 4 details an investigation into the reaction sequences, densification behaviour and microstructural development of three Ca-Si-Al-O-N compositions. Density measurements, x-ray diffraction (XRD), scanning electron microscopy (SEM), transmission electron microscopy (TEM) and energy dispersive x-ray spectroscopy (EDXS) are used to characterise samples pressureless sintered over a range of temperatures. Fracture behaviour of densified samples is analysed using SEM and R-curve analysis techniques.

Chapter 5 consists of an investigation into eight previously unstudied, high m and n-value Ca-Si-Al-O-N compositions. Crystalline phase assemblages of the densified samples are determined by XRD. This phase information is combined with data from Hewett et al. (1998a) to create a refined version of the phase behaviour diagram of the Ca α-sialon plane previously published by them. SEM is utilised to examine the

microstructures of the densified materials. Fracture surfaces of the eight samples are also examined by SEM. Finally, some interesting features observed in the AlN phase of a high m-value Ca-Si-Al-O-N sample are investigated using TEM.

Chapter 6 examines the effects on densification, and phase and microstructural development, of changing a range of compositional and processing parameters for several Ca-Si-Al-O-N compositions. The effects of using different firing schedules and compositional variations are investigated. Materials produced are characterised by density measurements, XRD and SEM.

Chapter 7 summarises the major achievements that arose from this study, and suggests a number of areas that could benefit from future work.

Chapter 2

Literature Review

2.1 Silicon Nitride

Before any understanding of sialon ceramics is possible, an understanding of silicon nitride (Si_3N_4), the ceramic upon which the sialons are based, is essential. A brief history of silicon nitride development will now be presented.

Silicon nitride was first mentioned in 1857 by Deville and Wohler. Its chemical formula was given as Si_3N_4, however it remained a chemical curiosity until the 1950's, when it was first developed for use as an engineering material (Jack 1987). It was at this time that refractories utilising silicon nitride as a bonding phase for silicon carbide and other materials were developed. At the same time, silicon nitride with good thermal stability was produced for use as thermocouple tubes, crucibles for molten metals, and rocket nozzles. This material was formed by the nitridation of silicon powder compacts and was termed reaction-bonded silicon nitride (RBSN).

Silicon nitride does not melt to form a liquid phase under normal atmospheric pressure, and it has poor self-diffusivity due to its highly covalent bonding, even at high temperatures (Jack 1976). Because of these factors, silicon nitride cannot be sintered to maximum density by pressureless sintering techniques, such as those employed in the fabrication of RBSN. Consequently, the high level of porosity and low strength of RBSN was a major obstacle to its use in engineering applications (Hampshire 1991). This problem was overcome by Deeley et al. (1961) by hot-pressing previously formed silicon nitride powder with a magnesium oxide sintering additive, forming a fully dense material called hot-pressed silicon nitride (HPSN). Densification was enhanced by reaction of the oxide additive with the silica layer that is always present on the surface of silicon nitride powders. This produces a liquid phase at high temperatures, and densification is promoted by liquid phase sintering. The resultant material possesses improved strength, however strength degradation and creep problems occur above

1000°C due to softening of the intergranular glass phase (Komeya and Matsui 1991). This problem can be overcome by the use of post-sintering heat treatments, which devitrify the intergranular glass phase.

The first evidence for the existence of two forms of silicon nitride was obtained by Vassiliou and Wilde (1957). They reported a "Type II" silicon nitride with a hexagonal crystal structure, in addition to an (incorrectly designated) orthorhombic "Type I". Turkdogan et al. (1958) found that X-ray diffraction patterns of silicon nitrides formed at different temperatures did not look alike, with some peaks disappearing at higher nitriding temperatures. Their work clearly established the existence of two crystallographic modifications of silicon nitride. The higher temperature phase was designated β, and the lower temperature phase α. Both had the same chemical composition, Si_3N_4. Following many earlier misinterpretations, Hardie and Jack (1957) showed that both the α and β forms observed by Turkdogan et al. had a hexagonal crystal structure. The essential difference between the two is that the *c* dimension of the α unit cell is approximately twice that of the β unit cell.

A complete structural determination assigns β-Si_3N_4 hexagonal symmetry, with space group $P6_3/m$ (Wang et al. 1996a). Each β-Si_3N_4 unit cell contains two Si_3N_4 units. Its structure is based on the phenacite type, Be_2SiO_4, with N atoms occupying O sites and Si atoms occupying Be sites (Hardie and Jack 1957). Bonding is such that a framework of slightly distorted SiN_4 tetrahedra are formed, joined at N corners, with each N atom being shared between three tetrahedra. The tetrahedra are arranged such that they form distorted rings of alternating Si and N atoms, which lie at fractional heights of z = 0.25 and 0.75. This is shown in Figure 2.1(a). This structure can be regarded as consisting of layers of silicon and nitrogen atoms that give β-Si_3N_4 a stacking sequence ABAB. This creates continuous tunnels that lie parallel to the *c*-axis of the unit cell (Ekström and Nygren 1992) (Figure 2.1(c)).

The α-Si_3N_4 structure was assigned the space group P31c by Hardie and Jack (1957). The α-Si_3N_4 structure differs to the ABAB stacking sequence of β-Si_3N_4, in that it has a stacking sequence ABCDABCD. The CD layer is similar to the AB layer, except it is rotated 180° about the *c*-axis, as shown in Figure 2.1(b). This results in the closing off of

the continuous channels of the β-Si_3N_4 structure, and instead, two large interstices are located in each unit cell (Figure 2.1(d)). Each α-Si_3N_4 unit cell contains four Si_3N_4 units.

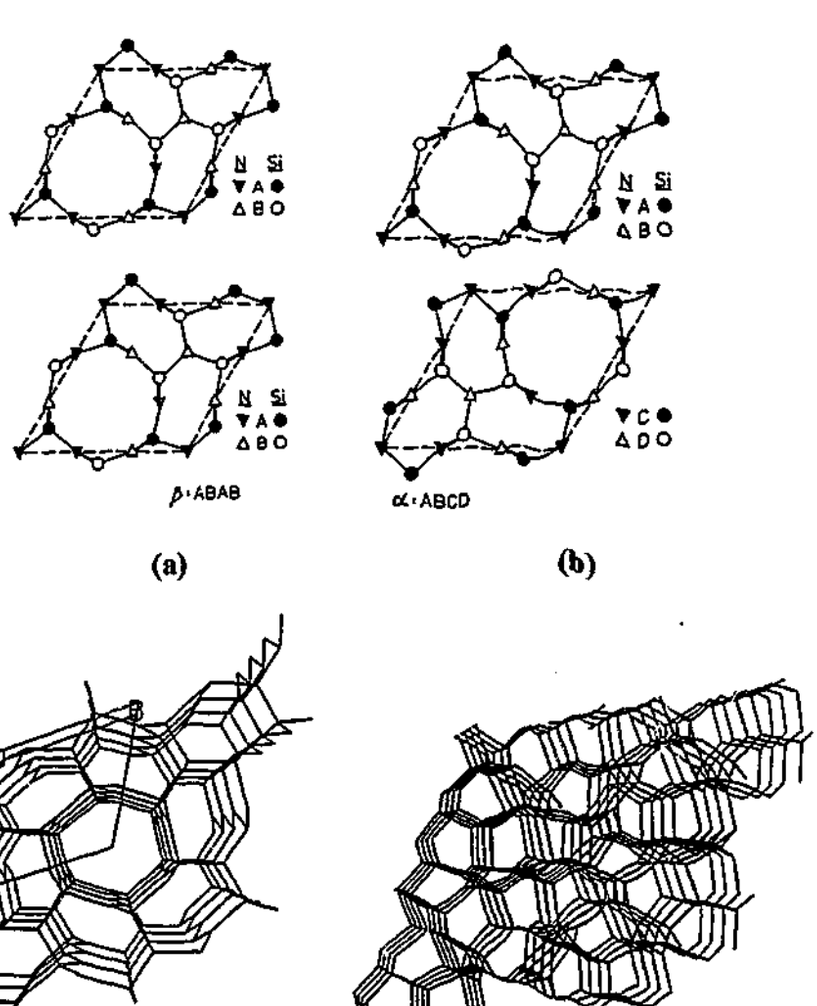

Figure 2.1. (a) The AB layers of the β-Si_3N_4 crystal structure, (b) the ABCD layers of the α-Si_3N_4 crystal structure, (c) structure of ABAB stacking in β-Si_3N_4, (d) structure of ABCD stacking in α-Si3N4 (Hampshire et al. 1978).

It is commonly held that α-Si_3N_4 is a low temperature modification, and β-Si_3N_4 is a high temperature modification, though thermodynamic data has not been sufficient to make an accurate decision on this (Cao and Metselaar 1991). Since the reverse β→α transformation has never been observed, it is assumed that β-Si_3N_4 is stable over all temperatures, whereas α-Si_3N_4 is formed only under special conditions, such as during

the nitridation of silicon. The higher stability of β-Si_3N_4 would also be reasonable given the higher strain of the α-Si_3N_4 structure (Cao and Metselaar 1991). The α→β transformation that does take place is a reconstructive transformation. A solution-reprecipitation mechanism is suggested, whereby α-Si_3N_4 dissolves into a liquid phase and β-Si_3N_4 precipitates out of the liquid. The transformation commences at about 1400°C and completes close to 1800°C, only in the presence of a liquid phase (Cao and Metselaar 1991). Without a liquid phase, α-Si_3N_4 can be stable to over 2000°C (Suematsu et al. 1997). Considerable controversy has surrounded an idea that α-Si_3N_4 is actually an oxynitride, with small amounts of oxygen substituting for nitrogen (Wang et al. 1996a). Though it is accepted that a small amount of oxygen can substitute into the α-Si_3N_4 structure, there is still no firm conclusion regarding the role of oxygen in α-Si_3N_4.

Since the early 1950's, the main incentive behind silicon nitride research was the development of the ceramic gas turbine and the ceramic engine. Early predictions estimated ceramic engines for automotive use would be in mass production by 1984 (Jack 1987). However, after years of international research and hundreds of millions of dollars, no commercial ceramic engine has ever entered production. Despite this, silicon nitride has remained one of the most attractive engineering ceramics for high temperature use. This has been a result of the excellent combination of properties that silicon nitride displays. These include high strength, wear resistance, high decomposition temperature, oxidation resistance, thermal shock resistance, low coefficient of friction, resistance to corrosive environments, and a high modulus to density ratio (Jack 1976). β-Si_3N_4 also often exhibits an intrinsic needle-like grain morphology, which can impart good fracture toughness to the material. Today, the main applications for silicon nitride ceramics are as cutting tool inserts, wear parts and metal processing components (Jack 2000).

2.2 The Si-Al-O-N System

The term "sialon" is an acronym for phases in the Si-Al-O-N and related systems. Hampshire (1991) describes how the existence of sialons was predicted in the late 1960's by Wild et al., when it was reported that α-Si_3N_4 was a defect structure in which

about 1 in 30 nitrogen atoms was replaced by oxygen. It was proposed that more oxygen could replace nitrogen if simultaneously, aluminium replaced silicon in order to maintain charge balance. The search for a new range of oxynitride materials led to sialons being discovered independently in Japan (Oyama and Kamigaito 1971) and England (Jack and Wilson 1972) in the early 1970's.

The two most significant sialon phases are α-sialon (α′) and β-sialon (β′). These phases are isostructural with α-Si_3N_4 and β-Si_3N_4 respectively. Sialons are solid solutions of their corresponding parent phases, and consequently, many physical and mechanical properties are shared between the parent phase and its respective solid solution. Similarities also exist in the processing routes used to form silicon nitride and sialons. Like silicon nitride, sialons require sintering aids if full density is to be attained by pressureless sintering. The sintering aids evolve large volumes of liquid phase during sintering. However, unlike for Si_3N_4, some of the liquid can be incorporated into the sialon structure after densification is complete (Ekström and Nygren 1992). This can substantially reduce the quantity of residual intergranular glass phase, and improvements in properties may result (Hampshire 1991). Additionally, post-sintering heat treatments may be used to devitrify the glass and improve properties such as strength and creep resistance at high temperatures (Jack 1987).

2.2.1 β-Sialon

β-Sialon is a β-Si_3N_4 solid solution formed by the simultaneous equivalent substitution of silicon and nitrogen by aluminium and oxygen. It is described by the formula:

$$Si_{6-z}Al_zO_zN_{8-z} \qquad \text{(Equation 2.1)}$$

where z lies between zero and 4.2 (Jack 1976). This formula shows the two Si_3N_4 units that make up a β-sialon unit cell.

β-Sialon, along with other phases that will be discussed further on, is found in the part of the Si-Al-O-N system with stable valency states, namely the quasi-ternary Si_3N_4-SiO_2-AlN-Al_2O_3 system (Ekström and Nygren 1992). A behaviour diagram of this system,

shown in Figure 2.2, is best represented as a reciprocal salt system, where concentrations are expressed as equivalents. This means any point on the behaviour diagram represents an equal number of anion and cation charges, with 12 positive and 12 negative valencies being represented in this case (Jack 1976). Consequently, all phases or mixtures of phases in which the combining elements Si^{4+}, Al^{3+}, O^{2-} and N^{3-} have their normal valencies lie within this diagram. Figure 2.2 is only an idealised behaviour diagram, and thus it does not necessarily represent true thermodynamic equilibrium (Jack 1976). The β′ phase field is a line that extends along the join Si_3N_4 - $^{1}/_{3}(Al_2O_3.AlN)$, and gives a constant metal to non-metal ratio, M/X equal to 3/4. The range of homogeneity with M/X unequal to 3/4 is quite limited (Jack 1976).

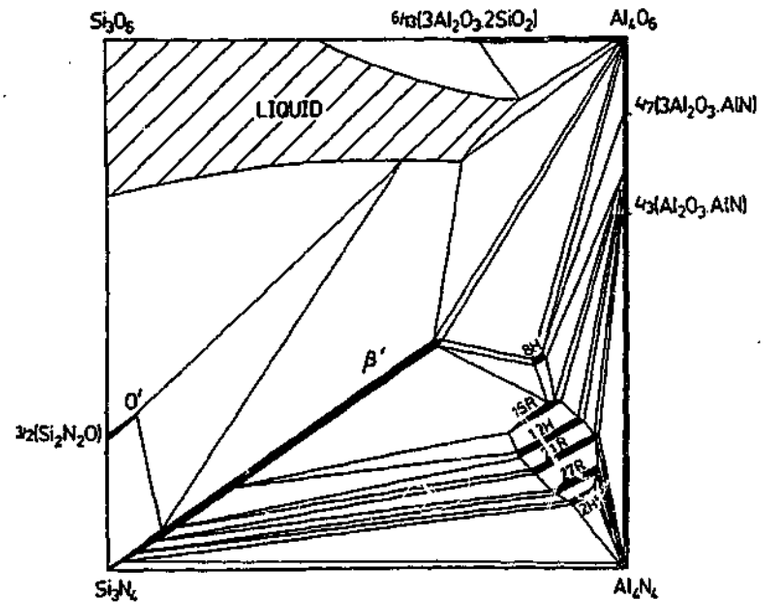

Figure 2.2. The Si-Al-O-N behaviour diagram at 1800°C (Jack 1987).

β-Sialon is the most extensively developed material in the Si-Al-O-N system (Jack 1987; Cao and Metselaar 1991). Much of the reason for this is the relative ease with which β-sialon can be processed. Commercial production of β-sialon utilises small quantities of oxide sintering additives in powder mixtures to enhance densification during pressureless sintering (Hampshire 1991). The oxide additives produce more low viscosity liquid than is formed solely from silicon nitride and its surface silica under similar conditions. Some of the liquid evolved during sintering can be incorporated into the β-sialon structure following densification, resulting in a reduction of residual

intergranular glass phase (Jack 1976). Yttria (Y_2O_3) is a commonly used additive as post-sintering heat treatments allow grain boundary glass and β-sialon grains to react, resulting in the crystallisation of the grain boundary phase and a concurrent improvement in high temperature mechanical properties (Jack 1987).

Because of their similar atomic arrangements, β-sialon and β-Si_3N_4 share similar physical and mechanical properties, such as high strength and a low coefficient of thermal expansion. However, chemically, β-sialon exhibits many characteristics of a[illegible]a (Al_2O_3) (Jack 1987). As β-sialon is a solid solution, it has a lower vapour pressure than β-Si_3N_4. This reduces volatilisation and decomposition at high temperatures, and hence β-sialon tends to be more thermodynamically stable than β-Si_3N_4 (Jack 1987). β-Sialon is more oxidation resistant than β-Si_3N_4 at elevated temperatures (Jack 1976). Furthermore, pressureless sintered β-sialons prepared with sintering aids can produce grains with an acicular, or elongated, morphology that enhance the fracture toughness of the material (Ekström and Nygren 1992).

2.2.2 α-Sialon

The first reporting of α-sialon was by Jack and Wilson (1972) when they reacted lithium silicon nitride ($LiSi_2N_3$) with alumina, and obtained an α-Si_3N_4 structure with a unit cell volume about 3% greater than that of α-Si_3N_4. In this and subsequent work, other phases were always present, and the product never contained more than about 30% of the α-sialon phase. The first pure α-sialons were prepared by Hampshire et al. (1978) from Si_3N_4-AlN-M_xO_y mixtures, where M was Li, Ca or Y.

Like β-sialon, α-sialon is a solid solution based on Si_3N_4. It is isostructural with the α-Si_3N_4 structure. Of most interest is the Me-Si-Al-O-N quinary system, where α-sialon is stabilised by added Me ions which may be Li^+, Mg^{2+}, Ca^{2+}, Y^{3+}, and most of the rare-earth metals (Ekström and Nygren 1992).

The α-sialon unit cell comprises of four Si_3N_4 units and is described by the general formula:

$$Me_xSi_{12-(m+n)}Al_{(m+n)}O_nN_{16-n} \qquad \text{(Equation 2.2)}$$

for a metal ion Me^{v+}, where x = m/v and is ≤2. In contrast to the purely substitutional solubility in β-Si_3N_4, the α-Si_3N_4 structure has two interstitial sites per unit cell that can be occupied by cations (Cao and Metselaar 1991). Consequently, two substitution mechanisms may act. The first, similar to that of β-sialon, involves n(Si-N) being replaced by n(Al-O). The second mechanism is further replacement of mSi^{4+} by mAl^{3+}, with the simultaneous incorporation of xMe^{v+} into the α-phase interstitial sites to maintain charge balance. It can be seen that chemically, β-sialon is in fact an α-sialon with an n-value equal to zero.

Stabilising cations are generally added to compositions as oxides, and it is found that the upper limit of cation solubility in the α-sialon structure decreases with increasing ionic radius (Cao and Metselaar 1991). As there are two interstitial sites per unit cell, a maximum of two cations per unit cell may be accommodated. There also exists a minimum value for the x-parameter of 0.3 to 0.5, indicating an immiscibility gap between α-Si_3N_4 and α-sialon phases (Mandal 1999). The highest solubility reported has been 1.83 Ca^{2+} per unit cell in Ca α-sialon (Jack 1983), and 1.5 Li^+ in Li α-sialon (Kuang et al. 1990). The rare-earth stabilised α-sialons have a much lower solubility limit, the lowest occurring with ~0.6 Nd^{3+} in a Nd α-sialon. Until recently, it was believed that Nd^{3+} (r = 0.99Å) was the largest cation able to enter the α-sialon structure on its own. However, work by Mandal and Thompson (1996) has shown that Ce^{3+} (r = 1.03Å) can enter the α-sialon structure on its own. Cations as large as La^{3+} (r = 1.06Å) and Sr^{2+} (r = 1.26Å) have also been observed to enter the α-sialon structure when combined with Ca^{2+} or Yb^{3+} in multi-cation compositions (Mandal 1999).

The addition of a fifth component to the Si_3N_4-SiO_2-AlN-Al_2O_3 behavior diagram, shown in Figure 2.2, means that the system can no longer be represented diagrammatically in two dimensions. This is overcome by representing the system as a three dimensional Jänecke prism. The concentrations of all components are expressed in

equivalence units, so any point in the prism represents a combination of 12 positive and 12 negative valencies (Hampshire 1991). The base of the prism is the familiar Si_3N_4-SiO_2-AlN-Al_2O_3 diagram, with the cation addition extending the diagram into the third dimension. The two triangular faces of the prism represent pure oxide and pure nitride ternary systems respectively.

Relative to β-sialon, the number of phase equilibrium studies over the range of α-sialon systems has been limited. The Y-Si-Al-O-N system has been the most extensively studied system to date (Cao and Metselaar 1991). A schematic of the Y-Si-Al-O-N Jänecke prism is shown in Figure 2.3.

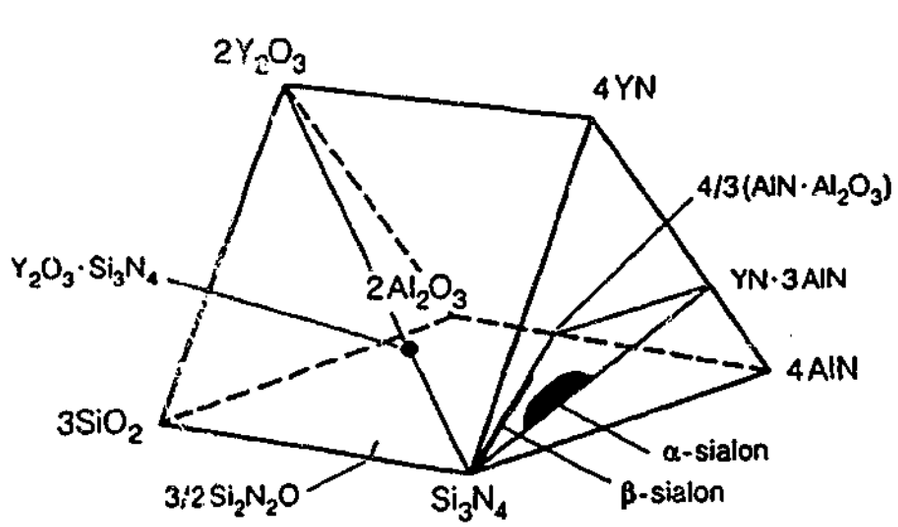

Figure 2.3. Schematic of the Y-Si-Al-O-N Jänecke prism (Hampshire 1991).

At any point within the prism, a number of phases, usually but not always four, will coexist (Sun et al. 1995). The region in which a particular combination of phases coexists is called a compatibility tetrahedron. Often, one of the phases in a compatibility tetrahedron is not crystalline, but rather is a liquid at sintering temperatures, which forms a glass upon cooling.

As phase relationships in the Me-Si-Al-O-N system are very complicated, it is often easier to deal with triangular planes that slice through the Jänecke prism. Phase regions on the plane are then described as two-dimensional compatibility triangles. In the Me-Si-Al-O-N Jänecke prism, the α-sialon phase region has a two-dimensional extension in the

plane with corners at Si_3N_4, $^4/_3(Al_2O_3.AlN)$, and MeN.3AlN (for a trivalent cation Me^{3+}) or $^1/_2(Me_3N_2).3AlN$ (for a divalent cation Me^{2+}). The metal to non-metal atomic ratio ((Si + Al)/(O + N)) on this plane is always 3:4. The β-sialon solid-solution line runs along the Si_3N_4 - $^4/_3(Al_2O_3.AlN)$ side of this triangular plane. Additionally, a two-dimensional monophase α-sialon region is formed along the join Si_3N_4 - MeN.3AlN. It is found that the size of the α-sialon forming region is dependent on cation size, with larger cations decreasing the size of the field (Cao and Metselaar 1991). A phase behavior diagram of the Y α-sialon plane is shown in Figure 2.4.

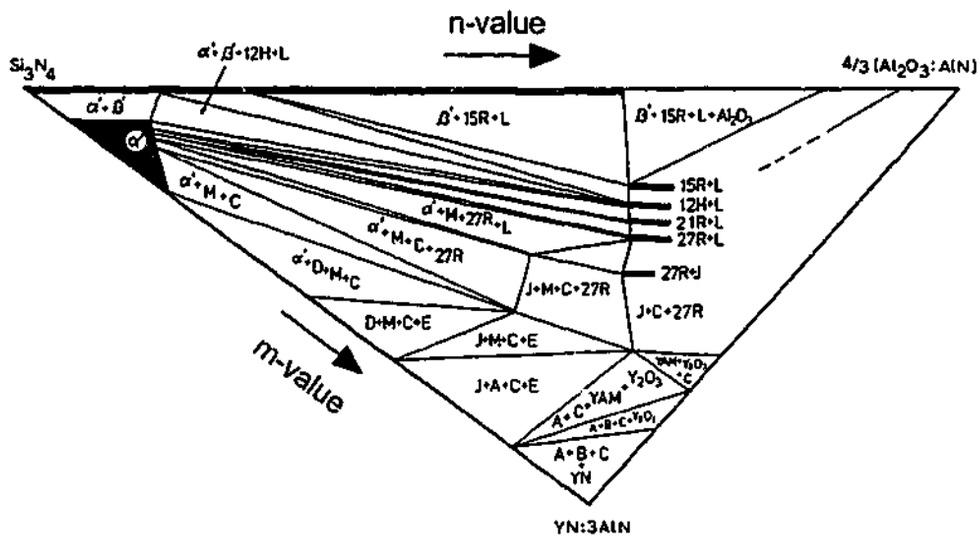

Figure 2.4. Phase relations on the yttrium α-sialon plane at 1750°C (Slasor and Thompson 1987).

The m and n values expressed in Equation 2.2 describe co-ordinates along two sides of the α-sialon plane. The m-value describes co-ordinates along the Si_3N_4 - MeN.3AlN edge, and the n-value describes the Si_3N_4 - $^4/_3(Al_2O_3.AlN)$ edge. Values range from zero for Si_3N_4 to 12 at the other corners. Thus, any composition that lies on the α-sialon plane can be defined entirely by its m and n value. An additional value, called the k-value, is defined as k = (Si + Al) / (O + N). On the α-sialon plane, k is always 0.75, while compositions that lie above or below the plane have lower or higher k-values respectively. This provides a means of describing any Me-Si-Al-O-N composition within the Jänecke prism by its m, n and k values.

In theory, it is possible for densified α-sialon compositions to have no residual intergranular glass phase, as the liquid can be incorporated into the α-sialon structure. In practice, the complete formation and densification of α-sialons is more difficult than for β-sialons, as the high nitrogen content produces an oxynitride liquid with a high viscosity (Hampshire 1991). Densification is further hindered as the liquid phase is consumed by the formation of α-sialon, until at equilibrium, much of the liquid has been incorporated into the α-sialon structure (Cao and Metselaar 1991). Almost all α-sialon microstructures contain some intergranular glass.

An important feature of the α-sialon plane is a compatibility region in which α′ and β′ coexist (Figure 2.4). By varying the composition in this phase field, ceramics can be formed with a tailored α′/β′ ratio (Ekström 1996). This feature is of significant interest, as it is found that the hardness of the composite increases linearly with increasing α-sialon content, while strength remains unchanged (Jack 1987). However, this is achieved at the expense of fracture toughness, which decreases linearly as the α′/(α′+β′) ratio increases. Therefore, (α+β)-sialon composites can be microstructurally tailored for specific applications (Ekström and Nygren 1992), whereby the α-sialon phase imparts hardness to the composite, and the β-sialon phase imparts toughness.

One of the most attractive properties of α-sialons is their high hardness, which is exceeded by only a small group of materials that includes silicon carbide, boron carbide and diamond. Because of its longer stacking sequence, the unit cell parameter of α-sialon in the *c*-direction is approximately double that for β-sialon. This doubles the Burgers vector of the crystal lattice, impeding dislocation motion and contributing to an increase in hardness (Lewis et al. 1981). α-Sialon also possesses strength comparable with β-sialon, good wear and oxidation resistance, and good thermal shock resistance. Unlike β-sialon, which often features highly acicular grain morphologies, α-sialon has generally been considered to occur only as equiaxed grains (Ekström and Nygren 1992). Consequently, monolithic α-sialon materials suffer from relatively poor fracture toughness. This, combined with processing difficulties, has meant that applications for α-sialon have not been nearly as extensive as for β-sialon. Instead, α-sialon has found use mainly as a supplementary phase in (α+β)-sialon composites.

As previously mentioned, α-sialon was always considered to occur only with equiaxed grain morphologies. However, recently a number of groups have achieved growth of α-sialon grains with an elongated morphology (Wang et al. 1996b; Chen and Rosenflanz 1997; Shen et al. 1997; Xu et al. 1997; Hewett et al. 1998a; Zhao et al. 1998). This is of great significance, as it offers the potential for forming microstructurally toughened α-sialons with high hardness, in much the same way as in-situ toughened β-sialons are formed. To date, elongated α-sialon has been observed in a number of different Me-Si-Al-O-N systems, most commonly in those utilising rare-earth oxides and pressure sintering techniques. However, pressureless sintering of Ca α-sialons has also successfully produced elongated grains (Zhao et al. 1998).

Though it has been encountered a number of times, there is currently no satisfactory explanation as to why α-sialon usually grows as equiaxed grains, but under certain conditions grows anisotropically. It has been suggested that large quantities of low-viscosity liquids provide a pathway for rapid diffusion, and room for the growth of elongated α-sialon crystals without steric hindrance (Shen et al. 1997). Large quantities of liquid would give the final material great amounts of grain boundary glass, which are undesirable as the glass can give rise to poor high temperature mechanical properties. Chen & Rosenflanz (1997) claim that using a β-rich Si_3N_4 powder provides fewer α-Si_3N_4 nuclei for α-sialon to nucleate on, allowing the unhindered growth of elongated α-sialon grains. This is analogous to the growth of elongated β-Si_3N_4 from an α-rich starting powder. However, work by Zhao et al. (1998) has shown the development of high aspect ratio α-sialon microstructures using α-rich Si_3N_4 powders and pressureless sintering.

2.2.3 O'-Sialon

O'-Sialon is an important phase in the Si-Al-O-N system, owing to the potential high temperature oxidation resistance of silicon oxynitride (Ekström and Nygren 1992). However, as they are outside the scope of this work, they will only be briefly discussed.

At 1800°C, there is a limited solubility of aluminium and oxygen in silicon oxynitride (Si_2N_2O). Approximately 10 mol.% Al_2O_3 is soluble in the Si_2N_2O structure, giving an O′-sialon solid solution (Jack 1987). O′-sialons are described by the formula:

$$Si_{2-x}Al_xO_{1+x}N_{2-x} \qquad \text{(Equation 2.3)}$$

where x varies from zero to ~0.2 (Ekström and Nygren 1992). The formation of Si_2N_2O from powder mixtures at high temperature is very sluggish due to kinetic hindrance. The addition of yttria and alumina as sintering aids increases the quantity of liquid phase evolved at high temperatures, allowing densification by pressureless sintering. Following densification, some constituents of the liquid phase can be incorporated into the structure, forming O′-sialon. The small volume of residual intergranular glass left over is yttria rich, and can be devitrified in a post-sintering heat treatment to give yttrium disilicate ($Y_2Si_2O_7$).

O′-Sialon is reported as having high strength, a low coefficient of thermal expansion, and good thermal shock resistance (Hampshire 1991). However, it is found that the combined addition of yttria and alumina has a pronounced negative effect on the high temperature properties of the material (Ekström and Nygren 1992). O′-Sialon also has poor fracture toughness, possibly as a result of very strong interfacial bonding between O′-sialon grains and the SiO_2-rich intergranular glass phase, which promotes transgranular crack propagation (Ekström and Nygren 1992). Devitrification of the intergranular glass via a heat treatment weakens the interfacial bond, and this has yielded dramatic increases in fracture toughness (Ekström and Nygren 1992).

2.2.4 Ca α-Sialon

Relative to rare-earth and Y-stabilised sialons, comparatively little work has been carried out on Ca-stabilised α-sialons. This has been partly due to the refractory grain boundary phases that can be produced via heat treatments in the former systems, making them more suited for medium/high temperature applications (Ekström 1996). However, interest in Ca α-sialon has recently increased with the discovery of the unusual microstructures that can be developed by this system.

The most significant feature of Ca α-sialon is the in-situ growth of α-sialon grains with an elongated morphology that may occur during sintering. This phenomenon was first observed in hot-pressed samples by Wang et al. (1996b). Subsequent work has shown that elongated Ca α-sialon grains also develop readily during pressureless sintering (Hewett et al. 1998a; Zhao et al. 1998). Unlike most systems in which anisotropically grown α-sialon has been observed, these materials utilised low-cost raw materials, and simple processing techniques.

In addition to displaying distinctive microstructural features, Ca α-sialon possesses a number of other attractive attributes. The calcium required in compositions is most commonly sourced from $CaCO_3$, an abundant and cheap natural mineral that decomposes at ~800°C to give CaO and CO_2 gas. This represents a significant cost saving over systems that use expensive rare-earth oxide starting powders. As previously mentioned, calcium has the highest reported solubility in the α-sialon lattice, with up to 1.83 Ca^{2+} cations per unit cell being accommodated (Jack 1983). This offers potential for significantly reducing the quantity of residual grain boundary phase in the sintered product, as large amounts of calcium in the grain boundary phase can be incorporated into the α-sialon structure during sintering (Zhao et al. 1998; Wang et al. 1999). The reaction of CaO with SiO_2 and Al_2O_3 on the surfaces of silicon nitride and aluminium nitride starting powders forms a eutectic at 1170°C (Levin et al. 1964). This appearance of liquid occurs at a significantly lower temperature than that observed in other systems (van Rutten et al. 1995), facilitating densification at reduced temperatures.

Ca α-sialon has been found to be more thermally stable than its rare-earth counterparts, and experiences little α′→β′ transformation at temperatures between 1100°C and 1500°C (Hewett et al. 1998b; Seeber and Cheng 1998). While the transformation can be beneficial if the material is to be used at temperatures not exceeding 1000°C, instability of α-sialon at higher temperatures causes a significant deterioration in properties. Recent work by Mandal and Thompson (1999) confirmed the stabilising influence of calcium. They found that α-sialon compositions containing calcium as the principal cation exhibited no α′→β′ transformation above 1450°C. They also noted that in mixed cation α-sialons, calcium acted as a stabiliser, inhibiting the transformation in compositions

that normally would readily have transformed. With all these attractive properties, there is now significant interest in the further development and study of Ca α-sialon.

Until recently, little work had been carried out on the study of phase equilibria in the Ca-Si-Al-O-N system. The first phase relationship diagram of the Ca α-sialon plane, shown in Figure 2.5, was proposed by Jack (1983). More extensive work performed by Hewett et al. (1998a) resulted in a more detailed diagram, shown in Figure 2.6. They found that phases present in fully reacted samples may include α′, β′, AlN and the AlN polytypoids 15R, 12H, 21R, 27R, 33R and $2H^{\delta}$. During the sintering of compositions located on the α-sialon plane, a number of low-temperature intermediate phases are also formed. Two identified by Hewett et al. (1994b) are M-phase ($2CaO.Si_3N_4.AlN$) and gehlenite ($2CaO.SiO_2.Al_2O_3$). M-phase is present at temperatures as low as 1200°C, however it is found to completely redissolve above 1350°C. Gehlenite, a melilite-type phase, is also present at 1200°C, and remelts above 1450°C. The melting of gehlenite evolves large quantities of liquid, which leads to accelerated densification and increased α-sialon formation (Hewett et al. 1994b).

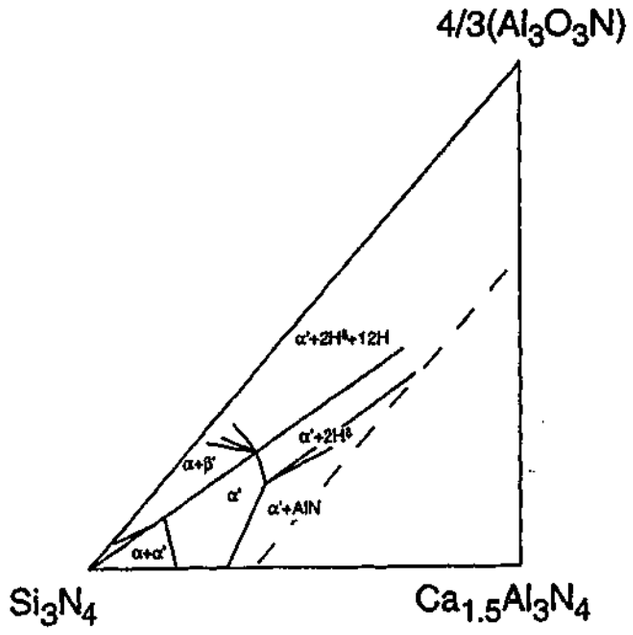

Figure 2.5. Tentative phase behaviour diagram proposed by Jack for the Ca-Si-Al-O-N system (modified from Jack, 1983).

Investigations into Ca α-sialon have increased in recent times (Hewett et al. 1998a; Zhao et al. 1998; Mandal and Thompson 1999; Wang et al. 1999). Work has mainly concentrated on the stabilising effects of calcium, and basic composition-phase-microstructure relationships. However, there is still not a significant amount of knowledge regarding the elongated grain morphologies that develop in this material. Grain growth mechanisms have not yet been explained, and to date there has been no major study into how different factors could influence phase and microstructural development in this material. A study of this nature is required in order to obtain a better understanding of Ca α-sialon, thus allowing it to be further developed into a useful structural material.

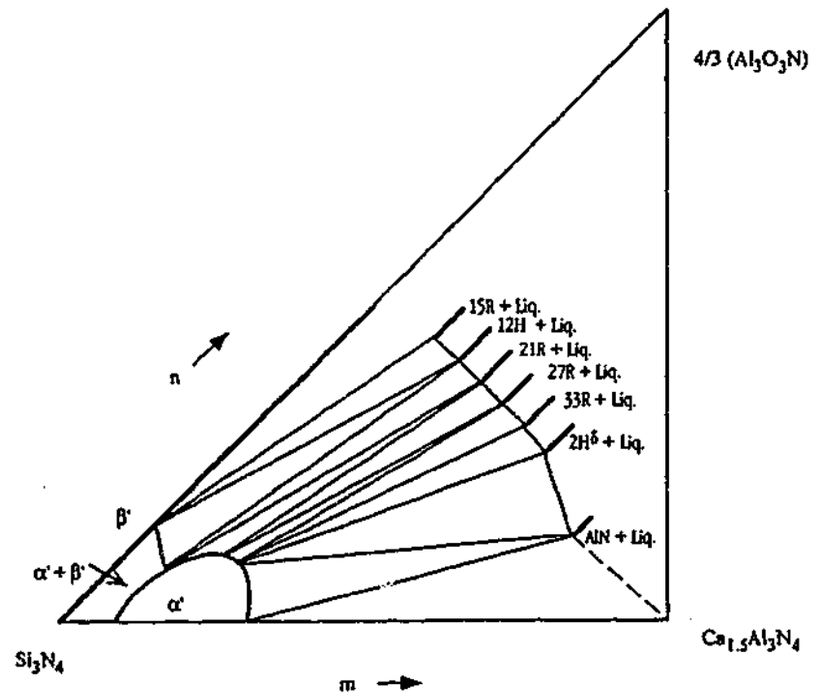

Figure 2.6. Experimentally derived phase behavior diagram of the Ca α-sialon plane from Hewett et al. (1998a).

2.2.5 AlN and the AlN-Polytypoids

In the Si-Al-O-N system, a group of phases termed polytypoids is located between β-sialon and AlN on the Si-Al-O-N phase behavior diagram (Figure 2.2). This group of phases intersects the α-sialon plane at its Al-rich end in the five component Me-Si-Al-O-

N Jänecke prism (Figure 2.3). Consequently, AlN and the AlN-polytypoids are of significant importance, as they frequently occur as equilibrium phases in liquid-rich α-sialon compositions.

A group of six uncharacterised phases located between β' and AlN was first reported by Gauckler et al. (1975). These were later fully characterised by Roebuck and Thompson (1977) as wurtzite-type structures related to AlN. These phases are AlN defect structures that arise from the incorporation of silica into the wurtzite-type 2H AlN structure, and they are termed AlN-polytypoids. Each phase extends along a line of constant metal to non-metal ratio, and has a narrow range of homogeneity (van Tendeloo et al. 1983). The 2H AlN structure has a metal to non-metal ratio (M/X) of 1, and can be designated MX. Structurally, the metal (Al) atoms form a hexagonal close packed arrangement, and the non-metal atoms (N) fill one half of the available tetrahedral interstitial sites, for example, all tetrahedra that point downwards, as is the case for AlN (Jack 1976). Incorporation of silica into the AlN structure causes the M/X ratio to decrease, reaching a minimum of 1/2 when all tetrahedra are filled (van Tendeloo et al. 1983). As the M/X ratio decreases, non-metal atoms have to fill tetrahedra that share faces with already filled tetrahedra. This would give rise to impossibly short interatomic distances between non-metal atoms, and so a stacking fault is introduced to the metal atom configuration, which can accommodate the excess non-metal atoms. This involves the stacking sequence changing locally from hexagonal (ABAB...) to cubic (ABC...), as shown in Figure 2.7. The excess non-metal atoms can then be incorporated into the faulted region, forming a layer where all tetrahedra are occupied. This layer can be designated MX_2 as all tetrahedra are filled with non-metal atoms. Because of the stacking fault, tetrahedra in adjacent half-filled layers only share an edge, which greatly increases the interatomic separation (Jack 1976; van Tendeloo et al. 1983).

Chemically, each of the polytypoids has a fixed metal to non-metal ratio. The structures of each of the phases are directly related to their compositions, which are described by the equation M_mX_{m+1} (where M = metal, X = non-metal). It is seen that the further that M/X deviates from 1, the closer is the stacking fault spacing. The polytypoids, described using Ramsdell notation, are 8H, 15R, 12H, 21R, 27R and $2H^{\delta}$. The H and R signify hexagonal and rhombohedral unit cells respectively, while the numerals indicate the

number of layers in the unit cell along the *c*-direction. The $2H^{\delta}$ polytypoid is a 2H structure expanded along the *c*-direction. It is obtained when M/X ratios are greater than 9/10 but less than 1/1. The concentration of additional non-metal atoms is too small to create an ordered structure, and as a result, the phase is designated $2H^{\delta}$, the δ signifying disorder in the sequence of MX_2 layers. Subsequent to earlier work by Gauckler et al. (1975), van Tendeloo et al. (1983) identified a further three polytypoid phases, 33R, 24H and 39R. The 33R polytypoid phase has been detected in Ca-Si-Al-O-N compositions (Hewett et al. 1998a).

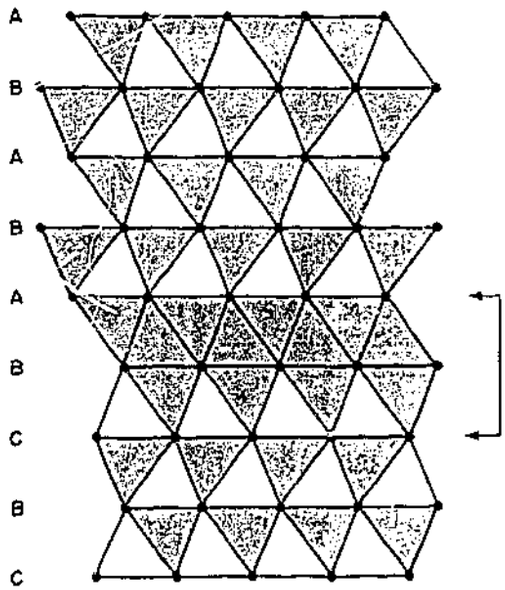

Figure 2.7. [100] projection of a stacking fault in the basic 2H AlN structure (van Tendeloo et al. 1983).

Of the many phases studied in the Si-Al-O-N system, the phases located in the AlN corner of the phase behavior diagram have received the least attention (Cannard et al. 1991). Aluminium nitride grains are often reported to exhibit equiaxed morphologies (Cannard et al. 1991; Zhao et al. 1998). The use of AlN as a structural material has been limited due to relatively poor mechanical properties, and oxidation problems at temperatures greater than 800°C (Hampshire 1991). Aluminium nitride has instead been developed mainly as an electrically insulating substrate material for use in electronics, where its high thermal conductivity allows good heat dissipation.

Studies concerning the fabrication and mechanical properties of AlN-polytypoid ceramics are relatively uncommon. This is despite the fact that as far back as the early 1970's, researchers such as Komeya et al. (1974) recognised that the fibrous microstructures of AlN sintered with SiO_2 additions (the phases they observed had not been fully characterised as polytypoids at this time) could give AlN advantageous mechanical properties. It is now well established that the AlN-polytypoids exhibit needle or plate-like grain morphologies (van Tendeloo et al. 1983; Hewett et al. 1998a), and that these grain morphologies potentially could be used to improve mechanical properties (Komeya et al. 1974; Jack 1976). It has been suggested that composites incorporating lath-like AlN polytypoid phases could enhance properties such as fracture toughness by their presence.

Work by Li et al. (1995) examined an α-sialon–12H polytypoid composite in which a 10 wt.% 12H content was found to improve the strength and toughness of the α-sialon material, without significantly impairing hardness. Recently, Wang et al. (2000) successfully fabricated a dense, near single-phase, 21R ceramic. They were unable to conclude whether the 21R material had potential as a useful structural material in comparison to Si_3N_4-based materials. Rather, they advocated the further development of α-sialon–AlN-polytypoid composites. The authors noted that liquid-rich compositions outside the single-phase α-sialon region that give AlN-polytypoids as equilibrium phases were also more conducive to developing α-sialon with an elongated grain morphology.

2.3 Toughening Mechanisms in Ceramics

The impressive strength and hardness of many high performance ceramics at elevated temperatures, particularly the non-oxide ceramics, makes them ideal for replacing high performance metal alloys in many structural applications. Indeed, Jack (1987) lists numerous programs over the last four decades dedicated to developing Si_3N_4-based ceramics for high performance applications. A number of techniques are available for forming fully dense ceramics that feature many outstanding mechanical properties. However, the inherently poor fracture toughness and reliability of ceramic materials is well established, and this limits their use in many applications. Fracture toughness

values for many structural ceramics are typically 4 - 5 MPa.m$^{1/2}$ (Becher et al. 1995). The brittle nature of these materials means that any flaw or crack existing in a microstructure may propagate rapidly under an applied stress, resulting in a drastic loss of strength and catastrophic failure. Despite these deficiencies, the use of ceramic materials in engineering applications has been pursued because of their many properties that are superior to those possessed by metals and polymers. Owing to the scope of this work, the following discussion will concentrate on Si_3N_4 based systems.

Due to the nature of brittle fracture, any improvement in fracture toughness necessitates the design of ceramics at the microstructural level (Becher et al. 1995). Efforts in this area have been approached in a number of ways. The role of microstructural morphology in fracture toughness was reported in the late 1970's, when it was noticed that fracture toughness was a function of the α/β-Si_3N_4 ratio in starting powders. This ratio controlled the formation of somewhat elongated grains in the sintered microstructure (Lange 1979). In the 1980's, further research led to the introduction of microscopic ceramic whiskers to the materials, forming ceramic composites. These whiskers were most commonly silicon carbide (SiC), and they possessed a similar morphology to the elongated β-Si_3N_4 previously observed (Becher et al. 1995). It was found that the presence of whiskers increased the energy required to propagate a crack, and thus the fracture toughness of the material was increased. These improvements in fracture toughness are found to be a result of the activation of mechanisms such as crack bridging, grain pullout, grain debonding and crack deflection (Iio et al. 1989; Becher et al. 1995). Figure 2.8 shows an example of an elongated Si_3N_4 grain bridging across a crack.

These types of toughening mechanisms are very effective, and fracture toughness values exceeding 10 MPa.m$^{1/2}$ have been attained in SiC whisker reinforced Si_3N_4 (Becher et al. 1995). These materials also often exhibit rising R-curve behaviour, where the resistance to crack propagation increases with crack extension (Kim et al. 1995). This assists in stabilising propagating cracks, and thus reliability is increased. The use of SiC whiskers as a reinforcing phase is now no longer acceptable, owing to health risks associated with inhalation of the microscopic fibres during handling of raw materials. Whisker breakage during processing and hindered densification caused by the whiskers also present significant problems.

In an effort to utilise the advantages of a reinforced ceramic microstructure, attention has been focused on self-reinforced, or 'in-situ toughened', silicon nitrides. In these materials, grains with an elongated morphology are developed during sintering from conventional starting powders. This is a preferred technique, as it eliminates most of the problems associated with using whisker additions, yet it can provide the same benefits. Careful composition selection and processing, and a good understanding of crystal growth mechanisms in supersaturated liquids, are critical factors in forming an in-situ toughened silicon nitride (Kang and Han 1995). Work on β-Si_3N_4 by Becher et al. (1998) found that grain size distributions are strongly related to both the fracture strength and fracture resistance of these materials. Work by the same authors (Sun et al. 1998) has also found that the structure and chemistry of the grain/intergranular glass interface affects fracture resistance.

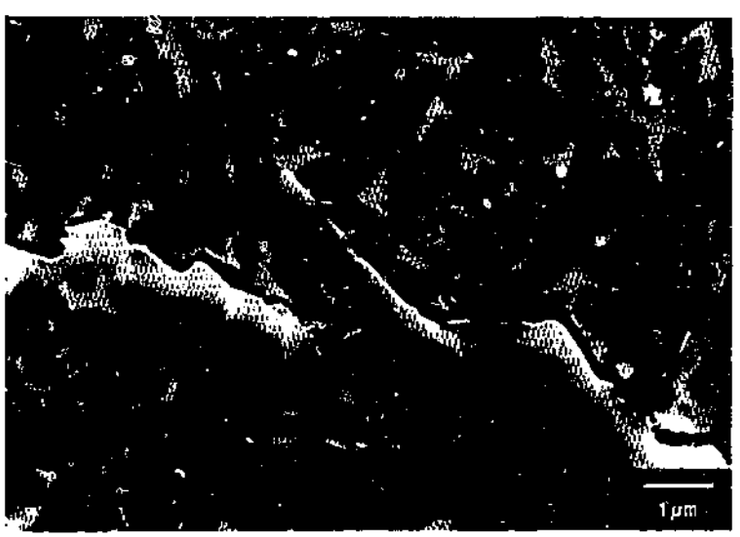

Figure 2.8. Crack bridging in a Si_3N_4 ceramic. The elongated Si_3N_4 grain is pulled out of the matrix as the crack opens (Pyzik and Carroll 1994).

Interfacial behaviour is a critical factor in controlling the effectiveness of elongated grains in toughening a ceramic composite material. For energy absorbing mechanisms such as grain pullout to occur, it is necessary for the reinforcing phase to debond from the matrix. Therefore, the energy required to fracture the grain/matrix interface should be considerably lower than that needed to fracture the reinforcement phase (Becher et al. 1995). The reinforcement phase must have sufficient strength to resist fracture during pullout, and when bridging across or deflecting a propagating crack. Frictional resistance at the interface, following debonding, is also an important factor in relation to effective

toughening via grain pullout. While high frictional resistance enhances fracture toughness, too high a resistance can lead to fracture of the reinforcing phase, and a negating of pullout contributions to fracture toughness (Becher et al. 1995).

2.3.1 Microstructural Toughening in β-Si_3N_4 / β-Sialon

Dense β-Si_3N_4 can be produced as fine equiaxed grains, coarser grains with an elongated morphology, or as a bimodal microstructure which contains elongated grains surrounded by a fine grained matrix, as shown in Figure 2.9.

Figure 2.9. SEM micrograph of plasma etched Si_3N_4 ceramic. The microstructure consists of elongated β-Si_3N_4 grains embedded in a matrix of fine, equiaxed β-Si_3N_4 grains and grain boundary phase (Hoffmann 1994).

How a microstructure is developed is dependent on three parameters; the properties of the Si_3N_4 starting powders, the additive composition, and the sintering conditions (Hoffmann 1994). Most Si_3N_4 ceramics are prepared using α-rich Si_3N_4 starting powders that transform to β-Si_3N_4 during sintering (Hoffmann 1994). As β-Si_3N_4 growth starts on β-Si_3N_4 nuclei present in the starting powders, the composition of Si_3N_4 starting powders is very important. A low β-Si_3N_4 content gives a large interparticle distance between β-Si_3N_4 grains. This allows the grains to grow to a large size, without impinging on each other. At the other extreme, a powder rich in β-Si_3N_4 effectively has grain impingement at the start of densification. This steric hindrance produces a fine-

grained microstructure featuring equiaxed grains (Hoffmann 1994). Emoto and Mitomo (1997) reported that a bimodal microstructure results if the β-Si_3N_4 content is between 0.1 and 10 wt.%. Work by Becher et al. (1998) found that 2 vol.% of β-Si_3N_4 seeds was optimal for producing a distinct bimodal distribution of grain diameters. Samples prepared in this manner exhibited rapidly rising R-curve behaviour, steady state fracture resistance values of over 10 MPa.$m^{1/2}$, and fracture strengths exceeding 1 GPa. Broader grain size distributions were found to be deleterious to both fracture strength and fracture resistance.

Parallels to this type of microstructural development are seen in other ceramic systems as well. Silicon carbide can also develop microstructures containing elongated grains by seeding techniques. Work by Kim et al. (1998) and Mitomo (1999) has shown that the liquid phase sintering of β-SiC powders seeded with α-SiC produces abnormal grain growth, resulting in improved fracture toughness. In a result similar to that for silicon nitride, α-SiC seed contents ≤10 vol.% were found to produce the highest grain aspect ratios (Kim et al. 1998). It was suggested that seed contents of 0.1 to 1 wt.% could produce distinctly bimodal microstructures.

β-Si_3N_4 and β-sialon exhibit very similar in-situ toughening behaviour, though β-sialon possesses a number of different features. β-Sialon is reported to exhibit a more homogeneous elongated microstructure than β-Si_3N_4, as prolonged heating appears to promote an equilibrium grain size (Einarsrud and Mitomo 1993). Average grain sizes are reported to increase with increasing z-value in the β-sialon equation (Eqn. 2.1) (Kim et al. 1995). It is also reported that β-sialons prepared from a powder mixture of α-Si_3N_4, Al_2O_3 and AlN show a higher rate of grain growth, and the development of a larger aspect ratio than samples prepared from single phase β-sialon powder (Einarsrud and Mitomo 1993). The exact mechanisms of β-Si_3N_4/β-sialon grain growth are the subject of much debate.

2.3.2 Microstructural Toughening in α-Si_3N_4 / α-Sialon

Densified α-Si_3N_4 materials are uncommon for a variety of reasons. Firstly, most Si_3N_4 processing routes involve liquid phases and high temperatures. These conditions

inevitably lead to the transformation of α-Si_3N_4 to β-Si_3N_4. Secondly, α-Si_3N_4 grains generally form with equiaxed morphologies. β-Si_3N_4 has an intrinsic needle-like morphology, and for this reason, β-Si_3N_4 is the preferred phase in densified Si_3N_4 components. The predominant use for α-Si_3N_4 is in Si_3N_4 starting powders, where high α-Si_3N_4 contents are critical to facilitating the solution-precipitation process, and to forming sintered β-Si_3N_4 microstructures with elongated grains. Consequently, there is little information regarding the fracture toughness properties of dense α-Si_3N_4 materials.

In contrast to α-Si_3N_4, dense monolithic α-sialons are significant structural materials. For many years, monolithic α-sialon materials had a reputation for poor fracture toughness. This resulted from their generally equiaxed grain morphology. However, as was mentioned earlier in this chapter, under certain circumstances, anisotropic growth of α-sialon grains can occur. This creates the potential for engineering monolithic α-sialons with improved fracture toughness. As elongated α-sialon is a relatively recent discovery, information concerning the anisotropic growth of α-sialon is limited. As such, the mechanisms of α-sialon grain growth, and the factors that can influence it, are not yet fully understood.

There is currently no standard method for developing elongated α-sialon microstructures that covers all α-sialon systems. Moreover, processing techniques employed for one system do not necessarily work for another. For example, Chen and Rosenflanz (1997) obtained elongated grain growth in hot-pressed Nd and Yb α-sialons by using β-Si_3N_4 starting powders seeded with α-Si_3N_4. The α-Si_3N_4 seeding was considered to be a critical step in this processing route. However, work by Hewett et al. (1998a) and Zhao et al. (1998) on pressureless sintered Ca α-sialon, has shown that high aspect ratio elongated grains develop readily in compositions that utilise only α-Si_3N_4 starting powders. It is clear that further research into the anisotropic grain growth of α-sialons is required in order to explain these types of inconsistencies.

The presence of elongated grains in α-sialon materials is expected to improve their fracture toughness, however this improvement has not always been observed. Many reports indicate significant improvements in fracture toughness for elongated α-sialons

(Chen and Rosenflanz 1997), while some have seen no variation with α-sialon morphology (Nordberg et al. 1997). Contrasting results like this could be explained by comparing them to the extensively studied β-Si_3N_4/β-sialon systems. As previously discussed, factors such as interfacial behaviour play a large role in the effectiveness of elongated grains in toughening a ceramic. Less than optimal interface conditions can significantly hinder the mechanisms that give rise to increased fracture resistance (Hoffmann 1994). It is a fair assumption that the same factors would apply for elongated grains in α-sialon materials. Therefore, it is reasonable to conclude that elongated grains in α-sialons do offer the potential to improve fracture toughness, if other properties of the material are optimised to allow for this.

Though not yet fully understood, the growth of elongated α-sialon grains is an important step in the development of high performance non-oxide ceramics. The production of hard α-sialons with improved fracture toughness and reliability should create numerous new applications for these materials.

2.4 Grain Growth in Si_3N_4-based Ceramics

Issues concerning the mechanisms of grain growth in silicon nitride and the sialons have been the subject of much debate over an extended period. Most of this debate has focused on the β-Si_3N_4/β-sialon systems. The rod-like morphologies of grains in these systems are critical to developing the good mechanical properties that these materials exhibit. However, an understanding of the mechanisms that produce the distinct faceted rods has, for the most part, been rudimentary (Kramer et al. 1994).

Control of grain growth in β/β′ systems can occur by two possible mechanisms. The first is control by the liquid/solid interfacial reaction. In this case, grain growth is controlled by the rate of reaction at the liquid/grain interface. The second alternative is control by diffusion. In this case, grain growth is limited by the rate of solute diffusion in the liquid phase (Kitayama et al. 1998a).

From experimental observations, it has been determined that the growth exponent, n, in the following empirical equation, indicates which of the two mechanisms governs grain growth:

$$r^n - r_0^n = kt \qquad \text{(Equation 2.4)}$$

where r and r_0 are the final and initial grain sizes respectively, n is the growth exponent, k is the rate constant, and t is time. Interfacial reaction control is indicated by $n = 2$, while diffusion control is represented by $n = 3$ (Kitayama et al. 1998a).

Work on this subject by a number of researchers has produced a range of results, many of which have been contradictory. For example, work by Einarsrud and Mitomo (1993) on β-sialon compositions found that grain size decreased with increasing liquid phase content. This was considered clear evidence for diffusion controlled grain growth. Contradicting this, work by Lee et al., (1988) on β-sialon found that mean grain size was independent of liquid content, indicating that grain growth was interfacial reaction controlled. The faceted shape of β-Si_3N_4/β-sialon rods has also been considered an indication of interfacial controlled grain growth (Kang and Han 1995; Kitayama et al. 1998c).

More recent work by Kitayama et al. (1998b) examined β-Si_3N_4 grain growth by modeling and simulation techniques. Their simulations were found to be in excellent agreement with experimental observations by other researchers. They concluded that grain growth in β-Si_3N_4 was completely controlled by interfacial reaction, in both the length and width directions of the crystal. They also suggest that different interfacial reaction constants in the *a* and *c* directions of a β-Si_3N_4 crystal determine and control the intrinsic rod-like shape of β-Si_3N_4. Differences in aspect ratios could be brought about by altering these parameters.

In a related study by Kitayama et al. (1998c), the effect of different lanthanide additives on the Ostwald ripening of β-Si_3N_4 was investigated. Three additives, La, Gd and Yb, were examined. It was found that large differences in the aspect ratios of β-Si_3N_4 grains existed for the three different compositions after Ostwald ripening. These differences

were not found to be an effect of the different glass viscosities from the different additives causing a shift from interfacial to diffusion control. Rather, it was proposed that the lanthanide ions had a catalytic effect on the growth planes of the crystal, causing altered interfacial reaction rates at the {100} and/or (001) planes.

Considerably less work has been done with respect to the nucleation and growth of α-sialon. For a long period it was believed that α-sialon always exhibited equiaxed grain morphologies (Ekström and Nygren 1992). However, the more recent discoveries of elongated α-sialon grains in a number of α-sialon systems has prompted increased interest in this subject (Wang et al. 1996b; Chen and Rosenflanz 1997; Shen et al. 1997; Xu et al. 1997; Hewett et al. 1998a; Zhao et al. 1998). Just as an understanding of the factors that control the anisotropic growth of β-Si_3N_4 and β-sialon is essential to the better engineering of these materials, a more complete understanding of grain growth in α-sialons is also necessary.

Work by Hwang and Chen (1994) on an yttrium α-sialon, prepared using α-Si_3N_4 powder, found that fully-grown α-sialon grains always contained an α-Si_3N_4 core. This was considered evidence of heterogeneous nucleation operating in the system. It was concluded that the growth of α-sialon on α-Si_3N_4 was epitaxial, despite compositional and lattice parameter differences between the two phases. Growth was observed to initiate at a number of sites on a single α-Si_3N_4 seed crystal, with the various growth fronts converging at irregular interfaces to form a single α-sialon grain. No growth habits were observed, and the resultant grain morphology was equiaxed. It was suggested that microstructural control could be achieved by controlling the size distribution of the starting α-Si_3N_4 powder.

Work by Chen and Rosenflanz (1997) adopted a derivative of this idea to achieve anisotropic grain growth in Nd and Yb α-sialons. They utilised β-Si_3N_4 starting powder, with the addition of α-Si_3N_4 seed particles. The seed crystals were added to provide a limited number of nucleation sites for α-sialon. This technique was reminiscent of the addition of coarse β-Si_3N_4 seeds to α-Si_3N_4 powders, used to produce large elongated β-Si_3N_4 grains in sintered β-Si_3N_4 materials (Emoto et al. 1999). The reduction in the

number of α-sialon nucleation sites proved successful, and elongated α-sialon microstructures resulted. However, the processing techniques used in this work were relatively complex, involving the use of gas pressure sintering (GPS) and extended sintering times of up to 12 hours to obtain extensive anisotropic grain growth.

Further work by Rosenflanz and Chen (1999) examined the effect of different Si_3N_4 starting powders on α-sialon formation. As most past work on α-sialons utilised α-Si_3N_4 starting powder, they examined the effects of using both α-Si_3N_4 and β-Si_3N_4 powders. They found that the β-Si_3N_4 → α-sialon transformation occurred at a slower rate than the α-Si_3N_4 → α-sialon transformation. They attributed this difference to the increased thermodynamic stability of β-Si_3N_4 creating a reduced driving force for the β-Si_3N_4 → α-sialon transformation. They also found that the transformation to α-sialon proceeded faster when smaller modifying cations were utilised. The faster transformation rate was attributed to the increased stabilisation of α-sialon by smaller cations, which creates a larger driving force for the transformation.

With the exception of Ca α-sialon, almost every observation of elongated α-sialon has been in samples prepared using hot-pressing or hot isostatic pressing techniques (Wang et al. 1996b; Chen and Rosenflanz 1997; Shen et al. 1997; Xu et al. 1997). These techniques are both complex and expensive. Whilst the initial observations of elongated Ca α-sialon were also made in hot-pressed samples (Wang et al. 1996b), it soon became apparent that the anisotropic growth of Ca α-sialon grains readily occurred during pressureless sintering (Hewett et al. 1998a). The ease with which elongated Ca α-sialon grains form currently appears unique, and offers significant potential to this system. However, a full understanding of this grain growth behaviour is currently lacking. Studies concerning the kinetics of elongated grain growth, and an examination of what factors affect this growth, are only now beginning to be addressed.

Chapter 3

Experimental Procedures

3.1 Introduction

This chapter describes the experimental procedures relevant to the discussion of the work undertaken. The calculation of compositions, the raw powders utilised in composition preparation, and the techniques used for powder processing and the shape forming of powders into green bodies are detailed in Section 3.2. The procedures used for the sintering of powder compacts are described in Section 3.3. Lastly, the techniques used in the characterisation of raw powders and densified materials are described in Section 3.4.

3.2 Powder Processing and Green Body Forming

Ca-Si-Al-O-N compositions produced as a part of this work were calculated according to the α-sialon formula (Eqn. 2.2). All compositions were designed to be positioned on the α-sialon plane in the Ca-Si-Al-O-N Jänecke prism, with molar quantities of the various components calculated to give overall charge neutrality. Calculations accounted for oxides present on the surfaces of the nitride starting powders. Once molar percentages of the components in a composition were calculated, the weight percentages of the required starting powders were ascertained. The weight percentage breakdowns of individual compositions are detailed in the relevant chapters.

The powders used in the processing of compositions are detailed in Table 3.1. Included are the grade, purity and particle size of the powders, where quoted by the manufacturers. The oxygen contents of the nitride powders are also recorded.

Table 3.1. Details of powders used in initial composition processing.

Powder	Manufacturer	Grade	Particle Size* (μm)	O content (wt.%)
α-Si_3N_4	HC Starck	LC10	0.50	1.94
α-Si_3N_4	HC Starck	M11	0.65	1.20
β-Si_3N_4	Denka	SN-F1	2.5	-
AlN	HC Starck	B	1.75	2.0
Al_2O_3	Ajax Chemicals	-	-	-
$CaCO_3$	Ajax Chemicals	-	-	-

*Particle size is the quoted mean particle size, where supplied by the manufacturer.

Following composition calculations, batches of 100g were weighed out using an electronic balance. Batches were then ball milled in polymer jars for 24 hours with 100 ml isopropyl alcohol and 250 g Si_3N_4 balls as milling media. After milling, jars were placed in a drying oven at 80°C to evaporate the isopropyl alcohol from the slurry. Once dry, powders were passed through a coarse mesh sieve to separate out the Si_3N_4 balls. Powders were then hand mixed for 5 minutes using a mortar and pestle to break up any powder agglomerates and remove any settling effects that may have resulted from the drying process.

When only a small amount of powder was required, batches of 20 g were prepared by hand mixing powders using an agate mortar and pestle. Isopropyl alcohol was added to the powders to create a slurry that was mixed for 15 minutes. The slurry was then dried at 80°C and given a final mix for 5 minutes to ensure homogeneity of the batch.

Processed powders were shape formed into cylindrical pellets by uniaxial pressing in a steel die under 25 MPa pressure. Two sizes of sample were fabricated. Either 4 g of powder was pressed into a 14 mm diameter pellet, or alternatively, 9 g was pressed into a 25 mm diameter pellet. Shape formed pellets were then vacuum-sealed in polymer bags and cold isostatically pressed at 200 MPa for 2 minutes.

3.3 Pressureless Sintering

All samples fabricated in this study were densified by pressureless sintering. For sintering, samples were contained in a covered graphite crucible. To reduce weight losses during sintering, samples were packed in a 50 wt.% Si_3N_4 - 50 wt.% BN powder bed. Up to four samples were contained in one crucible for sintering. Only samples with the same or similar compositions were sintered together so as to avoid any cross-contamination of the samples from vapour phases generated at high temperatures. Sintering was performed in a Thermal Technology graphite resistance furnace (Model 1000-4560-FP20) and proceeded as follows:

i. crucible with samples was loaded into the furnace, the furnace chamber was evacuated to –100 kPa, flushed with N_2, and re-evacuated.
ii. furnace heating commenced at 30°C/min.
iii. samples containing $CaCO_3$ were heated to 900°C and held for 1 hour under vacuum to decompose $CaCO_3$ to CaO. Samples not requiring a calcining step were heated under vacuum to 600°C.
iv. furnace chamber was backfilled with high purity N_2 up to atmospheric pressure, with a slight positive pressure maintained by flowing N_2 at a rate of 10 litres/hour.
v. furnace heating continued at 30°C/min. up to 1000°C.
vi. furnace was heated to the desired dwell temperature at the required heating rate.
vii. furnace was dwelled at the desired temperature for the required time.
viii. furnace was cooled at its natural rate by shutting off power, giving an average cooling rate of ~40°C/min from 1800°C to 1500°C, and ~20°C/min. to 1000°C.
ix. N_2 flow was maintained until 600°C.

Furnace temperature was monitored using a Raytek optical pyrometer. Furnace heating was controlled by an Eurotherm 902P programmer/controller connected to a W5%-W26% Re Type C thermocouple. When thermocouple failure occurred, furnace heating was performed manually using the pyrometer as a temperature guide. Manual control resulted in heating rates accurate to within ±2°C/min. of the desired rate.

3.4 Sample Characterisation

3.4.1 Weight Changes

Weight changes that occurred in samples during sintering were measured by weighing samples immediately before and after sintering. Calculations accounted for weight losses arising from the decomposition of $CaCO_3$. Weight changes could not be accurately determined for excessively liquid rich samples in cases where significant amounts of packing powder bonded to the bloated samples.

3.4.2 Density Determination

The apparent density of sintered samples was determined by the water immersion technique, using Australian Standard AS1774.5 (1989) as a guide. Prior to density measurements, samples had their surfaces lightly ground to remove any surface coating that formed during sintering. Once cleaned, samples were boiled in distilled water for 1 hour and allowed to cool to room temperature. Samples were then weighed on a balance whilst suspended in the distilled water to record their immersed mass. The temperature of the water was measured between samples in order to monitor the density of the suspension liquid. Samples were then removed from the water, had their surface water dried off with damp paper towel, and had their saturated mass recorded. Finally, samples were dried in an oven at 180°C for 2 hours, and had their dry mass recorded. From this data, the apparent bulk density was calculated using the following equation:

$$\text{Apparent Density} = \frac{M_D \times D_L}{M_S - M_I} \ (\text{gcm}^{-3}) \qquad \text{(Equation 3.1)}$$

where M_D = dry mass of the sample (in grams)

M_I = immersed mass of pellet suspended in distilled water (in grams)

M_S = saturated mass of the sample after boiling (in grams)

D_L = density of the suspension liquid (in gcm^{-3})

Each sample had M_D, M_I and M_S measured three times to improve the accuracy of the density measurement.

The bulk density of green bodies was determined using the mercury immersion technique. Each sample was first immersed in mercury and had its buoyancy force measured. The sample was then removed from the mercury and had its dry mass measured. A reading of the air temperature was taken as a guide for the temperature of the mercury, which was then used to determine the density of the mercury. These values were then used in the following equation to give the bulk density of the sample:

$$\text{Bulk Density} = \frac{M_{air} \times \rho_{Hg}}{M_{air} + M_{Hg}} \ (\text{gcm}^{-3}) \qquad \text{(Equation 3.2)}$$

where M_{air} = dry mass of the sample (in grams)

M_{Hg} = buoyancy force of sample, submerged in mercury (in grams)

ρ_{Hg} = density of the mercury (in gcm^{-3})

3.4.3 X-Ray Diffractometry (XRD)

Crystalline phase assemblages of sintered samples and raw powders were analysed by x-ray diffractometry. XRD analyses were performed on the inner bulk of sintered samples. Initial preparation for XRD analysis involved cutting samples in half with a diamond-edged wafering saw to expose a cross-section of the material. Exposed surfaces were then ground flat and polished with silicon carbide paper, finishing with #1200 grade paper. The outer edges of each sample had a bevel ground on them to prevent any surface anomalies from affecting the XRD analyses.

XRD work was carried out on a Rigaku-Geigerflex x-ray diffractometer using Ni-filtered CuK_α radiation, operating at 40 kV and 22.5 mA. XRD scans covered Bragg angles from 10° to 80°. Scans were carried out at a speed of 1°/min., with step intervals of 0.04°. Recorded data were processed with the TRACES® software package. Crystalline phase identification was made with reference to the JCPDS Powder Diffraction File.

Qualitative analyses of sample phase assemblages were made by comparing the relative intensities of the strongest peaks for each of the phases in a recorded spectrum, as shown in the relevant powder diffraction files. Alternative peaks were used when peak overlap occurred. The peak with the highest counts was assigned a relative intensity of 100, and the strongest peaks from any other phases were measured relative to this. Peak intensities were defined as follows: tr = trace (relative intensity ≤3); vw = very weak (3-9); w = weak (10-19); mw = medium weak (20-34); m = medium (35-49); ms = medium strong (50-64); s = strong (65-79); vs = very strong (80-100).

X-ray diffraction was also used to obtain lattice parameter measurements of crystalline phases. Small pieces of samples to be analysed were ground to a fine powder using an alumina mortar and pestle. Approximately 20 wt.% of –325 mesh Si powder was added to the crushed sample as an internal standard. Scans covered Bragg angles from 5° to 60°, using a scan speed of 0.2°/min. and step intervals of 0.01°. Recorded data was initially processed with TRACES®. Lattice parameters were then determined using the least squares refinement program CELSIZ (Scott 1986). The program utilised the Si standard diffraction peaks to correct for any errors that arose during the XRD scan acquisition.

3.4.4 Electron Microscopy

3.4.4.1 Scanning Electron Microscopy (SEM)

Scanning electron microscopy was used for microstructural and chemical analyses of sintered samples. Polished and fracture surfaces were both examined.

Polished samples for SEM examination were initially prepared by cutting a section of material from the sintered sample with a diamond-edged wafering saw. The surface to be examined was then ground with successively finer grades of SiC paper (#120, #320, #800, #1200). This was followed by polishing using 3μm and then 1μm diamond paste, and then ultrasonic cleaning in ethanol.

Almost no contrast exists between α-sialon and intergranular glass phase in back-scattered electron images of Ca α-sialons. This necessitates the etching of polished samples to remove grain boundary glass to highlight grain morphologies. Etching was accomplished by using NaOH. NaOH granules were placed in a Ni crucible and heated over a Bunsen burner until a hot, clear solution of molten NaOH was obtained. Polished sample surfaces were immersed in the molten solution and held for ~10 seconds after the first appearance of bubbles around the sample edge. Experience suggested that the appearance of bubbles indicated that etching was proceeding effectively. Once the sample was removed from the etchant, it was immediately rinsed thoroughly under running water to remove all traces of NaOH.

After etching and washing, samples were dried, mounted on Al discs, and had a conductive coating applied to prevent charging in the SEM. Samples for microstructural observation were coated with gold using a Dynavac sputter coater. Samples were coated for 3 ½ minutes using a sputter current of 40 mA. Samples for energy dispersive x-ray spectroscopy (EDXS) analysis were coated with carbon using a VCR Group IBS TM200S ion beam sputter coater. A 20 nm layer of carbon was applied.

Fracture surfaces for SEM examination were prepared by placing a section of material in a small polymer bag and compressing the material in a vise until it fractured. The fresh fracture surface was then mounted and gold coated using the method previously described.

Samples were observed in a JEOL JSM-840A SEM operated at 20 kV. Secondary electron images were recorded using either the photographic camera facility or digital image capture software. The SEM was equipped with an EDXS system comprising of an Oxford ultra-thin aluminium/mylar window detector and Moran Scientific multi-channel analyser (MCA). This allowed qualitative elemental analyses of microstructural features to be carried out. The electron probe had a diameter of ~1μm, and elements of $Z>5$ were detectable, though the performance of the detector for elements of $Z<10$ was relatively poor. Additionally, two micrographs contained in Chapter 6 were obtained using a JEOL JSM-6340F field emission gun SEM (FEGSEM) located at the National Industrial Research Institute of Nagoya, Japan.

3.4.4.2 Transmission Electron Microscopy (TEM)

Samples for TEM examination were prepared as thin foils. Foils were produced by first cutting a slice of material ~1 mm in thickness from the bulk sample with a diamond-edged wafering saw. The slice was then attached to a glass slide using wax as a bonding medium. A 3 mm disc was cut out of the slice with a Gatan ultrasonic cutter using fine boron carbide grit as a cutting medium. The disc was subsequently cleaned in acetone to remove any wax, had its thickness measured with a micrometer, and was attached to a small brass stub with wax. The sample was then mechanically ground with #1200 grade SiC paper to a thickness of 300μm, followed by polishing the ground surface of the disc with 3μm and 1μm diamond paste. The disc was then removed from the stub, measured, turned over, reattached to the stub, and mechanically ground to a thickness of 100μm. A Gatan dimple grinder was then used to dimple the disc to a central thickness of 20μm, followed by polishing the dimpled surface with 3μm and 1μm diamond paste. The dimpled disc was next mounted on a sample holder and placed in a Gatan dual ion beam mill to thin the disc to perforation. The mill was operated at a voltage of 4 kV and a combined beam current of 1 mA. Ion beam operating angles used were 15° for the first 4-6 hours of milling, followed by 8° for the remaining time. Once thinned to perforation, the foil was coated with a 5 nm layer of carbon to prevent charging, using the ion beam sputter coater.

Samples of powders that needed to be analysed by TEM were prepared by placing a sample of the powder in a small agate mortar. Chloroform was added to the powder, and then the powder was ground using a rocking motion of the pestle. This technique was used in order to cleave the small crystals in the powder, thus obtaining thin sections of crystal suitable for TEM analysis. Once the powder was ground, the finest particles in the chloroform were picked up with a pipette. A drop of the suspension was then placed on a holey carbon film supported on a copper grid. Once the chloroform evaporated, the sample was ready for examination in the TEM.

For TEM analysis, foils were mounted in a low-background double-tilt sample holder. Analyses were carried out on a Philips CM20 Analytical Scanning Transmission Electron Microscope (ASTEM) operated at 200 kV. The STEM was equipped with an Oxford ultra-thin aluminium/mylar window EDXS detector and a Moran Scientific

MCA. Work was performed in both conventional TEM and nanoprobe scanning modes. Nanoprobe scanning mode enabled elemental analyses of very small regions of a sample by virtue of an electron probe measuring only a few nanometres in diameter. Phases were characterised crystallographically using convergent beam electron diffraction (CBED) and selected area electron diffraction (SAED). EDXS was utilised for qualitative elemental analyses. Micrographs of images and diffraction patterns were recorded using the conventional TEM plate camera.

3.4.5 Hardness and Fracture Toughness Testing

3.4.5.1 Hardness Testing

Samples for hardness testing were prepared by grinding and polishing a flat section of sample down to a 1μm finish. Tests were conducted using a Vickers diamond pyramid indenter with a load of 20 kg. This produced a diamond shaped impression in the sample surface, as shown in Figure 3.1.

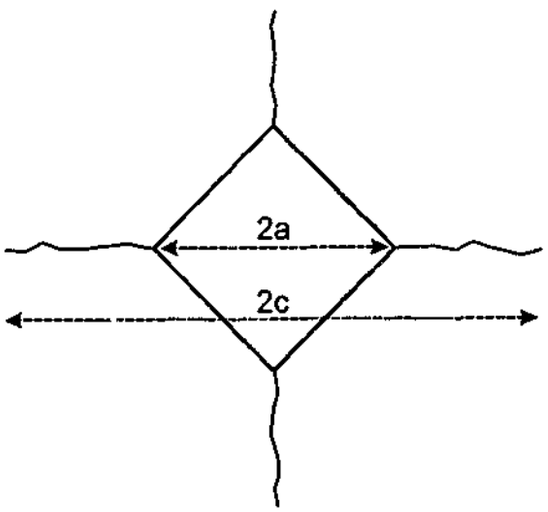

Figure 3.1. Schematic diagram of an indentation made on a sample surface by a Vickers diamond pyramid indenter. The indentation diagonal length, 2a, and crack tip to crack tip distance, 2c, are used in the calculation of sample hardness and fracture toughness.

The diagonal length of an indentation, defined as 2a, was measured in both directions and averaged. The hardness (in GPa) was then determined using the following equation, where P is the indenter load in Newtons (N):

$$H=P/2a \qquad \text{(Equation 3.3)}$$

Each hardness test comprised of six indentations. The highest and lowest values measured were discarded, and the mean of the four remaining values was determined to be the sample hardness.

3.4.5.2 Fracture Toughness and R-Curve Testing

The fracture toughness (K_C) of samples was determined using the indentation technique described by Anstis et al. (1981). This technique uses a Vickers diamond pyramid indenter in the same manner as for the hardness test. The indentation causes radial cracks to propagate from the vertices of the diamond shaped impression when the load is beyond a certain value. The diagonal crack tip to crack tip distance, shown as 2c in Figure 3.1, is then used in the following equation to calculate the fracture toughness:

$$K_c = \S_v(E/H)^{1/2}(P/c_O^{3/2}) \qquad \text{(Equation 3.4)}$$

where $\S_v$ is a material-independent constant for Vickers-produced radial cracks, E and H are the Young's modulus and Vickers hardness of the material respectively, P is the indenter load in Newtons, and c_O is the post-indentation equilibrium crack dimension (i.e. half of 2c). The value used for the constant $\S_v$ was 0.016, as determined by Anstis et al. (1981). The value used for E, Young's modulus, was 240 MPa.

Testing of this type may reveal a tendency for the measured fracture toughness to increase with increasing crack length, an effect referred to as rising R-curve behaviour. By using different indenter loads, a range of crack propagation lengths can be generated. A plot of the crack growth resistance parameter, K_R, versus crack length can then reveal what, if any, rising R-curve behaviour exists. The parameter K_R is equal to K_c in Equation 3.4.

Sections of samples for R-curve analyses were prepared and tested according to the procedure used by Kim et al. (1995). Samples were initially ground flat and polished to a 1μm finish. The surface to be tested was then sputter coated with a fine layer of gold to assist in following crack paths for accurate measurement. Prior to testing, samples were coated with a thin film of silicone oil to slow moisture-assisted post-indentation slow crack growth, a significant effect described by Anstis et al. (1981). Vickers indenter loads ranging from 0.0098N to 490N were used to generate cracks of varying lengths. R-curves for the materials were then established by plotting crack length against the crack growth resistance parameter, K_R.

Chapter 4

Reaction Sequence and Microstructural Development of Compositions in the Vicinity of the α-Sialon Phase Region

4.1 Introduction

For a significant period, the Ca-Si-Al-O-N system has received only limited research interest. Most α-sialon research has tended to concentrate on the yttrium and rare earth systems, mainly because of the good high temperature properties these materials typically possess. More recently, the Ca α-sialon system has been the subject of renewed attention. This interest has arisen from recent research that indicates the system possesses a number of attractive attributes.

The most notable work to date concerning Ca α-sialons has been carried out by Hewett and coworkers (1994b; 1998a; 1998b). They thoroughly examined phase relationships and microstructural development of Ca-Si-Al-O-N compositions located in the Si_3N_4 corner of the Ca α-sialon phase behavior diagram (Figure 4.1). They found that Ca α-sialon is compatible with a variety of crystalline phases, including AlN and AlN-polytypoids. β-Sialon is also found to be compatible with α-sialon in compositions located in the α′/β′ phase field near the Si_3N_4 corner of the phase behavior diagram. These compositions are in equilibrium with varying quantities of amorphous intergranular phase (Hewett 1998). It is possible to form single-phase α-sialons. However, in practice a small amount of residual amorphous intergranular phase is almost always present in these materials (Cao and Metselaar 1991).

In many of the Ca-Si-Al-O-N compositions examined by Hewett and coworkers, Ca α-sialon exhibited the characteristic equiaxed grain morphology of α-sialon (Hewett et al. 1994a). However, a number of compositions with higher m-values in the Ca α-sialon

equation (Eqn. 2.2) were observed to produce anisotropic α-sialon grain growth during pressureless sintering (Hewett et al. 1998a).

This observation of elongated Ca α-sialon grains is significant, as this type of grain morphology could be utilised to improve the relatively poor fracture toughness of monolithic α-sialon materials.

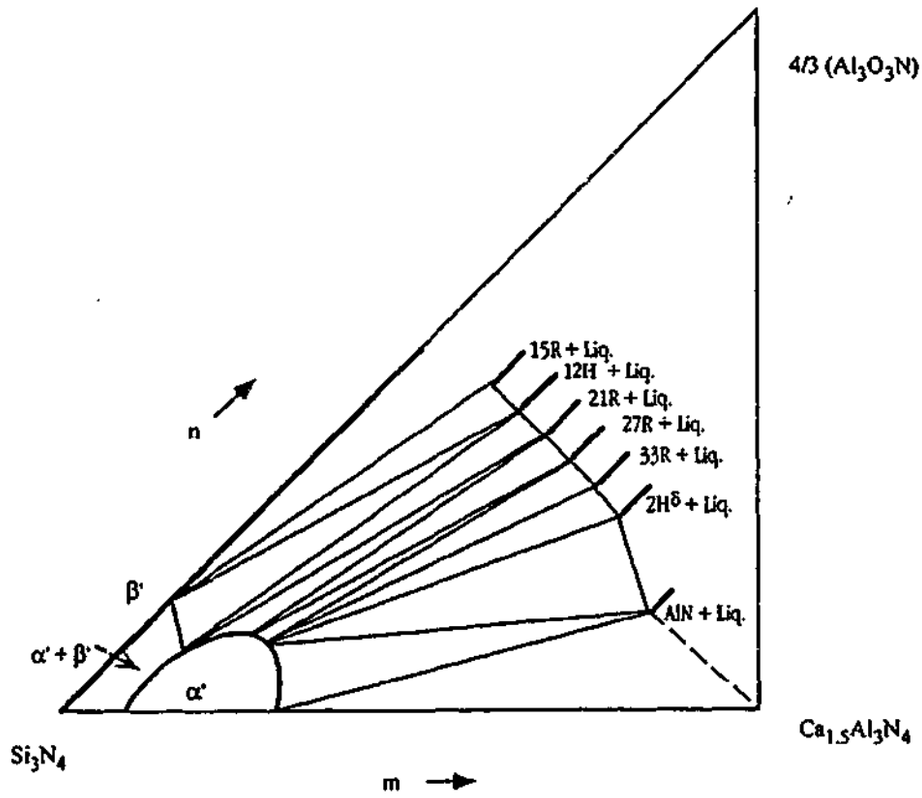

Figure 4.1. Phase behaviour diagram of the Ca α-sialon plane at 1800°C (Hewett et al. 1998a).

While the lower m-value portion of the Ca α-sialon phase behaviour diagram has been examined in detail, large regions of the diagram are yet to be investigated. A consequence of this is that the α-sialon grain morphologies that develop in these higher m-value compositions remain unknown. Anisotropic α-sialon grain growth is an important development in this system, and often, abnormal grain growth is more prominent in liquid-rich compositions. Therefore, there exists a need to examine a wider

range of compositions to determine how prevalent anisotropic α-sialon grain growth is in the Ca-Si-Al-O-N system.

This chapter describes an investigation into the reaction sequences and microstructural development of three high m-value, Ca and Al rich, Ca-Si-Al-O-N compositions. The three compositions are all located outside the single-phase α-sialon forming region. Compositions were pressureless sintered, as this technique is simpler than, and thus preferable to, the more conventional hot-pressing techniques usually utilised in α-sialon fabrication. The densification behaviour, phase evolution, and microstructural development of these compositions will be discussed. Fully densified Ca α-sialon materials will be characterised. Additionally, the fracture behaviour of densified samples will be examined to establish how effective elongated α-sialon grains may be in improving the fracture toughness properties of these materials.

4.2 Experimental Outline

Three Ca-Si-Al-O-N compositions were prepared for this investigation. Each was designated by its m and n-values in the α-sialon equation (Eqn. 2.2) where, for example, the composition designated 3015 had m and n-values of 3.0 and 1.5 respectively. All three compositions under investigation have m:n ratios of 2:1. The positions of these compositions on the Ca α-sialon plane are shown in Figure 4.2. Also indicated is the region previously studied by Hewett and coworkers (1998a). The chemical compositions and m and n-values of the three compositions are listed in Table 4.1. Table 4.2 gives the weight percentages of starting powders used in each composition.

Compositions were pressureless sintered for 4 hours, utilising isothermal hold temperatures ranging from 1400°C to 1800°C at 100° intervals. An additional sintering at 1550°C was also performed, as this was found to be a critical temperature in terms of the reaction sequence and densification. Samples were heated at 20°C/min. from 1000°C to the required isothermal hold temperature. Sintered samples were designated by their composition name followed by a subscript indicating the temperature at which they were sintered. For example, 3015_{1700} would be a sample of 3015 sintered at 1700°C for 4 hours.

Table 4.1. Chemical compositions and m and n-values of the three compositions examined in this section of work.

Composition name	Chemical Composition	m-value	n-value
3015	$Ca_{1.5}Si_{7.5}Al_{4.5}O_{1.5}N_{14.5}$	3.0	1.5
3618	$Ca_{1.8}Si_{6.6}Al_{5.4}O_{1.8}N_{14.2}$	3.6	1.8
5025	$Ca_{2.5}Si_{4.5}Al_{7.5}O_{2.5}N_{13.5}$	5.0	2.5

Table 4.2. Calculated weight percentages of the starting components for the three compositions examined in this section of work.

Composition	Si_3N_4 (wt.%)	AlN (wt.%)	$CaCO_3$ (wt.%)	equivalent to CaO (wt.%)
3015	58.29	28.49	23.60	13.22
3618	50.61	33.74	27.94	15.66
5025	33.47	45.45	37.64	21.09

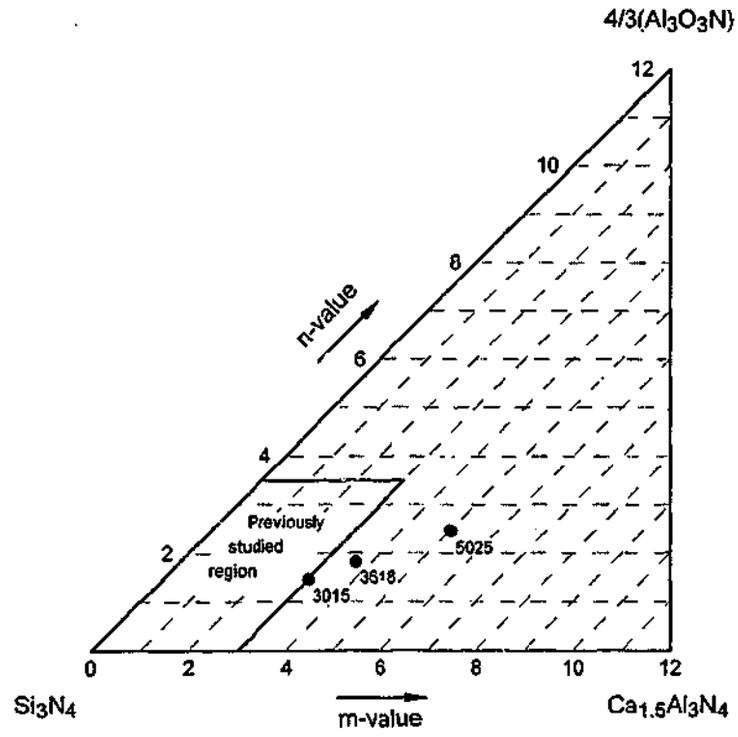

Figure 4.2. The locations on the Ca α-sialon plane of the three compositions examined in this chapter. Also shown is the compositional region previously examined by Hewett and coworkers (1998a).

4.3 Densification and Reaction Sequence of Pressureless Sintered Ca-Si-Al-O-N Compositions

The three compositions examined in this section of work were found to broadly follow similar routes in regard to densification and reaction sequences. However, the wide compositional range embodied in these three compositions did cause a number of significant differences to become apparent. These differences are most evident when the calcium and aluminium rich 5025 composition is compared with the other two compositions. The following discussion will highlight similarities observed between the three compositions, as well as addressing differences where they are observed.

4.3.1 1400°C Hold Temperature

Table 4.3 lists the crystalline phase assemblages of the three compositions sintered for 4 hours at temperatures ranging from 1400°C to 1800°C, as determined by XRD.

XRD analyses of the samples sintered at 1400°C reveal that as expected, reaction of the starting powders had commenced. The lowest eutectic point in the CaO-Al_2O_3-SiO_2 system is reported as 1170°C (Levin et al. 1964). Thus, liquid phase reactions between the oxide powders and surface oxides on the nitride powders should occur well below 1400°C. This is consistent with work by Hewett et al. on hot-pressed Ca α-sialons. Their work showed that reactions to form intermediate phases occurred at temperatures as low as 1200°C (Hewett et al. 1994b). Weight losses measured for the three compositions at various isothermal hold temperatures are plotted in Figure 4.3. Losses in the three 1400°C samples were negligible.

The formation of intermediate phases was apparent in all three of the compositions sintered at 1400°C. However, the types and proportions of the phases that precipitated differed among the three compositions. Gehlenite ($Ca_2Al_2SiO_7$) was the majority intermediate phase detected in 3015_{1400}. In addition to gehlenite, a small amount of a second, unidentified, intermediate phase, designated here as A-phase, was detected.

Table 4.3. Crystalline phase assemblages of the three compositions sintered for 4 hours at temperatures ranging from 1400°C to 1800°C.

Sample	Crystalline Phases									
	α-sialon	AlN	2H[δ]	33R	α-Si_3N_4	β-Si_3N_4	Gehlenite	A-phase	B-phase	$CaCO_3$
3015 Green		vs			vs	mw				mw
1400°C	vs	vs			vs	tr	vs	vw		
1500°C	vs	w					mw			
1550°C	vs	w								
1600°C	vs	w								
1700°C	vs		vw							
1800°C	vs		vw	tr						
3618 Green		vs			vs	vw				m
1400°C	m	vs			ms	tr	s	m		
1500°C	vs	m					m			
1550°C	vs	m								
1600°C	vs	m								
1700°C	vs	m								
1800°C	vs		w							
5025 Green		vs			m	vw				m
1400°C	vw	vs			mw		mw	m		
1500°C	s	vs					vw		w	
1550°C	s	vs							w	
1600°C	s	vs							vw	
1700°C	ms	vs								
1800°C	ms	vs								

(where w = weak, m = medium, s = strong, v = very, tr = trace for XRD peak intensity)

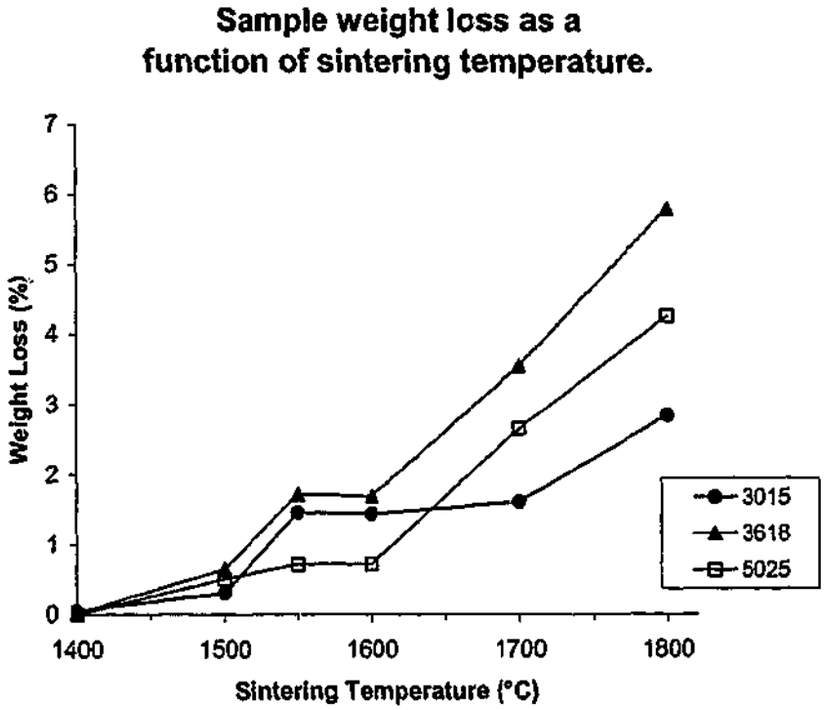

Figure 4.3. Plot of sample weight loss as a function of sintering temperature for the three compositions, isothermally held at temperatures ranging between 1400°C and 1800°C.

Sample 3618_{1400} exhibited a lesser, but still significant, amount of gehlenite. This was combined with an increased amount of A-phase. Sample 5025_{1400} exhibited no trace of gehlenite at all. Rather, A-phase was the only intermediate phase detected.

These XRD results clearly show that there was a steady decrease in the amount of gehlenite precipitated as the composition m-value increased from 3.0 to 5.0. This was accompanied by a concurrent increase in the amount of A-phase precipitated. No M-phase ($Ca_2Si_3AlO_2N_5$) was detected in any of the compositions sintered at 1400°C. This is consistent with work by Hewett et al. (1994b), which reports that M-phase is completely dissolved at around 1350°C in hot-pressed Ca α-sialons.

Despite extensive investigation, identification of the intermediate A-phase was unsuccessful. Figure 4.4 is an XRD spectrum of 5025_{1400}. The peaks attributed to this

unidentified phase are marked. All other peaks can be assigned to α-Si_3N_4, α-sialon and AlN. The d-spacings and estimated relative intensities of the XRD peaks of A-phase are listed in Table 4.4. Repeated, comprehensive searches of the JCPDS powder diffraction file found no matches corresponding to the unidentified peaks. A review of the literature also returned no results. Additionally, none of the phases identified on the CaO-Al_2O_3-SiO_2 ternary phase diagram, shown in Figure 4.5, have XRD spectra corresponding with the unidentified peaks. The possibility that the peaks are attributable to more than one unidentified phase was considered. However, this did not alter the result that the peaks could not be assigned to a known phase.

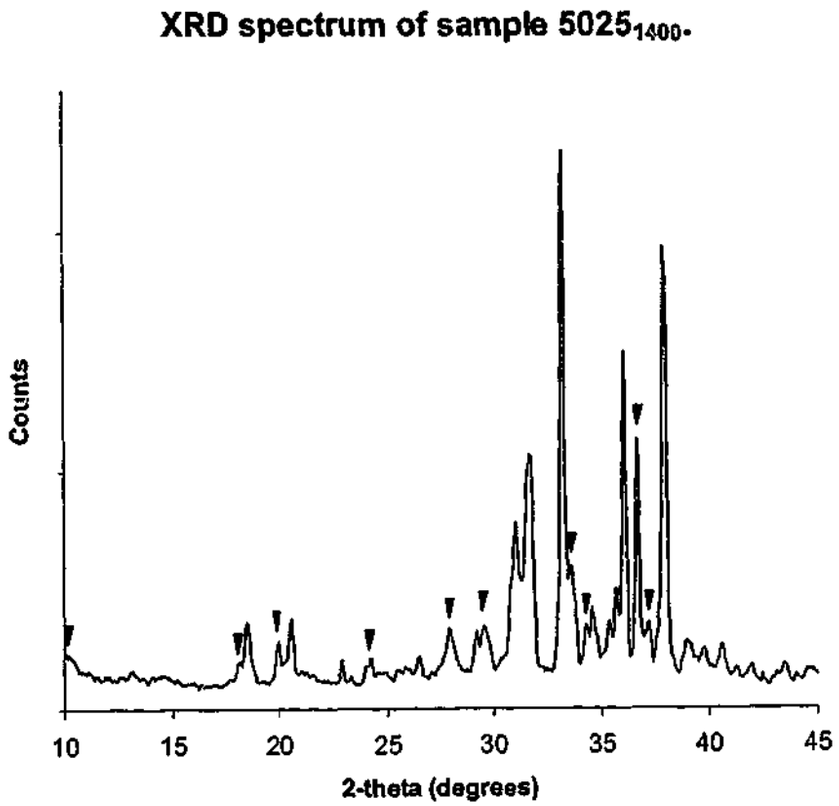

Figure 4.4. XRD spectrum obtained from sample 5025_{1400}. The peaks attributed to the unidentified A-phase are indicated. All other peaks can be attributed to α-Si_3N_4, α-sialon and AlN.

A full characterisation and identification of this phase by TEM analysis was beyond the scope of this work. However, it is likely that the phase is calcium-rich, such as a type of calcium aluminate, silicate or aluminosilicate. It may also be an oxynitride phase.

Table 4.4. d-Spacings and estimated relative intensities of unidentified XRD peaks found in sample 5025_{1400}.

Peak Number	d-Spacing (Å)	Estimated Relative Intensity
1	8.631	20
2	4.892	20
3	4.445	20
4	3.669	20
5	3.193	20
6	3.023	30
7	2.677	40
8	2.615	30
9	2.450	100
10	2.418	30

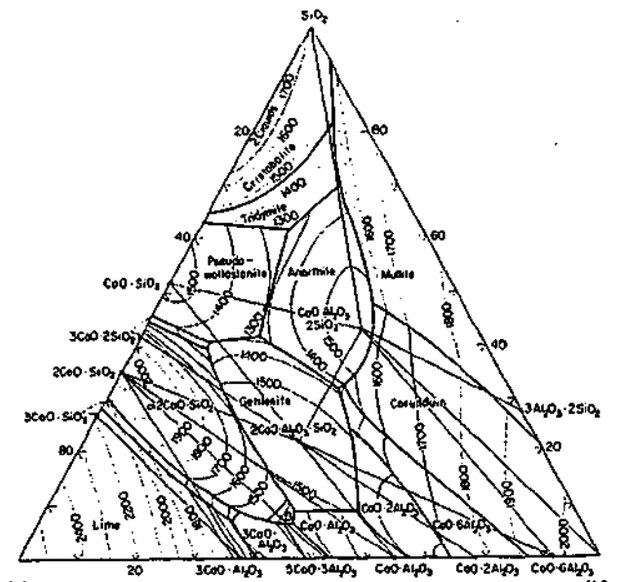

Figure 4.5. Ternary phase diagram of the CaO-Al_2O_3-SiO_2 system (Levin et al. 1964).

There are a number of reasons that this is likely. First, all the CaO starting material in the 5025_{1400} sample had been dissolved, while the majority of the original Si_3N_4 and AlN starting powder remained at this sintering temperature. This increases the likelihood that

any intermediate product phase that precipitated out of the Ca-rich oxide liquid phase would contain a significant amount of Ca in its composition. Second, the phase appears to be compatible with gehlenite, indicating that the two phases lie in adjacent phase fields. Gehlenite contains a significant amount of Ca, so it is quite likely that a phase located in an adjacent phase field would also contain a degree of Ca. Third, increasing the amount of Ca and Al in the composition increased the amount of A-phase that was precipitated. This again suggests that A-phase is a Ca-rich phase.

A strong possibility also exists that nitrogen is a component in this phase. This could explain why the XRD spectrum of the phase does not correspond to any of the phases identified on the CaO-Al_2O_3-SiO_2 ternary phase diagram (Figure 4.5).

Examination of the XRD data obtained from the samples sintered at 1400°C also reveals that α-sialon had begun to precipitate at this temperature. This was most apparent in 3015_{1400}. An appreciable amount of α-sialon was also present in 3618_{1400}. Only a trace amount of α-sialon was detected in 5025_{1400}. This trend indicates that compositions positioned closer to the α-sialon phase region precipitate a greater amount of α-sialon at 1400°C. Significant quantities of α-Si_3N_4 and AlN starting powders were detected in all three samples, indicating that higher temperatures are required to achieve complete reaction.

Figure 4.6 is a plot of sample apparent density as a function of sintering temperature for the three compositions under examination. Using the Hg immersion technique, the bulk density, prior to calcining, of cold isostatically pressed green bodies was determined to be approximately 2.000 gcm^{-3}. As the density of the green body reduces after calcining because of CO_2 mass loss, this value did not represent the true green density of a sample. A consequence of this is that the measured apparent densities of a sample sintered at a low temperature can actually appear to be less than the previously measured bulk density of the green body. The mass loss from $CaCO_3$ decomposition can be accounted for, thereby giving a more accurate estimate of the green body density. Green body densities after calcining are estimated to be 1.812, 1.781 and 1.716 gcm^{-3} for compositions 3015, 3618, and 5025 respectively.

In describing the apparent density of Ca-Si-Al-O-N samples in this study, maximum density has been defined as 3.210 gcm^{-3}. This is the maximum apparent density achieved in hot-pressed Ca-Si-Al-O-N compositions fabricated as a part of this work. The actual value for the maximum achievable density in a Ca-Si-Al-O-N composition varies slightly with composition and processing conditions. Therefore, the value of 3.210 gcm^{-3} is an approximation of maximum density. However, it is satisfactory for the comparative purposes required in this work.

Examination of the apparent density versus temperature data (Figure 4.6) shows that only a minor increase in density occurred in the three compositions when sintered at 1400°C. The three samples attained comparable apparent densities after sintering at this temperature, with values lying in the range 1.893–1.912 gcm^{-3}. This equated to approximately 59% of maximum density.

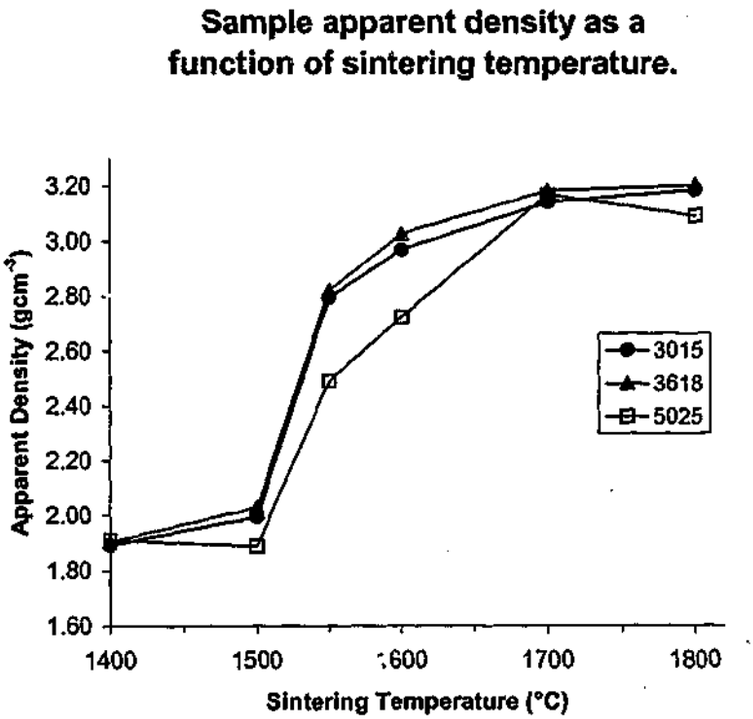

Figure 4.6. Plot of sample apparent density as a function of sintering temperature for the three compositions, isothermally held at temperatures ranging between 1400°C and 1800°C for 4 hours.

Though the increases in density observed at 1400°C were small, the relative increases were larger with higher compositional m-values. This was believed to be a result of the increased oxide content of the higher m-value compositions, which resulted in larger volumes of liquid phase at this sintering temperature. However, despite the oxide-rich nature of these compositions, it is apparent that the characteristics of the liquid phase formed at 1400°C are not conducive to allowing any significant particle rearrangement or densification. Factors influencing the characteristics of the liquid phase include the volume of liquid produced, the viscosity of the liquid, the wetting behaviour of the liquid on the nitride powders, and the formation of intermediate crystalline phases, which deplete the systems of liquid phase until they melt or redissolve at higher temperatures.

4.3.2 1500°C Hold Temperature

Increasing the isothermal hold temperature to 1500°C gave rise to significant developments in the three compositions, especially with regard to the reaction sequence. Chemical reactions clearly proceeded faster at this temperature than at 1400°C. Reference to Table 4.3 shows that after 4 hours at this temperature, the Si_3N_4 starting powder in all three samples had completely dissolved. This was accompanied by an increase in the amount of precipitated α-sialon. Weight losses of less than 1% occurred in the three samples (Figure 4.3).

The phase assemblages of all three samples were composed of three crystalline phases - α-sialon, AlN and an intermediate phase. In both 3015_{1500} and 3618_{1500}, α-sialon was the dominant crystalline phase. As the phase behaviour diagram in Figure 4.1 predicts, the ratio of α-sialon to AlN was greatest in 3015, and decreased with increasing m-value. In the aluminium-rich sample 5025_{1500}, the strongest AlN peak on the XRD spectrum was larger than the strongest α-sialon peak, suggesting that AlN was the dominant crystalline phase in this sample.

Gehlenite continued to persist in 3015_{1500} and 3618_{1500}. The small amounts of A-phase detected in these compositions at 1400°C were not detected at 1500°C. This was also the case for 5025_{1500}. The A-phase detected in this sample at 1400°C appeared to have

dissolved by 1500°C. However, it differed from the other two compositions in that a second intermediate phase, designated here as B-phase, was precipitated.

This unusual development is reflected in the densification data in Figure 4.6. The densities of 3015_{1500} and 3618_{1500} increased by a small amount, attaining values of 1.996 and 2.032 gcm^{-3} respectively. Contrasting this, no increase in density occurred in 5025_{1500}, relative to the density obtained at 1400°C. The most likely explanation for this observation is that the dissolution of A-phase in 3015_{1500} and 3618_{1500} provided some measure of extra liquid phase which, combined with the increased temperature, assisted liquid phase densification. In 5025_{1500}, B-phase precipitated subsequent to the dissolution of A-phase, depriving the system of a quantity of liquid phase, and thus retarding densification.

As with A-phase, B-phase also remains unidentified after extensive investigation. Figure 4.7 shows an XRD spectrum from sample 5025_{1500}. The unidentified peaks are marked. All other peaks can be assigned to α-sialon and AlN. Table 4.5 lists the d-spacings and estimated relative intensities for the XRD peaks attributed to B-phase. Searching of the JCPDS powder diffraction file found no matches with this set of peaks, and a search of the literature provided no information regarding the identity of this phase. As with A-phase, the scope of this work did not allow time to fully identify and characterise this phase. However, as the following paragraphs will explain, a clear relationship between densification and the presence of B-phase was apparent.

Table 4.5. d-Spacings and estimated relative intensities of unidentified XRD peaks found in sample 5025_{1500}.

Peak Number	d-Spacing (Å)	Estimated Relative Intensity
1	5.012	50
2	3.388	60
3	3.243	60
4	3.027	100
5	2.781	80

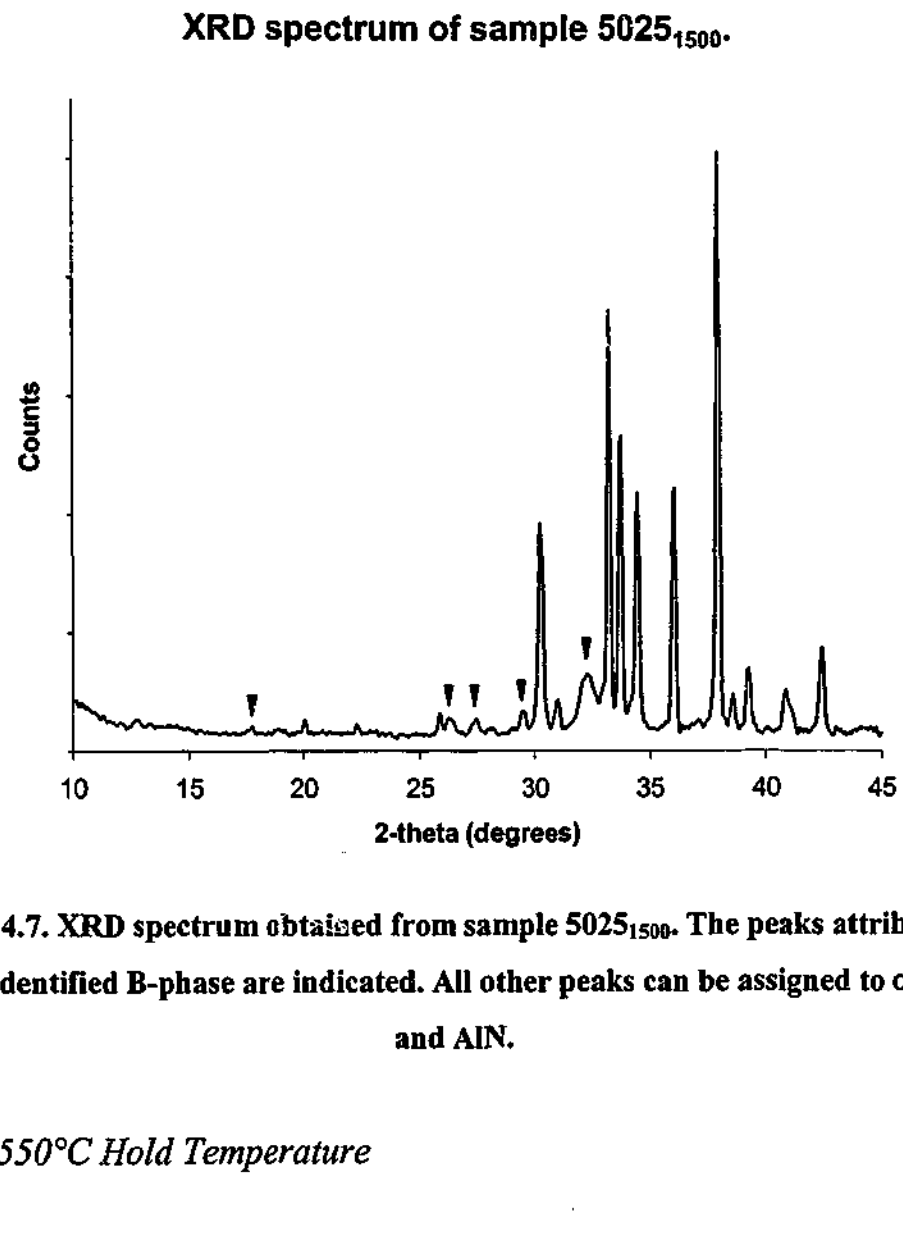

Figure 4.7. XRD spectrum obtained from sample 5025_{1500}. The peaks attributed to the unidentified B-phase are indicated. All other peaks can be assigned to α-sialon and AlN.

4.3.3 1550°C Hold Temperature

The isothermal hold at 1550°C was found to be the most significant in regard to both the reaction sequence and densification. For the 3015 and 3618 compositions, all the basic chemical reactions were complete after a 4 hour hold at this temperature. XRD spectra obtained from these samples showed that the only crystalline phases detected were α-sialon and AlN (Table 4.3). No gehlenite was detected, indicating that it had completely dissolved after 4 hours at 1550°C. While AlN is one of the raw materials in the starting compositions, it also occurs as an equilibrium phase in a range of Ca-Si-Al-O-N compositions sintered at varying temperatures. Thus, AlN may remain present in samples that can be considered to have fully reacted.

A sharp increase in the densification rate between 1500°C and 1550°C was also observed in these two compositions, as Figure 4.6 shows. This was attributed to the melting of the intermediate gehlenite phase, which released a significant amount of liquid phase and accelerated the liquid phase densification process. Gehlenite has the chemical formula $Ca_2Al_2SiO_7$. Its melting temperature is reported as 1590°C (Lide 1989). However, lattice parameter measurements made by van Rutten et al. (1996) led them to believe that gehlenite may exist as a solid solution with the formula $Ca_2Al_{2-x}Si_{1-x}O_{7-x}N_x$. The incorporation of N into the gehlenite structure could have the effect of lowering the melting temperature of the solid solution relative to that of pure gehlenite. This can account for the apparent melting of gehlenite at between 1500°C and 1550°C, rather than at the reported 1590°C.

After 4 hours of sintering at 1550°C, 3015_{1550} and 3618_{1550} obtained densities of 2.796 and 2.823 gcm^{-3} respectively. This represented increases in density of 40.1% and 38.9% respectively, relative to the densities obtained 50° lower at 1500°C.

It is clear that the formation, and subsequent melting, of the intermediate crystalline phases that form during sintering is an important factor in the control of the densification process during pressureless sintering of Ca-Si-Al-O-N materials. The rapid increase in the densification rate between 1500°C and 1550°C displays a marked contrast to that observed in the rare earth and yttrium α-sialon systems, where the highest densification rates mostly appear in the temperature range between 1550°C and 1600°C (Wang et al. 1994). A rapid increase in the rate of weight loss also became apparent in these two samples at 1550°C (Figure 4.3). This was attributed to the volatility of the increased amount of Ca-rich liquid phase that resulted from the melting of gehlenite.

Contrasting the behaviour of the two lower m-value compositions, the phase assemblage of 5025_{1550} remained unchanged from that obtained at 1500°C. The intermediate B-phase that precipitated in the 1500°C sample was retained at 1550°C. α-Sialon and AlN were also present in the same proportions as that observed at 1500°C.

The differing reaction sequence of 5025 continued to affect densification, relative to the other two compositions. An increase in the densification rate between 1500°C and

1550°C did occur (Figure 4.6). However, the increase in density of 31.9% was significantly less than that seen in the other two compositions. The sample attained a density of only 2.492 gcm^{-3}. This was approximately 0.3 gcm^{-3} less than the densities achieved by the other two samples. This hindered densification can be attributed to the lack of any gehlenite to melt, and the stable nature of the intermediate B-phase, which deprives the sample of some of the liquid phase that it requires for densification. A reduced volume of liquid phase at 1550°C may also account for the absence of any significant increase in weight loss at this temperature, an observation that is in contrast to the other two samples sintered at 1550°C.

4.3.4 1600°C Hold Temperature

Increasing the isothermal hold temperature to 1600°C caused almost no changes to the crystalline phase assemblages of the three compositions comparing to the results observed at 1550°C. The proportions of α-sialon and AlN remained constant in all three compositions. The amount of B-phase in 5025 also remained constant, having not dissolved by this temperature. Weight losses in the samples sintered at 1600°C were essentially unchanged from those measured at 1550°C (Figure 4.3).

In comparison to the previous 50°C temperature increment from 1500°C to 1550°C, the rate of density increase over the 1550°C to 1600°C increment was reduced. However, substantial increases in density continued to take place. Samples 3015_{1600} and 3618_{1600} developed densities of 2.970 and 3.028 gcm^{-3}, respectively. This equates to approximately 92.5% and 94.3 % of maximum density respectively, if maximum density is approximated as 3.21 gcm^{-3}.

A significant increase in density was also observed in 5025_{1600}. However, the density of 2.725 gcm^{-3} developed by this sample was still significantly below that of the other two lower m-value compositions. This value represented only 84.9% of maximum density. The extent to which the densification of the 5025 composition is hindered is made very clear in Figure 4.6.

The continued hindered densification of the 5025 composition appears to be a result of the stability of the intermediate B-phase. The melting or dissolution of any intermediate phases is an essential part of the liquid phase sintering sequence, as this step releases significant amounts of liquid into the system. By remaining stable to at least 1600°C, the 5025 sample is deprived of a significant amount of liquid phase that if released, would allow densification to proceed rapidly, particularly at this elevated temperature.

4.3.5 1700°C Hold Temperature

Further increasing the isothermal hold temperature to 1700°C led to additional changes in the crystalline phase assemblages of two of the samples. No change in phase assemblage was observed in 3618. α-Sialon and AlN continued to remain as compatible phases. In composition 3015, the AlN that was present at 1600°C was not detected at 1700°C. Instead the second crystalline phase detected was $2H^{\delta}$ polytypoid phase. It appeared that by increasing the temperature to 1700°C, the simultaneous dissolution of AlN and precipitation of $2H^{\delta}$ occurred.

In 5025, the intermediate B-phase observed from 1500°C to 1600°C dissolved. The dissolution of the B-phase had no effect on the proportions of the other two crystalline phases, α-sialon and AlN. These remained in the same proportions as observed at 1600°C, with AlN as the majority crystalline phase.

The increased isothermal hold temperature caused a significant increase in the rate of weight loss in both 3618 and 5025. Weight losses increased by factors of ~2 and ~3 respectively, relative to the losses that resulted at 1600°C. The higher vapour pressure of the low-viscosity, Ca-based liquid phase at 1700°C, comparing to 1600°C, can account for these large observed weight losses in these two compositions. The very large increase in the weight loss of the 5025 composition arises from the fact that at 1600°C, this composition has a low volume of liquid phase, and therefore a reduced weight loss from liquid phase volatility. This resulted from a significant proportion of the liquid phase being tied up in the crystalline B-phase. At 1700°C the B-phase dissolved. This greatly increased the amount of liquid phase in the sample, and consequently, the rate of weight loss in the sample significantly increased.

Increased density was observed in all three compositions (Figure 4.6). The most significant change in density occurred in 5025. Whereas the densification of 5025 lagged behind the other two compositions up to 1600°C, the increased amount of liquid available at 1700°C, a result of the dissolution of B-phase, allowed densification to proceed unhindered. After 4 hours at 1700°C, 5025 attained a density equal to that of the other two samples. These results show a clear correlation between the densification of the 5025 composition and the behaviour of the intermediate B-phase.

The densities of all three samples approached the maximum attainable density at the 1700°C sintering temperature. Samples 3015_{1700}, 3618_{1700}, and 5025_{1700} developed densities of 3.143, 3.184 and 3.169 gcm^{-3} respectively. This represented 97.9%, 99.2% and 98.7% of maximum density respectively.

4.3.6 1800°C Hold Temperature

The highest isothermal hold temperature to be investigated was 1800°C. Some changes in crystalline phase assemblages arose from the increase in temperature.

The phase assemblage of 3015_{1800} remained essentially the same as at 1700°C, with α-sialon and $2H^{\delta}$ existing as compatible crystalline phases. However, in addition to these two phases, a trace of 33R polytypoid was also detected by XRD. This was consistent with the fact that the $2H^{\delta}$ and 33R polytypoids are compatible phases according to the phase behaviour diagram produced by Hewett et al. (Figure 4.1). It is possible that the starting composition was located in the $\alpha' + 2H^{\delta} + 33R$ phase compatibility triangle. Alternatively, the composition may have been located in the $\alpha' + 2H^{\delta}$ phase compatibility triangle, and compositional changes due to weight losses at high temperatures slightly shifted the composition into the adjacent $\alpha' + 2H^{\delta} + 33R$ region.

A more significant change occurred in 3618_{1800}, similar to the change in phase assemblage observed in 3015 at 1700°C. α-Sialon remained as the majority crystalline phase. However, the AlN previously observed at 1700°C was no longer detected.

Instead, $2H^6$ polytypoid was the only secondary phase detected. It appeared that between 1700°C and 1800°C, the AlN dissolved and the $2H^6$ phase precipitated.

No phase changes from the increased holding temperature were observed in 5025_{1800}. Aluminium nitride remained as the majority crystalline phase, with a significant amount of α-sialon as the second crystalline phase. The appearance of AlN as the majority crystalline phase was consistent with the Al-rich nature of the composition.

The final phase assemblages of the three compositions are consistent with the Ca α-sialon phase behaviour diagram produced by Hewett et al., which puts high m-value Ca α-sialons compatible with AlN and nitrogen rich AlN-polytypoid phases (Figure 4.1) (Hewett et al. 1998a).

All three samples exhibited significant weight losses at 1800°C. Indeed, examination of the plot of weight loss against isothermal hold temperature for the two highest m-value compositions (Figure 4.3), shows an almost linear increase in weight loss with increased temperature from 1600°C to 1800°C. The liquid-rich nature of these high m-value compositions can account for the large weight losses observed in these samples over extended sintering times. The increased amount of Ca and Al in these compositions increases the amount of intergranular liquid phase present at sintering temperatures. Additionally, the increased Ca content decreases the viscosity of the liquid phase. The combination of a significant volume of reduced viscosity liquid phase results in significant weight losses, associated with the high vapour pressure of the liquid phase at elevated temperatures. Embedding the samples in a powder bed can assist in reducing weight loss, but cannot completely alleviate it, especially in these liquid-rich samples.

The increase in holding temperature produced a further increase in the densities attained by 3015 and 3618. They reached 3.186 and 3.204 gcm^{-3} respectively, or 99.3% and 99.8% of maximum density. An interesting observation was the density of 5025 sintered at this higher temperature. The sample exhibited a density of 3.092 gcm^{-3}, or 96.3% of maximum density. This value was significantly lower than that attained by sintering at 1700°C. The low apparent density was attributed to bloating of the sample that occurred during sintering. The bloating was a result of the rapid evolution of large volumes of

liquid and vapour phases in this composition at high sintering temperatures. The liquid and vapour become trapped in the bulk of the sample when the open porosity of the sample becomes closed off during densification. The result is a distribution of cavities, 1 to 2 mm in size, throughout the bulk of the sample, which significantly influence the measured apparent density. An SEM micrograph showing the distribution of cavities in 5025_{1800} is shown in Figure 4.8.

Neglecting bloating effects, it was clear from this work that when pressureless sintering Ca-Si-Al-O-N compositions with an m-value of 3.0 or greater, a holding temperature of 1800°C is sufficient to complete all chemical reactions and achieve full densification.

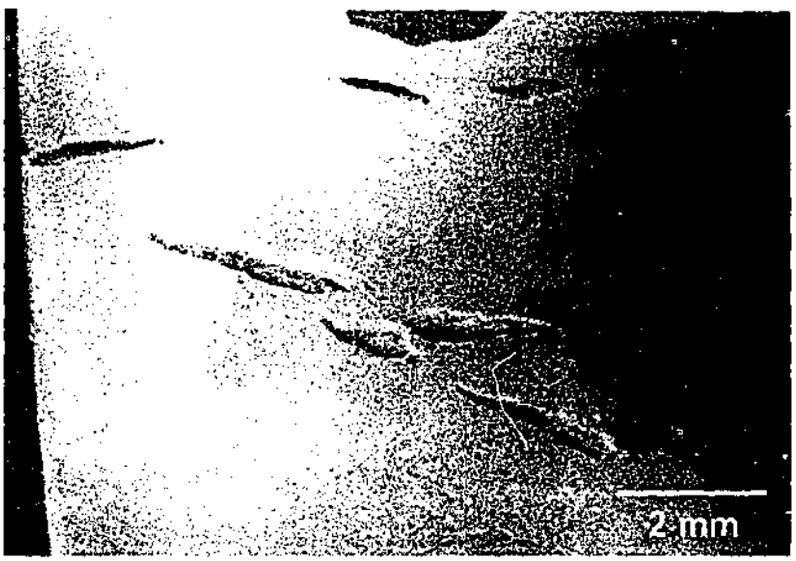

Figure 4.8. Secondary electron micrograph of sample 5025_{1800}, showing the distribution of cavities in the sample that resulted from bloating at 1800°C.

4.3.7 Summary of Densification and Reaction Sequence of Pressureless Sintered Ca-Si-Al-O-N Compositions

This section of work examined the reaction sequences and densification behaviour of three pressureless sintered Ca-Si-Al-O-N compositions. Chemical reactions that included the precipitation of α-sialon occurred during the lowest isothermal hold at 1400°C. Three intermediate phases were detected in this sequence of samples. These were gehlenite, and two unidentified phases, designated A-phase and B-phase. The formation and subsequent melting/dissolution of the intermediate phases was found to be

critical to the densification kinetics of pressureless sintered Ca α-sialons. The melting of gehlenite in the two lower m-value compositions in the 1500°C to 1550°C temperature range released significant amounts of liquid phase. This greatly enhanced the chemical reaction kinetics and led to the highest observed rate of densification. The precipitation of the more stable intermediate phase, B-phase, resulted in the hindered densification of the 5025 composition. Only when this unidentified phase melted/dissolved in the 1600°C to 1700°C temperature range was this composition able to develop good density. All three compositions achieved >99% of maximum density when sintered for 4 hours at 1700°C and/or 1800°C.

After sintering at the maximum temperature of 1800°C, all three compositions developed crystalline phase assemblages consisting of α-sialon in equilibrium with AlN and/or the $2H^{\delta}$ and 33R AlN-polytypoids. α-Sialon was the majority crystalline phase in samples 3015_{1800} and 3618_{1800}. Aluminium nitride was the dominant crystalline phase in 5025_{1800}, with α-sialon occurring as a significant secondary phase.

The following section of work deals with the microstructural characterisation of the samples fabricated in this investigation. The sequence of samples fabricated from the 3618 composition is examined in detail. Fully dense samples of the other two compositions are also examined. SEM, TEM and EDXS are used to characterise the samples.

4.4 Microstructural Characterisation

4.4.1 Scanning Electron Microscopy

Scanning electron microscopy was used to observe the microstructures of polished and etched samples. This section of work follows microstructural development in the 3618 composition. The general microstructural development in this composition was considered to be representative of all three compositions being studied in this work. The microstructures of the 3015 and 5025 compositions sintered for 4 hours at 1800°C are also examined, in order to study differences between the fully densified compositions.

1400°C Sample

As expected from density measurements, 3618_{1400} exhibited a very porous microstructure. This is apparent in Figure 4.9(a). Evidence of the evolution of small quantities of liquid phase was observed, and bonding between particles was apparent. Signs of any significant particle rearrangement were negligible. An abundance of generally sub-micron particles was the most prominent feature of this microstructure. These small grains were a combination of raw starting powders and reaction products, such as α-sialon and gehlenite. The grain sizes were too small for the identification of specific phases by EDXS.

1500°C Sample

Increasing the sintering temperature to 1500°C yielded little difference in microstructure from the sample sintered at 1400°C. An SEM micrograph of this sample is shown in Figure 4.9(b). As density measurements indicated, only a minimal increase in density occurred at this temperature. The microstructure remained very porous, though some small regions of initial densification are observed. XRD analysis indicated that α-sialon was the majority crystalline phase in this sample. However, the grain size continued to remain too small to distinguish between different phases. Despite no significant grain growth occurring at temperatures this low, it was evident from XRD evidence that the conversion of α-Si_3N_4 to α-sialon proceeds with little difficulty at 1500°C.

1550°C Sample

The microstructure of 3618 sintered at 1550°C, shown in Figure 4.10, exhibited significant development in comparison to the samples sintered at lower temperatures. Most obvious was the greatly reduced porosity of the microstructure. This observation correlated with the rapid increase in the densification rate observed between 1500°C and 1550°C that resulted from the melting of the gehlenite intermediate phase (Figure 4.6).

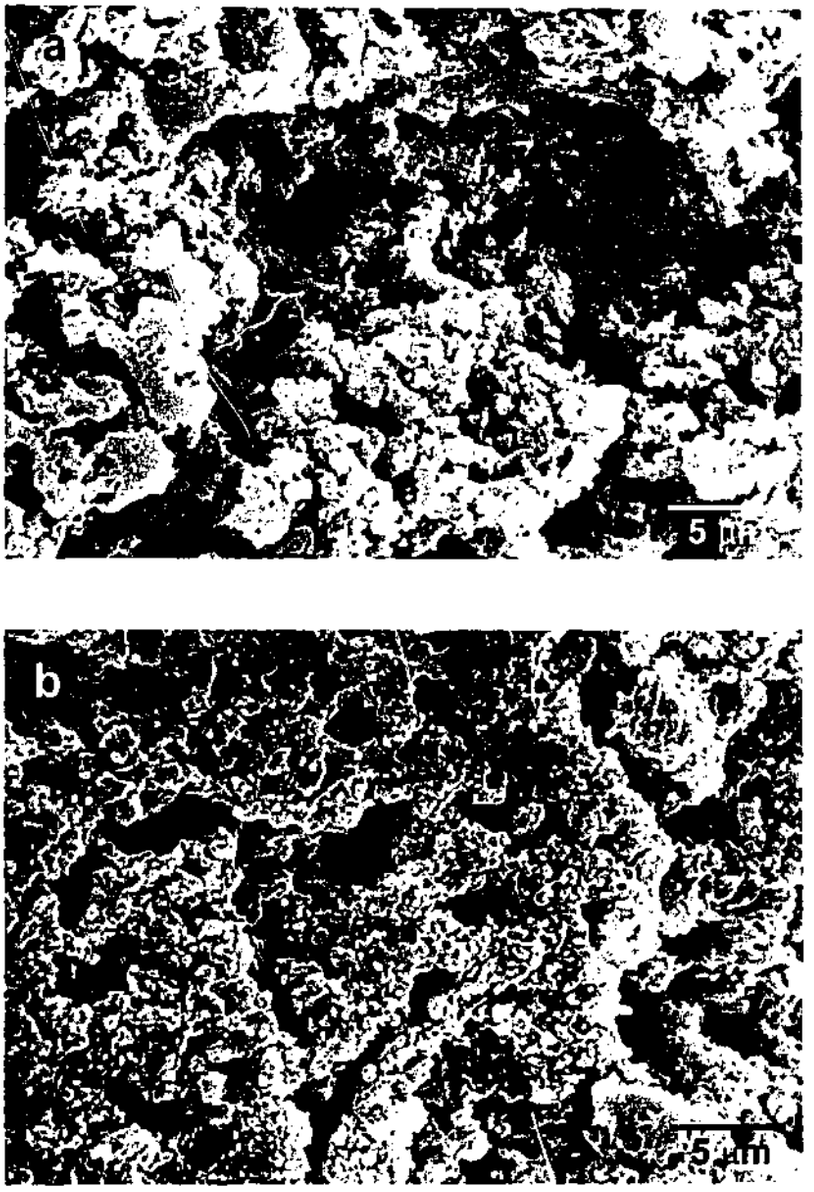

Figure 4.9. Secondary electron micrographs of polished and etched sections of composition 3618 sintered for 4 hours at (a) 1400°C and (b) 1500°C.

Figure 4.10. Secondary electron micrograph of a polished and etched section of composition 3618 sintered for 4 hours at 1550°C.

According to XRD analysis, only two crystalline phases, α-sialon and AlN, were present in the microstructure. No Si_3N_4 or intermediate phases remained. A small degree of grain growth was apparent in this sample, though grain sizes still averaged less than 1 μm.

1600°C Sample

Increasing the sintering temperature to 1600°C produced a small degree of grain growth, as Figure 4.11 shows. This allowed the two crystalline phases, α-sialon and AlN, to become easily distinguishable from each other. Two morphologically distinct phases were observed. One phase exhibited an acicular morphology, with the needle-like grains exhibiting lengths in the range 1 – 2 μm. The other phase consisted of equiaxed grains, with diameters of 2 – 5 μm.

EDXS analysis of the two distinct phases was carried out on the two grains indicated in Figure 4.11. The EDXS spectrum from the elongated grain was found to include Ca, Si, and Al (Figure 4.12(a)). These grains were thus identified as Ca α-sialon. Owing to limitations in the detection capability of the EDXS system, the O and N present in the α-sialon could not be detected to any significant degree.

Figure 4.11. Secondary electron micrograph of a polished and etched section of composition 3618 sintered for 4 hours at 1600°C.

EDXS spectra obtained from elongated and equiaxed grains in sample 3618_{1600}.

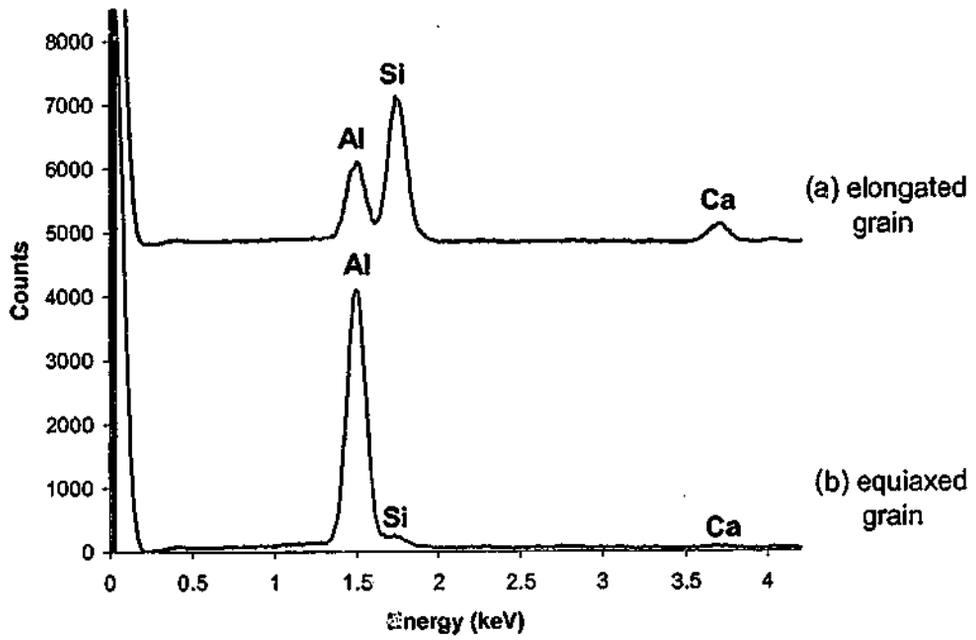

Figure 4.12. EDXS spectra obtained from the two grains indicated in Figure 4.11.

Aluminium was the only significant element detected in the equiaxed grains, along with a trace amount of Si and Ca (Figure 4.12(b)). It was concluded that these grains were

AlN. The trace amount of Si and Ca detected is believed to be due to the interaction volume of the electron probe detecting intergranular phase outside the grain being analysed.

1700°C Sample

Sintering at 1700°C resulted in further sample densification, and the accelerated growth of elongated α-sialon grains. Micrographs obtained from this sample are shown in Figure 4.13(a). Growth across the width of elongated α-sialon grains appeared to be quite limited. However, growth along their length proceeded quite rapidly. This produced a significant increase in the aspect ratio of the α-sialon grains.

Close examination of the equiaxed AlN grains, arrowed in Figure 4.13(b), revealed that the polished surfaces of the phase actually appeared to be composed of many tiny particles, averaging a few hundred nanometres in diameter. This speckled appearance is not believed to be a part of any sub-structure of the AlN grains. Rather, it is a by-product of the chemical etching process used to remove intergranular glass. It is reported that AlN is completely decomposed by hot, dilute NaOH solutions over a short period of time (Weimer 1997). The chemical etching process used in this work takes place in pure, molten NaOH, at over 400°C. This etching process is believed to decompose the polished surface of the AlN grains, giving them this characteristic appearance. The α-sialon is not aggressively attacked by the NaOH, and thus it retains its smooth appearance. Further discussion of the microstructural features of the AlN phase will be presented in a later section of TEM study.

1800°C Samples

Sintering at 1800°C, the maximum temperature to be studied, resulted in a further increase in α-sialon grain growth. As Figure 4.14 shows, growth across the widths of the grains continued to be limited, with the majority of growth occurring along the lengths of the grains. The average α-sialon grain length in 3618_{1800} was ~8 μm. The range of grain lengths present was quite large, with grains exceeding 20μm occasionally being observed.

Figure 4.13. Secondary electron micrographs of a polished and etched section of composition 3618 sintered for 4 hours at 1700°C (a). Micrograph (b) reveals the unusual surface features of the etched AlN phase (arrowed).

The average width of the α-sialon grains was ~0.9 μm, and this did not vary significantly between grains. As a result of the relatively narrow range of α-sialon grain widths and the highly variable grain lengths, the aspect ratios of the α-sialon grains had a large range. The α-sialon aspect ratio averaged ~9, but individual grains were typically in the range 5 to 15.

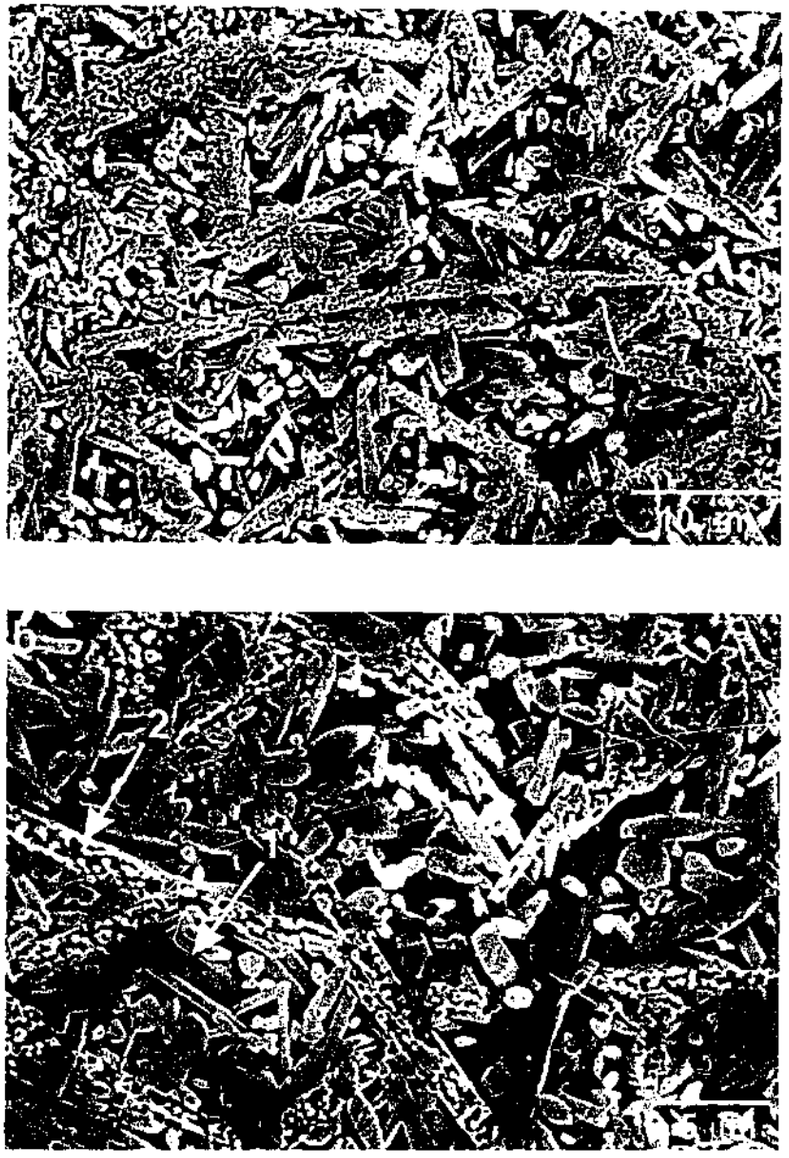

Figure 4.14. Secondary electron micrographs of polished and etched sections of composition 3618 sintered for 4 hours at 1800°C. Grains in (b) labeled '1' and '2' were analysed by EDXS (Figure 4.15).

XRD analysis revealed that AlN, present at 1700°C, was replaced by the $2H^{\delta}$ polytypoid phase at 1800°C. This change was very apparent in the microstructure of the sample. Whereas AlN had equiaxed morphologies, the $2H^{\delta}$ phase exhibited a high aspect ratio, needle or plate-like appearance. Examination of this phase around pores revealed that it actually had a plate morphology, not needle-like. In cross-section, the $2H^{\delta}$ grains exhibited lengths ranging from 15 μm, to over 35 μm. They generally exhibited widths of approximately 2 μm, giving the grains very high aspect ratios in cross-section.

Distinguishing between elongated α-sialon and the high aspect ratio $2H^{\delta}$ grains was relatively simple. Firstly, the $2H^{\delta}$ grains were substantially longer than the α-sialon grains, and were formed as plates, not elongated rods. Secondly, chemical etching gave the $2H^{\delta}$ grains the same characteristic speckled appearance as the AlN in the lower temperature samples. The α-sialon grains remained smooth after etching. Thirdly, the completely different chemistry of the α-sialon and $2H^{\delta}$ phases, recorded by EDXS, left no confusion as to the identity of the phases. The two grains labeled in Figure 4.14(b) were analysed by EDXS. The different chemistries are clearly apparent in the spectra shown in Figure 4.15. Spectrum (a) in Figure 4.15, obtained from grain 1, clearly shows the characteristic Ca, Si, Al and N peaks of Ca α-sialon. Spectrum (b), obtained from grain 2, appears quite different, exhibiting a large Al peak and a small Si peak. This is characteristic of the $2H^{\delta}$ AlN-polytypoid phase.

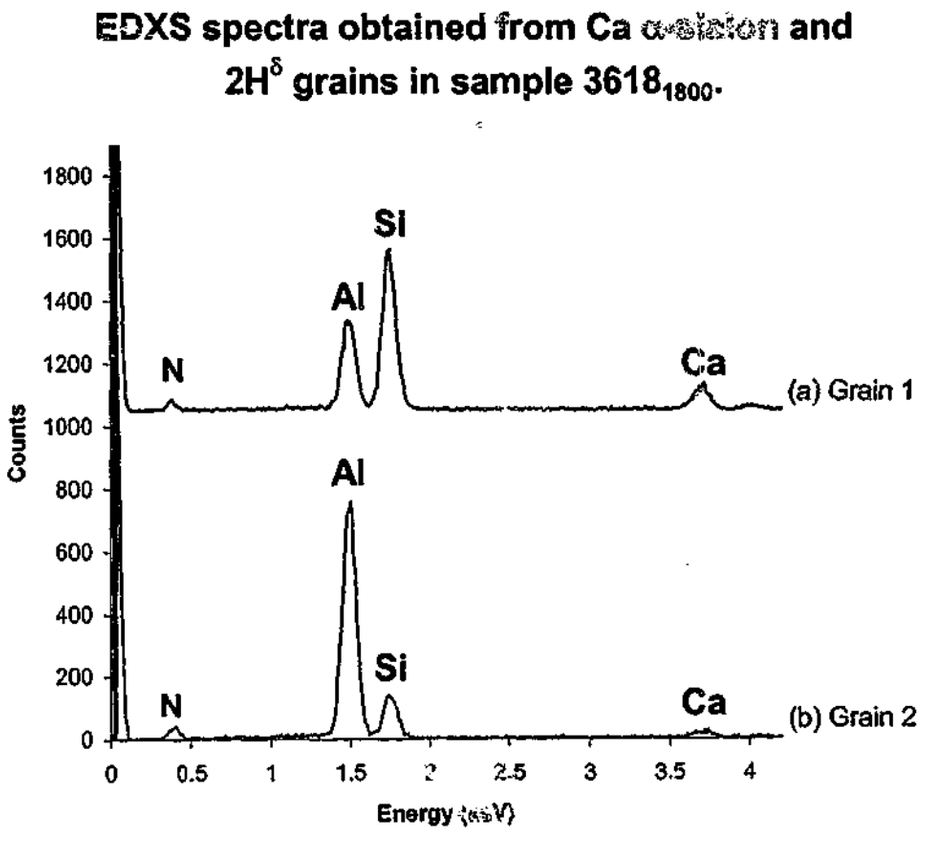

Figure 4.15. EDXS spectra obtained from (a) Ca α-sialon and (b) $2H^{\delta}$ polytypoid grains in sample 3618_{1800} sintered for 4 hours at 1800°C. Analysis was conducted on the two grains indicated in Figure 4.14(b).

The small Ca peak in spectrum (b) most likely arose from the interaction volume of the electron beam interacting with some intergranular phase adjacent to the grain being analysed. XRD analysis showed that at no stage was β-sialon detected as a component phase, eliminating the possibility that any of the high aspect ratio grains in the sample were β-sialon. The significant amount of intergranular glass present in this sample is evident in Figure 4.14. Though the intergranular glass phase has been etched out of the sample surface, the volume that the intergranular phase occupied is readily apparent.

Composition 3015 sintered for 4 hours at 1800°C exhibited similar microstructural features to 3618_{1800} (Figure 4.16). This was not unexpected, as both compositions displayed similar phase assemblages of α-sialon and AlN-polytypoid. A significant difference was the reduced amount of intergranular glass in 3015_{1800}. The sample also contained less of the polytypoid phase. This was consistent with the closer proximity of the 3015 composition to the α-sialon forming region on the Ca α-sialon plane (Figure 4.1).

Similar to 3618_{1800}, the α-sialon grains in 3015_{1800} exhibited an elongated morphology. The grains were shorter in this composition, averaging ~5 μm in length. However, the α-sialon grain widths were almost the same, averaging ~0.8 μm. The $2H^{\delta}$ grains were also smaller, averaging ~10μm in length. These reduced grain sizes may be attributable to the reduced volume of intergranular glass present, and the resultant higher density of crystalline grains in the microstructure. A large volume of intergranular liquid phase at the sintering temperature could allow grains to grow considerably before they impinge upon each other. The reduced volume of intergranular phase that develops in 3015, relative to 3618, would cause grains to impinge on each other sooner. Consequently, shorter elongated grains and polytypoid plates are developed.

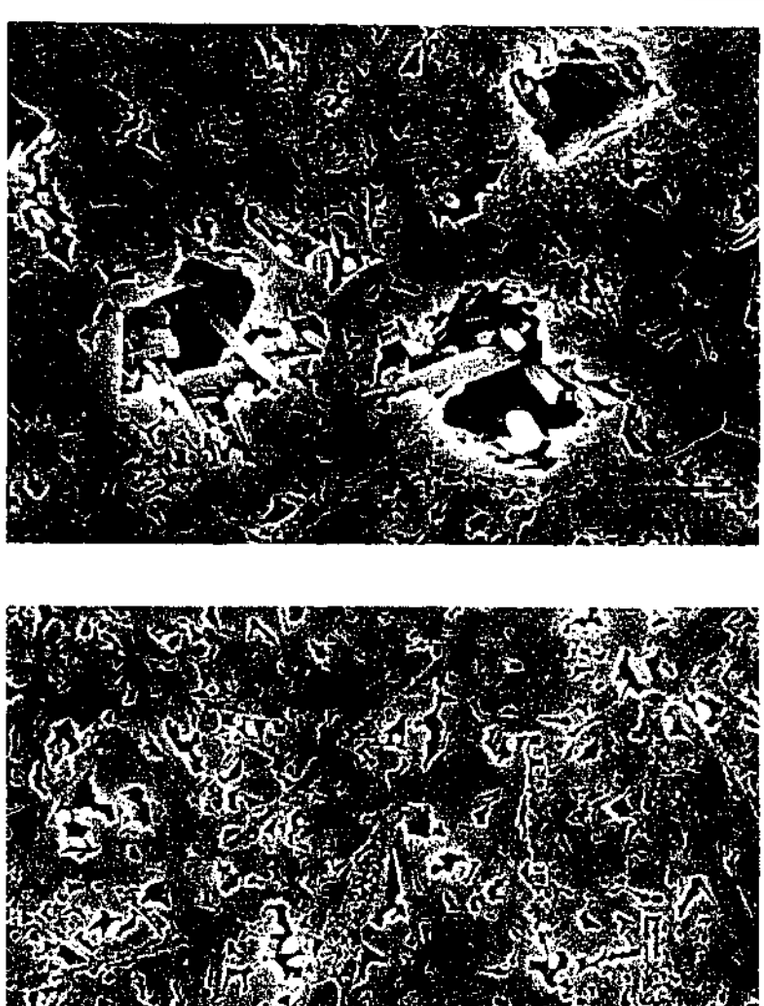

Figure 4.16. Secondary electron micrographs of polished and etched sections of composition 3015 sintered for 4 hours at 1800°C.

According to XRD analysis, composition 5025 sintered at 1800°C for 4 hours was comprised of two crystalline phases, α-sialon and AlN. Microstructural examination of this sample revealed the distinct morphology of these two phases (Figure 4.17). As in the other two compositions, α-sialon exhibited a high aspect ratio, elongated morphology. Grain lengths averaged ~10 μm. Grain widths were slightly increased over the other two compositions, averaging ~1.2 μm. In contrast to the highly anisotropic growth observed for the $2H^{\delta}$ polytypoid phase, AlN grains typically exhibited a well defined, elliptical morphology. The AlN grains averaged ~4 μm in diameter. Also notable in this composition was the large proportion of intergranular glass phase. This was expected,

given the Ca and Al-rich nature of the 5025 composition. The AlN and AlN-polytypoid phases located on the Ca α-sialon plane are, in fact, AlN-liquid and polytypoid-liquid tielines that intersect the Ca α-sialon plane. Consequently, as the amount of AlN or polytypoid in a reacted composition is increased, the amount of intergranular glass concurrently increases. This explains why the amount of intergranular phase observed in these three sintered compositions increased with increasing proportions of AlN and/or AlN-polytypoids.

Figure 4.17. Secondary electron micrographs of polished and etched sections of composition 5025 sintered for 4 hours at 1800°C.

In addition to exhibiting a trend of increasing intergranular phase, examination of the three fully dense samples clearly revealed a trend of an increasing average α-sialon grain length with increasing m-value. Average α-sialon grain lengths were approximately 5 μm and 10 μm in 3015_{1800} and 5025_{1800} respectively. This trend is reasonable in terms of grain growth and impingement, as an increased volume of intergranular phase will allow grains to undergo growth that is more extensive before impinging upon one another. Indeed, previous studies on α-sialons have indicated that Al-rich liquids may help facilitate elongated grain growth (Nordberg et al. 1997). It is notable that even the sample with the least intergranular phase, 3015_{1800}, did develop high aspect ratio α-sialon grains.

4.4.2 Transmission Electron Microscopy

Transmission electron microscopy was utilised to provide a detailed examination of the microstructure, chemistry and crystallography of the three densified compositions. TEM foils were fabricated from the three samples sintered at 1800°C for 4 hours.

3015_{1800}

All three densified compositions examined in this work are comprised of Ca α-sialon in compatibility with one or two AlN-type phases. XRD identified α-sialon as the majority crystalline phase in 3015_{1800}, with the $2H^{\delta}$ AlN-polytypoid as a minor phase, along with a trace of 33R.

Figure 4.18 shows two bright field micrographs of the general microstructure of sample 3015_{1800}. These micrographs reveal the comparatively dense grain structure present in this sample. Though this sample was glass-rich in comparison to a conventional low m-value α-sialon, it exhibited a relatively small volume of intergranular glass when compared to the two higher m-value compositions. The amorphous intergranular phase was generally located in large pockets at grain junctions, though some larger regions of glass were also present.

Nearly all of the grains visible in these two micrographs were α-sialon. Some elongated α-sialon grains were apparent. However, many α-sialon grains in this sample appeared to be more equiaxed in their morphology, displaying a faceted, hexagonal appearance.

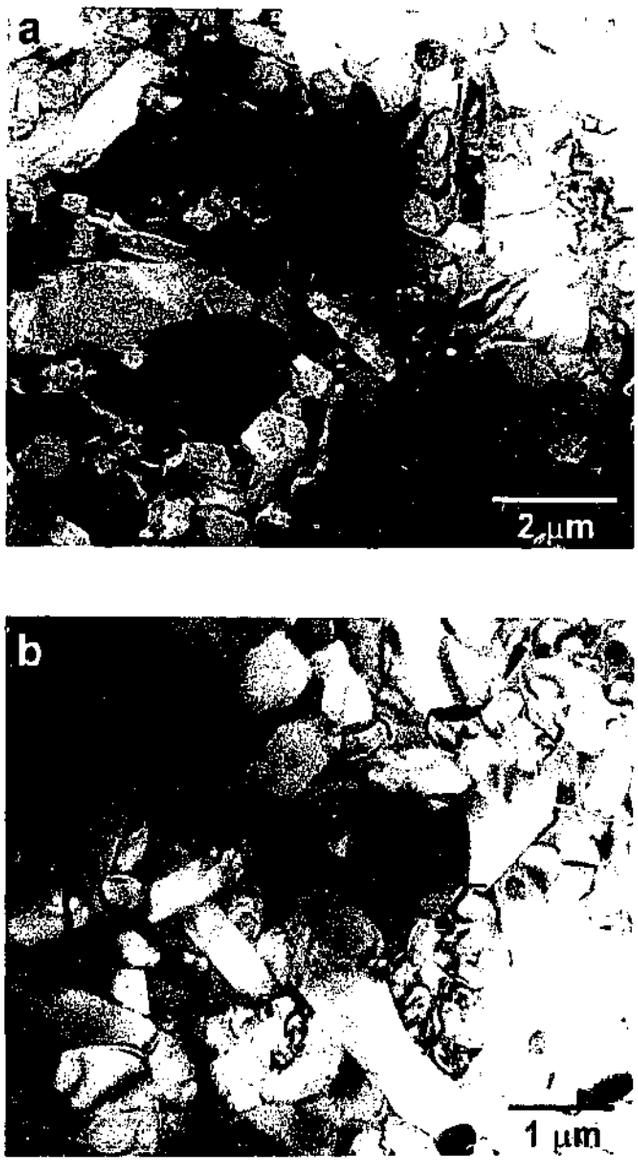

Figure 4.18. Bright field TEM micrographs of sample 3015_{1800}.

The apparent lack of elongated α-sialon grains arises from the fact that only the small fraction of α-sialon grains oriented parallel with the foil surface will exhibit an elongated morphology. The majority of α-sialon grains intersect the foil at other orientations, and thus hexagonal cross-sections were observed more frequently. Many fine α-sialon grains exhibiting equiaxed morphologies were also observed. It was not

possible from these micrographs to determine whether these equiaxed grains were actually grains of equiaxed α-sialon, or whether they were cross-sections of elongated α-sialon rods. The morphology of the AlN-polytypoid phase was not readily observed in these two micrographs, owing to the low proportion of this phase in this sample.

3618_{1800}

Figure 4.19(a) shows a TEM micrograph of the general microstructure of sample 3618_{1800}. Similar to sample 3015_{1800}, observations of elongated α-sialon grains were infrequent. The cross-sections of the rod-shaped α-sialon grains most often appeared as hexagonally faceted, equiaxed grains.

The increased proportion of intergranular glass phase in this higher m-value sample, comparing to sample 3015_{1800}, was noticeable. However, the most striking feature in this sample was the large dimensions of the $2H^{\delta}$ polytypoid grains. Because of the plate morphology of $2H^{\delta}$, cross-sections of these grains often took on the appearance of very long, high aspect ratio needles. Some of these grains are indicated in Figure 4.19(a). Only occasional $2H^{\delta}$ grains exhibited orientations that allowed their plate morphology to be observed. One of these is shown in Figure 4.19(b). The $2H^{\delta}$ polytypoid present in this sample had a very distinctive appearance. Whereas the α-sialon exhibited even contrast throughout the grains, the polytypoids displayed a streaky, fibrous appearance in bright field viewing conditions. This effect is very clear in Figure 4.19(b). This appearance was attributed to the high density of stacking faults in the $2H^{\delta}$ phase.

5025_{1800}

Examination of the highest m-value sample, 5025_{1800}, clearly revealed the very large proportion of intergranular phase present in this sample. As Figure 4.20 shows, the glass formed what was essentially a continuous matrix, within which α-sialon and AlN grains were located. The crystalline grains were almost completely surrounded by glass phase. Only small areas of contact between adjacent grains were observed.

A number of α-sialon grains exhibiting the commonly observed hexagonal morphology of α-sialon rods cut near to perpendicular to their growth direction are visible in micrographs (a) and (b). Additionally, a few α-sialon grains were oriented in such a way that their elongated morphology was apparent. These grains are indicated by arrows.

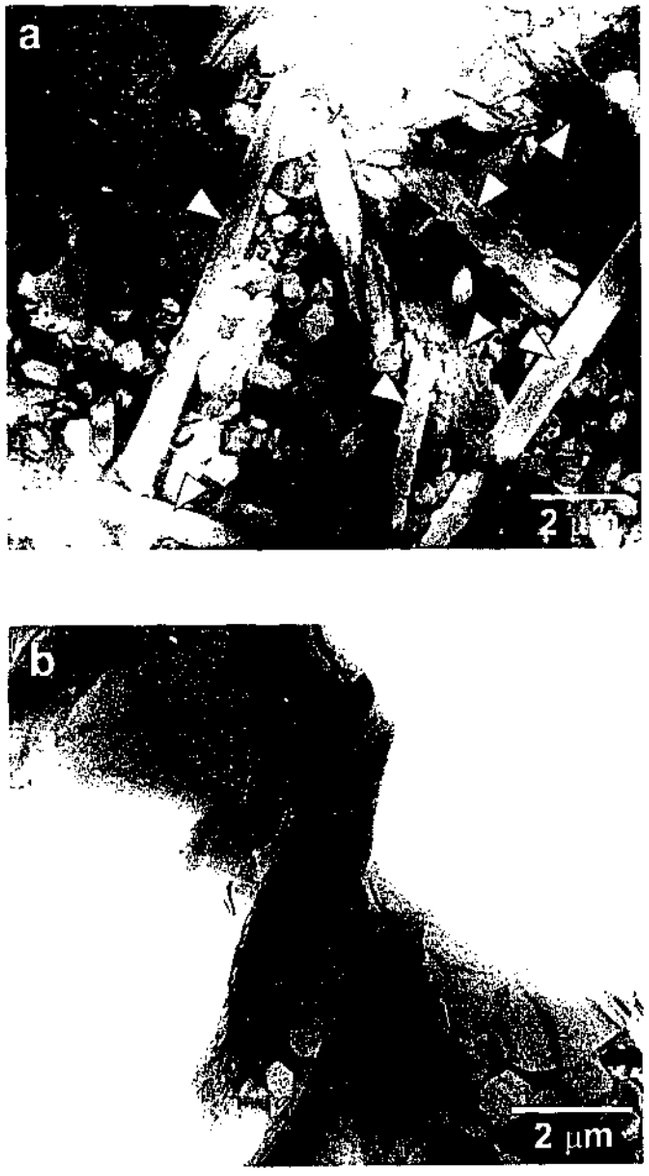

Figure 4.19. Bright field TEM micrographs of the microstructure of 3618_{1800}. Micrograph (a) reveals the high aspect ratio, needle-like morphology of cross-sections of the $2H^{\delta}$ grains (arrowed). Micrograph (b) reveals the plate morphology of a $2H^{\delta}$ grain when viewed nearer to perpendicular to the growth habit.

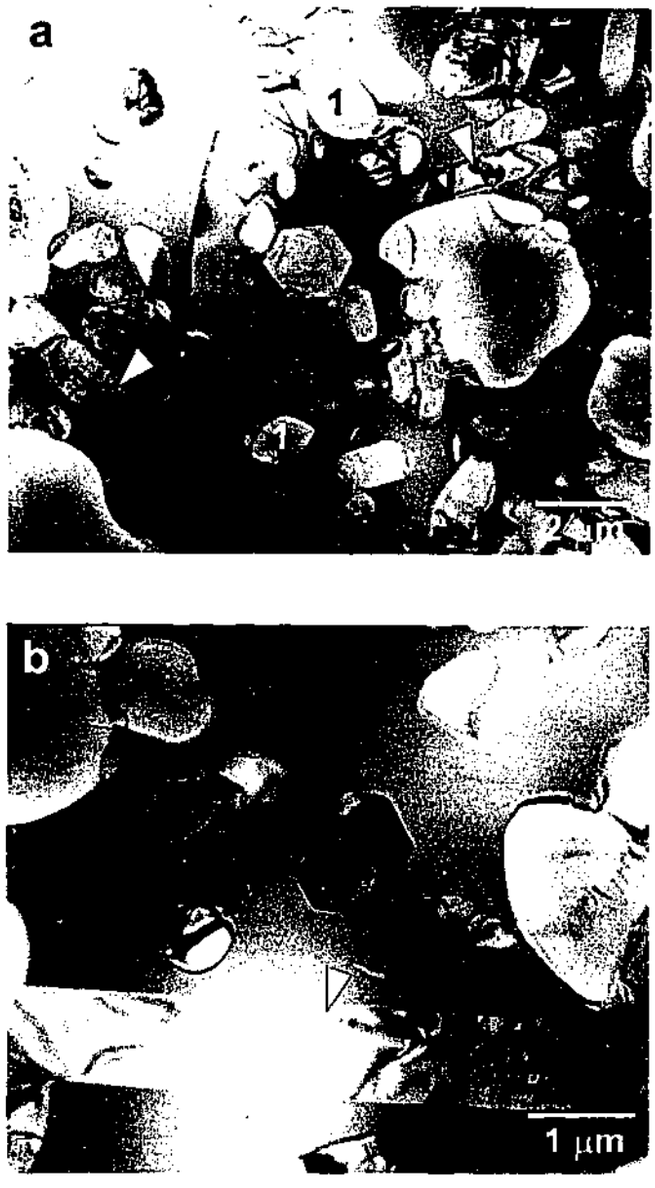

Figure 4.20. Bright field TEM micrographs of the microstructure of 5025_{1800}.

The majority crystalline phase in this sample identified by XRD was AlN. Examination of the microstructure of 5025_{1800} revealed that AlN was present in two distinct morphologies. Some AlN grains exhibited a smooth, rounded or elliptical morphology. These grains typically ranged in size from 1 – 4 μm. Two of these grains are labeled '1' in Figure 4.20(a). Other AlN grains were larger, and exhibited a more irregular, equiaxed morphology. These grains were up to 10 μm in size. One of these grains is labeled '2' in Figure 4.20(a). A detailed study of these different AlN morphologies follows in Section 4.4.4.

4.4.3 TEM Characterisation of Ca α-Sialon

The α-sialon phases in all three densified compositions were found by EDXS analyses to have very similar chemical compositions. An EDXS spectrum obtained from an α-sialon grain in 5025_{1800}. This grain is arrowed in Figure 4.20(b). The Ca, Si, Al, O, and N peaks characteristic of Ca α-sialon are all prominent on this spectrum. The small carbon peak arises from the conductive thin film applied to the foil.

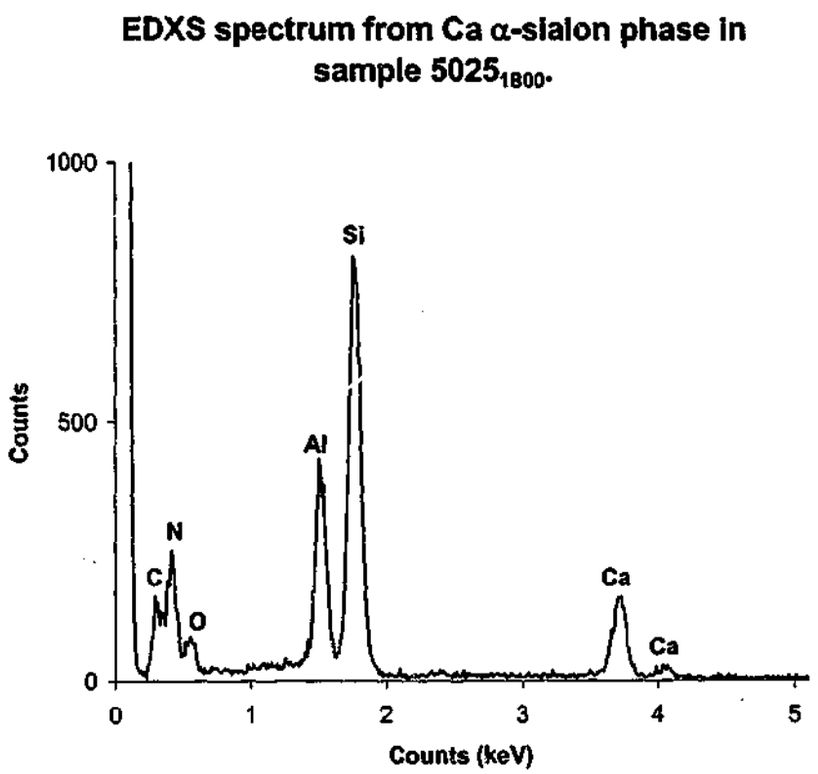

Figure 4.21. EDXS spectra obtained from Ca α-sialon grain 5025_{1800}. The Ca, Si, Al, O, and N peaks, characteristic of Ca α-sialon, are all prominent in this spectrum.

The highly anisotropic growth of faceted α-sialon grains indicates that crystal growth occurs along a preferential direction. Earlier work by Xu et al. (1997) determined that the growth direction for elongated yttrium α-sialon grains is parallel to [001]. In order to establish whether this was also true for Ca α-sialon, the growth direction of the elongated crystals was examined in 3618_{1800}.

An α-sialon grain exhibiting a growth direction perpendicular to the TEM electron beam was located. This grain is indicated in Figure 4.22(a). A selected area electron diffraction pattern obtained from this grain is shown in Figure 4.22(b). This pattern was indexed to the $<1\bar{2}0>$ zone axis of Ca α-sialon. The [100] direction of the grain is indicated in Figure 4.22(a). It can be seen that the grain growth appears to have taken place along the [001] direction, the *c*-axis of the crystal.

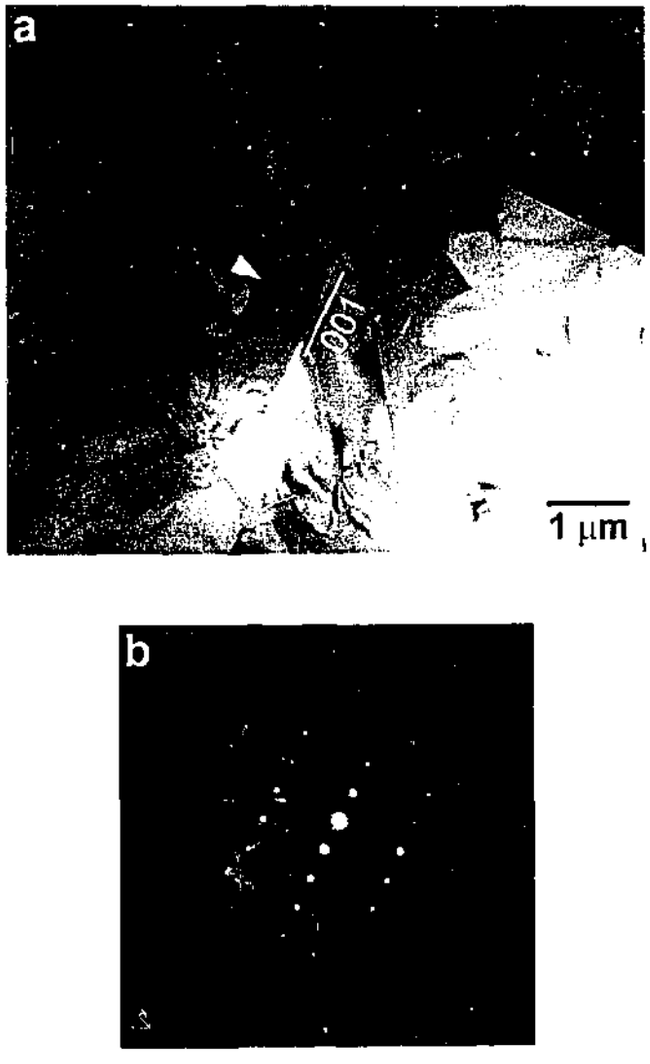

Figure 4.22. (a) Bright field micrograph of a Ca α-sialon grain in 3618_{1800}. Micrograph (b) is a selected area electron diffraction pattern obtained from the arrowed grain in (a). This pattern corresponds to the $<1\bar{2}0>$ zone axis of the Ca α-sialon crystal.

SEM observations of many Ca α-sialon grains indicate that the hexagonal facets of the grains are oriented parallel to the grain growth direction. Therefore, an α-sialon grain with a hexagonal shape was located to provide a zone axis along the growth direction of the grain. This grain is indicated in Figure 4.23(a). A convergent beam electron diffraction pattern, shown in Figure 4.23(b), was obtained from this grain.

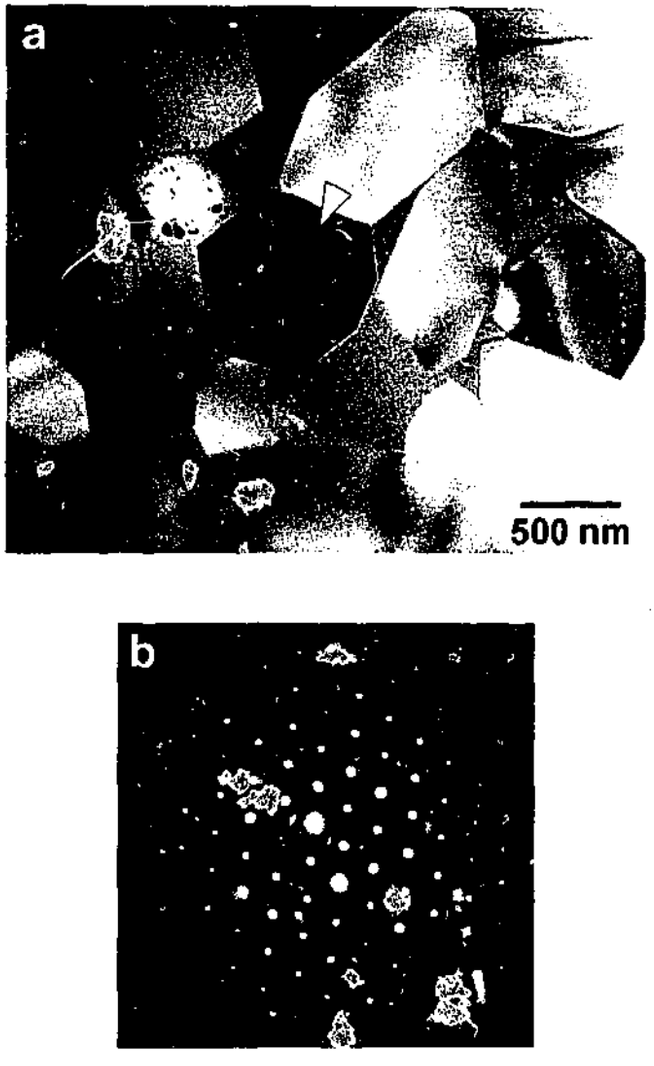

Figure 4.23. (a) Bright field micrograph of a Ca α-sialon grain in 3618_{1800}. Micrograph (b) is a selected area electron diffraction pattern obtained from the dark grain in (a). This pattern corresponds to the <001> zone axis of the Ca α-sialon crystal.

The six-fold symmetry of the diffraction pattern confirmed that this was the zone axis lying parallel to the hexagonal faceting of the crystal. This zone axis was identified as

<001>, again indicating that the growth habit for Ca α-sialon is along the [001] direction, the c-axis of the crystal.

4.4.4 TEM Characterisation of AlN and AlN-Polytypoid Phases

Both AlN and two AlN-polytypoid phases have been shown to be present among the three densified compositions being examined. The $2H^{\delta}$ polytypoid phase was detected as a minor crystalline phase in two of the samples, 3015_{1800} and 3618_{1800}. The long, plate-shaped, $2H^{\delta}$ grains that were observed in SEM micrographs are easily distinguished from α-sialon grains by TEM because of their large grain size, their distinctive streaky appearance, and their different chemistry. The EDXS spectrum shown in Figure 4.24 was obtained from the large grain shown in Figure 4.25(a). Visible on this spectrum are Al, N, Si and O peaks. This is consistent with the chemical composition of the $2H^{\delta}$ phase, which is essentially AlN with small Si and O substitutions.

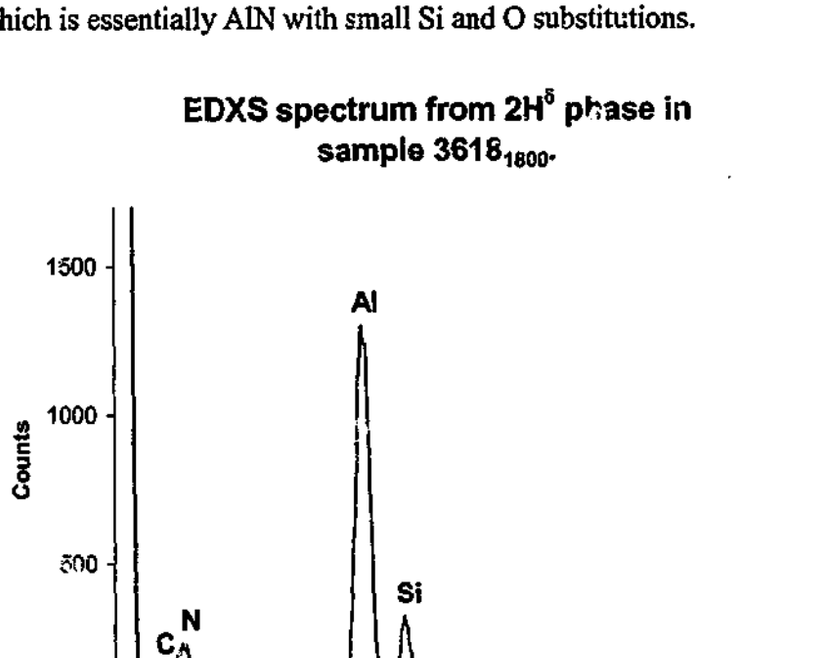

Figure 4.24. EDXS spectrum obtained from $2H^{\delta}$ grain in sample 3618_{1800}.

Electron diffraction patterns offered further confirmation that this phase was the $2H^{\delta}$ polytypoid. Figure 4.25(b) is a convergent beam electron diffraction pattern obtained

from the grain in Figure 4.25(a). The spots in this pattern corresponded to the <002> zone axis of $2H^{\delta}$.

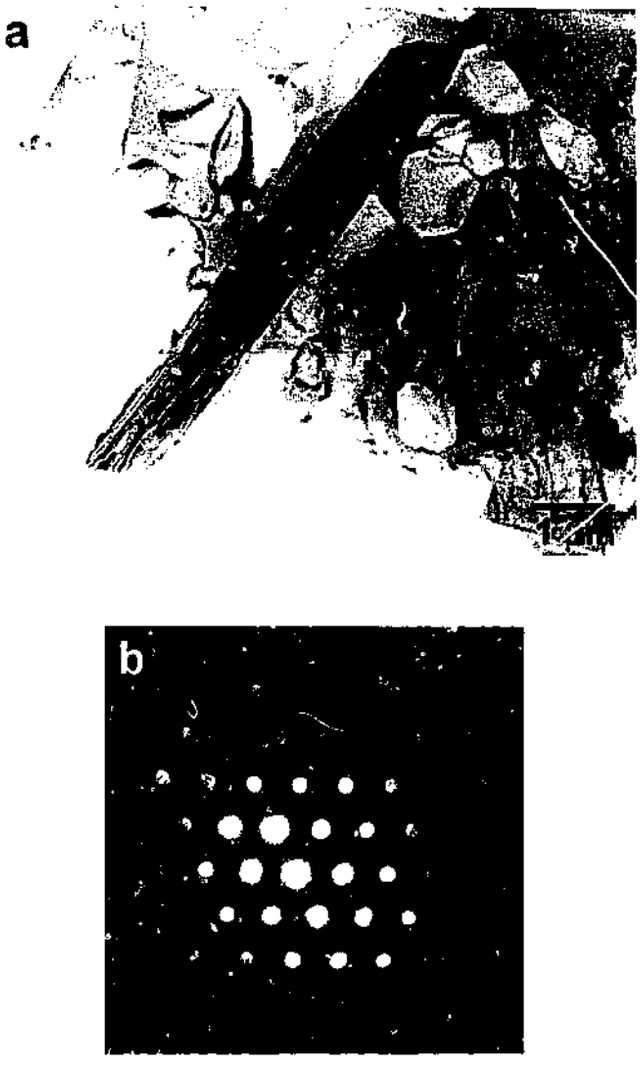

Figure 4.25. (a) Bright field micrograph of a $2H^{\delta}$ polytypoid grain in 3618_{1800}. Micrograph (b) is a convergent beam electron diffraction pattern obtained from this grain. This pattern corresponds to the <002> zone axis of $2H^{\delta}$.

3015_{1800} also contained a small amount of the 33R polytypoid ($SiAl_{10}O_2N_{10}$). Due to the morphological and chemical similarities of 33R to $2H^{\delta}$, and the fact that only trace amounts were detected by XRD, the specific identification of 33R grains in the sample was not attempted.

As a result of its Al-rich nature, AlN formed the majority crystalline phase in 5025_{1800}. None of the AlN-polytypoids were detected in this sample. As was previously mentioned, a close examination of the AlN grains in this sample revealed that AlN existed with two distinct morphologies. Some grains had a smooth, rounded or elliptical morphology, exhibiting typical grain sizes of 1 - 4 μm. This type of grain is shown in Figure 4.26(a).

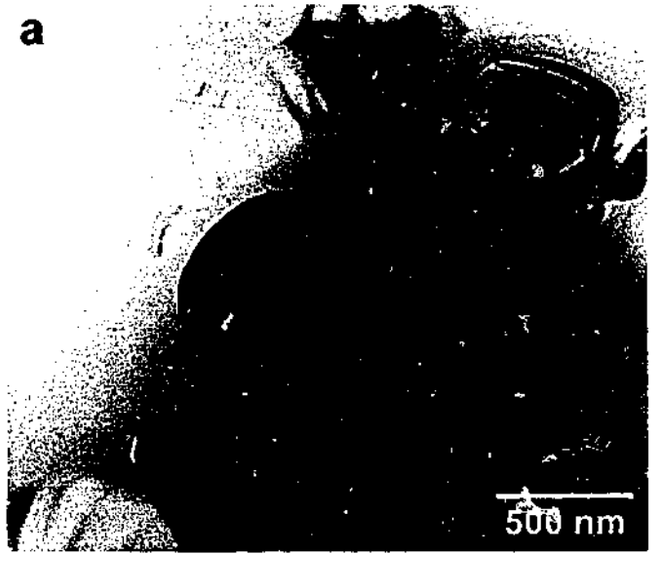

EDXS spectrum obtained from rounded AlN grains in sample 5025_{1800}.

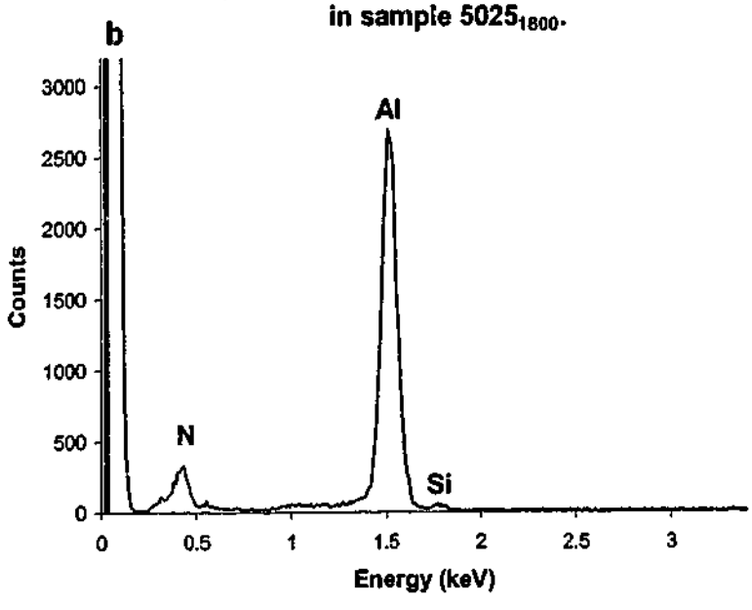

Figure 4.26. (a) Bright field micrograph of the rounded AlN grains found in 5025_{1800}. The EDXS spectrum in (b) was obtained from this grain. Only Al and N and a trace of Si are detected in the grains with this morphology.

This AlN will be referred to as Type 1 AlN in the subsequent discussion. This grain morphology was consistent with the grains commonly observed in the microstructure of this sample in the SEM. EDXS analysis of these grains detected Al, N, and a trace of Si (Figure 4.26(b)). The other distinct AlN grains were larger, with a more irregular, equiaxed morphology (Figure 4.27(a)). These will subsequently be referred to as Type 2 AlN.

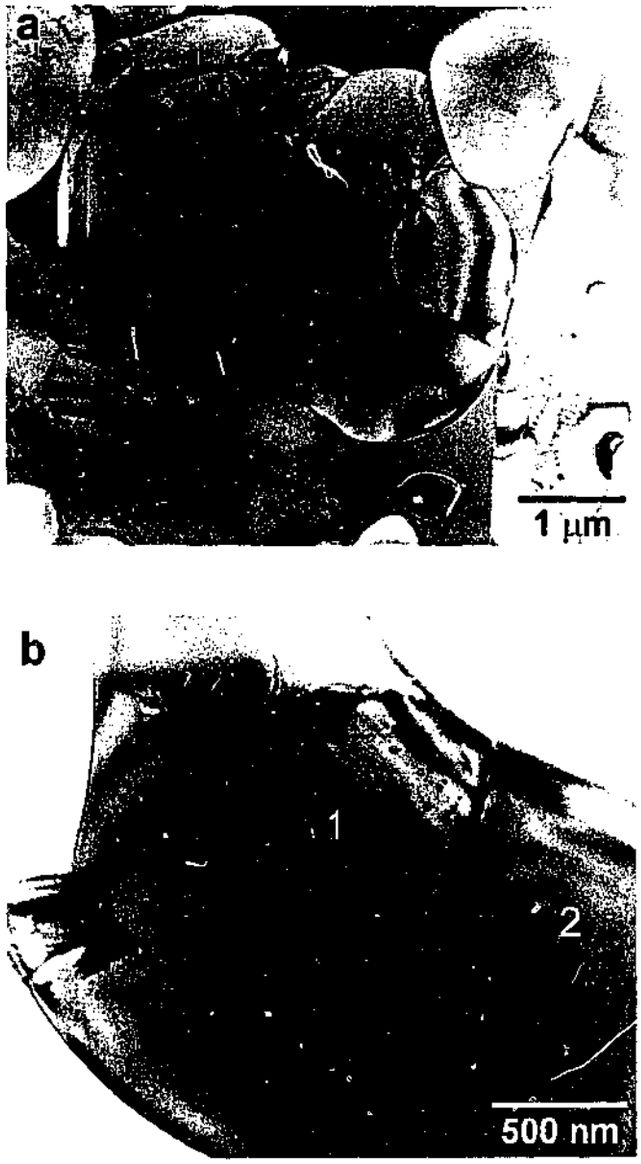

Figure 4.27. Bright field micrograph of an irregular-shaped AlN grain found in 5025_{1800}. The sub-grain structure is clearly apparent. Micrograph (b) shows two sub-grains in one of these AlN grains, labeled 1 and 2, from which the EDXS spectra in Figure 4.28 were obtained. Small inclusions are visible in sub-grain 1.

Examination of these irregular shaped grains in the TEM revealed that the structure of the grains was quite complex. Bright field micrographs revealed that each grain was composed of a number of sub-grains. The boundaries between the sub-grains are quite clear in Figures 4.27(a and b). A further observation was the presence of many small inclusions, less than 100 nm in diameter, in some sub-grains. These are clearly visible in the sub-grain labeled '1' in Figure 4.27(b).

EDXS analyses of the different sub-grains contained in a single grain revealed that some significant chemical differences existed between sub-grains. Typically, one sub-grain possessed a pure Al and N chemistry. In all the other sub-grains, a small amount of Si was detected, in addition to Al and N. Interestingly, it was only the sub-grains that exhibited the nano-sized inclusions that possessed the pure Al and N chemistry. Figure 4.27(b) shows two adjacent sub-grains in a single grain of AlN. Figure 4.28 shows EDXS spectra obtained from each of these sub-grains. The different chemistries of the two sub-grains are clearly apparent.

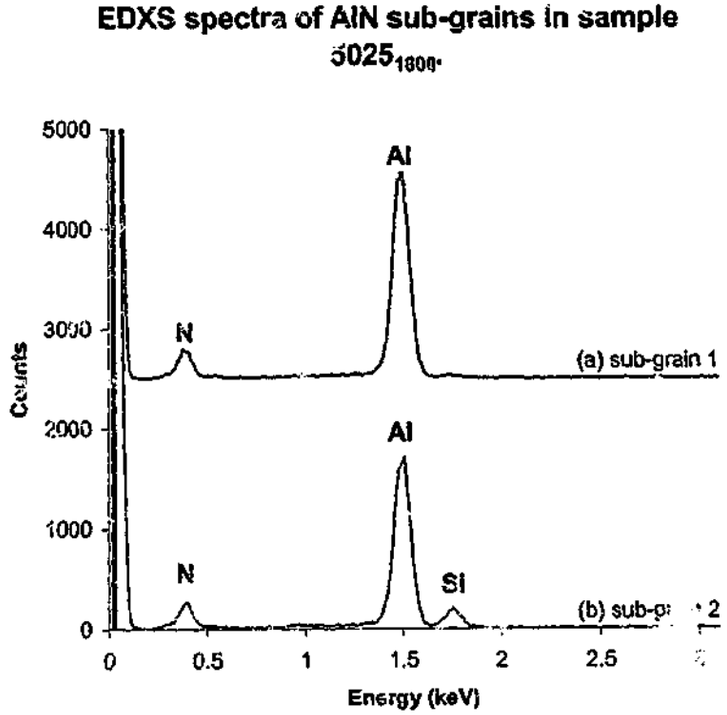

Figure 4.28. EDXS spectra obtained from the two sub-grains labeled 1 and 2 in Figure 4.27(b). The spectrum of sub-grain 1 shows a pure Al and N chemistry. The spectrum of sub-grain 2 reveals the presence of a significant Si content in addition to Al and N.

A selected area electron diffraction pattern was obtained from an area overlapping these two same sub-grains. The selected area is indicated by the circle in Figure 4.29(a). The diffraction pattern in Figure 4.29(b) reveals that the two sub-grains appear to share the same crystallography and crystallographic orientation relationship.

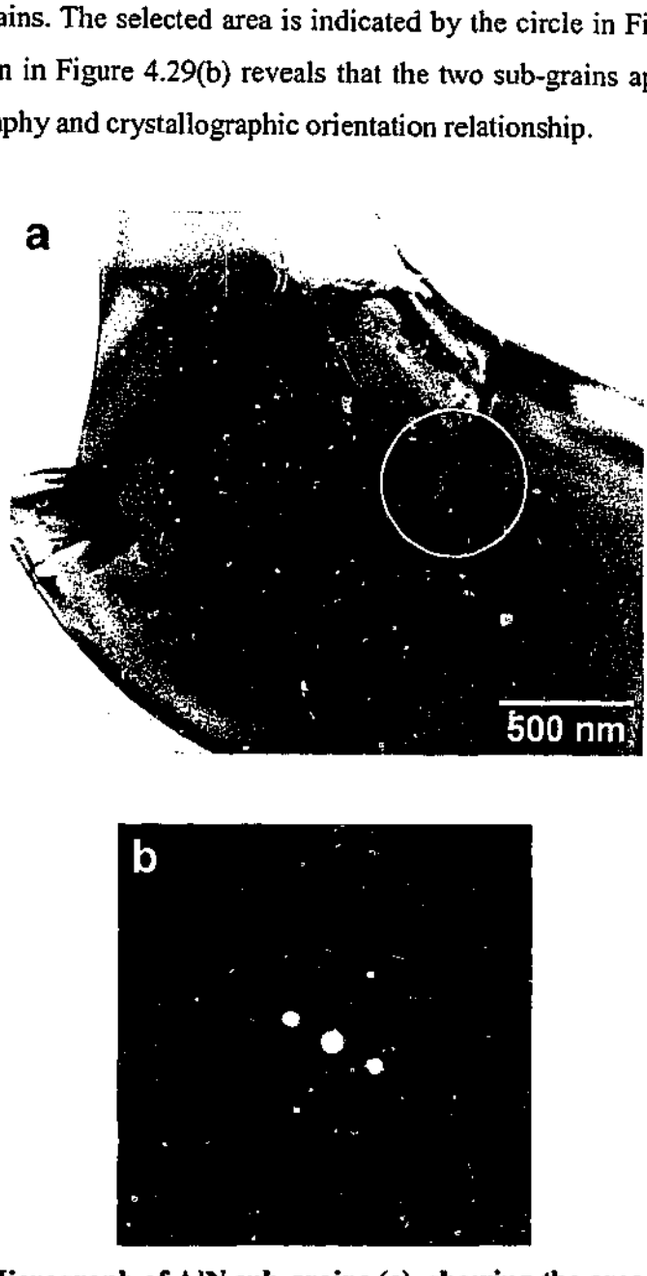

Figure 4.29. Micrograph of AlN sub-grains (a), showing the area (circled) from which the selected area electron diffraction pattern (b) was obtained. This area covers two sub-grains exhibiting both of the different types of chemistry found by EDXS analysis. The diffraction pattern corresponds to the <220> zone axis of AlN.

This combination of chemical and crystallographic information suggests that the single central sub-grain, with the pure Al-N chemistry, is a particle of the original AlN raw material. The sub-grains with the Si impurity are believed to be AlN that has heterogeneously nucleated on the particle of raw material. The Si arises because the AlN

has precipitated out of a Si-rich liquid phase, thus producing AlN with a small quantity of Si in solid solution. It appears that nucleation occurs at a number of sites on an AlN particle, with the individual sub-grains growing epitaxially, and eventually forming a single grain. The interfaces visible in Figure 4.27 are where the growth fronts of the different sub-grains have met.

Work in the following chapter will show that the 'nano-precipitates' found in some sub-grains are indicative of original AlN starting material. This is further evidence that the sub-grain with the Al-N chemistry and nano-precipitates is a particle of original AlN starting powder.

Like the pure Al-N sub-grains in the larger Type 2 AlN, the smaller, rounded Type 1 AlN grains also often exhibited an array of small nano-sized inclusions. These are clearly visible in Figure 4.26(a). Consequently, these AlN grains are believed to be particles of partially dissolved AlN starting powder. The exact nature of these nano-precipitates is addressed in the following chapter.

4.4.5 Summary of Microstructural Characterisation

The work presented in this section examined the microstructures of three sintered Ca-Si-Al-O-N samples using SEM, TEM and EDXS techniques.

The microstructural evolution of the 3618 composition, sintered at temperatures between 1400°C and 1800°C, was examined in detail using SEM. Grain sizes in the very porous samples sintered at 1400°C and 1500°C were too small to be examined with any degree of detail. The first notable grain growth was observed to occur during the 1550°C isothermal hold. This temperature also coincided with a large reduction in the porosity of the sample, which was a result of the melting of gehlenite. At 1600°C, α-sialon grains clearly possessed an elongated morphology. The anisotropic growth of α-sialon continued up to the maximum sintering temperature of 1800°C. Growth across the width of the α-sialon grains was very limited at all the temperatures investigated, which imparted a high aspect ratio to the grains.

Examination of the three fully dense samples revealed that a higher composition m-value resulted in a higher volume of intergranular phase, and a longer average α-sialon grain length. α-Sialon grain lengths averaged ~5 μm in 3015_{1800}, increasing to an average of ~10 μm in 5025_{1800}. The growth direction of elongated α-sialon grains was determined by electron diffraction to be along the [001] direction.

AlN-polytypoid grains, composed mainly of the $2H^{\delta}$ phase, were observed to occur with a plate morphology. These grains grew to quite large dimensions, reaching cross-sectional lengths of up to 35 μm in sample 3618_{1800}. AlN grains in 5025_{1800} were observed with two distinct morphologies. Some grains exhibited a smooth, rounded morphology. These were determined by TEM and EDXS techniques to be partially dissolved particles of original AlN starting powder. Other AlN grains had larger, more irregular equiaxed morphologies. These grains were found to be composed of a single, pure AlN sub-grain, surrounded by other AlN sub-grains that contained a Si impurity. These grains were determined to be composed of a core particle of raw AlN starting powder, upon which new AlN heterogeneously nucleated and grew epitaxially from the liquid phase.

4.5 Fracture Behaviour

The toughening effect of elongated grains in ceramic materials has been recognised in many systems, especially the β-Si_3N_4 and β-sialon systems. The elongated grains interact with propagating cracks, activating toughening mechanisms such as crack bridging, crack deflection and grain pullout. All these mechanisms may increase the energy required to propagate a crack through the material. Consequently, the fracture toughness of the material is improved. The high aspect ratio, elongated, Ca α-sialon grains observed in these three compositions are typical of the grain morphologies used to improve fracture toughness in a range of ceramic systems. Therefore, the potential exists for fabricating in-situ toughened Ca α-sialon materials.

4.5.1 Fracture Surface Characterisation

Fracture surfaces of each of the three compositions sintered at 1800°C for 4 hours were obtained. These were examined using SEM. Figure 4.30 shows two micrographs of the fracture surface of sample 3015_{1800}. A number of interesting features indicative of microstructural toughening mechanisms were observed on this fracture surface. Large elongated imprints with morphologies similar to that of the elongated α-sialon grains were clearly visible. Some of these are indicated in Figure 4.30(a).

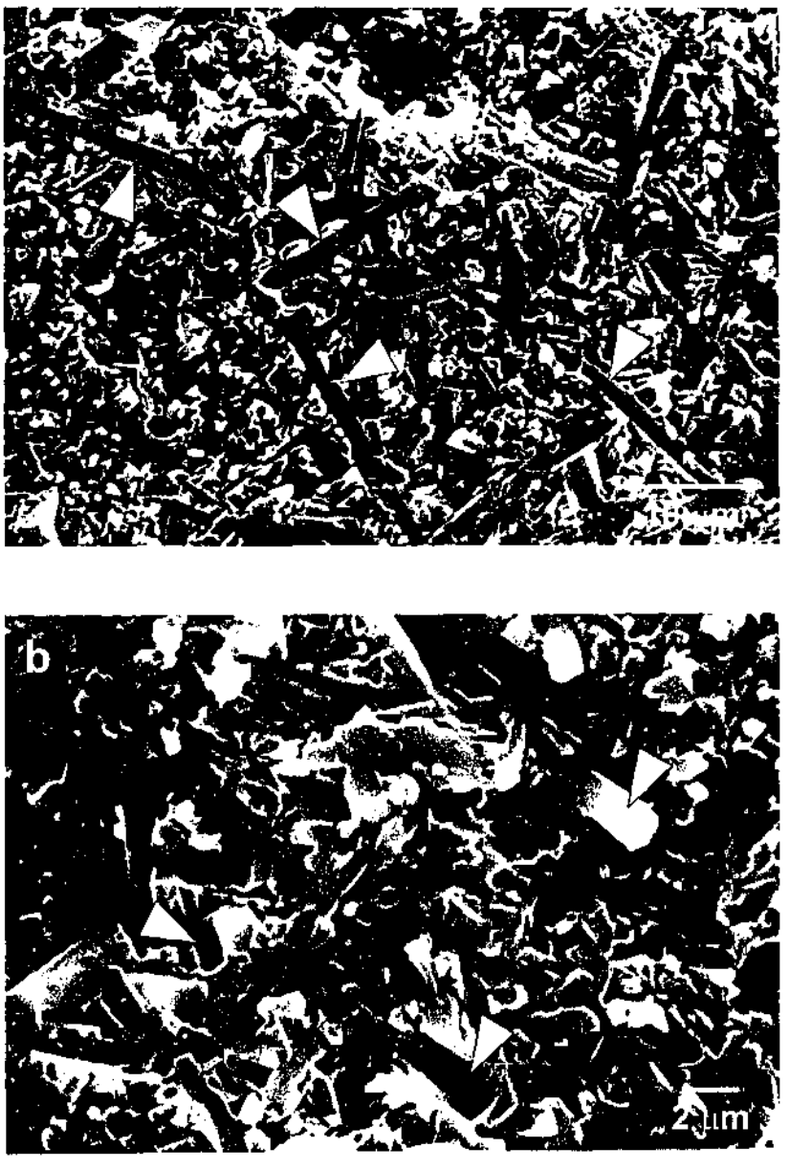

Figure 4.30. Secondary electron micrographs of the fracture surface of sample 3015_{1800}. Examples of grain debonding and pullout are arrowed.

These arose from the debonding of elongated α-sialon grains, oriented approximately parallel to the fracture surface. Also visible were rod-like grains protruding from the fracture surface, and faceted holes in the matrix. Some of these are indicated in Figure 4.30(b). These features are indicative of grain pullout, where elongated α-sialon grains have debonded from the matrix, and then pulled out during fracture. All of these features are consistent with microstructural toughening mechanisms associated with elongated grains.

No significant evidence of contributions to toughening by the plate-shaped $2H^{\delta}$ grains was observed. This is considered to be due to the relatively large surface area of the $2H^{\delta}$ grains, which results in a strong interfacial bond between the grain and the intergranular glass phase. This would make grain debonding and pullout difficult, and consequently transgranular, rather than intergranular, fracture would typically occur at these grains.

The fracture surface of sample 3618_{1800} appears very similar to that of 3015_{1800} (Figure 4.31). This was not unexpected, considering the similar phase assemblages and microstructures of the two samples. Similar indications of the presence of microstructural toughening mechanisms are observed in this sample.

The fracture surface of sample 5025_{1800} differed noticeably from the other two samples (Figure 4.32). It yielded a fracture surface that showed less evidence of microstructural toughening mechanisms. Evidence of grain debonding and pullout of elongated α-sialon grains was observed, but to a lesser extent than in the other two samples. Some dimple-shaped imprints and rounded grains were visible on the fracture surface (Figure 4.32(a)). These can be attributed to the debonding of the smooth, rounded, AlN grains in the sample. Grains with this equiaxed type of morphology offer no significant contribution to microstructural toughening. The high proportion of intergranular glass phase in the sample is also apparent when examining the fracture surface (Figure 4.32(b)).

Though AlN constituted the majority crystalline phase in this sample, it also contained a significant proportion of elongated α-sialon grains. These grains averaged approximately 10 μm in length. It was expected that because of the long, high aspect ratio nature of these grains, this sample would exhibit significant evidence of toughening

mechanisms. However, this was not the case. It appeared that the high proportion of intergranular glass in this sample promoted fracture through the glass matrix. Though some interaction of α-sialon grains with the propagating crack occurred, significant areas of glassy fracture were apparent on the fracture surface (Figure 4.32(b)).

Figure 4.31. Secondary electron micrographs of the fracture surface of sample 3618_{1800}.

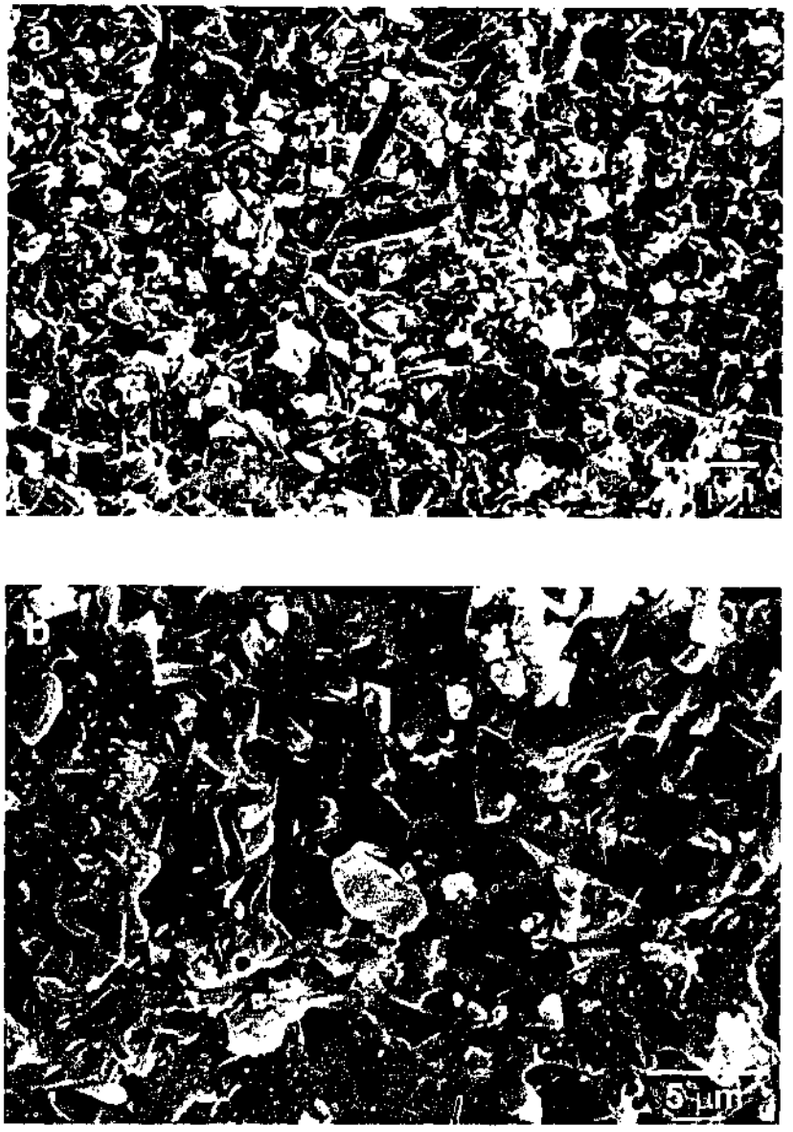

Figure 4.32. Secondary electron micrographs of the fracture surface of sample 5025_{1800}.

4.5.2 Fracture Toughness and R-Curve Determination

To obtain a quantitative idea of the fracture properties of the three samples, an R-curve analysis was carried out using the indentation technique (Anstis et al. 1981). A rising R-curve indicates the activity of microstructural toughening mechanisms in whisker reinforced ceramics. Figure 4.33 plots the crack growth resistance parameter, K_R, as a function of crack length for each of the three samples. It is clear from this plot that both

3015_{1800} and 3618_{1800} exhibit rising R-curve behaviour. This correlates with the evidence for toughening mechanisms observed on the fracture surfaces of these two samples.

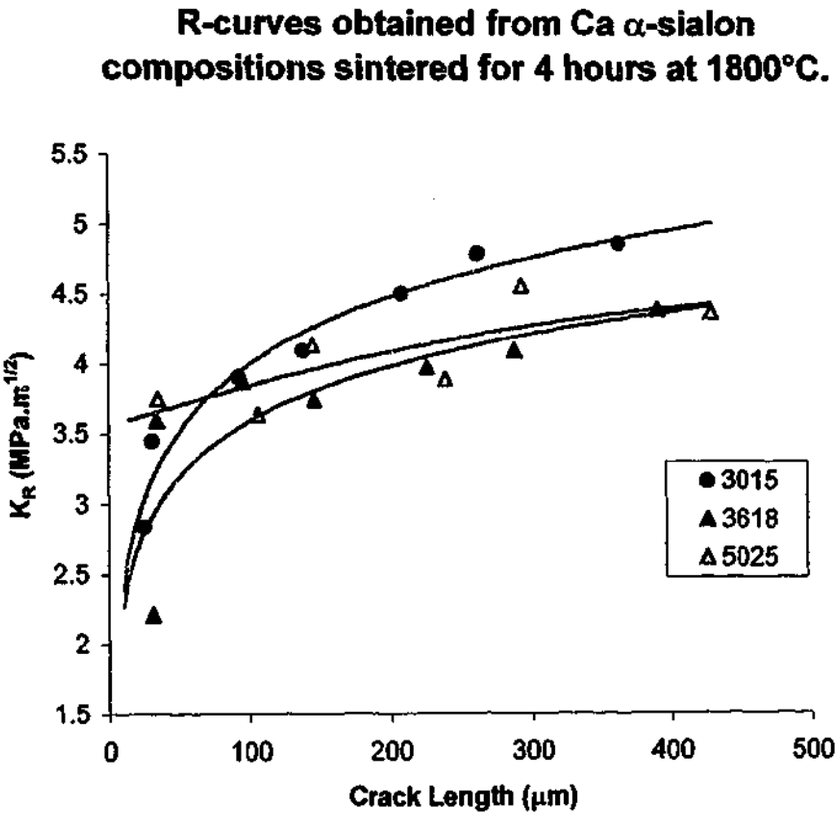

Figure 4.33. A plot of the crack growth resistance parameter, K_R, as a function of crack length for the three compositions sintered for 4 hours at 1800°C.

In contrast to these two samples, the glass-rich 5025_{1800} sample exhibited obscure rising R-curve behaviour. Only a minimal increase in crack growth resistance with increased crack extension was observed. This result was consistent with the features observed on the fracture surface of this sample, which showed significantly less evidence of the activity of microstructural toughening mechanisms. Despite this, the steady-state fracture toughness of 5025_{1800} approached a value very close to that of 3618_{1800} (Figure 4.33). The maximum fracture toughness values measured in the 3015, 3618 and 5025 samples were 4.87, 4.39 and 4.37 MPa.m$^{1/2}$ respectively.

Secondary electron micrographs of indentation cracks generated in the 3618_{1800} test specimen are shown in Figure 4.34. Grains in the microstructure are not easily distinguished as these specimens still contain their intergranular glass phase. Examining the cracks that have propagated through the sample, examples of toughening mechanisms such as crack deflection and grain debonding are observed. It is apparent that the elongated α-sialon grains in the microstructure act to hinder crack propagation.

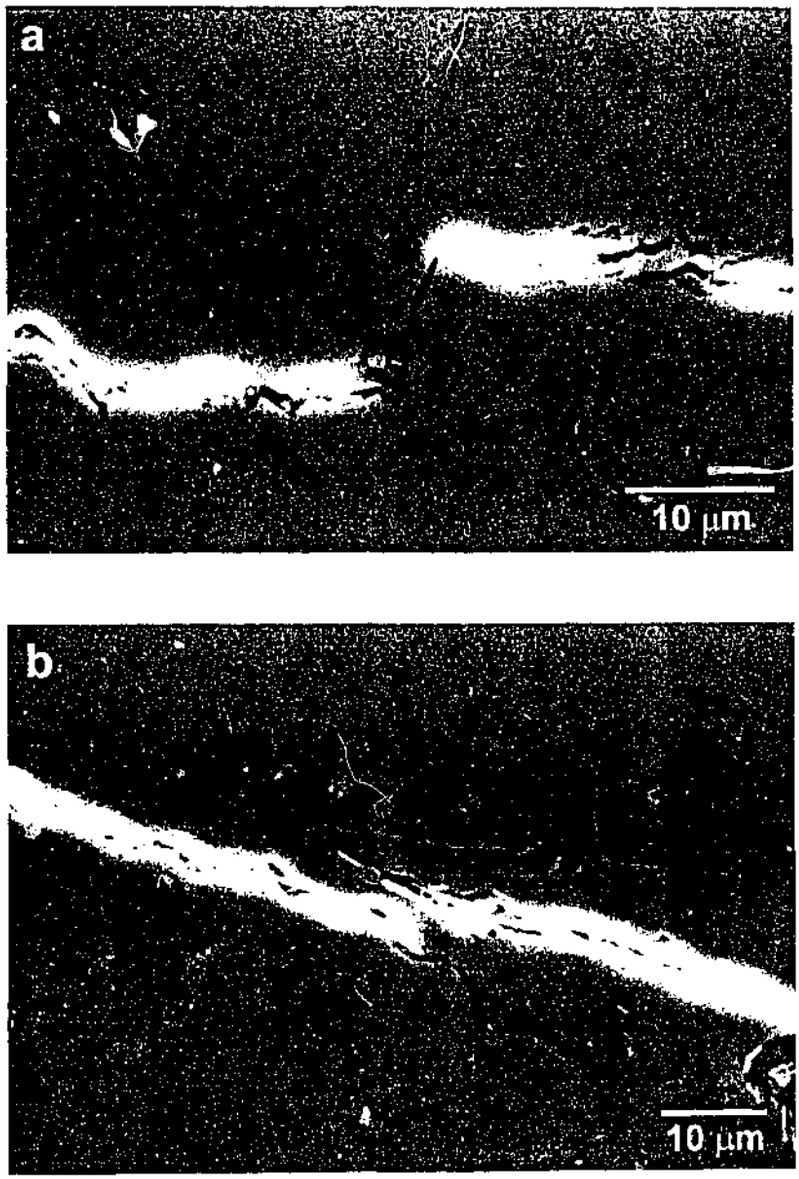

Figure 4.34. Secondary electron micrographs of crack paths in the 3618_{1800} specimen used in R-curve testing. Evidence of toughening mechanisms such as crack deflection and grain debonding are evident in this sample.

Both qualitative fracture surface analysis, and quantitative R-curve measurements, demonstrate that the sample with the longest and highest aspect ratio α-sialon grains, 5025_{1800}, obtained the least benefit from the elongated grains in terms of R-curve response. Conversely, a significant rising R-curve was seen in 3015_{1800}, the sample with the shortest average α-sialon grain length.

A number of factors may have contributed to the poor response of 5025_{1800} to the elongated α-sialon grains. A significant contribution can be attributed to the reduced proportion of elongated α-sialon present in this sample in comparison to the other two samples. The reduced amount of elongated α-sialon grains would certainly reduce the potential for significant microstructural toughening in the sample. Furthermore, whereas 3015_{1800} and 3618_{1800} exhibited plate-shaped AlN-polytypoids as secondary crystalline phases, which may have assisted in toughening to some degree, 5025_{1800} exhibited equiaxed AlN as the dominant crystalline phase. Grains exhibiting this morphology would offer little or no contribution to microstructural toughening.

5025_{1800} also exhibited a large proportion of glass phase in its microstructure. This would have a deleterious effect on the fracture toughness of the material. Because of their similar chemistries, the intergranular glass phase would easily wet the α-sialon grains, allowing a strong interfacial bond to form. A strong interfacial bond increases the energy required to debond an α-sialon grain from the glass matrix. This increases the likelihood of transgranular fracture over intergranular fracture, and consequently the elongated grains can't contribute significantly to improved fracture toughness. Additionally, the volume of intergranular glass phase in this sample is so great that a propagating crack could simply travel through the glass matrix, only occasionally having to fracture or debond α-sialon grains.

Referring back to the TEM micrographs obtained from these three samples (Figures 4.18, 4.19 and 4.20) helps to further demonstrate the physical relationship of the intergranular glass to the elongated α-sialon grains. In 3015_{1800}, a relatively small amount of intergranular phase exists, and it is mostly contained at grain junctions. In contrast to this, grains in 5025_{1800} are almost fully surrounded by intergranular phase. It is clear from these micrographs that the volume of intergranular glass in 5025_{1800} is such

that a crack could easily propagate through the glass phase, and this would lead to less opportunity for the crack to interact with a crystalline grain.

4.6 Conclusions for Chapter 4

The key conclusions that were reached as a result of the examination into the three Ca-Si-Al-O-N compositions are as follows:

- Anisotropic grain growth of Ca α-sialon occurs in Ca-Si-Al-O-N compositions with m-values ranging from 3.0 to 5.0, for m:n ratios of 2:1. The α-sialon forms as high aspect ratio, elongated rods. Average α-sialon grain lengths and aspect ratios, which increased with increasing m-value in the α-sialon equation, were 5 μm and 6 for composition 3015, 8 μm and 9 for 3618, and 10 μm and 9 for 5025.

- All three compositions can attain >99% of maximum density by pressureless sintering for 4 hours at 1700°C and/or 1800°C. Compositions that generate large quantities of liquid phase suffer from severe bloating after sintering at 1800°C.

- Increasing composition m-values increases the proportions of intergranular glass and AlN/AlN-polytypoid phases present in sample microstructures. The proportion of Ca α-sialon decreases with increasing m-value. XRD analyses record very strong α-sialon peaks in samples 3015_{1800} and 3618_{1800}, and medium strong peaks in 5025_{1800}.

- Three intermediate phases are observed in the three Ca-Si-Al-O-N compositions over the 1400°C to 1800°C temperature range. One of these is gehlenite. The other two remain unidentified. The intermediate phases are found to have a significant effect on densification during pressureless sintering. The precipitation of an intermediate phase that remains stable to a high temperature can significantly hinder densification.

- Evidence of fracture toughness improving mechanisms such as grain debonding, crack deflection and grain pullout is observed on the fracture surfaces of samples containing elongated Ca α-sialon. Rising R-curve behaviour, which is indicative of the elongated α-sialon grains acting to improve fracture toughness in the materials, is observed in the densified materials. Rising R-curve behaviour diminishes as composition m-values are increased. Maximum K_R values measured for the 3015_{1800}, 3618_{1800} and 5025_{1800} samples were 4.87, 4.39 and 4.37 $MPa.m^{1/2}$ respectively.

Chapter 5

Investigation of High m-value Ca-Si-Al-O-N Compositions

5.1 Introduction

Previous chapters have established that Ca α-sialons attracted only limited research interest over many years. A consequence of this situation was that for much of this time, the Ca-Si-Al-O-N system remained relatively uncharacterised. For a long period, only a basic partial phase behaviour diagram of the Ca α-sialon plane existed (Figure 2.5).

The first comprehensive characterisation of the system was carried out by Hewett and co-workers in the 1990's (Hewett et al. 1994b; Hewett et al. 1994a; Hewett 1998; Hewett et al. 1998a; Hewett et al. 1998b). They extensively studied a region of compositions bounded by the lines m = 3.0 and n = 3.5 on the Ca α-sialon plane. This work led to the formation of a more complete phase behaviour diagram of the Ca α-sialon plane (Figure 4.1).

Whilst undertaking this work, observations of anisotropic growth of α-sialon grains were made in higher m and n-value compositions. Further investigations of compositions with even higher m and n-values, presented here in the preceding chapter, have shown that anisotropic α-sialon growth occurs over a significant compositional range.

Despite this extensive study of the Ca-Si-Al-O-N system, a large portion of the Ca α-sialon phase behaviour diagram remains uncharacterised. The high m and n-value compositions located in this uncharacterised region are of some interest, as anisotropic α-sialon grain growth has been shown to be promoted in higher m and n-value Ca-Si-Al-O-N compositions (Hewett 1998; Zhao et al. 1998). These compositions are Ca and Al-rich, and based on the phase behavior diagram published by Hewett et al. (Figure 4.1), they would be expected to form materials exhibiting large proportions of AlN and/or

AlN-polytypoid phases, coexisting with α-sialon. Substantial volumes of grain boundary glass phase would also be expected in these compositions. These compositions further depart from the sialon phase region, and may not be useful as high performance engineering materials. However, an examination of these compositions is nonetheless warranted as a part of developing a better understanding of anisotropic α-sialon grain growth, and improving the overall knowledge of the Ca-Si-Al-O-N system.

This chapter presents an investigation of eight previously unstudied Ca and Al-rich Ca-Si-Al-O-N compositions. The phase assemblages and microstructures developed in these densified materials will be described, with particular emphasis on the morphology of the α-sialon grains that result from sintering. Phase assemblage information obtained from this work will be combined with the data of Hewett et al. (1998a) to create a refined version of the phase behaviour diagram previously published by them. Fracture surfaces of the eight samples will be examined to observe what, if any, evidence of microstructural toughening effects is present in the AlN-polytypoid and grain boundary glass-rich materials.

In addition to this, some unusual features observed in a densified sample of 5025 will be presented. This high m-value composition was examined in detail in the previous chapter. The work in this chapter investigates some features related to the AlN phase present in this composition.

5.2 Experimental Outline

Eight Ca-Si-Al-O-N compositions were examined as a part of this work. Each was designated by its m and n-value in the α-sialon equation (Eqn. 2.2) where, for example, the composition designated 2040 had m and n-values of 2.0 and 4.0 respectively. The eight compositions are detailed in Table 5.1. Their positions on the Ca α-sialon plane are shown in Figure 5.1. The weight percentages of the starting powders used in each composition are displayed in Table 5.2.

Table 5.1. Chemical compositions and m and n-values of the eight compositions examined in this section of work.

Composition name	Formula	m-value	n-value
2040	$Ca_{1.0}Si_{6.0}Al_{6.0}O_{4.0}N_{12.0}$	2.0	4.0
2050	$Ca_{1.0}Si_{5.0}Al_{7.0}O_{5.0}N_{11.0}$	2.0	5.0
3040	$Ca_{1.5}Si_{5.0}Al_{7.0}O_{4.0}N_{12.0}$	3.0	4.0
3050	$Ca_{1.5}Si_{4.0}Al_{8.0}O_{5.0}N_{11.0}$	3.0	5.0
4040	$Ca_{2.0}Si_{4.0}Al_{8.0}O_{4.0}N_{12.0}$	4.0	4.0
4050	$Ca_{2.0}Si_{3.0}Al_{9.0}O_{5.0}N_{11.0}$	4.0	5.0
5040	$Ca_{2.5}Si_{3.0}Al_{9.0}O_{4.0}N_{12.0}$	5.0	4.0
5050	$Ca_{2.5}Si_{2.0}Al_{10.0}O_{5.0}N_{11.0}$	5.0	5.0

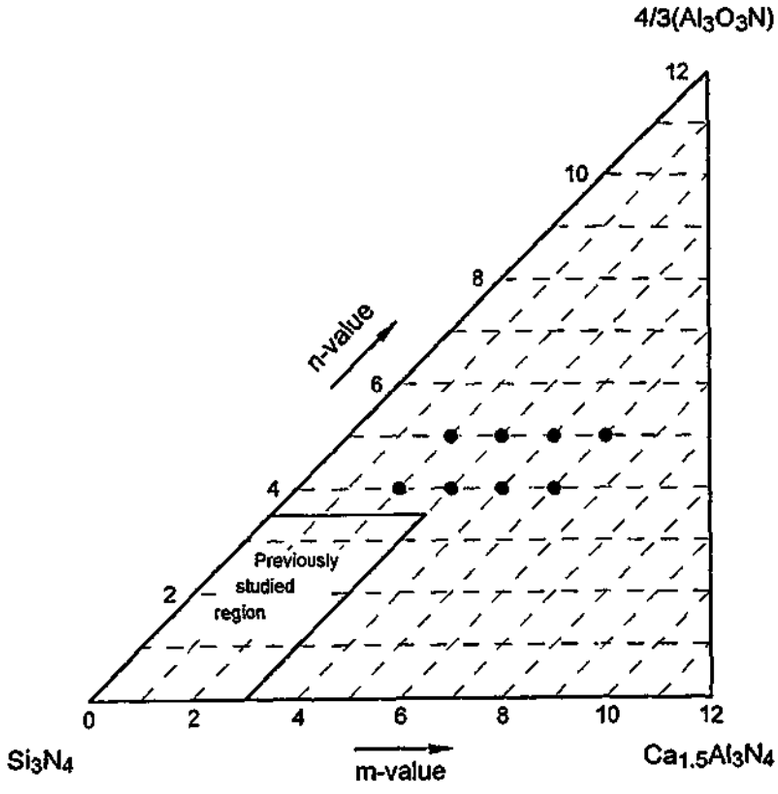

Figure 5.1. The locations on the Ca α-sialon plane of the eight compositions examined in this section of work. Also shown is the compositional region previously examined by Hewett and coworkers (Hewett et al. 1998a).

Samples were pressureless sintered for 2 hours at 1800°C. Heating rates used were 30°C/min. to 1000°C, followed by 10°C/min. up to 1800°C. Samples were cooled in the

furnace by switching off the power after sintering. Characterisation was performed using XRD, SEM, and EDXS, as described in Chapter 3. The densified sample of composition 5025 was sintered for 4 hours at 1800°C, as described in the preceding chapter. A foil made from this sample was examined using TEM and EDXS.

Table 5.2. Calculated weight percentages of the starting components for the eight compositions examined in this section of work.

Composition	Si_3N_4 (wt.%)	AlN (wt.%)	Al_2O_3 (wt.%)	$CaCO_3$ (wt.%)	equivalent to CaO (wt.%)
2040	46.94	30.04	13.70	16.61	9.31
2050	39.06	32.09	19.56	16.59	9.29
3040	37.93	38.05	10.49	24.16	13.54
3050	30.30	40.02	16.16	24.12	13.52
4040	29.44	45.58	7.46	31.26	17.51
4050	22.05	47.49	12.97	31.21	17.49
5040	21.50	52.68	4.61	37.95	21.26
5050	14.28	54.52	9.96	37.90	21.23

5.3 Densification and Crystalline Phase Assemblages

5.3.1 Weight Changes

Weight changes of the eight samples are summarised in Table 5.3. Accurate measurements for samples 5040 and 5050 could not be performed. This resulted from the reaction of these samples with the surrounding powder bed during sintering. The large quantities of liquid phase generated in these samples caused significant amounts of packing powder to react with, and bond to, the sample surfaces. Consequently, measured weight changes of these samples would not reflect the true weight changes resulting from sintering.

The weight losses of the five samples that were measured varied considerably. Weight losses in the m = 2.0 and 3.0 samples were all less than 1.3%. However, weight losses in the m = 4.0 samples were significantly higher, at over 3.0%. This resulted from the

substantially higher quantity of liquid phase present in the higher m-value samples. As described in the previous chapter, an increased quantity of grain boundary liquid phase causes increased weight losses during sintering, a result of the high vapour pressure of the liquid phase at elevated temperatures. Reference to the phase behavior diagram of this system, shown in Figure 4.1, shows that high m-value compositions contain more liquid phase than lower m-value compositions. Consequently, a higher m-value is usually associated with a higher weight loss, under equivalent sintering conditions.

Table 5.3. Measured weight losses and apparent densities of the eight samples sintered for 2 hours at 1800°C.

Sample	Weight Loss (%)	Apparent Density (gcm^{-3})
2040	0.68	2.690
2050	1.19	2.570
3040	0.72	2.673
3050	1.22	2.529
4040	3.01	2.838
4050	3.58	*
5040	*	*
5050	*	*

*Values marked with an asterix could not be measured accurately, a result of the liquid-rich samples bloating and reacting with the powder bed during sintering.

Examination of the weight loss data obtained from the five samples that were measured shows that for a given m-value, the samples with an n-value of 4.0 had significantly higher weight losses than the n = 3.0 samples. Again, reference to the phase behavior diagram in Figure 4.1 can explain this observation. For a constant m-value, increasing the n-value directly shifts the composition away from the single-phase α-sialon region, towards the AlN/AlN-polytypoid + liquid regions. Consequently, more liquid phase is present in these compositions at sintering temperatures, and weight losses increase.

5.3.2 Densification

The measured apparent densities of the samples are displayed in Table 5.3. Accurate density measurements could not be carried out on samples 4050, 5040 and 5050. The large volumes of liquid and vapour phases generated in these samples during sintering caused extensive bloating. This created large cavities throughout the bulk of the samples. This, combined with the bonded packing powder described previously, prevented accurate density measurements from being obtained.

The apparent densities of the five samples that were measured ranged from 2.529 to 2.838 gcm^{-3}. These were all relatively low when compared to the samples with m:n ratios of 2:1 described in the previous chapter. Based on the previously used maximum achievable density figure of 3.210 gcm^{-3}, the densified samples are between 79% and 88% of the maximum density. It was seen that for a constant m-value, increasing the n-value (i.e. making the sample richer in AlN-polytypoids and grain boundary phase) lowered the apparent density. Compositional differences could account for lower theoretical densities for the higher m and n-value samples. However, these densities appeared to be too low for this to be the major factor contributing to the poor densities. The poor densification of the samples was mainly attributed to increased porosity that arose during microstructural development. This issue is explored further in Section 5.5.

5.3.3 Crystalline Phase Assemblages

All of the eight compositions studied in this section of work were relatively rich in Al and Ca. Examination of the phase behaviour diagram proposed by Hewett et al. (Figure 4.1) suggested that as these compositions were located further from the single phase α-sialon forming region, the sintered samples would contain increasing proportions of AlN and/or AlN-polytypoid phases, and decreasing quantities of α-sialon. XRD results confirmed that this was indeed the case. Table 5.4 displays the crystalline phases detected in the eight samples.

Phase analyses revealed that all the samples, except one, contained α-sialon, coexisting with AlN and/or AlN-polytypoid phases. The exception was the most Al and Ca-rich composition, 5050. AlN was the only crystalline phase detected in this sample.

Table 5.4. Crystalline phase assemblages of the eight samples sintered for 2 hours at 1800°C.

Sample	α-sialon	AlN	$2H^{\delta}$	27R	21R	12H
2040	vs				s	vw
2050	ms				mw	vs
3040	vs			mw	vw	
3050	m			vs	m	
4040	s	vs	vw			
4050	w	vs	vw			
5040	w	vs				
5050		vs				

XRD spectrum peak intensities were used to compare the relative amounts of the various crystalline phases contained in the samples. Though this technique does not give an exact volume percentage of each of the component crystalline phases, it is a satisfactory technique for comparison between samples. It should be noted that these AlN and polytypoid-rich samples contained large proportions of amorphous grain boundary phase that was not distinguishable on XRD spectra. Thus, the volume percentage expressed is the percentage of total crystalline phases, not of total sample volume. Using this method, the highest proportion of α-sialon contained in any sample was 77 vol.%, in 3040. The next highest amount was 56 vol.%, in 2040. The other samples all contained 42 vol.% or less of α-sialon, with none at all being detected in 5050.

As the amount of α-sialon in the samples decreased, a corresponding increase in the amount of AlN and AlN-polytypoids occurred. XRD analyses demonstrated that the types of AlN-polytypoid phases occurring in the samples varied significantly among the compositions. Within the eight compositions under investigation, five AlN-based phases were identified – AlN, $2H^{\delta}$, 12H, 21R, and 27R. This diversity of phases among the eight compositions resulted from the close proximity of the AlN-polytypoid phases to

one another on the phase behaviour diagram (Figure 4.1). This creates narrow phase compatibility triangles on the α-sialon plane, and consequently, small variations in the m and n-values of compositions may lead to substantial variations in the type and quantity of polytypoid phases observed in a sintered sample. Identification of the polytypoid phases by XRD was difficult in some cases, owing to extensive peak overlapping of α-sialon and AlN/AlN-polytypoid peaks in the spectra. This was especially so with $2H^{\delta}$, which gave very low intensity diffraction peaks, even when present in significant quantities. Figure 5.2 shows an example of an XRD spectrum from the 2040 sample. Three crystalline phases were identified in this spectrum – α-sialon, 21R and 12H.

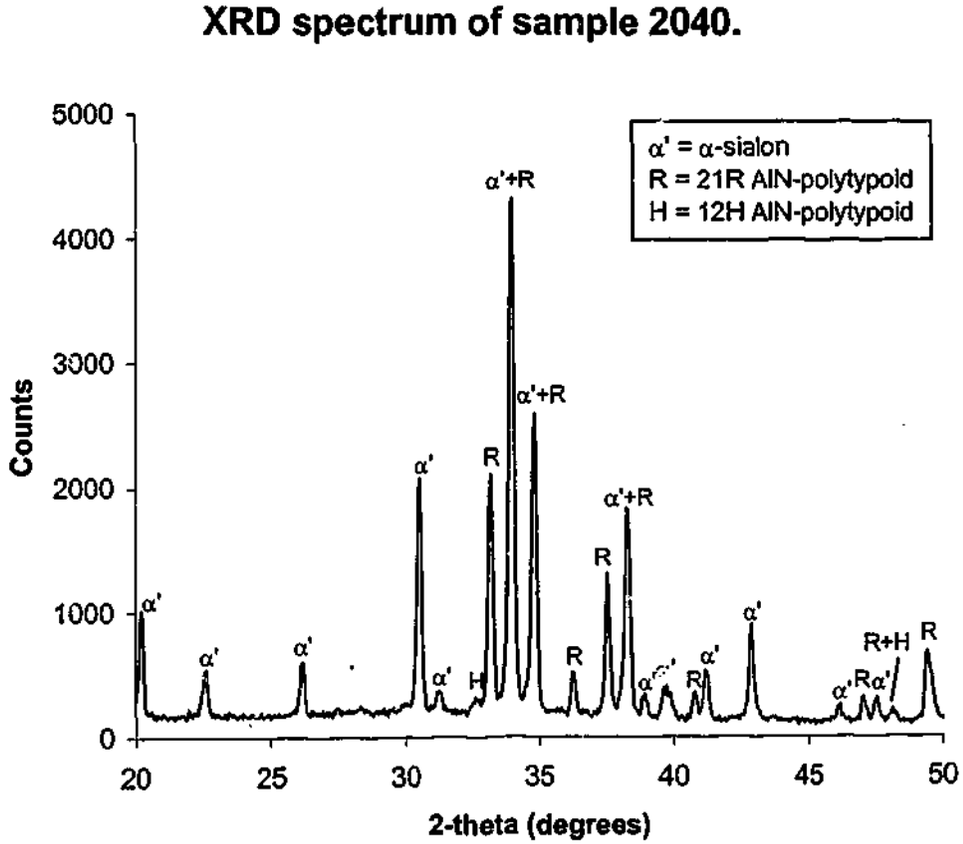

Figure 5.2. XRD spectrum obtained from sample 2040. Three crystalline phases were identified in this spectrum – α-sialon, 21R and 12H.

The manner in which the polytypoid phases varied was consistent with the phase compatibility triangles on the behaviour diagram constructed by Hewett et al. (Figure 4.1). However, the actual phases that evolved from a given composition differed from the ones predicted by the diagram. The diagram in Figure 4.1 was constructed from Ca

α-sialon compositions with m and n-values no greater than 3.0 and 3.5 respectively. Consequently, while the diagram was correct for lower m and n-value compositions, it proved less accurate when employed for higher m and n-values.

The present results, combined with the three compositions examined in Chapter 4, provide supplementary phase information from higher m and n-value compositions. Therefore, they can be used in conjunction with the phase assemblage data of Hewett et al. to produce a more precise phase behaviour diagram, drawing from a broader range of compositions than previously done. This modified phase behaviour diagram of the Ca α-sialon plane is presented in Figure 5.3.

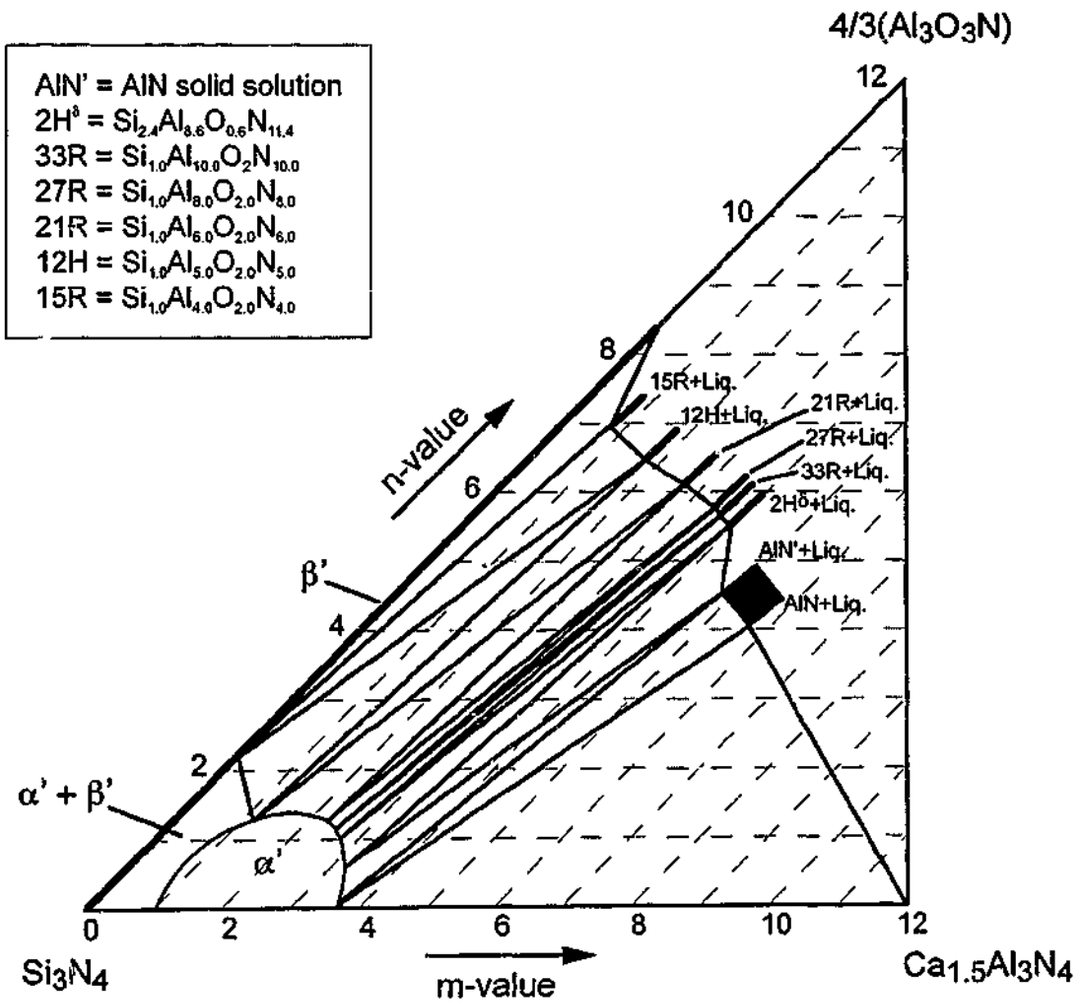

Figure 5.3. Modified phase behaviour diagram of the Ca α-sialon plane at 1800°C, incorporating phase data from work by Hewett and coworkers (Hewett et al. 1998a).

The AlN and AlN-polytypoid phases represented on the diagram do not locate directly on the α-sialon plane, as there is presently no evidence for a significant amount of Ca in these phases. Rather, it is tie-lines between the different AlN and AlN-polytypoid phases and the liquid phase that intersect the α-sialon plane. As a result of this, an increase in the amount of AlN/AlN-polytypoid detected by XRD is also indicative of an increase in the amount of glass phase in the sample.

The AlN solid solution, designated AlN' on the diagram, represents AlN with a small amount of Si in solid solution. This phase was detected in a 5025 composition, and is detailed in Section 4.4.4 in the preceding chapter. The region of solid solubility shown on the diagram is arbitrary, and does not represent the exact solubility limits of Si in AlN.

5.4 Microstructural Characterisation

Microstructural characterisation of polished and etched samples was performed by SEM examination. Polished surfaces were chemically etched with molten NaOH to remove residual grain boundary glass, allowing grain morphologies to be more easily observed. For ease of presentation, samples are discussed by their m-value groupings.

5.4.1 m = 2.0 Samples

Scanning electron micrographs of samples 2040 and 2050 are displayed in Figures 5.4(a and b). The crystalline phases in both samples appeared as elongated grains, surrounded by grain boundary phase. XRD analyses established that in addition to α-sialon, both 2040 and 2050 contained two polytypoid phases – 12H and 21R. However, SEM micrographs appear to show only two distinct crystalline phases in each sample – elongated α-sialon and an elongated polytypoid phase. This resulted from the similar grain morphologies of the various polytypoids. The AlN-polytypoids all possess large plate morphologies (Jack 1976), which often appears to be long needle morphologies in cross-section. This makes exact identification of the different polytypoids difficult simply from SEM observations. Thus, though two polytypoids may have been present in a sample, microstructural observations could not easily distinguish between them.

The more important task of distinguishing between polytypoid phases and α-sialon was relatively easy. When viewed edge-on, the polytypoid phases tended to be longer, and have higher aspect ratios, than elongated α-sialon.

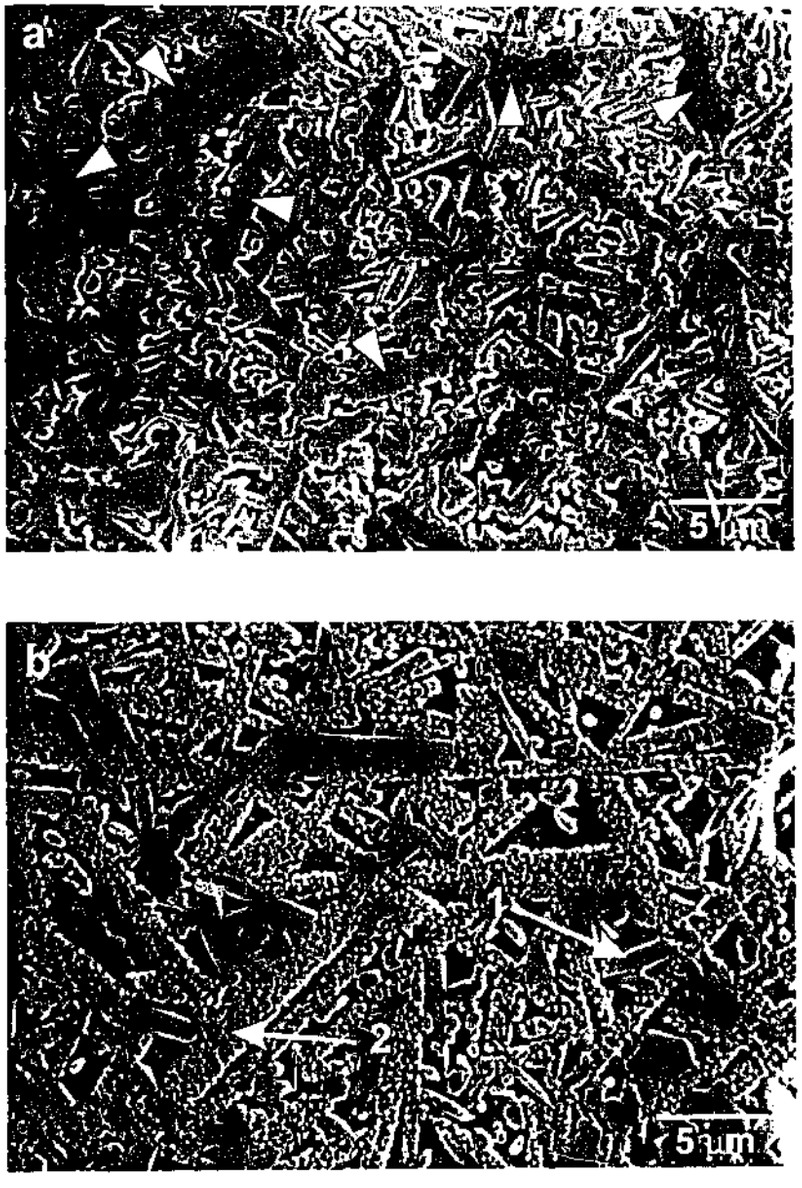

Figure 5.4. Secondary electron micrographs of polished and etched samples of (a) 2040 and (b) 2050, sintered for 2 hours at 1800°C. Polytypoid grains are arrowed in (a). Grains analysed by EDXS are labeled in (b).

The EDXS spectra in Figure 5.5 were obtained from the two grains indicated in Figure 5.4(b). These spectra show the distinct compositional differences between Ca α-sialon

(Grain 1) and the AlN-polytypoid phases (Grain 2) in 2050. Additionally, the chemical etching process utilised in this work often gave the polytypoid phases a distinctive speckled appearance while the α-sialon phase remained smooth. The speckled appearance arises from the NaOH decomposing the surface of the AlN-polytypoid grains, as was described in the previous chapter. This effect was not always apparent in all of the samples, possibly a result of the NaOH etchant being at a lower temperature than was normally utilised.

EDXS spectra obtained from Ca α-sialon and AlN-polytypoid grains in sample 2050.

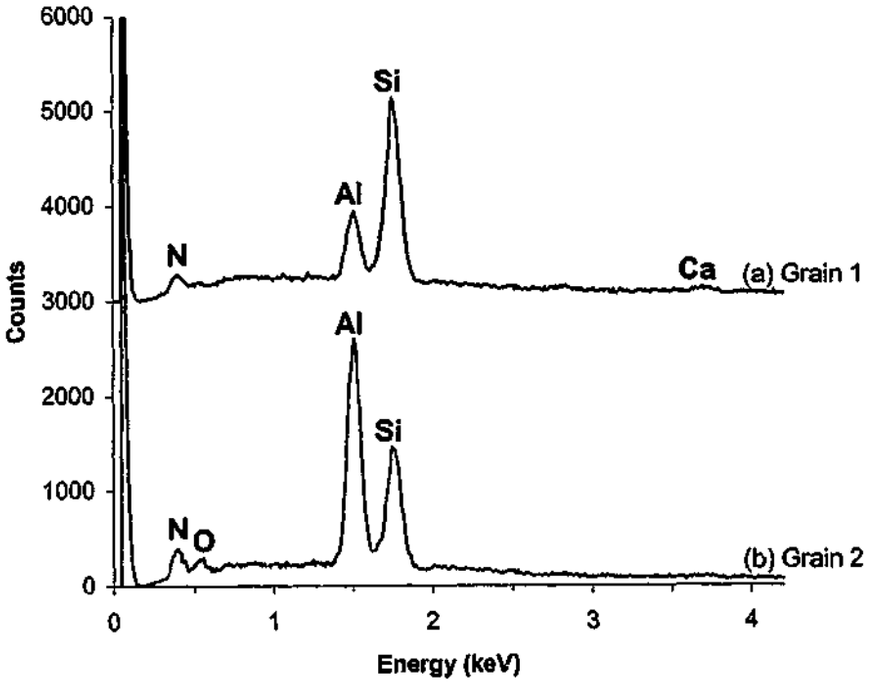

Figure 5.5. EDXS spectra of (a) Ca α-sialon and (b) AlN-polytypoid phase in sample 2050, obtained from the two grains indicated in Figure 5.4(b).

XRD analyses of the two samples indicated that 2040 had a significantly higher α-sialon to polytypoid ratio than 2050. SEM observations confirmed this. The comparatively high α-sialon content of 2040 was clearly apparent. Elongated α-sialon grains dominated the microstructure, with grains averaging ~5 μm in length and ~0.8 μm in width. Some grains of polytypoid phases were identified, though not many were visible in the microstructure. Some AlN-polytypoid grains in 2040 are indicated in Figure 5.4(a). The

plate morphology of the polytypoid grains was distinguishable in some grains, though others displayed a more needle-like morphology in cross-section.

The plate morphology of the AlN-polytypoid phases was much more apparent in pores in the samples. Figure 5.6 shows a large region of porosity in sample 3040. The plate morphology of the AlN-polytypoid grains is clearly visible in this micrograph. The needle-like appearance of most of the polytypoid grains was a result of the thin cross-sections of the plates at most grain orientations. Only occasional grains that had an orientation approximately parallel to the polished sample surface clearly revealed the plate morphology. The polytypoid grains in sample 2040 averaged ~7-8 μm in length.

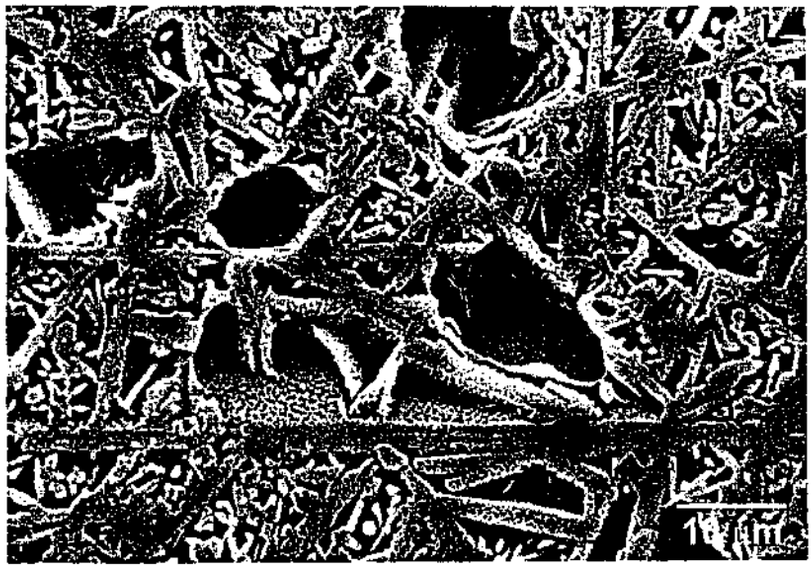

Figure 5.6. Secondary electron micrograph of a pore in sample 3040, showing the plate morphology of the AlN-polytypoid phase.

Contrasting 2040, the 12H and 21R polytypoids were the majority crystalline phase in 2050 (Figure 5.4(b)). The polytypoid plates were large, averaging ~15 μm in length and often exceeding 20 μm. Elongated α-sialon was present as a minor phase. The α-sialon grains were substantially smaller than the polytypoid grains, averaging ~3 μm in length. This was also shorter than the α-sialon grains in 2040. The smaller α-sialon grain size was attributed to the abundance of polytypoid in the microstructure. The large quantity of polytypoid plates formed a network, limiting the amount of space for elongated α-sialon to grow in. This caused α-sialon grain growth to be hindered as the

anisotropically growing grains impinged on the large polytypoid plates. Evidence of elongated α-sialon grains impinging upon polytypoid grains can be seen in a number of locations in the SEM micrograph of 2050 (Figure 5.4(b)). These observations indicate that the AlN-polytypoid grains grow at a significantly faster rate than α-sialon. This allows the polytypoid network to develop prior to any significant α-sialon grain growth, and consequently, α-sialon growth is restricted.

Another prominent difference between the two samples was the amount of grain boundary phase present in the microstructures. XRD analyses were unable to detect this amorphous phase. However, based on the higher polytypoid content detected in 2050, this sample would be expected to contain a higher proportion of grain boundary phase. Examination of the SEM micrographs shows that this was indeed the case. Though the surface grain boundary phase was removed by etching, the visible underlying grain boundary phase and the porosity left by the glass removal clearly revealed that sample 2050 possessed a substantially higher proportion of grain boundary phase than 2040.

5.4.2 m = 3.0 Samples

The microstructure of 3040, shown in Figure 5.7(a), was comparable to that of 2040, except for an increased proportion of AlN-polytypoid phase. This was consistent with the similar locations of the two compositions on the α-sialon plane. Like 2040, α-sialon was a significant phase in this sample. It co-existed with two polytypoid phases – 21R and 27R.

The α-sialon grains in this sample were slightly smaller than for 2040, though they exhibited the same high aspect ratio, elongated morphology. α-Sialon grains averaged ~2-3 μm in length and ~0.5-0.8 μm in width. The polytypoid grains were significantly larger than the α-sialon, with typical cross-sectional lengths in the range 10-15 μm. As described earlier, no distinction could be made between the two polytypoid phases, owing to their similar morphologies and chemistry. Sample 3040 exhibited similar proportions of grain boundary phase to 2040.

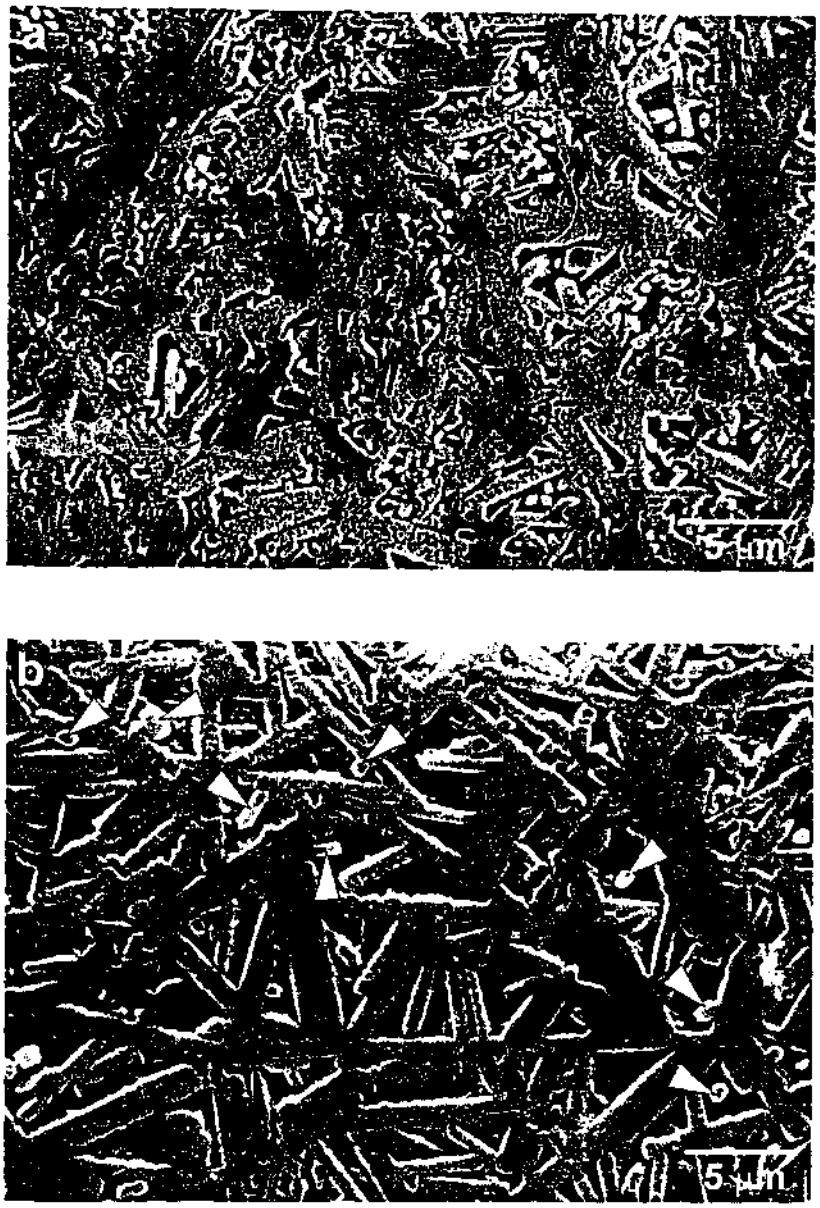

Figure 5.7. Secondary electron micrographs of polished and etched samples of (a) 3040 and (b) 3050, sintered for 2 hours at 1800°C. α-Sialon grains are indicated by the arrows in (b).

Sample 3050, shown in Figure 5.7(b), appeared markedly different to 3040. α-Sialon content, estimated from XRD peak intensities, was only 19 vol.% of the crystalline phases in this sample. This was reflected in the microstructure of the sample, which was dominated by plate-shaped 21R and 27R polytypoid grains. The polytypoid grains exhibited cross-sectional lengths in the range 10-20 μm. The large dimensions of these phases caused the plate-shaped grains to form a network as they impinged upon one another. The large cavities located within the network of polytypoid plates were filled by

Sample 4050, shown in Figure 5.8(b), had a significantly higher glass content than 4040. Crystalline phases were composed mostly of AlN and $2H^{\delta}$. The high glass content allowed the AlN and $2H^{\delta}$ to grow to substantial dimensions, the most prominent feature being $2H^{\delta}$ plates exceeding 40 μm in length. Weak α-sialon peaks appeared on the 4050 XRD spectrum, and SEM confirmed its presence. However, the elongated α-sialon grains appeared only intermittently throughout the microstructure.

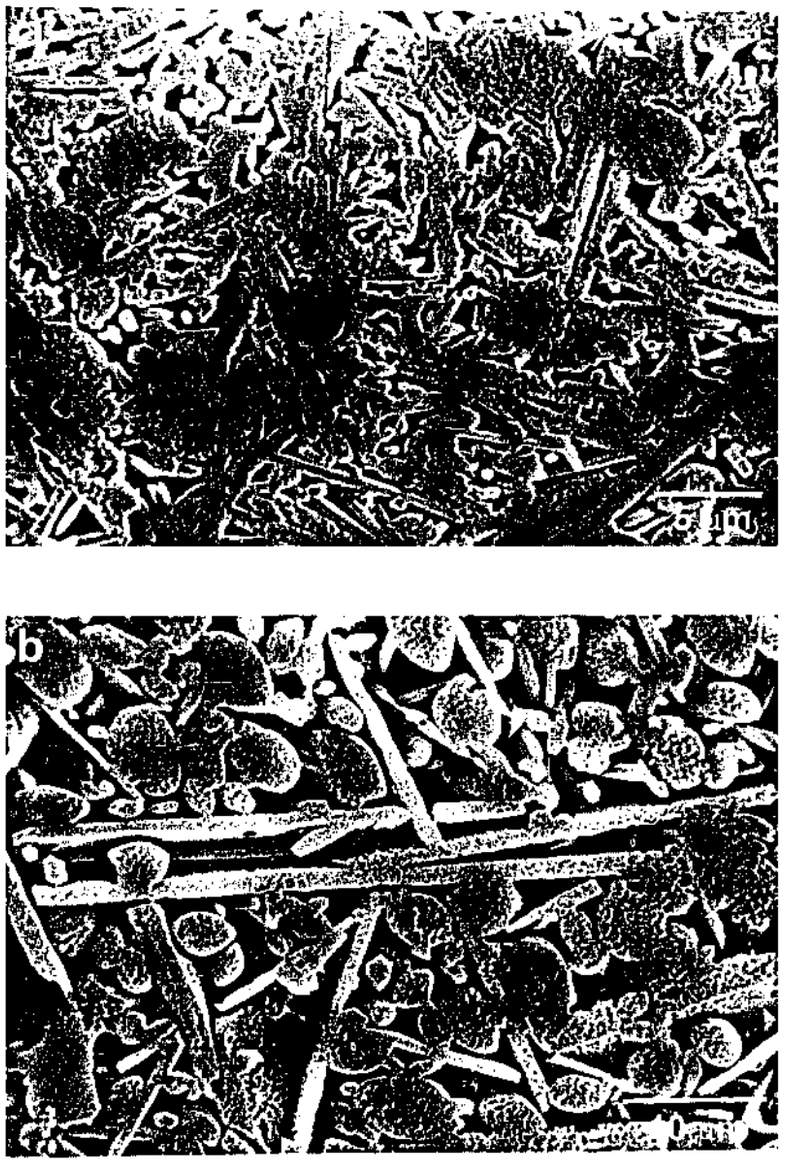

Figure 5.8. Secondary electron micrographs of polished and etched samples of (a) 4040 and (b) 4050, sintered for 2 hours at 1800°C.

5.4.4 m = 5.0 Samples

Sample 5040, shown in Figure 5.9(a), was a liquid rich composition that evolved two morphologically distinct crystalline phases, AlN and α-sialon. Within the abundant glass matrix, AlN grains with a distinctive rounded morphology were the majority phase. They exhibited diameters typically in the range 3 - 5 μm. The second crystalline phase observed in the microstructure was elongated α-sialon.

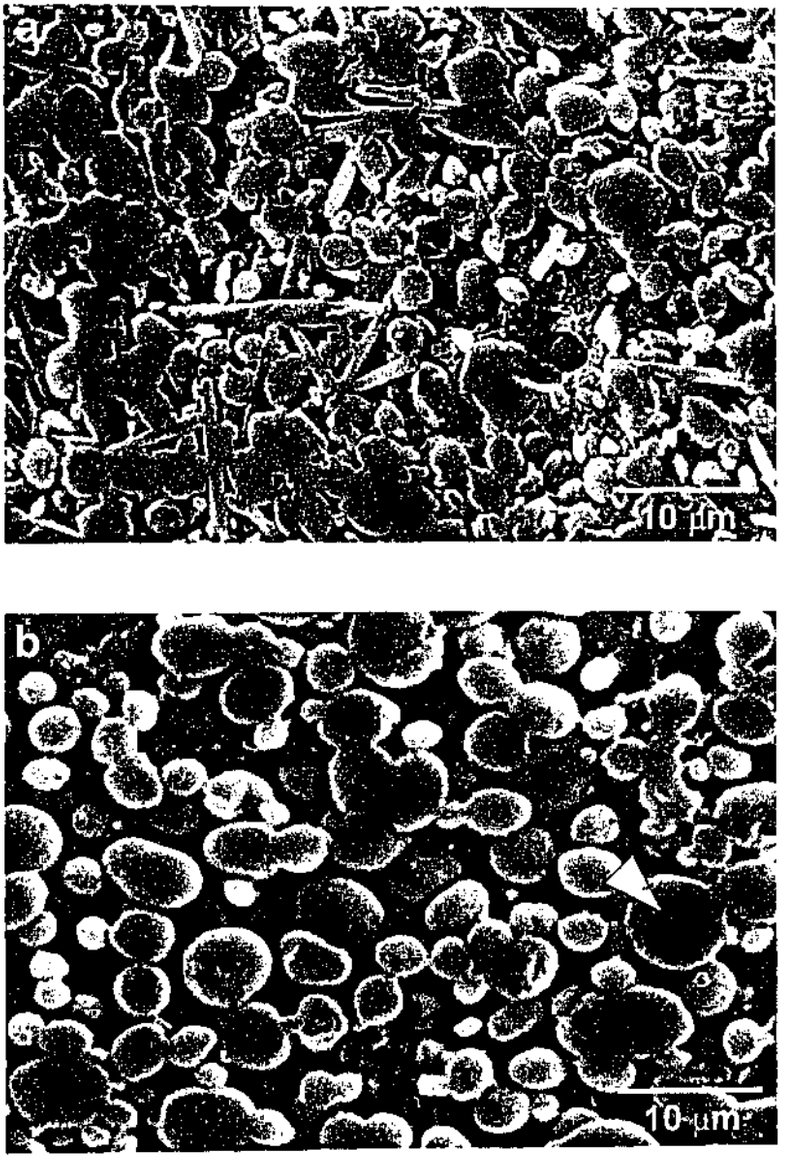

Figure 5.9. Secondary electron micrographs of polished and etched samples of (a) 5040 and (b) 5050, sintered for 2 hours at 1800°C. An EDXS spectrum (Figure 5.10) was obtained from the grain arrowed in (b).

The large liquid volume at the sintering temperature, combined with a lack of bulky polytypoid plates, allowed α-sialon grains to grow with minimal hindrance. Consequently, the small number of α-sialon grains present in the sample were relatively long in comparison to the samples dominated by polytypoid plates. The average α-sialon grain length was about 8 – 10 μm, though grains approaching 15 μm were occasionally observed.

Composition 5050, shown in Figure 5.9(b), appeared to have been positioned outside any α-sialon-containing compatibility triangle, as AlN was the only crystalline phase observed. SEM micrographs showed the sample to contain very large volumes of glass phase, so much so that adjacent AlN grains were barely in contact with each other. The AlN morphology was the same as described for sample 5040, though the larger proportion of liquid phase allowed the grains to grow up to 8 μm in diameter. Chemical analysis by EDXS of a grain indicated in the SEM micrograph of 5050 (Figure 5.10) and lattice parameter measurements (Table 5.5) confirmed that the round-shaped phase observed in the higher m-value samples was AlN, and not an AlN-polytypoid.

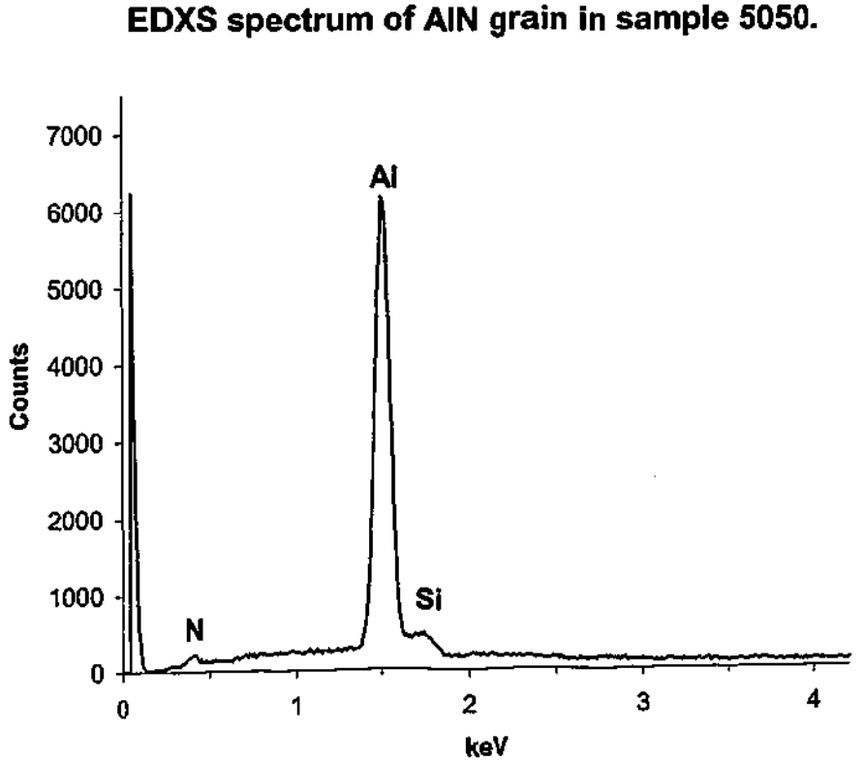

Figure 5.10. EDXS spectrum of an AlN grain in sample 5050.

Table 5.5. Lattice parameters of AlN phase in sample 5050, and pure AlN reference.

Phase	*a*-parameter (Å)	*c*-parameter (Å)
AlN in 5050	3.112±0.001	4.984±0.003
Pure AlN*	3.111	4.979

*JCPDS Powder Diffraction File #25-1133

The small Si peak adjacent to the Al peak most likely arose from the interaction volume of the electron beam interacting with grain boundary glass phase.

5.4.5 Discussion

The most significant result obtained from this work was the observation of α-sialon with an elongated morphology in all seven α-sialon-containing samples. No equiaxed α-sialon was observed in any of the sample microstructures. This shows that the elongated morphology is the preferred α-sialon grain morphology over a wide range of α-sialon forming compositions. Work presented in Chapter 4 indicated that in Ca α-sialon compositions with a design m-value equal to or higher than 3.0, α-sialon had an intrinsically elongated grain morphology. These results add further evidence to the suggestion that anisotropic α-sialon grain growth is an intrinsic feature of the Ca-Si-Al-O-N system.

The previous chapter described the effect of increased amounts of liquid phase enhancing the growth of elongated α-sialon grains. The samples studied in the present chapter could all be considered liquid-rich. However, enhanced growth of the α-sialon grains was not apparent in many of the samples. This was mainly a result of the plate morphology of the polytypoid grains. The polytypoid phases appeared to grow at a significantly higher rate than α-sialon. This created a network of plates that provided little room for α-sialon growth. The impingement of the α-sialon grains on the polytypoid plates hindered their growth and consequently, though the compositions were rich in liquid phase, the growth of α-sialon grains was not unusually enhanced.

Only when samples were comprised of equiaxed AlN rather than polytypoid plates, such as in sample 5040, was the growth of α-sialon enhanced. α-Sialon grains averaged 8 – 10 μm, and grains up to 15 μm were frequently observed. Thus, it is clear that increased amounts of liquid phase at sintering temperatures can enhance elongated α-sialon growth, provided that other phases do not interfere with that growth.

5.5 Fracture Behaviour

Work in the preceding chapter demonstrated how samples dominated by elongated α-sialon grains displayed R-curve behaviour. The fracture surfaces of these materials showed evidence of microstructural toughening mechanisms such as grain debonding and grain pullout. The eight samples examined in this work contain significant quantities of AlN/AlN-polytypoid phases and glass phases. The mechanical properties of materials exhibiting these types of phase assemblages are uncertain, and their use as potential engineering materials may be limited. Consequently, these samples are useful for examining the fracture behaviour of α-sialon-containing samples rich in grain boundary glass and AlN/AlN-polytypoid phases. Fracture surfaces were obtained from the eight densified samples. These were examined by SEM to determine how large volumes of glass phase and AlN/AlN-polytypoid phases altered the fracture surface characteristics.

As described in the microstructural characterisation section (Section 5.4), samples 2040 and 3040 exhibited the least grain boundary glass. Elongated α-sialon was also the majority crystalline phase in these two samples. Consistent with their polished and etched microstructures, the fracture surfaces of these two samples also bore some similarities (Figures 5.11(a) and 5.12(a)). The prominence of elongated α-sialon grains in these samples was reflected in their fracture surfaces. Features such as needle shaped imprints and elongated grains protruding out of the surface were comparable to fracture surface micrographs obtained from samples examined in the previous chapter. However, these features were less extensive than those observed in the previously examined samples that exhibited rising R-curve behaviour. This was most likely a result of the shorter average length of the α-sialon grains in 2040 and 3040.

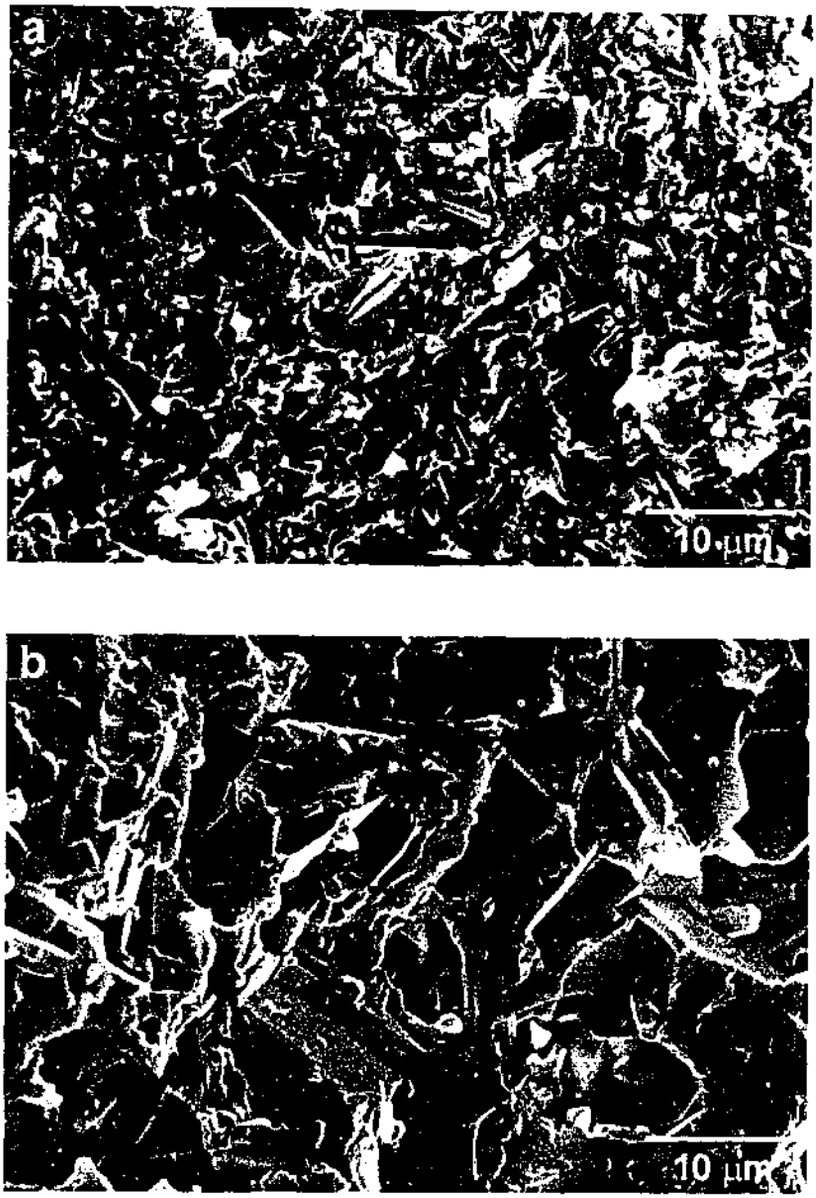

Figure 5.11. Secondary electron micrographs of fracture surfaces from samples (a) 2040 and (b) 2050.

Debonding of polytypoid plates from the glass matrix was evident on the fracture surfaces, but the effect of the plates in the microstructures was less clear. Small areas of smooth surface appeared to indicate regions where polytypoid plates had debonded from the intergranular glass. This debonding occurred when the growth directions of the polytypoid plates were oriented approximately parallel to the fracture surface. Few observations of polytypoid plates protruding directly out from the fracture surface were made. This indicated that the interfacial bonding of the polytypoid grains with the grain boundary phase was generally too strong for the plates to be debonded and pulled out of

the glass matrix. The large surface area of the plate-shaped polytypoid grains would certainly increase the energy required to debond and pullout a grain, relative to a needle or rod-shaped grain. As a result of this, the polytypoid grains appear to undergo transgranular fracture in samples 2040 and 3040 when they are not oriented near to parallel with the fracture surface.

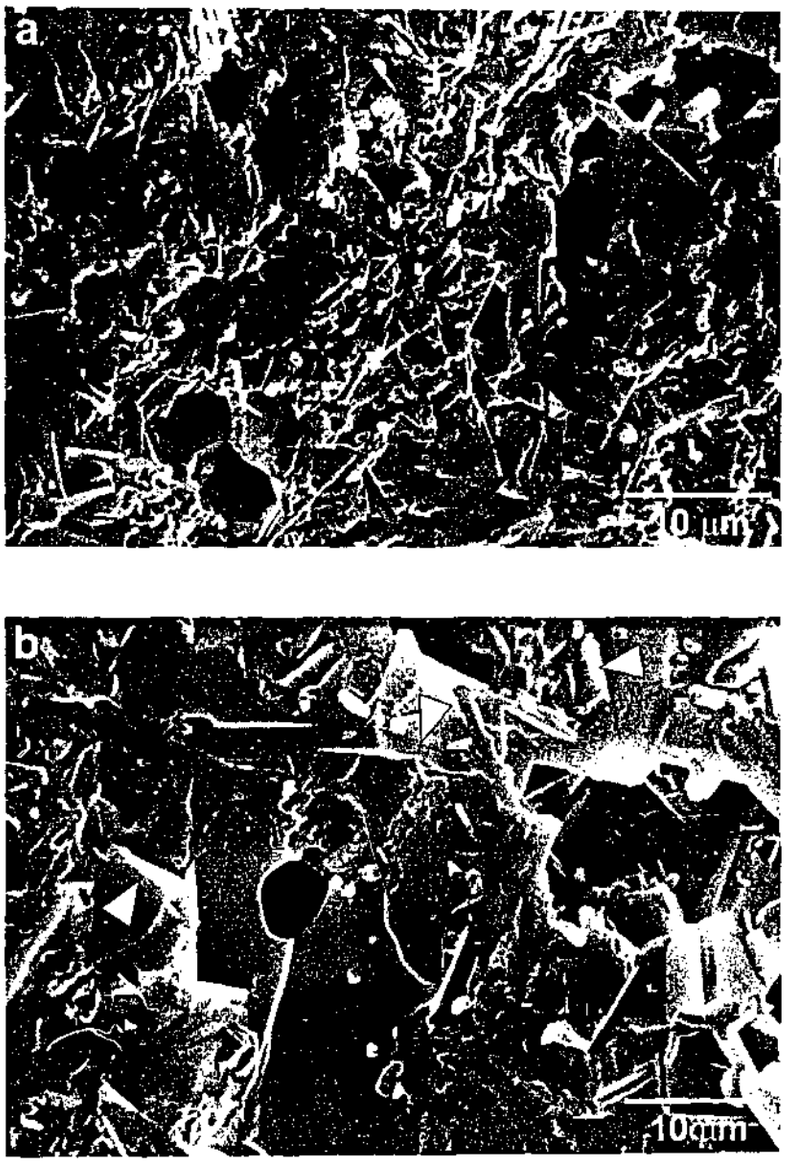

Figure 5.12. Secondary electron micrographs of fracture surfaces from samples (a) 3040 and (b) 3050. Some points of transgranular fracture of polytypoid plates are indicated in (b).

Contrasting these two samples, 2050 and 3050 contained polytypoid phases as their majority crystalline phases, with lesser quantities of elongated α-sialon. A consequence of this was that the samples also possessed large volumes of intergranular glass in their microstructures. Fracture surfaces of these two samples, shown in Figures 5.11(b) and 5.12(b), were markedly different from the two previously discussed samples. The fracture surfaces of the previous two samples exhibited lots of fine, rough detail, resulting from the debonding and pullout of the fine α-sialon needles. 2050 and 3050 exhibited almost none of this topographical relief. Rather, their fracture surfaces were dominated by extensive smooth regions and sharp, angular edges. These fracture surface features were attributable to the large proportion of grain boundary glass and the morphology of the AlN-polytypoid plates.

The polytypoid grains appeared to most frequently debond from the grain boundary glass matrix when their growth direction was oriented approximately parallel to the fracture surface. The debonding of the flat faces of the polytypoid grains from the abundant glass matrix was the origin of the smooth, flat areas on the fracture surface. The sharp, faceted edges of these grains were also responsible for many of the more abrupt, angular features on the fracture surface.

Instances of polytypoid plates projecting out of the fracture surface were observed very infrequently. This indicated that transgranular fracture was more likely to occur when polytypoid plates were oriented closer to perpendicular to the fracture surface. The interfacial bonding strength of the grain-glass interface is important in determining how the grains interact with a propagating crack. In-situ toughening relies on an interfacial bond that is weak enough to debond and deflect a propagating crack, resulting in intergranular fracture. If the bond is too strong, a crack fractures the grain rather than being deflected around it (i.e. transgranular fracture) and the grain does not contribute to improving fracture toughness.

The effect of a strong interfacial bond between the polytypoid plates and the glass matrix was apparent in samples 2050 and 3050. Only plates with an orientation roughly parallel to the fracture surface readily debonded from the glass. When a propagating crack encountered a plate oriented perpendicular to the crack front, transgranular fracture

typically occurred. Some points of transgranular fracture are indicated in the micrograph of sample 3050 (Figure 5.12(b)). This fracture mechanism occurred because fracturing the grain required less energy than propagating the crack around the grain, debonding it from the glass. This would be partially attributable to the large surface area of the plate-shaped AlN-polytypoid grains, which gives the grains a strong bond with the grain boundary glass. Some evidence of pullout and debonding of elongated α-sialon grains was present in these two samples, though observations of these were scarce, due to the low α-sialon content of these samples.

Many large pores were evident in these samples and others examined in this chapter. Some of these are visible in the micrographs of samples 3040 and 3050 (Figure 5.12). The networks of large polytypoid plates present in the microstructures of many of these samples do not allow a good packing arrangement of the crystalline phases. Consequently, liquid phase densification is hindered. The awkward packing arrangement leaves large regions around the polytypoid grains that often are not fully occupied by α-sialon and grain boundary glass. The porosity in these regions is effectively trapped, and cannot be removed during sintering. The relatively poor measured densities of the samples examined in this chapter can, in part, be attributed to this trapped porosity.

The fracture surface of 4040, shown in Figure 5.13(a), appeared significantly different to the previously examined samples. The minimal α-sialon content and high intergranular glass content produced a fracture surface that exhibited minimal topographic detail. Evidence of any significant grain debonding or pullout was scarce. Some debonded α-sialon was observed but overall, fracture of the grain boundary glass and transgranular fracture of the polytypoid plates produced a relatively smooth fracture surface. Sample 4050, shown in Figure 5.13(b), was also dominated by grain boundary glass phase. Fracture of the glass and debonding of polytypoid plates produced characteristic areas of smooth surface. The presence of significant amounts of rounded AlN grains was evident from the many debonded AlN grains that were observed.

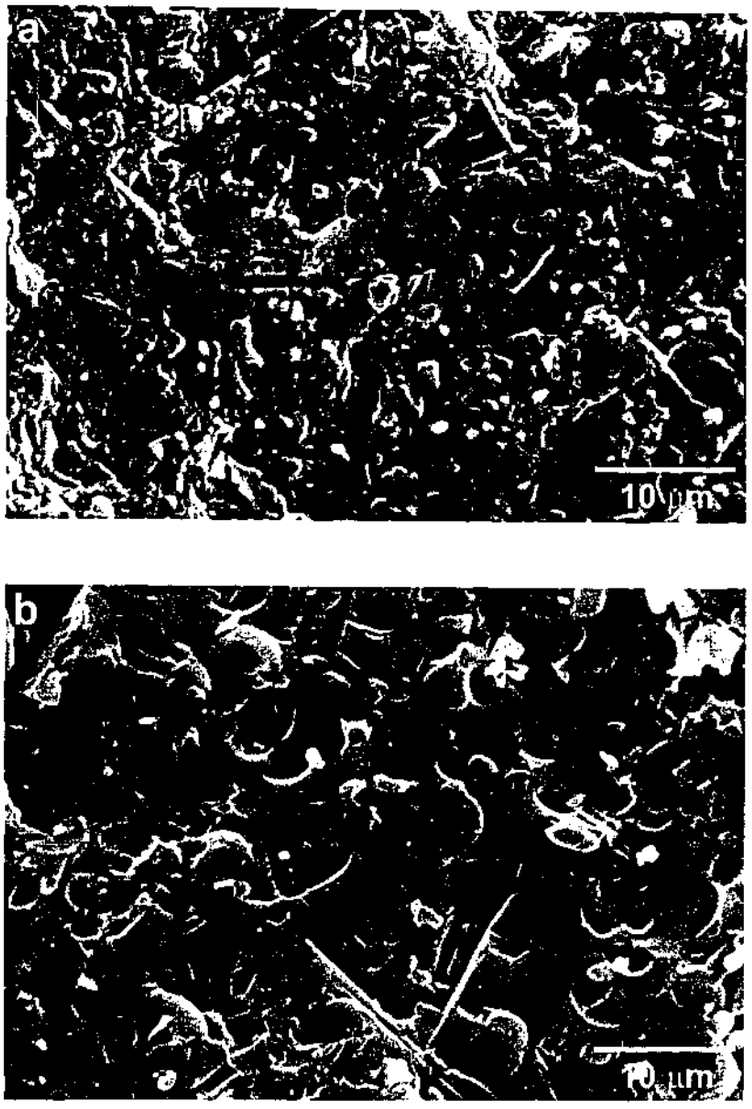

Figure 5.13. Secondary electron micrographs of fracture surfaces from samples (a) 4040 and (b) 4050.

The lack of surface features that were indicative of toughening mechanisms in these samples was a result of a number of factors. First, α-sialon was only a minor phase in these samples, and the α-sialon grains that were present were relatively short – in the order of 2 – 3µm. This made it difficult for the α-sialon grains to have a prominent impact on the features of the fracture surface. Second, the polytypoid plates embedded in glass phase are more inclined to undergo transgranular fracture, so they don't often display evidence of grain pullout. When they do debond, they are generally oriented parallel to the fracture surface, and consequently, they produce a region of smooth

topography. Third, the samples contain large volumes of grain boundary glass phase, which appears smooth when fractured. These factors combine to produce fracture surfaces more reminiscent of brittle fracture in an untoughened material.

The fracture surfaces of 5040 and 5050 appeared very similar to each other (Figures 5.14(a and b)). Both microstructures were dominated by smooth, rounded, AlN grains and an abundance of grain boundary glass phase. This created fracture surfaces with the characteristic dimples that arose from the debonding of the rounded AlN grains.

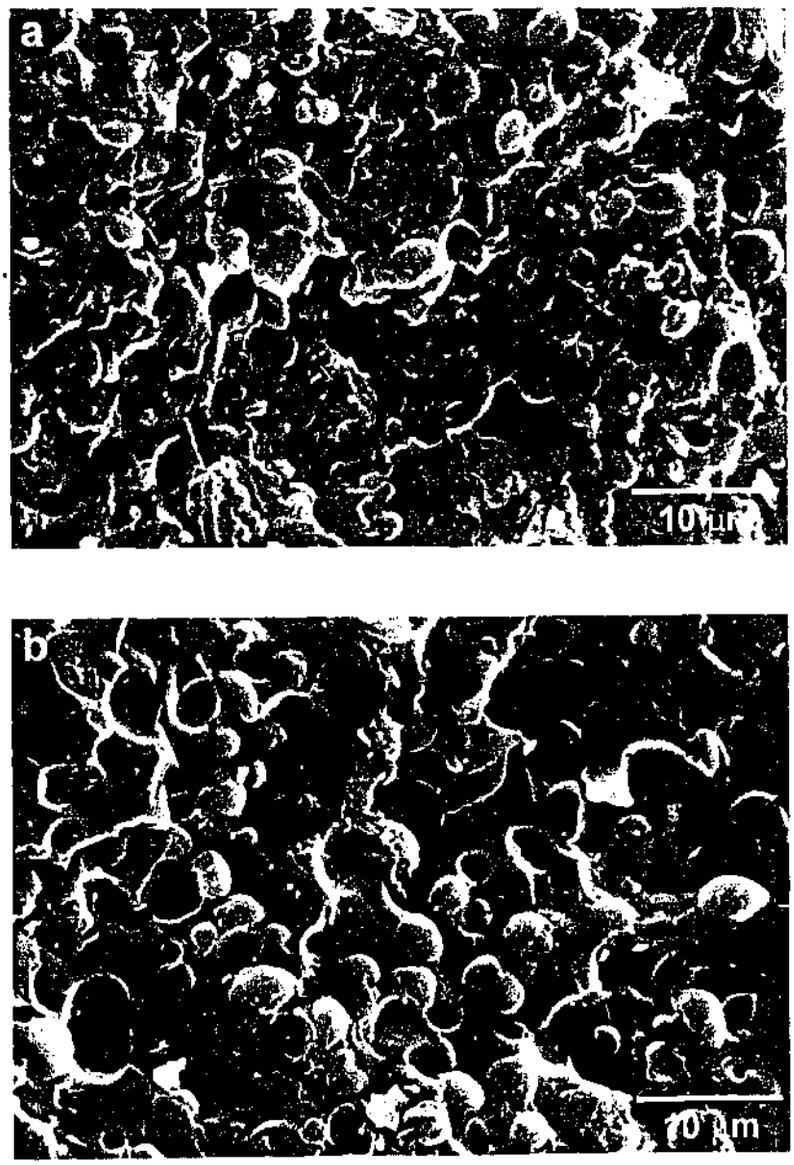

Figure 5.14. Secondary electron micrographs of fracture surfaces from samples (a) 5040 and (b) 5050.

5040 contained a small amount of elongated α-sialon. A few debonded α-sialon grains were observed. However, they constituted only a minor part of the overall fracture surface. No α-sialon was present in 5050.

Comparing the microstructures and fracture surfaces of these eight samples to samples located closer to the single phase α-sialon region of the phase behaviour diagram, it was evident that high m and n-value compositions held little potential for the design of in-situ toughened Ca-Si-Al-O-N ceramics. The high proportions of intergranular glass phase in the sample microstructures would cause a significant deterioration in properties such as hardness, and high temperature strength and creep resistance. High glass volumes also have the effect of creating a low-toughness glass matrix that a crack can easily propagate through. The replacement of elongated α-sialon needles with large plates of AlN-polytypoid phase has a deleterious effect, as these phases tended to undergo transgranular fracture, rather than intergranular fracture. This fracture mechanism does not enhance fracture toughness like the debonding and pullout of elongated α-sialon grains does. Compositions abundant in rounded AlN grains did exhibit intergranular fracture. However, this grain morphology does not appreciably alter the crack path or require significant energy to debond the grain-glass interface, and thus fracture toughness is not enhanced.

Based on this and earlier work, it is reasonable to conclude that considerable improvements in the fracture toughness of ceramics in the Ca-Si-Al-O-N system require microstructures consisting predominantly of anisotropically grown α-sialon grains, combined with a relatively small volume of AlN/AlN-polytypoid phases and grain boundary glass.

5.6 AlN Nano-Precipitates in a High m-value Composition

An unusual feature was noticed during the microstructural observation of a high m-value Ca-Si-Al-O-N sample. During the TEM examination of a densified 5025 composition, small, faceted precipitates, ranging in size from 10 nm to 100 nm, were observed within many of the AlN grains. These nano-precipitates had not been observed in the AlN-polytypoid grains of any other sample examined in the TEM in Chapter 4.

The reaction sequence and microstructural development of this composition were examined in detail in the previous chapter. This section of work describes these nano-precipitates, and attempts to explain their origin.

5.6.1 Origin of the Nano-Precipitates

The previous chapter described how two distinct AlN grain morphologies were apparent in sample 5025_{1800}. Some AlN grains had a smooth, rounded morphology, and exhibited sizes in the range 1 – 4 μm (Figure 4.26). Other AlN grains were larger, and had an irregular, equiaxed morphology. These grains were up to 10 μm in size (Figure 4.27). These grains also exhibited a sub-grain structure, which is described in Chapter 4.

The nano-precipitates described here were observed in both types of AlN. However, the way the nano-precipitates were distributed in the grains differed between the two types. In the smaller, rounded AlN, the nano-precipitates were generally distributed randomly throughout the grain, such as the grain shown in Figure 5.15. Contrasting this, nano-precipitates in the larger, irregular-shaped AlN that possessed the sub-grain structure were confined to a single sub-grain (Figure 5.16). The nano-precipitates were never observed in more than one sub-grain.

This distribution of nano-precipitates in the two types of AlN was interesting, as some correlation with observations described in the previous chapter was apparent. Analyses of the two types of AlN in Chapter 4 concluded that the smaller AlN grains were partially dissolved particles of AlN starting powder. The larger AlN grains were believed to be a new AlN phase, precipitated on a core particle of AlN starting powder during sintering. This gave rise to the sub-grain structure. These nano-precipitates were observed in both the smaller, rounded particles of residual AlN starting powder, and in a single sub-grain of the larger AlN grains. This suggested the possibility that the nano-precipitates were only occurring in particles of original AlN starting powder.

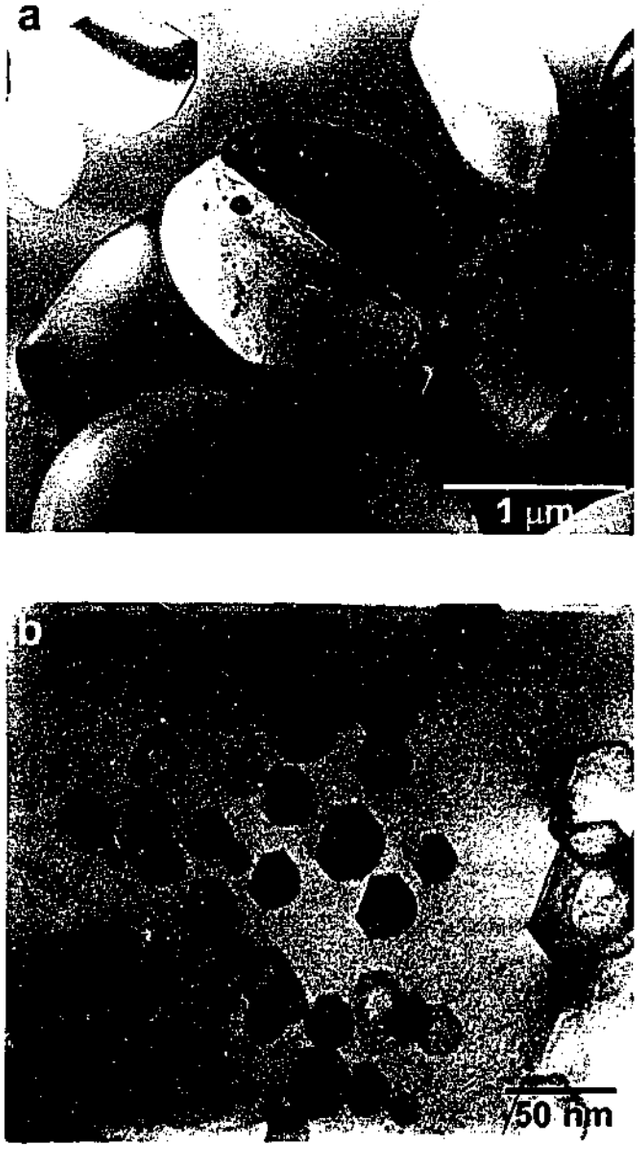

Figure 5.15. Transmission electron micrographs of nano-precipitates in the smaller, rounded type of AlN grains.

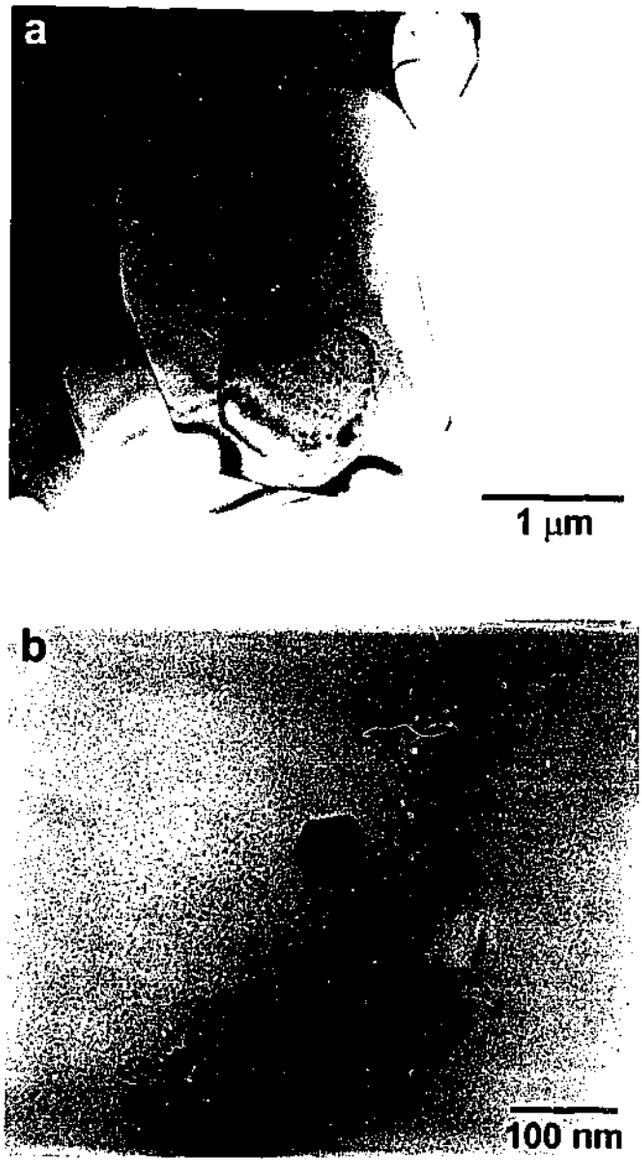

Figure 5.16. Transmission electron micrographs of nano-precipitates in the larger, irregular-shaped type of AlN grains. Micrograph (a) shows the nano-precipitates confined to one sub-grain of the whole AlN grain. Micrograph (b) highlights the hexagonal faceting of the nano-precipitates. A clear orientation relationship between the matrix and the nano-precipitates is apparent in micrograph (b).

To further investigate this, EDXS analyses were conducted on the different types of AlN grains. Analysis of the larger, irregular-shaped grain with the sub-grain structure, shown in Figure 5.16(a) found that the nano-precipitates only occurred in the sub-grain that had an almost pure Al-N chemistry. The EDXS spectrum of the sub-grain with the nano-precipitates is shown in Figure 5.17(a). This result was repeated over a number of

similar grains. The smaller, rounded AlN grain containing the nano-precipitates, shown in Figure 5.15 (a), was also found to have an almost pure Al-N chemistry (Figure 5.17(b)). Again, this result was repeated over many similar grains.

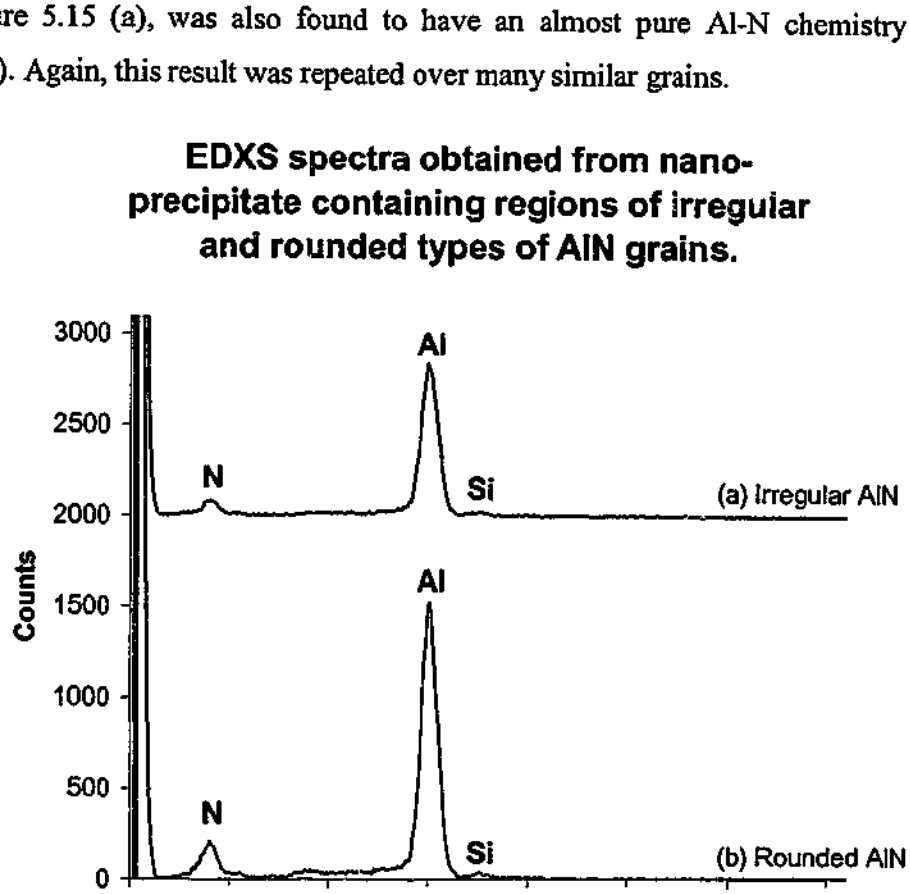

Figure 5.17. EDXS spectra obtained from nano-precipitate containing regions of (a) irregular and (b) rounded AlN grains.

The nano-precipitates were never observed in the AlN sub-grains that contained a significant Si impurity, which, as discussed in Chapter 4, is believed to an indication of new AlN precipitated during sintering. These observations suggest that the nano-precipitates are only occurring in what is believed to be particles of original AlN starting powder.

If this hypothesis is correct, then the nano-precipitates most likely have their origin in the AlN starting powder, and are not related to the Ca-Si-Al-O-N composition of the sample. This was investigated by examining cleaved crystals obtained from a sample of the original as-received AlN powder in the TEM. Observation of many thin crystals found no evidence of these nano-precipitates in any of the grains. This did not offer any

similar grains. The smaller, rounded AlN grain containing the nano-precipitates, shown in Figure 5.15 (a), was also found to have an almost pure Al-N chemistry (Figure 5.17(b)). Again, this result was repeated over many similar grains.

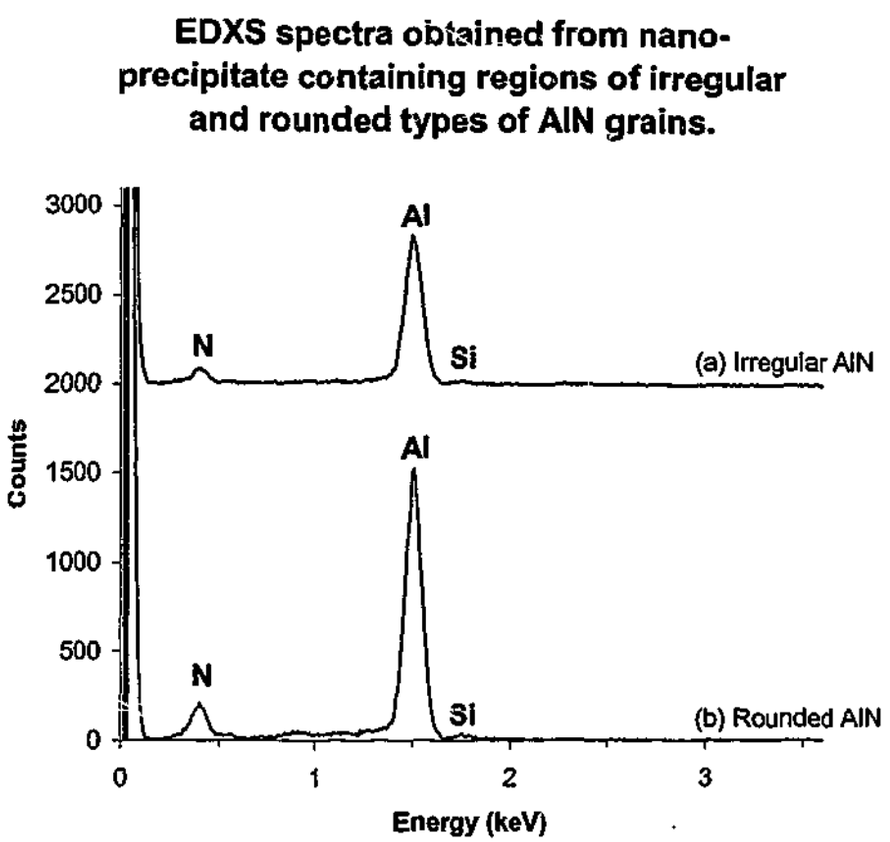

Figure 5.17. EDXS spectra obtained from nano-precipitate containing regions of (a) irregular and (b) rounded AlN grains.

The nano-precipitates were never observed in the AlN sub-grains that contained a significant Si impurity, which, as discussed in Chapter 4, is believed to an indication of new AlN precipitated during sintering. These observations suggest that the nano-precipitates are only occurring in what is believed to be particles of original AlN starting powder.

If this hypothesis is correct, then the nano-precipitates most likely have their origin in the AlN starting powder, and are not related to the Ca-Si-Al-O-N composition of the sample. This was investigated by examining cleaved crystals obtained from a sample of the original as-received AlN powder in the TEM. Observation of many thin crystals found no evidence of these nano-precipitates in any of the grains. This did not offer any

support to the hypothesis that the nano-precipitates originated in the AlN starting powder. A TEM micrograph of this sample is shown in Figure 5.18.

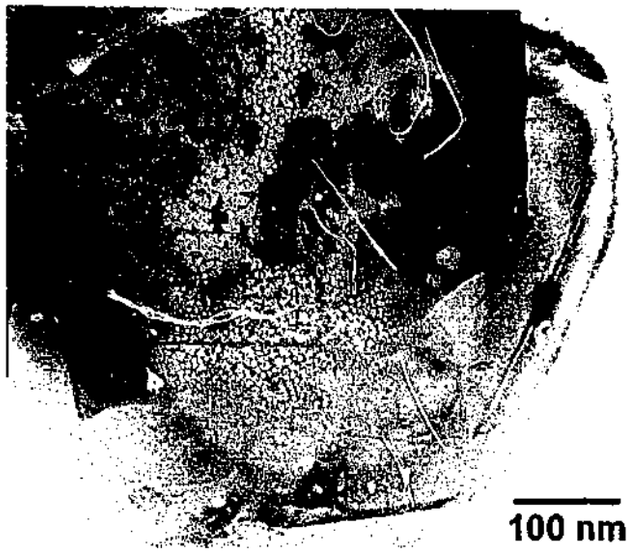

Figure 5.18. TEM micrograph of cleaved crystals of AlN powder, in the as-received condition. No nano-precipitates are visible in this sample.

As a further step, a sample of the original AlN powder was heat treated for 4 hours at 1800°C, the same firing schedule that the 5025_{1800} sample with the nano-precipitates in the AlN grains experienced. Cleaved crystals were obtained from the heat-treated powder and examined in the TEM. This time, small precipitates were observed throughout the AlN crystals, as the micrograph in Figure 5.19 shows. These precipitates ranged in size from approximately 10 – 40 nm, a size comparable to the nano-precipitates previously observed in the sample of 5025_{1800} (Figure 5.15(b)). This was clear evidence that the nano-precipitates arise in the original AlN starting powder as a result of a high temperature heat treatment. The morphology of the nano-precipitates is unclear in Figure 5.19(b). This is a result of the sample being a thicker cleaved crystal, rather than a sample ion milled to electron transparency. Despite this, what appears to be faceting is visible on a few of the nano-precipitates in Figure 5.19(b).

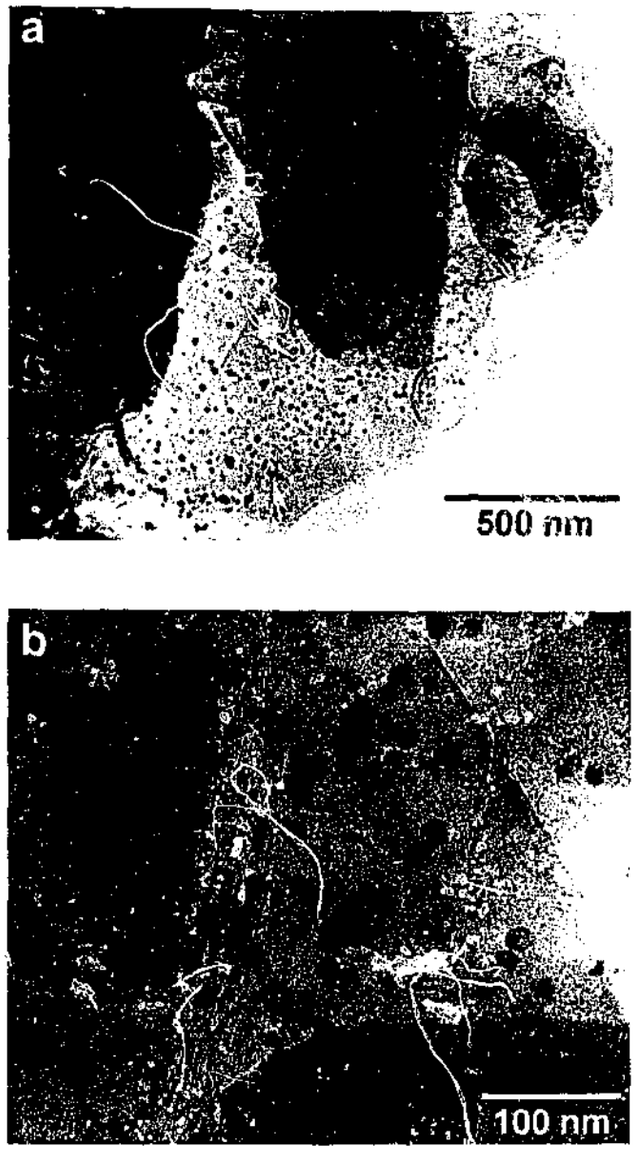

Figure 5.19. TEM micrographs of cleaved crystals of AlN powder, heat-treated at 1800°C for 4 hours.

Two conclusions can be reached from these results. First, the nano-precipitates are only occurring in particles of original AlN starting powder. They do not arise in precipitated AlN. Second, the hypothesis in Chapter 4 that the AlN grains and sub-grains with a pure Al and N chemistry were particles of original starting powder would appear to be supported here.

5.6.2 Characterisation of the Nano-precipitates

EDXS analysis of the nano-precipitates could establish no chemical differences between the nano-precipitates and the AlN matrix in which they were located. Figure 5.20(a) shows an EDXS spectrum obtained from one of the nano-precipitates shown in Figure 5.16(b). An electron beam width of 15 nm was used for this analysis. Figure 5.20(b) shows an EDXS spectrum obtained from an area of AlN matrix adjacent to the precipitate. No discernible differences could be detected between the two regions, with both spectra exhibiting Al and N peaks characteristic of AlN. This indicates that any chemical difference that may exist between the nano-precipitate and the matrix grain was too minor to be detected by this technique. This analysis was not particularly sensitive to the exact composition of the nano-precipitates, given that the nano-precipitates were so small that they had AlN matrix above and below them. This made it almost impossible to obtain an EDXS spectrum solely from a precipitate, with no contribution from the AlN matrix. Nonetheless, any chemical impurity in the precipitates should have been detectable.

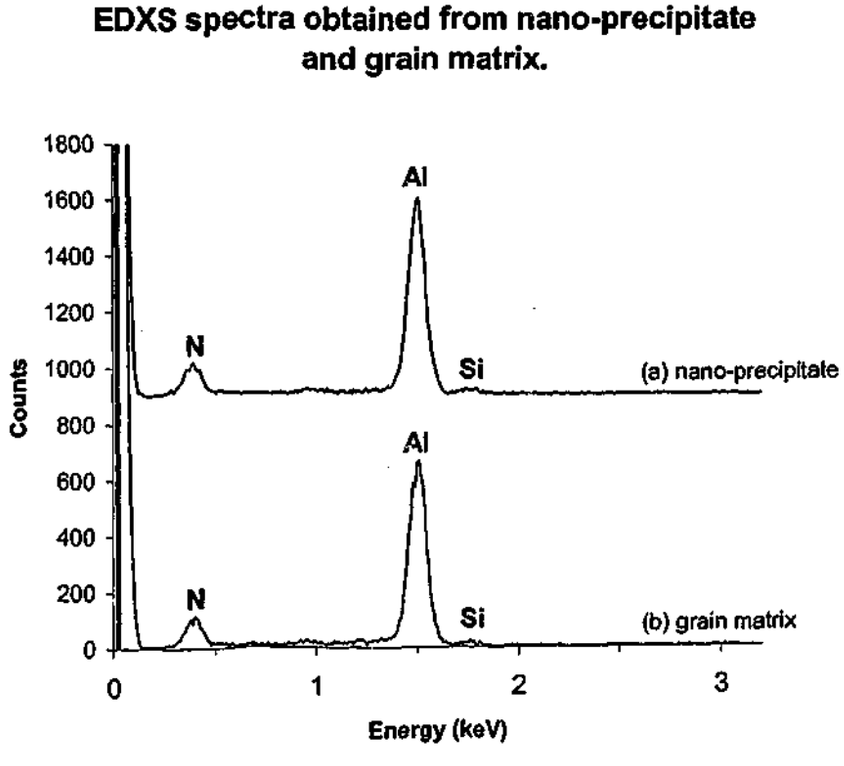

Figure 5.20. EDXS spectra obtained from (a) nano-precipitate and (b) grain matrix of a precipitated AlN grain in 5025_{1800}.

A convergent beam electron diffraction pattern obtained from the precipitate-containing sub-grain shown in Figure 5.21(a) is shown in Figure 5.21(b). This pattern can be indexed to the <011> zone axis of AlN. No distinct diffraction information from the nano-precipitates could be discerned. This was unexpected, given the high number of nano-precipitates in some of the grains. Many other precipitated AlN grains were analysed, however none of these yielded any diffraction information from the precipitates. Only diffraction spots attributable to AlN were observed. This suggested that the nano-precipitates shared a crystallography very similar to that of the AlN matrix.

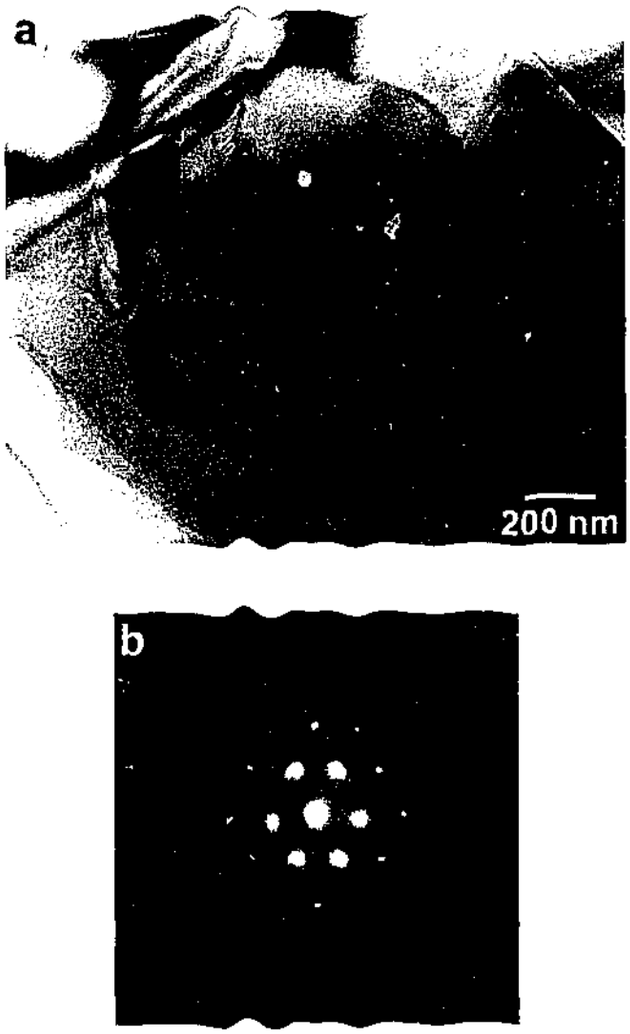

Figure 5.21. (a) Bright field TEM micrograph of a precipitated AlN grain in sample 5025_{1800}. Micrograph (b) is a convergent beam electron diffraction pattern obtained from the precipitated region of the grain in (a). This pattern can be indexed to the <011> zone axis of AlN. Only spots attributable to AlN are observed in this diffraction pattern.

It is most likely that the nano-precipitates were formed due to minor amounts of impurities in the AlN at temperatures that are higher than that at which the AlN powder was originally manufactured. The impurities are in a solid solution in the as-received powder, but exposure to high temperatures for extended periods causes them to precipitate as distinct phases within the AlN grains.

Due to a lack of any distinct chemical or crystallographic information concerning the nano-precipitates, and their lack of relevancy to the scope of this work overall, no further effort to characterise the nano-precipitates was carried out. Nonetheless, these observations are interesting, as they may be relevant to the manufacture of AlN substrate materials. Owing to its high electrical resistivity and high thermal conductivity, dense AlN finds extensive use as a substrate material for electronic chip modules. The good electrical and thermal properties of AlN are highly dependent on using high purity AlN raw materials (Weimer 1997). There exists a possibility that distributions of these nano-precipitates within dense AlN materials could affect these properties. Many techniques used in the manufacture of AlN powder involve processing temperatures in the range 1000°C to 1500°C, while dense AlN materials are sintered in the region of 1800°C (Weimer 1997). As 1800°C is the processing temperature at which the nano-precipitates became apparent in the present work, there is a significant possibility of the nano-precipitates developing in dense AlN materials. It is not possible to speculate on the possible effects of the nano-precipitates on the properties of dense AlN from this work. However, as the commercially important properties of these materials are very sensitive to processing methods and impurities, it could prove to be an interesting area of study.

5.7 Conclusions for Chapter 5

Eight high m and n-value Ca-Si-Al-O-N compositions with m = 2.0, 3.0, 4.0 and 5.0 and n = 4.0 and 5.0 were examined. The key conclusions that were reached as a result of the investigation into these compositions are as follows:

- Ca α-sialon is an equilibrium phase in seven of the eight compositions examined. No α-sialon was detected in the 5050 composition. Ca α-sialon possesses an elongated morphology in all seven of these compositions.

- Knowledge of the Ca α-sialon phase behaviour diagram has been extended to cover a broader range of compositions. Phase compatibility regions have been defined with more accuracy for compositions which possess m-values >3.0 and/or n-values >3.5. In addition, a new phase compatibility region, α' - AlN - AlN' - liquid, has been identified. This new phase region is bounded by the approximate points m = 3.5, n = 0, m = 5.0, n = 5.0 and m = 5.5, n = 4.0 on the phase behaviour diagram.

- AlN-polytypoid grains possess plate-shaped grain morphologies. These plates appear to grow rapidly. High proportions of AlN-polytypoid phases in samples form networks of plates that restrict the growth of elongated α-sialon.

- Increasing composition m and n-values increases the proportions of intergranular glass and AlN/AlN-polytypoid phases present in sample microstructures. Analysis of sample fracture surfaces shows that increased levels of these phases greatly decreases the amount of surface feature indicative of microstructural toughening mechanisms.

- Nano-precipitates observed in AlN grains in a 5025 sample were determined to originate in the AlN starting powder. AlN precipitated during reaction sintering may contain a Si impurity in a solid solution.

Chapter 6

Effects of Processing Parameters on Microstructural Development

6.1 Introduction

When fabricating pressureless sintered Ca α-sialon materials, there is a number of processing parameters that can be modified. These parameters encompass both the raw materials used to make up the compositions, and the firing schedules utilised to react and densify them.

These parameters are highly relevant to the processing of Me-Si-Al-O-N compositions that exhibit elongated α-sialon grain growth. Some recent studies, such as that by Chen and Rosenflanz (1997), have concluded that very specific powder compositions and firing schedules can allow elongated grains to develop in α-sialon ceramics. It follows that changes to these very specific parameters could have a significant effect on microstructural development.

Any effort to better understand the microstructural development of Ca-Si-Al-O-N compositions, especially the phenomenon of elongated grain growth, requires an understanding of the effects of changing various parameters. By better understanding how these changes influence phase and microstructural evolution, the task of engineering a material with a desired combination of properties would be made easier.

This chapter examines the effects that changes to a range of sintering and raw material parameters had on the development of three Ca-Si-Al-O-N compositions. Sintering parameters were investigated by examining a range of heating rates and holding times during pressureless sintering. Raw material parameters were investigated by examining the effects of substituting α-Si_3N_4 powder with β-Si_3N_4 powder in the raw compositions.

The resultant effects that these changes had on densification, phase assemblages and microstructural development are discussed.

The experimental plan for each section of work is detailed at the beginning of each of the relevant sections.

6.2 Effects of Using Different Holding Times

6.2.1 Experimental Outline

This section of work investigated the effects of utilising different isothermal holding times during pressureless sintering. Three Ca-Si-Al-O-N compositions located on the Ca α-sialon plane, 2014, 3019, and 3622, were examined in this section of work. Each composition was designated by its m and n-value in the α-sialon equation (Eqn. 2.2) where, for example, the composition designated 2014 had m and n-values of 2.0 and 1.4 respectively. The three compositions are detailed in Table 6.1. The weight percentages of the starting powders used in each composition are displayed in Table 6.2.

The locations of the compositions on the Ca α-sialon plane are shown in Figure 6.1. It can be seen that the 2014 composition lies on the edge of the α-sialon forming region. This composition would therefore be expected to form a single-phase α-sialon material. The other two compositions, 3019 and 3622, lie outside of the α-sialon forming region, and would be expected to form materials exhibiting both α-sialon and AlN/AlN-polytypoid phases, as well as quantities of grain boundary glass.

Holding times ranging from 1 minute to 4 hours were utilised at each of the two isothermal hold temperatures investigated, 1550°C and 1800°C. 1550°C was chosen as earlier work found that basic reactions of starting powders and intermediate phases in these types of compositions were complete after 4 hours at this temperature. This would allow the progression of chemical reactions to be followed in the different compositions. The higher 1800°C temperature was chosen as this represents the typical temperature used to pressureless sinter Ca-Si-Al-O-N samples to full density.

Table 6.1. Chemical compositions and m and n-values of the three compositions examined in this section of work.

Composition name	Chemical Composition	m-value	n-value
2014	$Ca_{1.0}Si_{8.6}Al_{3.4}O_{1.4}N_{14.6}$	2.0	1.4
3019	$Ca_{1.5}Si_{7.1}Al_{4.9}O_{1.9}N_{14.1}$	3.0	1.9
3622	$Ca_{1.8}Si_{6.2}Al_{5.8}O_{2.2}N_{13.8}$	3.6	2.2

Table 6.2. Calculated weight percentages of the starting components for the three compositions examined in this section of work.

Composition	Si_3N_4 (wt.%)	AlN (wt.%)	Al_2O_3 (wt.%)	$CaCO_3$ (wt.%)	equivalent to CaO (wt.%)
2014	67.25	23.36	0.04	16.67	9.34
3019	53.85	32.54	0.03	24.23	13.58
3622	46.16	37.79	0.06	28.54	15.99

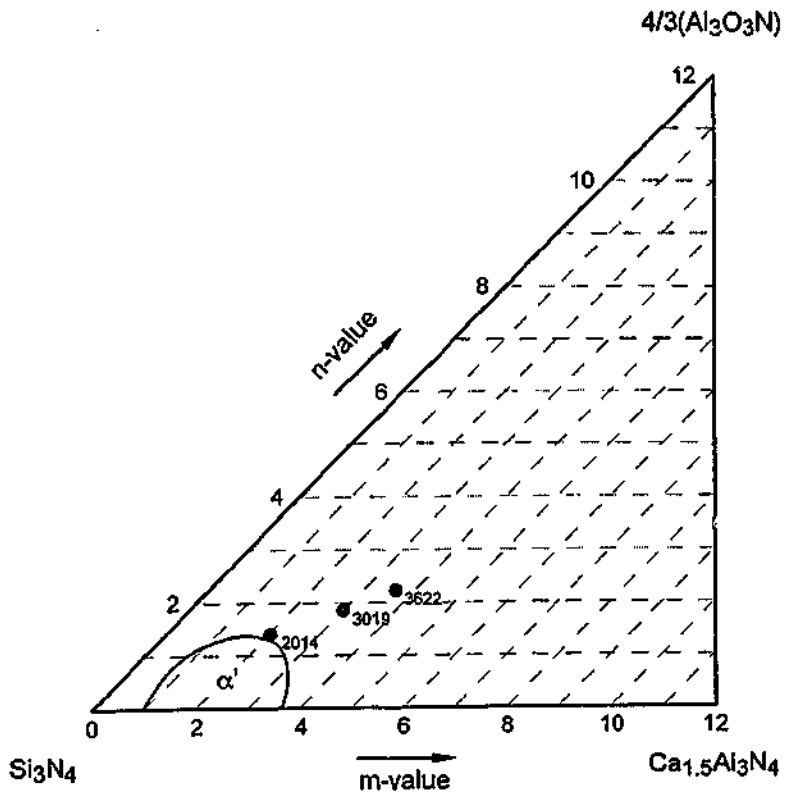

Figure 6.1. The locations on the Ca α-sialon plane of the three compositions examined in this section of work.

It will allow an examination of how densification, phase evolution, and microstructural development proceed with time in Ca-Si-Al-O-N compositions. All the samples in this section of work were pressureless sintered. A heating rate of 25°C/min. was utilised to reach the desired isothermal holding temperature. Samples were cooled in the furnace by switching off power after sintering.

6.2.2 1550°C Isothermal Hold Temperature

6.2.2.1 Crystalline Phase Assemblages and Sample Densification at 1550°C

X-ray diffraction data acquired from the samples sintered at 1550°C are displayed in Table 6.3. By examining samples held at 1550°C for various times, a picture of how the dissolution of raw materials and precipitation of reaction products progresses with time is obtained. Differences between the three compositions can also be observed.

Immediately noticeable in this data is the rapid precipitation of α-sialon that has taken place in all three compositions. Even at this relatively low temperature, significant α-sialon peaks were detected after only 1 minute. After 30 minutes, the strongest peaks in the XRD spectra of all three compositions were attributable to α-sialon.

Gehlenite was detected as an intermediate phase in all three compositions after 1 minute at 1550°C. This phase completely disappeared after 30 minutes at 1550°C. It suggests that gehlenite forms on heating below 1550°C and melts above the gehlenite melting point, which was established in Chapter 4 to lie between 1500°C and 1550°C.

Significant quantities of α-Si_3N_4 raw material were evident in all three of the samples after 1 minute. This was gradually dissolved as the sintering time was extended. The complete dissolution of α-Si_3N_4 occurred sooner in higher m-value compositions. In composition 2014, a trace of α-Si_3N_4 was still evident after 2 hours at 1550°C. Only after 4 hours was total dissolution evident. Contrasting this, only a small amount of α-Si_3N_4 was detected after 30 minutes in 3622, and none was detected after 1 hour. The increased volume of liquid phase in the more Ca-rich compositions would contribute to the more rapid dissolution of α-Si_3N_4, as would the location of these compositions

further away from the Si_3N_4 corner of the Ca α-sialon plane. The fact that the higher m-value compositions also contain less Si_3N_4 powder in the starting composition would also contribute to the reduced time required to completely dissolve the Si_3N_4.

Table 6.3. Crystalline phase assemblages of the three compositions held at 1550°C for times ranging from 1 minute to 4 hours.

Sample Composition and Holding Time		Crystalline Phases				
		α-sialon	AlN	α-Si_3N_4	β-Si_3N_4	Gehlenite
2014	1 min.	s	ms	vs	vw	w
	30 mins.	vs	w	mw		
	1 hour	vs	w	w		
	2 hours	vs	vw	tr		
	4 hours	vs	tr			
3019	1 min.	vs	vs	ms		w
	30 mins.	vs	m	vw		
	1 hour	vs	mw	vw		
	2 hours	vs	mw			
	4 hours	vs	mw			
3622	1 min.	m	vs	mw		vw
	30 mins.	vs	ms	vw		
	1 hour	vs	ms			
	2 hours	vs	ms			
	4 hours	vs	ms			

(where w = weak, m = medium, s = strong, v = very, tr = trace for XRD peak intensity)

After 2 hours at 1550°C, the phase assemblages of the 3019 and 3622 compositions remained essentially the same, indicating that the basic chemical reactions were complete after this time. In 2014, the amount of AlN continued to decrease up to 4 hours, at which point only a trace amount was detected. α-Sialon was the majority crystalline phase in all three samples after 4 hours. The only other crystalline phase detected was AlN. XRD could not determine whether the detected AlN was original starting material, newly precipitated AlN, or a combination of the two. As expected from

the phase behaviour diagram, the ratio of AlN to α-sialon increased with increasing composition m-value.

A plot of apparent density as a function of sintering time for the three compositions sintered at 1550°C is displayed in Figure 6.2. A number of features are apparent in this plot that require explanation.

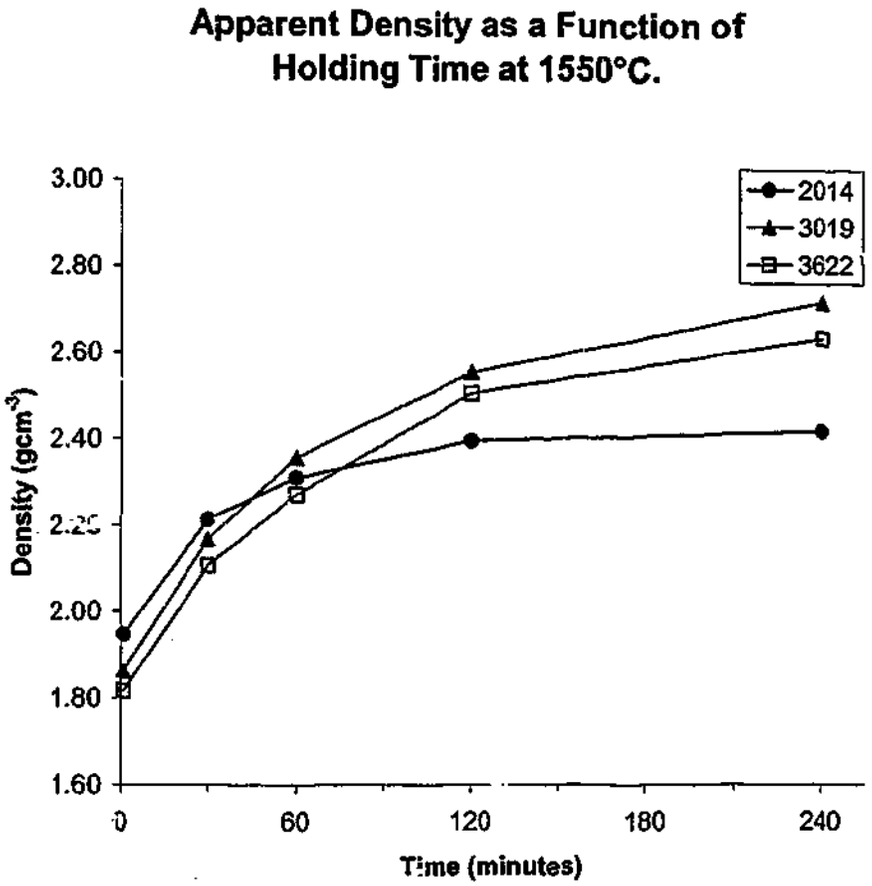

Figure 6.2. Plot of apparent density as a function of holding time for the three Ca-Si-Al-O-N compositions held at 1550°C.

Looking at the samples sintered for 1 minute, it can be seen that the lowest m-value sample, 2014, has the highest density, and that the highest m-value sample, 3622, has the lowest. This observation was somewhat unexpected, given that the higher m-value 3622 composition should generate significantly more liquid phase than 2014 at a given temperature. It can be explained by the fact that after calcining at 900°C, the green body density of a sample of 3622 is significantly lower than that of a sample of 2014, a result of the decomposition of $CaCO_3$. All the compositions exhibit a pre-calcined green body

density of ~2.000 gcm^{-3}. As was described in Chapter 4, mass loss during calcining causes the more Ca-rich compositions to exhibit a lower post-calcination green body density. A consequence of this is that it takes a degree of time for the more Ca-rich samples to reach the same density as a lower m-value sample. This is especially so at a lower sintering temperature such as that used here, as densification proceeds relatively slowly. It can be seen that as the sintering time is extended, the better densification kinetics of the more liquid-rich samples becomes apparent. The densification rates of the more liquid-rich 3019 and 3622 compositions greatly exceeded that of the lower m-value 2014 composition after 30 minutes at 1550°C.

Another interesting feature of the densification data is the observation that the density of the 3622 composition did not catch up with that of the lower m-value 3019 composition. Furthermore, between 2 and 4 hours, 3019 actually exhibited a slightly higher densification rate. This was evidenced by the slightly higher gradient of the slope of the plot of 3019 between 2 and 4 hours in Figure 6.2. This was somewhat unexpected, given that the higher m-value 3622 composition should evolve a higher volume of liquid phase at sintering temperatures, thus enhancing liquid phase densification.

This lower rate of densification for 3622 was attributed to the higher AlN content of this composition, and is related to the wetting behaviour of the different nitride components in a sample. The concept of different temperatures existing for the wetting of Si_3N_4 and AlN by a liquid phase, and the effect that this may have on densification, was introduced in Chapter 4. It has been established by Menon and Chen (1995a) that a Ca-based liquid phase will preferentially wet Si_3N_4, and only when higher temperatures are reached will AlN be wetted, thus allowing densification to proceed further. It is possible that the 1550°C temperature being examined here is below the temperature required for the wetting of AlN. This would have the effect of hindering densification in more AlN-rich samples. Work by Menon and Chen (1995b) on a low m-value Ca α-sialon composition (m = 1.0, n = 1.0) found that the wetting of AlN appeared to occur at 1660°C, while the wetting of Si_3N_4 took place at 1410°C. While compositional differences of the liquid phase in 3622 would most probably change these temperatures to some extent, it is likely that the 1550°C sintering temperature utilised here is below the temperature

required for the wetting of AlN. This would explain why the densification rate is lower in a more liquid-rich, but also AlN-rich, composition.

6.2.2.2 Microstructural Characterisation of Samples Held at 1550°C

Though chemical reactions proceeded without difficulty at 1550°C, microstructural observations of sintered samples revealed that little grain growth took place at this temperature, even over extended periods. Figures 6.3 and 6.4 show SEM micrographs of compositions 2014 and 3019 respectively, with each composition sintered for (a) 1 minute and (b) 4 hours.

Examination of these micrographs reveals that the samples sintered for 4 hours display finer grain size distributions than the samples sintered for 1 minute. This was most prominent in the 2014 composition. This unusual observation arises because the α-sialon that precipitates over 4 hours has a finer grain size than the raw powders that dominate the 1 minute sample microstructures. Referring to Table 6.3, it can be seen that α-Si_3N_4 and AlN dominate the 1 minute samples, whereas α-sialon is the majority phase in the 4 hour samples. The precipitated α-sialon does not exhibit significant grain growth at 1550°C, and consequently, a finer grain size distribution develops as raw materials are dissolved and α-sialon is precipitated.

Referring to the 1 minute micrographs, it is apparent that the 3019 sample, shown in Figure 6.4(a) has a finer grain size distribution than the 2014 sample, shown in Figure 6.3(a). This was a result of the more rapid dissolution of raw materials and precipitation of α-sialon that took place in the higher m-value 3019 composition. XRD analysis data presented in Table 6.3 shows that the dissolution of raw materials and precipitation of α-sialon proceeded more rapidly in the higher m-value compositions.

Examination of the samples sintered for 4 hours at 1550°C reveals that a degree of elongated grain growth took place in the 3019 sample that was not apparent in 2014. The microstructures shown in these micrographs are composed mainly of α-sialon.

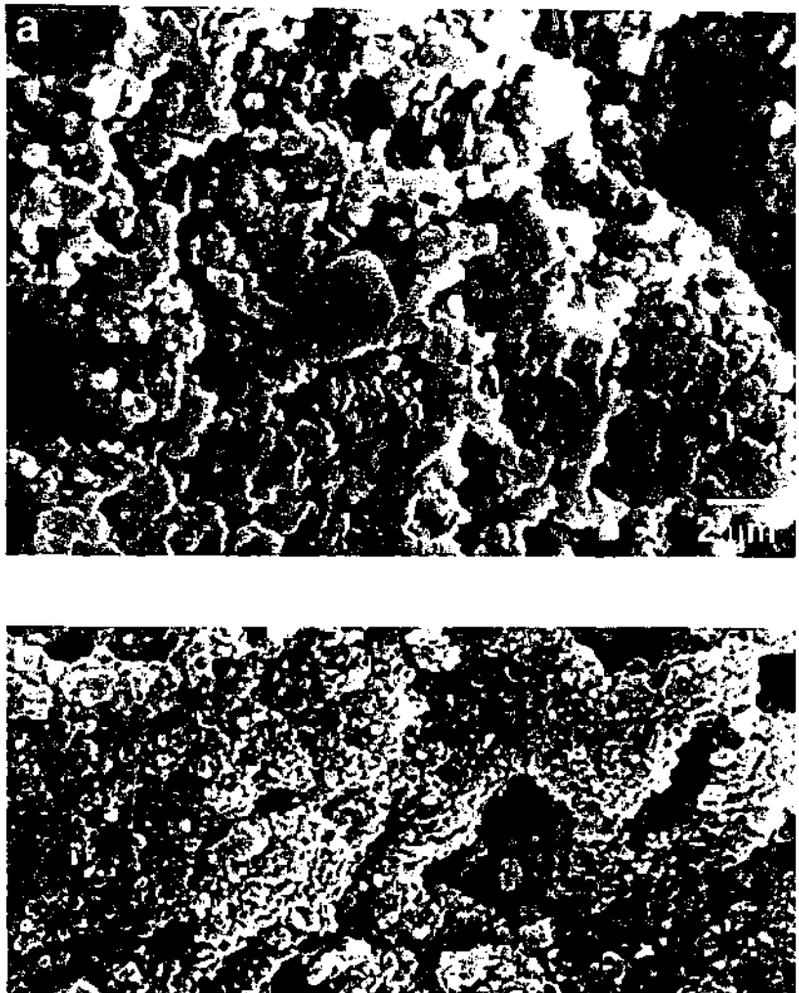

Figure 6.3. Secondary electron micrographs of polished and etched samples of 2014 held at 1550°C for (a) 1 minute and (b) 4 hours.

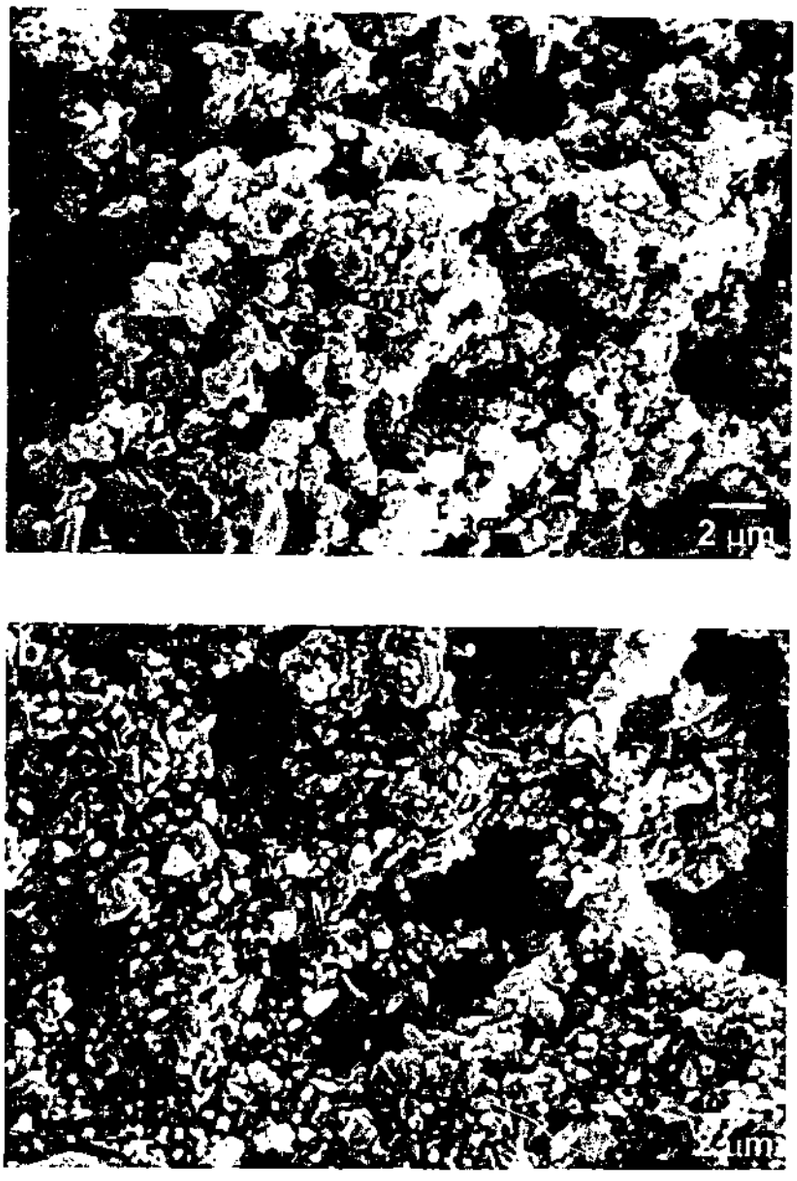

Figure 6.4. Secondary electron micrographs of polished and etched samples of 3019 held at 1550°C for (a) 1 minute and (b) 4 hours.

It is clear in Figure 6.3(b) that the precipitated α-sialon grains in 2014 possesses equiaxed morphologies. Contrasting this, the micrograph of 3019 shown in Figure 6.4(b) reveals the development of many fine, elongated α-sialon grains. The enhanced grain growth in the 3019 sample is believed to be a result of the higher liquid phase content of this sample, relative to the 2014 sample. The increased proportion of liquid phase in 3019 could enhance diffusion, allowing elongated grain growth to proceed more easily. Furthermore, 3019 contains more Ca, which would also be expected to enhance diffusion by creating a lower viscosity liquid phase. In the case of 2014, the combination

of a lesser proportion of higher viscosity liquid phase could have reduced the diffusion rate to the extent that equiaxed, rather than elongated, grains developed.

6.2.3 1800°C Isothermal Hold Temperature

6.2.3.1 Crystalline Phase Assemblages and Sample Densification at 1800°C

Examining the crystalline phase assemblages of samples sintered at this temperature allows phase evolution in the Ca-Si-Al-O-N compositions to be monitored at a commonly utilised densification temperature. X-ray diffraction data obtained from the samples sintered at 1800°C is displayed in Table 6.4.

Table 6.4. Crystalline phase assemblages of the three compositions held at 1800°C for times ranging from 1 minute to 4 hours.

Sample Composition and Holding Time		Crystalline Phases		
		α-sialon	AlN	$2H^{\delta}$
2014	1 min.	vs	tr	
	30 mins.	vs		
	1 hour	vs		
	2 hours	vs		
	4 hours	vs		
3019	1 min.	vs	m	
	30 mins.	vs	w	vw
	1 hour	vs	vw	w
	2 hours	vs	tr	w
	4 hours	vs		w
3622	1 min.	vs	s	
	30 mins.	vs	s	
	1 hour	vs	ms	
	2 hours	vs	ms	
	4 hours	vs	ms	

(where w = weak, m = medium, s = strong, v = very, tr = trace for XRD peak intensity)

Data obtained from the samples sintered for 1 minute reveals that the basic chemical reactions are essentially complete by the time 1800°C is reached. No intermediate phases or Si_3N_4 raw material was detected in any of the samples after this period. A trace of unreacted AlN was detected in 2014 after 1 minute.

The crystalline phase assemblages of the 2014 and 3622 compositions remained essentially unchanged over holding times ranging from 1 minute to 4 hours. Composition 2014 exhibited only α-sialon, with a trace of AlN phase only detected at 1 minute. Sample 3622 exhibited α-sialon as the majority crystalline phase, with a significant amount of AlN as a secondary phase.

The phase evolution of the 3019 composition differed from the other two compositions, in that a constant change in phase assemblage occurred over the 4 hours of sintering at 1800°C. After 1 minute at 1800°C, the crystalline phases detected in the sample were α-sialon and AlN. At 30 minutes, the data in Table 6.4 shows that the amount of AlN decreased, while some $2H^{\delta}$ became evident. Sintering up to 4 hours, the amount of $2H^{\delta}$ continued to increase, while AlN decreased to a negligible amount. Figure 6.5 shows the XRD spectra obtained from the samples sintered for 1 minute and 4 hours. The disappearance of AlN peaks and emergence of $2H^{\delta}$ peaks in the 4 hour spectrum (Figure 6.5(b)) can clearly be seen.

These results suggested that AlN was not a stable phase in the 3019 composition at 1800°C. Rather, the composition appeared to lie within an $\alpha' + 2H^{\delta}$ + liquid phase compatibility triangle on the Ca α-sialon plane (Figure 5.3). The reaction kinetics of the AlN to polytypoid transformation in this composition appeared quite sluggish. The composition required 4 hours of sintering at 1800°C to come close to completely dissolving the AlN in the sample and precipitating the AlN-polytypoid phase. A possible explanation for this observation is that the transformation of AlN to $2H^{\delta}$ proceeded because of a slight composition shift during sintering. Many adjacent phase compatibility triangles on the Ca α-sialon plane are very narrow (see Figure 5.3), and consequently, a gradual change in composition can shift a sample into a different phase compatibility triangle.

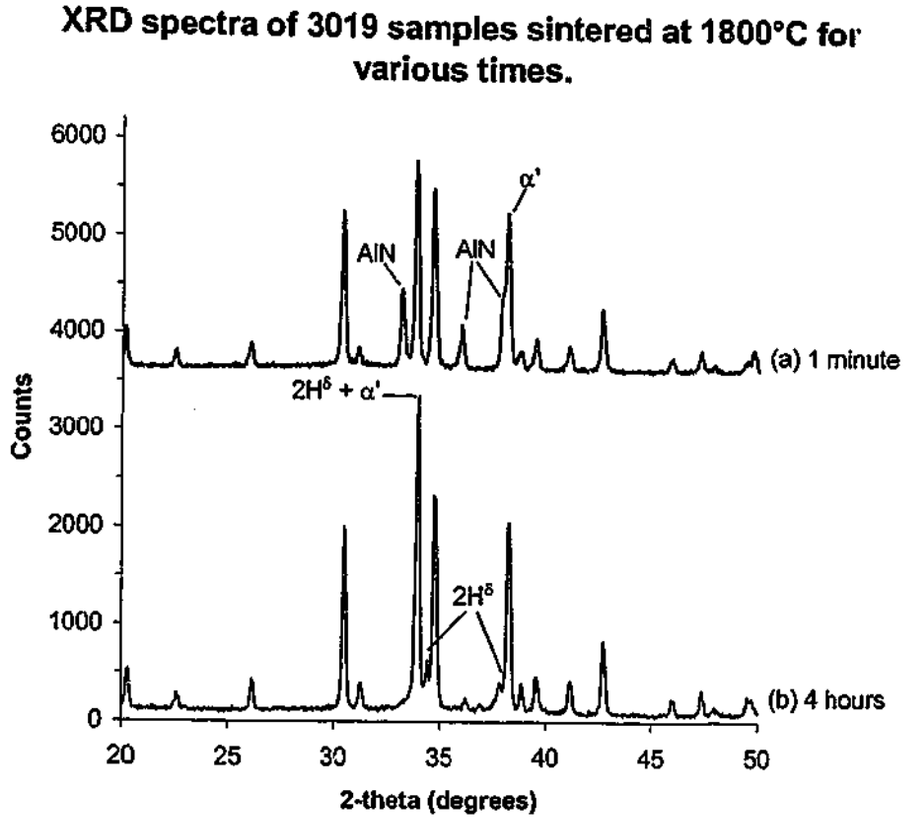

Figure 6.5. XRD spectra obtained from samples of composition 3019 sintered at 1800°C for (a) 1 minute and (b) 4 hours. Peaks attributable to AlN and $2H^{\delta}$ are indicated. All other peaks can be assigned to Ca α-sialon.

A shift in composition could have two possible origins. As α-sialon is a solid solution, the composition of the phase can change with time. This could promote the dissolution of increased amounts of AlN. and the precipitation of $2H^{\delta}$. Alternatively, mass loss resulting from volatilisation of the liquid phase during sintering can also alter the overall composition of the sample, which could cause $2H^{\delta}$ to precipitate in favour of AlN. Possibly, a combination of these two factors was causing the observed gradual reduction of AlN and increase of $2H^{\delta}$ in this composition over time.

A plot of apparent density as a function of sintering time for the three compositions sintered at 1800°C is displayed in Figure 6.6. One of the most prominent features of this data is the high level of densification achieved over a short period. If the maximum density of hot-pressed Ca-Si-Al-O-N samples is taken as 3.210 gcm^{-3} (as described in Chapter 4), then all three compositions attained greater than 90% of maximum density

after only 30 minutes at 1800°C. This period of rapid density increase over a short time was attributed to massive particle rearrangement. It follows the release of significant volumes of liquid phase when gehlenite melts at around 1550°C. The small grain sizes present at the time that gehlenite melts greatly assists the liquid phase densification process, as does the low viscosity of the liquid at elevated temperatures. Massive particle rearrangement is described by Menon and Chen (1995b) as the dominant mechanism of densification in α-sialons.

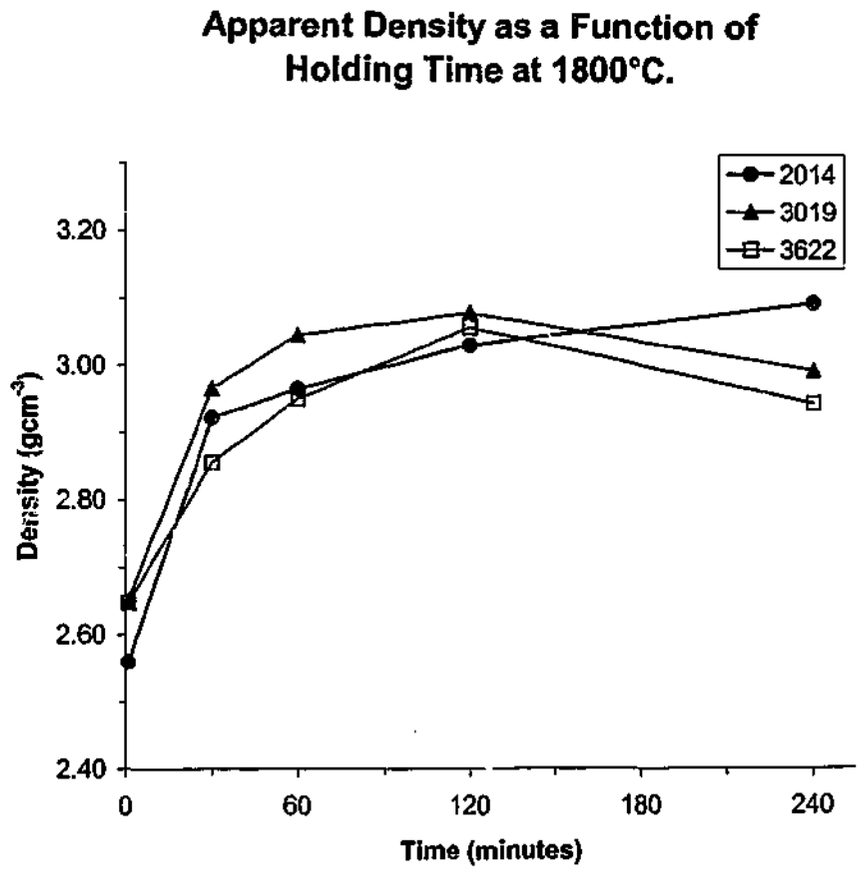

Figure 6.6. Plot of apparent density as a function of holding time for the three Ca-Si-Al-O-N compositions held at 1800°C.

A significant reduction in the densification rate from 30 minutes is apparent in Figure 6.6, especially in the 2014 composition. This drop in the sample densification rates can be attributed to a number of causes. Firstly, as anisotropic grain growth proceeds, densification via particle rearrangement becomes increasingly difficult, and the densification rate is reduced. Secondly, as time progresses, the volume of liquid phase present in a sample decreases, which may also reduce the densification rate. The

reduction in the volume of liquid phase arises from the consumption of liquid phase as crystalline phases precipitate, and from volatilisation of the liquid at high temperatures. The reduction in density was most prominent in the low m-value 2014 composition, which was consistent with the fact that this composition contained the least equilibrium liquid phase. After 1 hour at 1800°C, the 3019 composition exhibited the highest density. After 2 hours, all three compositions achieved similar densities in the range 95 - 96% of maximum density.

Examination of the data obtained from the samples sintered for 2 and 4 hours reveals some interesting trends. It is over this time range that some significant disparities in the densification behaviour of the three compositions become apparent. The most significant was the reduction in density of the higher m-value compositions when holding times were extended from 2 to 4 hours. Looking at Figure 6.6, it can be seen that the density of the 2014 composition continued to increase over the 2 to 4 hour timeframe, with the composition reaching 96% of maximum density after 4 hours. The other two compositions contrasted this behaviour, with both exhibiting a reduction in density when sintering continued from 2 hours to 4 hours. A higher m-value corresponded to a larger reduction in density. The density of 3019 dropped from 96% of maximum density after sintering for 2 hours, to 93% after sintering for 4 hours. Likewise, the density of 3622 dropped from 95% of maximum density at 2 hours to 92% after 4 hours.

The drop in the density of these high m-value samples is attributable to the significant volumes of liquid phase present in these samples at the holding temperature. The density losses are believed to result from volatilisation of the low viscosity intergranular liquids present in the densified samples during sintering. The 3019 and 3622 compositions held for 4 hours at 1800°C exhibited significant weight losses of 4.7% and 5.7% respectively. The reacted samples containing elongated α-sialon grains are unable to further densify to make up for this mass loss, so consequently, a reduction in density is observed. Clearly, once a sample with a significant amount of intergranular liquid phase attains its maximum density, further sintering time will have a deleterious effect on density.

6.2.3.2 Microstructural Characterisation of Samples Held at 1800°C

The microstructural development of samples sintered at 1800°C for various times were examined using SEM. The present section details the microstructural evolution of the 2014 and 3019 compositions. These two compositions were examined as they display the two types of phase evolution observed. In the case of the 2014 composition, the phase assemblage remained essentially the same over all sintering times at 1800°C. Contrasting this, significant phase changes occurred in 3019 over 4 hours. The final microstructure of the 3622 composition is also examined. Due to over-etching, the polished sample surfaces were removed from some of these samples, giving them a rougher than normal appearance.

The micrograph of 2014 sintered for 1 minute, shown in Figure 6.7(a), reveals the high porosity present in the sample. This sample exhibited a significant increase in density over its green body density, though significant porosity remained, as was indicated by its density of only 80% of maximum density. According to XRD analysis (Table 6.4), chemical reactions were almost complete in this sample. Only a trace of AlN raw material was present in this microstructure. The majority crystalline phase was α-sialon. The higher magnification micrograph, shown in Figure 6.7(b), clearly shows the sub-micron size of the fine, equiaxed, α-sialon grains. No significant growth of the α-sialon phase had occurred at this point in time.

Extending the sintering time to 30 minutes resulted in considerable microstructural development. The density of this sample increased to 91% of maximum density. This reduction in porosity is evident in the micrograph of the sample in Figure 6.7(c). More remarkable though is the extent of α-sialon grain growth that has occurred over a relatively short period. Extending the sintering time from 1 minute to 30 minutes transformed the α-sialon from sub-micron equiaxed grains to high aspect ratio, elongated needles.

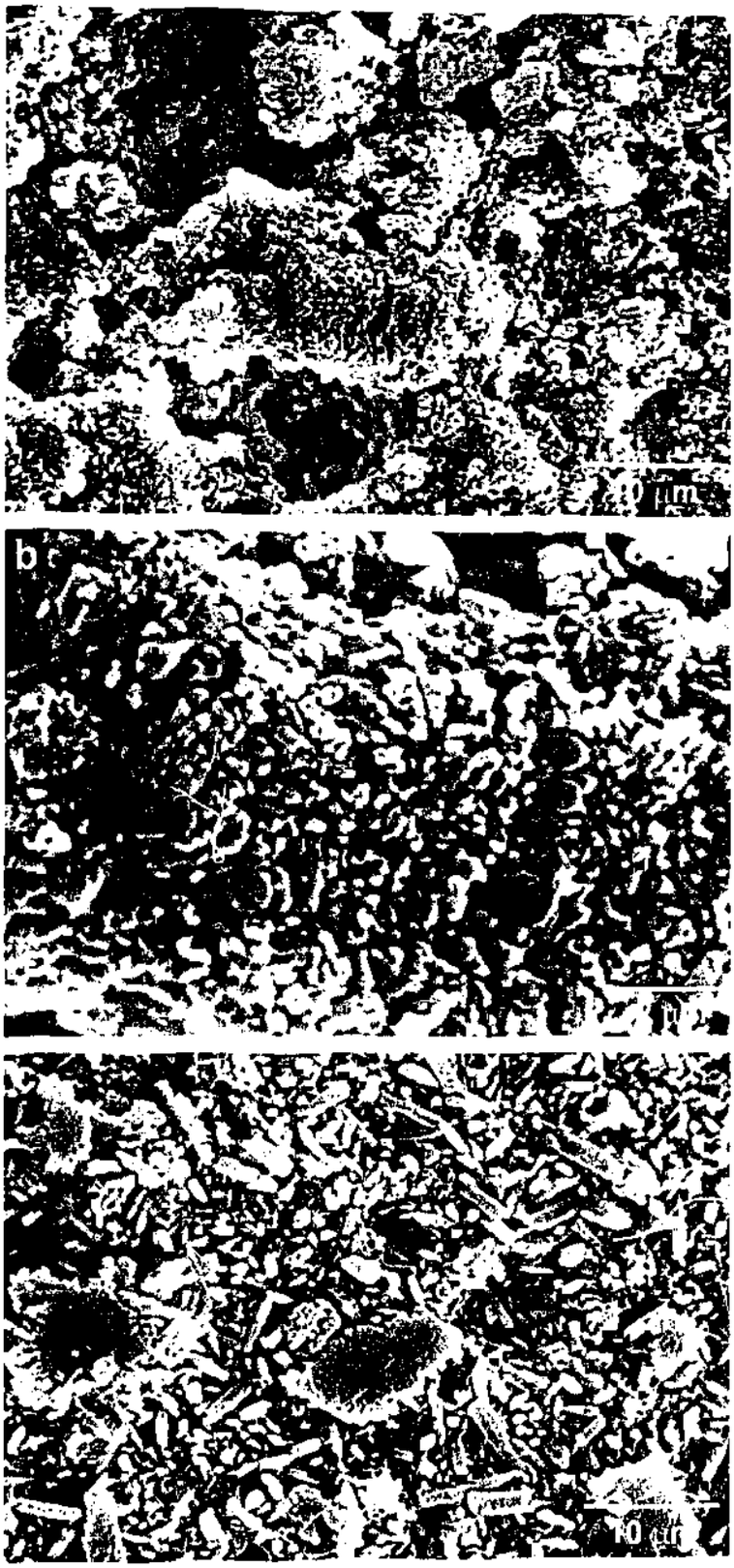

Figure 6.7. Secondary electron micrographs of polished and etched samples of 2014, held at 1800°C for (a and b) 1 minute and (c) 30 minutes.

While a substantial proportion of the α-sialon grains were relatively small, many exceeded 5 μm in length. Though no AlN was detected in this sample by XRD, a few remaining equiaxed grains of AlN are also visible in the micrograph. These grains were relatively large, approaching 10 μm in size.

Density data presented in Figure 6.6 shows that increasing the sintering time to 1, 2 and 4 hours further reduced the porosity of the 2014 samples. The overall effect of the longer sintering times on microstructure was a coarsening of the elongated α-sialon grains and a reduction in the amount of AlN observed, as Figures 6.8 (a-c) reveal. The micrographs show that very little difference can be seen between the samples sintered for 2 and 4 hours. α-Sialon grains averaged ~5 μm in length after 4 hours at 1800°C, though grains up to 10 μm in length were frequently observed. Only occasional equiaxed particles of AlN were observed in the samples sintered for 2 and 4 hours. This small proportion of AlN was too little to be detected by XRD, which indicated that α-sialon was the only crystalline phase in these samples.

According to XRD data in Table 6.4, 3019 sintered for 1 minute exhibited only α-sialon and AlN as crystalline phases. Micrographs of this sample, shown in Figures 6.9(a and b), reveal the fine precipitated α-sialon grains and larger, equiaxed grains of AlN. While appearing similar in size to the fine α-sialon grains in 2014 sintered for 1 minute, the high magnification micrograph of this sample, Figure 6.9(b), shows that many of the fine α-sialon grains exhibit a definite elongated morphology, whereas the α-sialon grains in 2014 were more equiaxed. Some of these elongated grains approached 1 μm in length.

The more pronounced anisotropic growth of α-sialon grains in 3019 in the early stages of sintering can be attributed to the increased amount of liquid phase in this composition. As previously described, it is likely that the higher volume of liquid phase in 3019, relative to 2014, enhances the rate of α-sialon grain growth via enhanced diffusion. Anisotropic grain growth requires mass transport to the ends of the anisotropically growing grains. Good diffusion kinetics are required for this to occur. In cases where diffusion may not be as effective, such as in a 2014 sample where less liquid phase is present, the reduced rate of mass transport may slow anisotropic grain growth.

Figure 6.8. Secondary electron micrographs of polished and etched samples of 2014, held at 1800°C for (a) 1 hour, (b) 2 hours and (c) 4 hours.

Figure 6.9. Secondary electron micrographs of polished and etched samples of 3019, held at 1800°C for (a and b) 1 minute and (c) 30 minutes. Some $2H^{\delta}$ polytypoid grains are arrowed in (c).

Extending the sintering time to 30 minutes led to significant elongated α-sialon grain growth (Figure 6.9(c)). The growth did not appear to be quite as extensive as that observed in the equivalent 2014 sample, though elongated α-sialon grains approaching 5 μm in length were frequently observed. A prominent feature in the micrograph of this sample is the emergence of some very large plate-shaped grains. Some of these are arrowed in Figure 6.9(c). These grains are thought to be the $2H^{\delta}$ phase detected by XRD, and they are very distinct from the equiaxed morphology of AlN.

XRD analysis revealed that over 4 hours, the AlN initially present gradually transformed to the $2H^{\delta}$ AlN-polytypoid. The rapid growth of the polytypoid phase is clearly apparent in this micrograph. After 1 minute, only equiaxed AlN was observed. At 30 minutes, polytypoid grains exceeding 20 μm were observed throughout the microstructure. Clearly, the polytypoid phases grow at a remarkable rate when compared to the rate of α-sialon grain growth.

As with 2014, extending the sintering time to 1, 2 and 4 hours led to further α-sialon grain growth (Figures 6.10 (a-c)). By 4 hours, α-sialon grains were typically 7 – 10 μm in length. The continued dissolution of equiaxed AlN and precipitation of polytypoid plates were also evident in this series of samples.

A secondary electron micrograph of the 3622 sample sintered for 4 hours is shown in Figure 6.11. The elongated α-sialon grains in this sample exhibited similar dimensions to those in 3019 sample sintered for 4 hours, ranging in size from 5 to 10 μm. This sample also included AlN and a trace of $2H^{\delta}$ according to XRD analysis. An AlN grain exhibiting the distinctive speckled topography that results from etching in NaOH is clearly visible towards the bottom left of Figure 6.11. Smaller areas of AlN are also visible, interspersed throughout the microstructure.

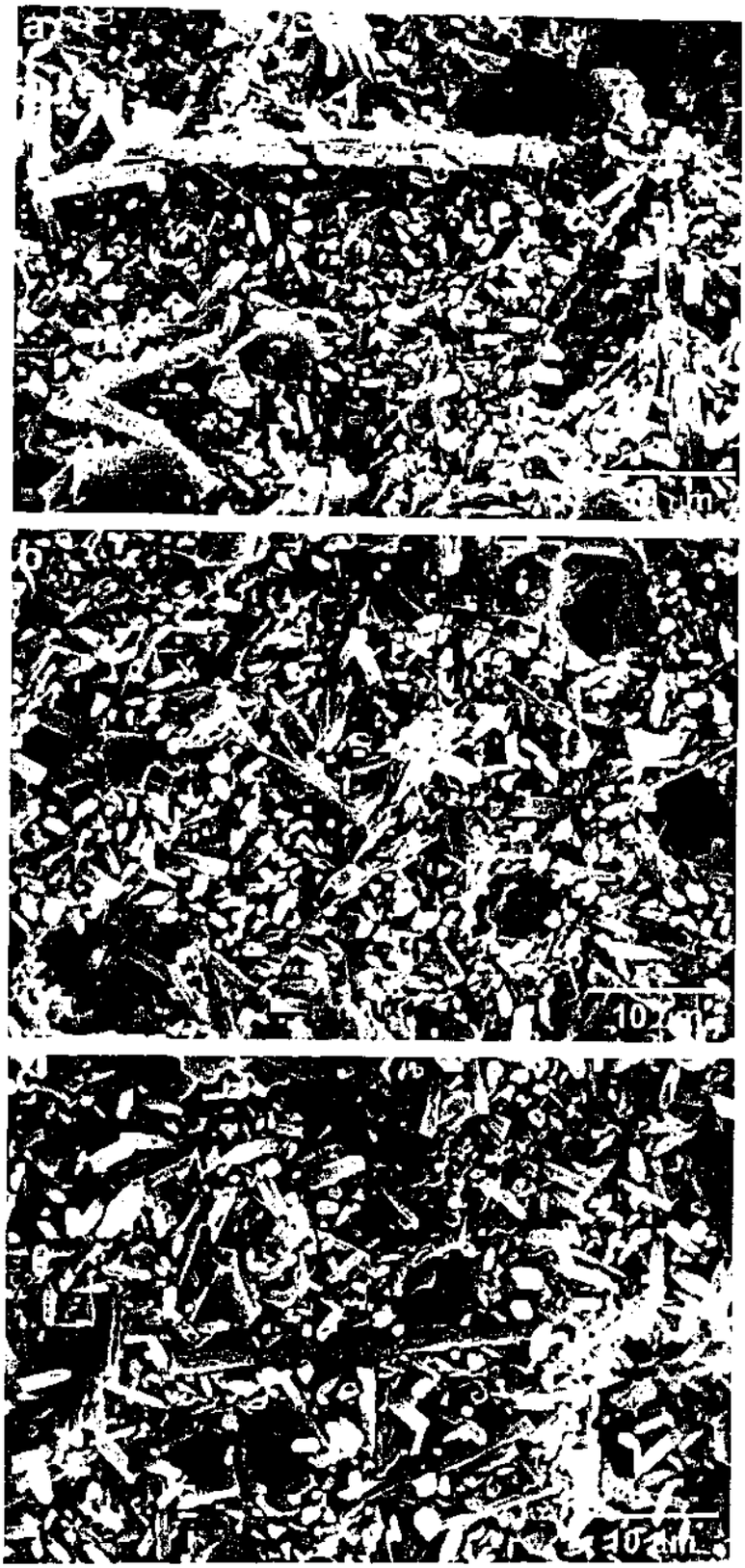

Figure 6.10. Secondary electron micrographs of polished and etched samples of 3019, held at 1800°C for (a) 1 hour, (b) 2 hours and (c) 4 hours.

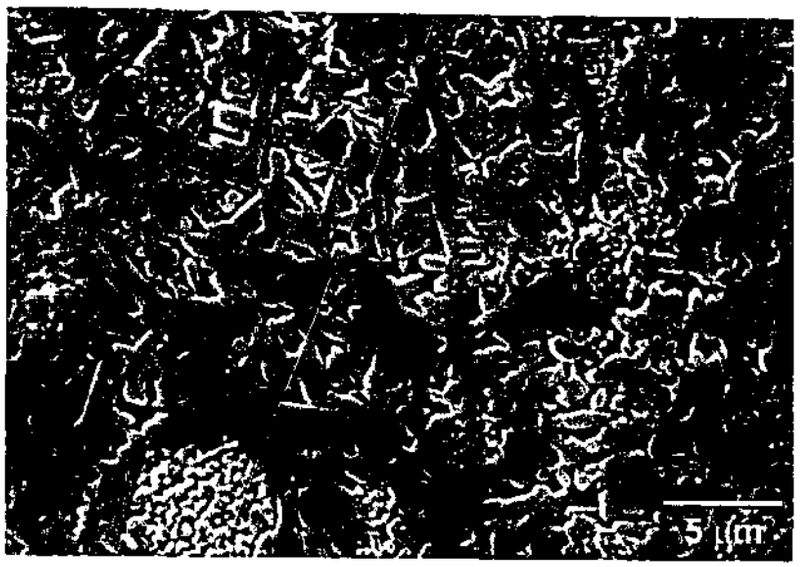

Figure 6.11. SEM micrograph of polished and etched samples of 3622, held at 1800°C for 4 hours.

6.2.4 Summary of the Effects of Using Different Holding Times

Examination of crystalline phase assemblages of the three compositions sintered at 1550°C found that basic chemical reactions are completed at this temperature. All α-Si_3N_4 and intermediate phases were dissolved. Reactions were found to proceed more rapidly in compositions with a higher m-value. Reactions were complete in composition 3622 after 1 hour. Contrasting this, the dissolution of AlN in the lower m-value 2014 continued up to 4 hours. α-Sialon was observed to precipitate rapidly in all three compositions, with significant amounts being detected after only 1 minute at 1550°C.

When sintering at 1800°C, chemical reactions were found to be essentially complete by the time the isothermal hold temperature was reached. The phase assemblage of 2014 and 3622 remained stable over sintering times up to 4 hours. Composition 3019 differed from the other two, in that AlN gradually transformed to $2H^{\delta}$ polytypoid phase over sintering times up to 4 hours. This was attributed to a shifting of the sample composition from the α′ + AlN + $2H^{\delta}$ + liquid compatibility triangle, into the α′ + $2H^{\delta}$ + liquid triangle during sintering.

Samples did not attain full density when sintered at 1550°C. The densification of the most Ca and Al-rich composition, 3622, was found to be slightly hindered at 1550°C, relative to the lower Ca and Al-containing samples. This was attributed to the higher AlN content of this composition. It was thought that AlN raw material was poorly wetted by liquid phase at this temperature, causing the more AlN-rich composition to have its densification hindered to a small degree.

Densification at 1800°C proceeded rapidly. All three compositions attained greater than 90% of maximum density after only 30 minutes at 1800°C. The highest density of the 2014 composition was reached after 4 hours at 1800°C. For 3019 and 3622, this occurred after 2 hours. Further extending the sintering time for these two compositions to 4 hours caused a reduction in density. This decrease in density was attributed to mass loss via the volatilisation of liquid phase in the high m-value samples.

Though reactions to form α-sialon completed at 1550°C, microstructural observations found that the growth of α-sialon grains at this temperature was minimal. After 4 hours at 1550°C, examination of sample microstructures found that α-sialon grain growth was greater in the 3019 sample comparing to the 2014 sample. This was attributed to the greater amount of liquid phase in 3019, which was thought to enhance grain growth by improving the diffusion kinetics in the sample. After 1 minute at 1800°C, α-sialon grain sizes were very small, typically less than 1 μm. However, after 30 minutes, significant anisotropic grain growth was observed, with α-sialon grains growing to up to 5 μm in length. Grain growth was observed to continue up to 2 hours. Further extending the sintering time to 4 hours did not result in any appreciable grain growth. The 3019 and 3622 composition displayed the longest α-sialon grains, averaging ~7 μm in length. The shortest average grain length was in 2014, with α-sialon grains averaging ~5 μm in length.

6.3 Effects of Using Different Si_3N_4 Starting Powders

6.3.1 Experimental Outline

The fabrication of α-sialon ceramics generally utilises α-Si_3N_4 powder as the main raw material. β-Si_3N_4 is not often used as it is more expensive, and does not usually realise any benefits. However, recent research on gas-pressure sintered α-sialon materials doped with Nd and Yb found that elongated α-sialon grains were formed when β-Si_3N_4, rather than the more conventional α-Si_3N_4, was used as the starting powder (Chen and Rosenflanz 1997). This research was based around the fact that α-sialon has been shown to epitaxially nucleate on α-Si_3N_4 particles (Hwang and Chen 1994). In this work, β-Si_3N_4 starting powder seeded with α-Si_3N_4 crystals was utilised. The seed crystals were added to provide a limited number of nucleation sites for α-sialon. The reduction in the number of α-sialon nucleation sites was proved successful, and elongated α-sialon microstructures resulted. However, the processing techniques used in this work were relatively complex, involving the use of gas pressure sintering (GPS), and extended sintering times of up to 12 hours.

As a part of developing a better understanding of elongated α-sialon grain growth in the Ca-Si-Al-O-N system, this section of work investigated the effects of substituting β-Si_3N_4 for varying amounts of α-Si_3N_4. The same three base compositions used in the previous section of this chapter, 2014, 3019 and 3622, were used in this section of work. Three variations of each base composition were made. The first was a conventional composition, utilising only α-Si_3N_4 powder. The second variation replaced enough of the α-Si_3N_4 with β-Si_3N_4 to obtain a 50:50 α:β wt.% ratio. The third variation involved the total substitution of α-Si_3N_4 powder by β-Si_3N_4.

The β-Si_3N_4 powder used in this work had an α-Si_3N_4 content of 6.1 wt.%. α-Si_3N_4 impurities in the β-Si_3N_4 powder, and vice versa, were accounted for in compositional calculations. However, compositions that utilised only β-Si_3N_4 powder unavoidably had an α:β ratio of approximately 6:94. Effectively, these compositions were seeded with a small proportion of α-Si_3N_4 crystals. Composition names had subscripts of α, β, or α–β

added to them to indicate that the composition was made with only α-Si_3N_4, only β-Si_3N_4, or the α:β mix respectively. For example $3019_{\alpha-\beta}$ indicates the 3019 composition made with a 50:50 ratio of α-Si_3N_4 and β-Si_3N_4.

Samples were pressureless sintered for 4 hours at 1550°C and 1800°C. The lower 1550°C temperature was utilised as this is the temperature at which samples composed of conventional α-Si_3N_4 powder complete their basic chemical reactions. This would allow differences in reaction rates and phase and microstructural development to be observed. The 1800°C temperature was utilised in order to examine densification behaviour, crystalline phase assemblages and microstructures of densified samples. Additional samples of 3019_{α} and 3019_{β}, sintered for 1 minute at 1800°C, were fabricated in order to examine microstructural development in the early stages of sintering. All samples were heated at 30°C/min. up to the required isothermal hold temperature, and cooled in the furnace by switching off the power after sintering.

6.3.2 Crystalline Phase Assemblages of Samples Made with Different Si_3N_4 Powders

Each of the three base compositions, 2014, 3019, and 3622, was made in three variations; with only α-Si_3N_4, with only β-Si_3N_4, and with an equal mix of the two Si_3N_4 powders. This made a total of nine compositions for the investigation. Crystalline phase assemblages of the nine compositions sintered for 4 hours at each of the two temperatures investigated, 1550°C and 1800°C, were determined by XRD. They are listed in Tables 6.5 and 6.6 respectively.

The substitution of β-Si_3N_4 for α-Si_3N_4 did not have a significant effect on the phase assemblages of the compositions sintered at 1550°C for 4 hours. The XRD data in Table 6.5 reveals that no changes in the product phases occurred in any of the three compositions, though some small differences in the proportions of phases were apparent.

Table 6.5. Crystalline phase assemblages of samples held at 1550°C for 4 hours.

Sample	Crystalline Phases		
	α-sialon	AlN	β-Si_3N_4
2014_{α}	vs	tr	
$2014_{\alpha\text{-}\beta}$	vs	vw	tr
2014_{β}	vs	vw	vw
3019_{α}	vs	mw	
$3019_{\alpha\text{-}\beta}$	vs	mw	
3019_{β}	vs	w	
3622_{α}	vs	ms	
$3622_{\alpha\text{-}\beta}$	vs	ms	
3622_{β}	vs	m	

(where w = weak, m = medium, s = strong, v = very, tr = trace for XRD peak intensity)

Table 6.6. Crystalline phase assemblages of samples held at 1800°C for 4 hours.

Sample	Crystalline Phases			
	α-sialon	AlN	$2H^{\delta}$	33R
2014_{α}	vs			
$2014_{\alpha\text{-}\beta}$	vs			
2014_{β}	vs			
3019_{α}	vs	tr	w	vw
$3019_{\alpha\text{-}\beta}$	vs		w	vw
3019_{β}	vs		mw	w
3622_{α}	vs	ms		
$3622_{\alpha\text{-}\beta}$	vs	mw		
3622_{β}	vs	tr	w	w

(where w = weak, m = medium, s = strong, v = very, tr = trace for XRD peak intensity)

One significant observation made in regard to these samples was the detection of some unreacted β-Si_3N_4 in both the $2014_{\alpha\text{-}\beta}$ and 2014_{β} compositions sintered at 1550°C. No unreacted α-Si_3N_4 was detected in any of the 2014 samples sintered at this temperature

for 4 hours. XRD spectra obtained from these three samples are displayed in Figure 6.12. This observation was important, as it indicated that β-Si_3N_4 was reacting more slowly than α-Si_3N_4 at 1550°C.

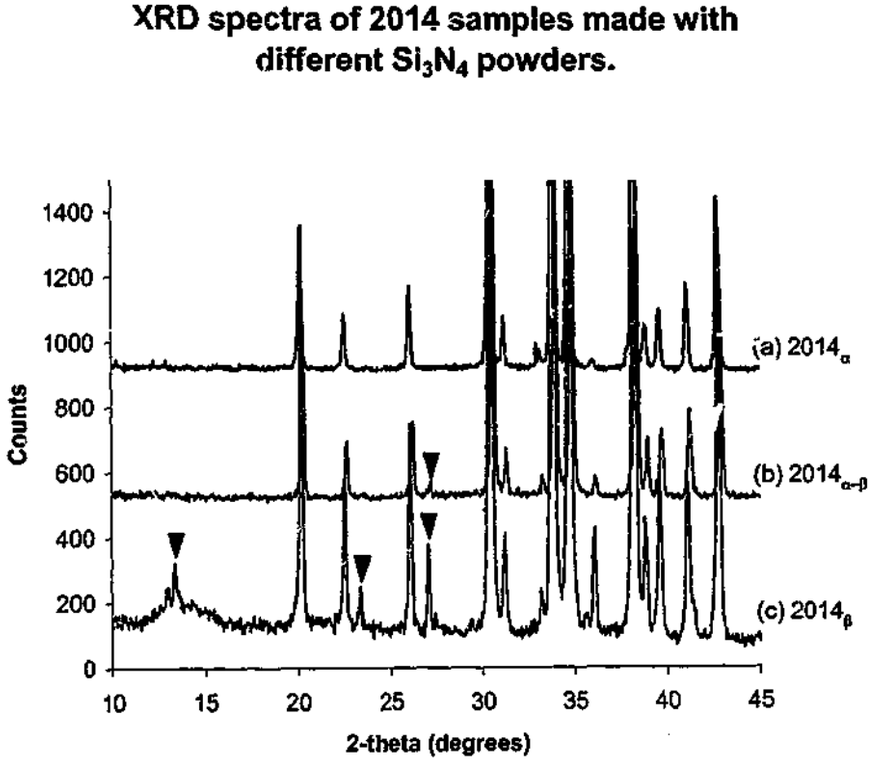

Figure 6.12. XRD spectra obtained from samples of composition 2014 made with (a) only α-Si_3N_4, (b) an equal weight mix of α-Si_3N_4 and β-Si_3N_4, and (c) only β-Si_3N_4. Samples were sintered at 1550°C for 4 hours. Peaks attributable to β-Si_3N_4 are marked. All other peaks can be assigned to α-sialon and AlN.

Further evidence of the slower reaction of β-Si_3N_4 was found when two 3019 compositions, one made with only α-Si_3N_4 and one with β-Si_3N_4, were sintered for 1 minute at 1800°C. Phase analysis data, listed in Table 6.7, reveals that the sample made with α-Si_3N_4 powder had no unreacted Si_3N_4 material after 1 minute at 1800°C. Contrasting this, the sample made with β-Si_3N_4 still exhibited unreacted β-Si_3N_4. XRD spectra obtained from these two samples are displayed in Figure 6.13. These samples further demonstrate that in identical compositions, α-Si_3N_4 reacts faster than β-Si_3N_4 under the same sintering conditions. These observations are consistent with work reported by Rosenflanz and Chen (1999). They found that the β-Si_3N_4 → α-sialon

transformation occurs at a slower rate than the α-$Si_3N_4 \rightarrow \alpha$-sialon transformation. This difference was attributed to the increased thermodynamic stability of β-Si_3N_4 creating a reduced driving force for the β-$Si_3N_4 \rightarrow \alpha$-sialon transformation.

Table 6.7. Crystalline phase assemblages of 3019 samples made with different Si_3N_4 powders, held at 1800°C for 1 minute.

Sample	Crystalline Phases			
	α-sialon	AlN	α-Si_3N_4	β-Si_3N_4
3019_α	vs	mw		
3019_β	vs	m		vw

(where w = weak, m = medium, s = strong, v = very, tr = trace for XRD peak intensity)

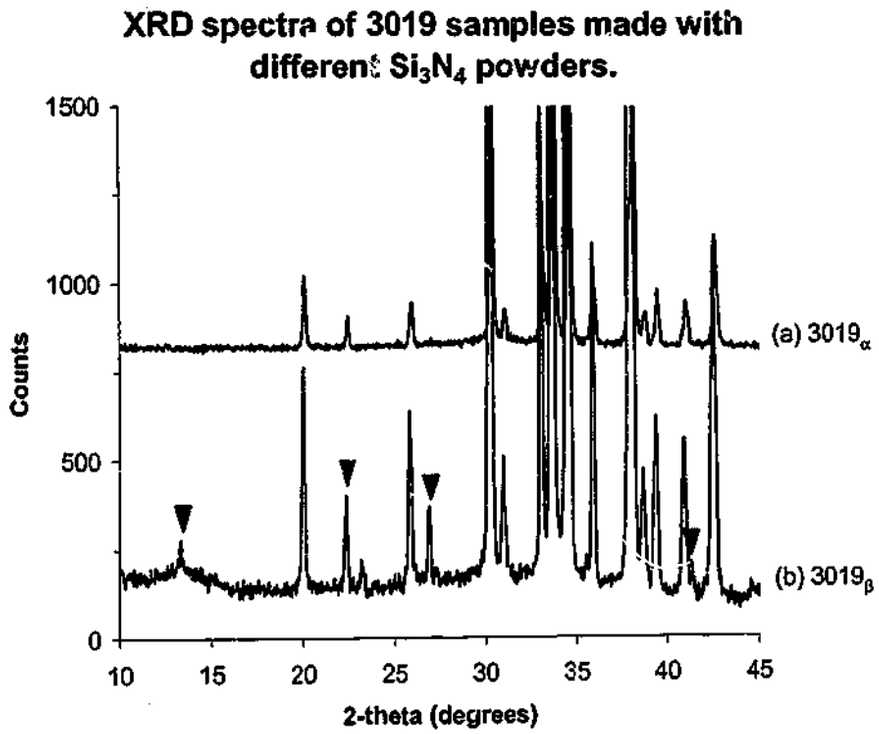

Figure 6.13. XRD spectra obtained from samples of composition 3019 made with (a) only α-Si_3N_4 and (b) only β-Si_3N_4. Samples were sintered at 1800°C for 1 minute. Peaks attributable to β-Si_3N_4 are marked. All other peaks can be assigned to α-sialon and AlN.

The phase assemblages of the compositions sintered at 1800°C for 4 hours were affected to a small degree by the substitution of α-Si_3N_4 with β-Si_3N_4. The XRD data presented in Table 6.6 shows that some small variations in the phase assemblages occurred. The most significant difference occurred in 3622_β, which contained AlN, $2H^\delta$ and 33R AlN-polytypoids. This differed from the other two 3622 compositions, which only exhibited AlN.

The lack of any major differences in the crystalline phase assemblages of compositions made with α-Si_3N_4 and β-Si_3N_4 was consistent with the fact that α-Si_3N_4 and β-Si_3N_4, though structurally different, are chemically identical. Therefore, products of the reactions that take place during sintering should be approximately the same in a given composition. Despite this, some variations in the XRD data were apparent, and these need to be accounted for.

Looking at the XRD data obtained from samples sintered at both 1550°C and 1800°C (Table 6.5 and 6.6), it can be seen that for the 3019 and 3622 compositions, AlN appeared to have dissolved at a more rapid rate in the β-Si_3N_4-based samples compared to that in the samples made using only α-Si_3N_4. The increased reactivity of AlN in the β-Si_3N_4-based samples is believed to be a result of the higher thermodynamic stability of β-Si_3N_4 relative to α-Si_3N_4. Earlier results have shown that in a conventional α-Si_3N_4-based Ca-Si-Al-O-N composition, α-Si_3N_4 reacts rapidly, while AlN requires higher temperatures and longer holding times to fully react. This occurs because α-Si_3N_4, being the low temperature form of Si_3N_4, is relatively unstable at elevated temperatures. When β-Si_3N_4 replaces α-Si_3N_4, a different set of conditions arises. β-Si_3N_4, being the high temperature form of Si_3N_4, is more stable at elevated temperatures. The increased stability of β-Si_3N_4 appears to cause AlN to become more reactive, and consequently, AlN dissolves at a faster rate in the β-Si_3N_4-based compositions than in the α-Si_3N_4-based compositions.

6.3.3 Densification of Samples Made With Different Si_3N_4 Powders

The substitution of β-Si_3N_4 for α-Si_3N_4 was found to have a very significant effect on the densification of the three Ca-Si-Al-O-N compositions. Figure 6.14 is a plot of

density as a function of the β:(α+β) ratio for the three base compositions sintered for 4 hours at 1550°C. This is the temperature at which a significant increase in density typically occurs in samples made from α-Si_3N_4, a result of the melting of the intermediate gehlenite phase that typically forms in these compositions.

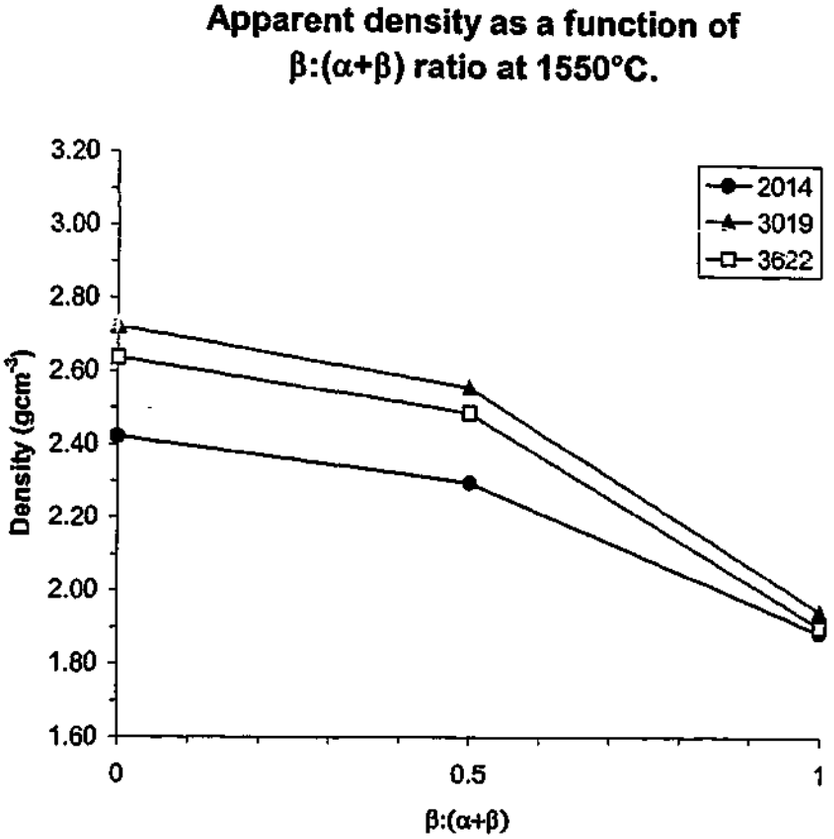

Figure 6.14. Apparent density as a function of β:(α+β) ratio for samples held at 1550°C for 4 hours.

This data reveals a clear trend of decreasing density with increasing β-Si_3N_4 content. The samples made with the α:β combination exhibited only a slightly lower density than the samples made using only α-Si_3N_4. Relative to maximum density, these samples were on average 5% lower in density. The effect on densification that resulted from using only β-Si_3N_4 powder was far more dramatic. After 4 hours at 1550°C, these samples barely increased their densities above that of green bodies, with densities lying in the range 1.889 – 1.948 gcm^{-3}. Comparing to equivalent samples made using α-Si_3N_4, these samples were lower in relative density by an average of 21%.

It can be seen in Figure 6.14 that the spread of density values is much narrower in the three pure β-Si_3N_4 samples comparing to the samples that contain α-Si_3N_4. This is attributable to the fact that almost no densification has occurred in the pure β-Si_3N_4 samples. The wider spread of densities for the pure α-Si_3N_4 samples and the α-β mix samples results from the fact that significant liquid phase densification has taken place in these samples, and that this densification proceeds at different rates depending on composition m and n-values.

Density data obtained from the same compositions sintered at 1800°C for 4 hours yielded similar trends. Figure 6.15 is a plot of density as a function of β:(α+β) ratio for the three base compositions sintered for 4 hours at 1800°C.

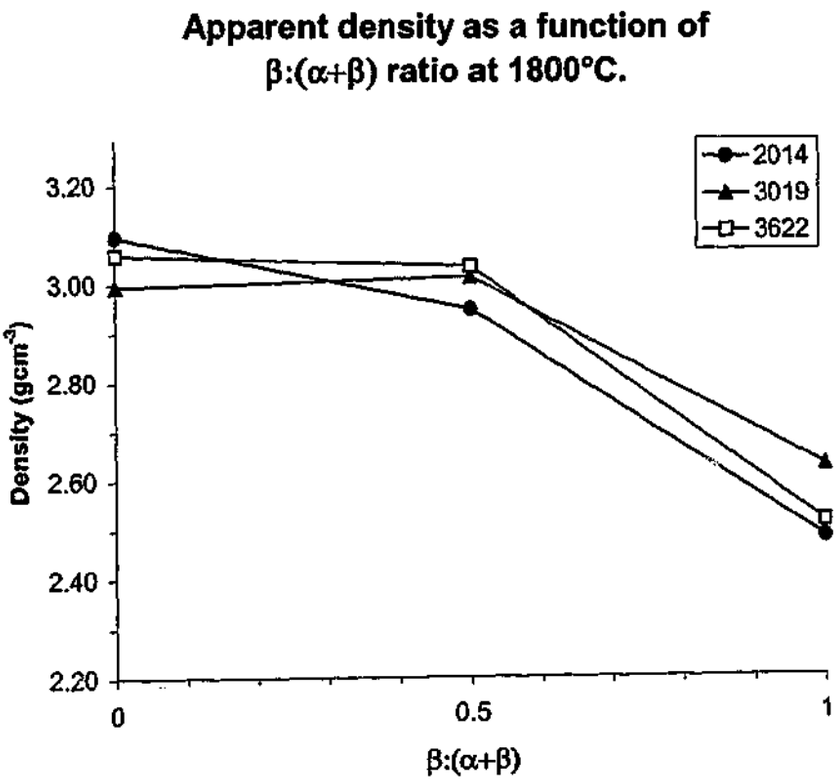

Figure 6.15. Apparent density as a function of β:(α+β) ratio for samples held at 1800°C for 4 hours.

This data clearly shows that the samples made with only β-Si_3N_4 suffered from significantly hindered densification. These samples exhibited relative densities that on

average, were 15% lower than equivalent samples made using α-Si_3N_4. The samples made with a 50:50 α:β ratio exhibited densities comparable to samples made using only α-Si_3N_4. The density of $2014_{\alpha-\beta}$ was slightly lower, while the densities of $3019_{\alpha-\beta}$ and $3622_{\alpha-\beta}$ were fractionally higher. Apparently, a 50 wt.% substitution of β-Si_3N_4 in place of α-Si_3N_4 had a negligible effect on the final density of the materials, whereas completely substituting α-Si_3N_4 with β-Si_3N_4 had a drastic effect. As Figure 6.15 shows, all of the samples made using only α-Si_3N_4 or the α-β mix attained densities in the range 92%–96% of maximum density. The samples fabricated from only β-Si_3N_4 powder were only able to achieve densities in the range 77%–82% of maximum density.

The poor densification of samples made with β-Si_3N_4 can be partly attributed to the higher thermodynamic stability of β-Si_3N_4 relative to α-Si_3N_4. As previously mentioned, work by Rosenflanz and Chen (1999) found that because of the increased thermodynamic stability of β-Si_3N_4, the β-Si_3N_4 → α-sialon transformation occurs at a slower rate than the α-Si_3N_4 → α-sialon transformation. Furthermore, the present work also found evidence for the slower reaction of β-Si_3N_4 relative to α-Si_3N_4, as is described in Section 6.3.2. It is this slower reaction of β-Si_3N_4 that is a cause of the hindered densification observed in the β-Si_3N_4-based samples.

The reaction sintering of Ca-Si-Al-O-N compositions involves the dissolution of raw materials into a transient liquid phase. As some intergranular phase remains in the densified samples, the term transient is not strictly accurate for these compositions. However, a significant proportion of the liquid can be considered transient. The liquid phase facilitates the densification of the sample, while at the same time, product phases such as α-sialon precipitate out of the liquid. The precipitation of crystalline phases gradually consumes a proportion of the liquid phase as sintering proceeds.

The sintering of Ca-Si-Al-O-N materials relies on the liquid phase to facilitate densification. An adequate amount of liquid needs to be present, otherwise full density cannot be achieved through pressureless sintering. This difficulty has been observed in low m-value Ca-Si-Al-O-N compositions that generate only a small amount of liquid phase and cannot be fully densified by pressureless sintering (Hewett et al. 1998a).

It is believed that relative to α-Si_3N_4, the slower dissolution rate of β-Si_3N_4 may reduce the amount of liquid phase available to assist densification in the early stages of sintering. During reaction, starting materials dissolve into the liquid phase, while concurrently, crystalline phases precipitate out of the liquid. As β-Si_3N_4 dissolves more slowly than α-Si_3N_4, it is likely that the volume of liquid phase present at any given time is less in a β-Si_3N_4-based sample, comparing to an α-Si_3N_4-based sample. Consequently, there is not an adequate quantity of the transient liquid phase present to facilitate full densification. The fact that the reduction in the volume of liquid phase occurs in the early stages of sintering, when β-Si_3N_4 is not yet completely dissolved, is critical. As Figure 6.6 shows, the majority of densification during the pressureless sintering of Ca-Si-Al-O-N compositions takes place in the period up to the first 30 minutes at 1800°C. This occurs because for most of this period, grain sizes are quite small, typically less than 1 – 2 μm, and the liquid phase is at a relatively low viscosity. This small grain size allows densification via the particle rearrangement mechanism to proceed rapidly. Beyond 30 minutes, significant grain growth of both α-sialon and AlN-polytypoid phases occurs, making particle rearrangement difficult because of the awkward grain morphologies.

This work suggests that the amount of liquid phase present is most critical in the initial stages of sintering, when grain sizes are small. This is when particle rearrangement contributes significantly to densification. If the amount of liquid is reduced, such as by using a starting powder that dissolves more slowly, densification becomes hindered in this early stage of sintering, and full densification is unable to be attained by pressureless sintering.

To further investigate the poor densification that resulted from using β-Si_3N_4 in place of α-Si_3N_4, the microstructures of polished and etched samples were examined using SEM.

6.3.4 Microstructural Characterisation of Samples Made with Different Si_3N_4 Powders

Work presented earlier has shown that 1550°C represents the temperature at which raw materials are completely converted to product phases over a number of hours. The XRD

data in Table 6.5 confirms that this was the case in this section of work. Except for $2014_{\alpha-\beta}$ and 2014_{β}, no Si_3N_4 raw material was detected in any of the samples. In the case of $2014_{\alpha-\beta}$ and 2014_{β}, small amounts of unreacted β-Si_3N_4 were detected. Work in Section 6.2 has shown that grain growth over 4 hours at 1550°C is negligible in typical Ca-Si-Al-O-N compositions. Consequently, these samples can provide significant information concerning the nucleation and growth of α-sialon in these β-Si_3N_4-based compositions.

Figures 6.16(a and b) are micrographs of $2014_{\alpha-\beta}$ and $3622_{\alpha-\beta}$ sintered for 4 hours at 1550°C. Some clear differences exist between these samples and those fabricated with only α-Si_3N_4 powder. The α-sialon grains in these samples are noticeably larger than the sub-micron grains typically found in the α-Si_3N_4-only samples sintered under the same conditions (cf. Figures 6.3(b) and 6.4(b)). Grain sizes up to 2 μm in size were frequently observed. Many grains were also observed with a definite acicular morphology, whereas the grains in the α-Si_3N_4 only samples were typically equiaxed or only slightly elongated. It is apparent that a degree of grain growth has occurred in these samples that was not apparent in the α-Si_3N_4-only samples.

Figures 6.17(a and b) are micrographs of the same two base compositions, this time fabricated using only β-Si_3N_4 powder. Very apparent features in these microstructures are the porous nature of the samples, and the extensive α-sialon grain growth that has occurred, especially in 3622_{β}. α-Sialon grains were smaller in the 2014_{β} composition, ranging in size from 1 to 2 μm. In 3622_{β} they were significantly larger and clearly elongated, with sizes ranging from 2 to 5 μm. This type of grain growth was quite abnormal at 1550°C. Typically, α-sialon grains in an α-Si_3N_4-based composition are no larger than 1 μm after 4 hours at 1550°C. Little grain growth occurs until higher temperatures are reached. Clearly, the use of β-Si_3N_4 in place of α-Si_3N_4 has a significant effect on the nucleation and growth kinetics of α-sialon.

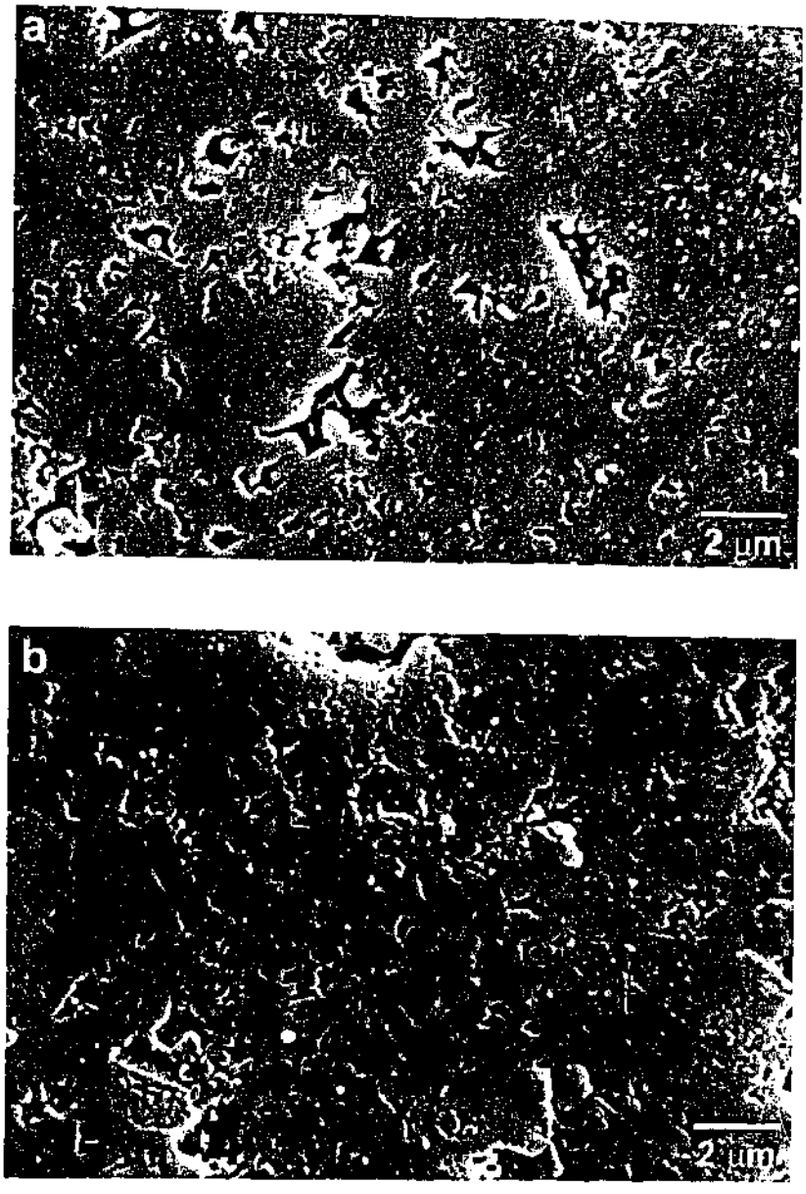

Figure 6.16 Secondary electron micrographs obtained from polished and etched samples of (a) $2014_{\alpha\text{-}\beta}$ and (b) $3622_{\alpha\text{-}\beta}$ sintered for 4 hours at 1550°C.

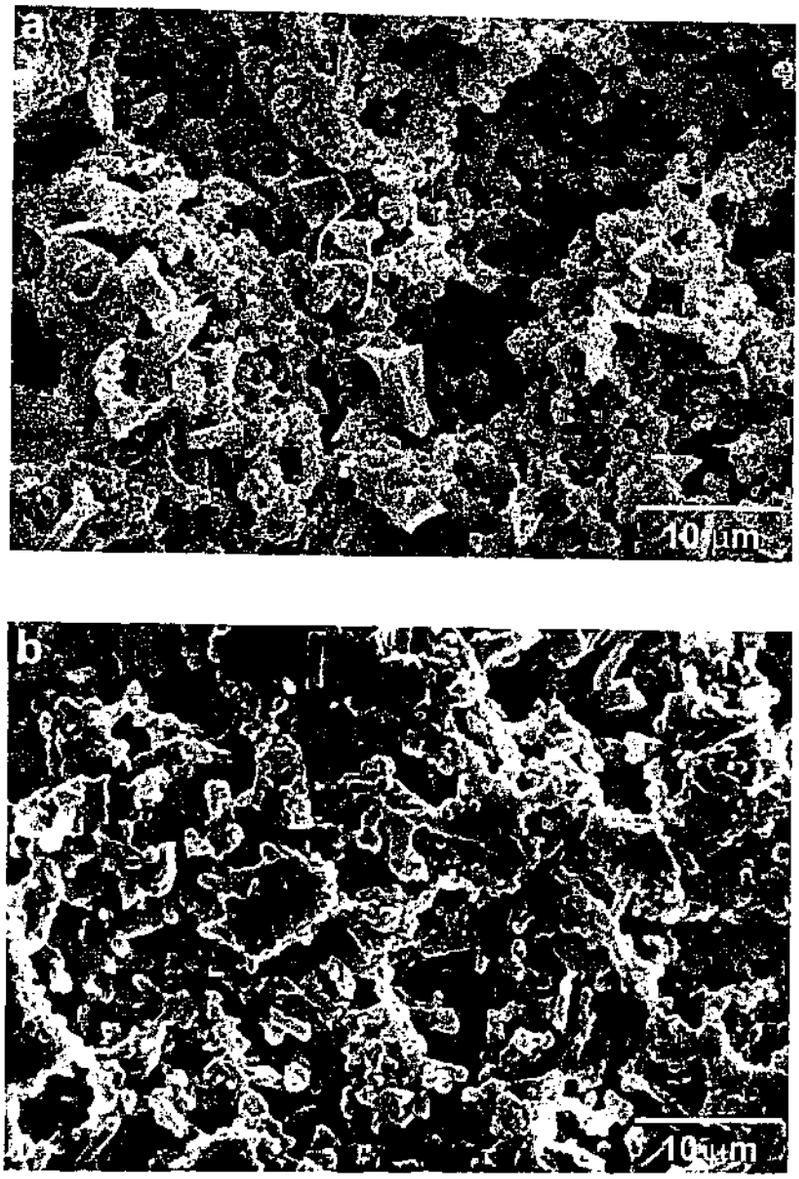

Figure 6.17 Secondary electron micrographs obtained from polished and etched samples of (a) 2014_{β} and (b) 3622_{β}, sintered for 4 hours at 1550°C.

A similar effect was observed in samples sintered for 1 minute at 1800°C. Figures 6.18(a and b) are SEM micrographs of two 3019 samples, one made with α-Si_3N_4 and one with β-Si_3N_4. These micrographs are effectively a snapshot of microstructural development in the early stages of sintering. Comparing these two samples, it is evident that the α-sialon grains in the sample made with β-Si_3N_4, Figure 6.18(a), are significantly larger than the grains in the sample made with α-Si_3N_4, Figure 6.18(b). Clearly, grain growth has proceeded at an unusually high rate in the β-Si_3N_4-based sample. Some grains of unreacted β-Si_3N_4 are indicated in Figure 6.18(a).

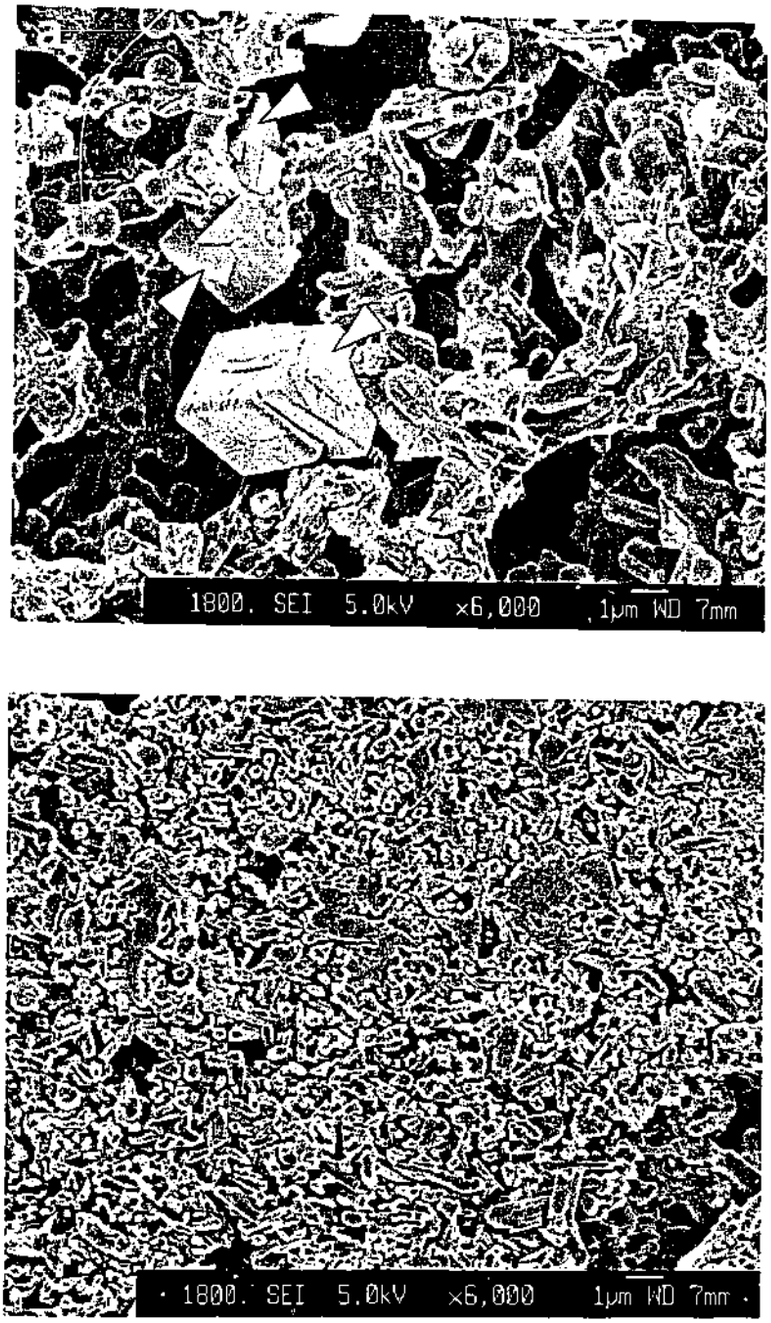

Figure 6.18. Secondary electron micrographs obtained from polished and etched samples of (a) 3019_{β} and (b) $3019_{\alpha s}$ sintered for 1 minute at 1800°C. Some unreacted grains of β-Si_3N_4 are arrowed in (a).

This series of SEM micrographs indicates that the type of Si_3N_4 powder used in the processing of Ca α-sialon materials plays an important role in grain growth, especially with regard to lower temperatures and short sintering times. Micrographs of samples

show that α-sialon grain growth is accelerated in samples made with β-Si_3N_4, relative to samples made with α-Si_3N_4.

This accelerated α-sialon grain growth can be attributed to the mechanism of α-sialon nucleation. α-Sialon has previously been shown to epitaxially nucleate on α-Si_3N_4 grains (Hwang and Chen 1994). This means that when a sample is made using α-Si_3N_4, a very high density of potential α-sialon nucleation sites exists. Earlier work in this chapter has shown that the conversion of α-Si_3N_4 to α-sialon occurs rapidly in Ca α-sialon compositions.

Typically, complete conversion has taken place by the time a sample has reached 1800°C. A result of this is that in the early stages of microstructural evolution, following the conversion of α-Si_3N_4 to α-sialon, a high density of small α-sialon grains are present in the sample microstructure. This is evident in Figures 6.7(b) and 6.9(b).

Though they are chemically identical, substituting α-Si_3N_4 with β-Si_3N_4 in a composition has the effect of reducing the number of available α-sialon nucleation sites per unit volume. If only β-Si_3N_4 is used, then only the small fraction of α-Si_3N_4 in the β-Si_3N_4 raw material will act as heterogeneous nucleation sites for α-sialon. This situation is the cause of the considerably different microstructures that result when identical compositions made with α-Si_3N_4 and β-Si_3N_4 exhibit drastically different microstructures.

During sintering at 1550°C, thermodynamics dictate that Si_3N_4 and other starting powders will dissolve, and α-sialon will precipitate. In an α-Si_3N_4-based composition, the myriad of α-Si_3N_4 particles all act as potential nucleation sites for α-sialon. The result is that when the conversion of α-Si_3N_4 to α-sialon has completed, the α-sialon is present as a large number of small grains. Significant grain growth does not occur until temperatures in the range of 1700°C to 1800°C. At these temperatures, grain growth proceeds by an Ostwald ripening-type mechanism, in which smaller grains are consumed and larger grains grow.

A very different situation arises when β-Si_3N_4 powder is used in place of α-Si_3N_4. The β-Si_3N_4 powder contains a certain amount of α-Si_3N_4 impurity, in this case 6.1 wt.%. This provides the β-Si_3N_4-based compositions with only a small fraction of the α-sialon nucleation sites found in an α-Si_3N_4-based composition. α-Sialon will initially precipitate on the few α-Si_3N_4 particles. However, because of a shortage of suitable nucleation sites, further α-sialon precipitation facilitates growth of the relatively few nucleated α-sialon grains. The overall effect of this is that in the early stages of sintering, where the α-Si_3N_4-based composition forms a microstructure made up of tiny sub-micron α-sialon grains, the β-Si_3N_4-based composition develops a microstructure of relatively large, elongated α-sialon grains. Consequently, significant development of elongated α-sialon grain growth is observed at temperatures that would not normally produce any significant grain growth in an α-Si_3N_4-based composition.

This indicates that elongated α-sialon grain growth may actually occur by two different mechanisms. When abundant α-sialon nucleation sites exist in a sample, elongated α-sialon growth proceeds by an Ostwald ripening-type mechanism, whereby fine α-sialon grains formed in the early stages of sintering grow at the expense of other fine α-sialon grains formed in the early stages of sintering. When few α-sialon nucleation sites exist, such as in a sample made with β-Si_3N_4, elongated grain growth occurs by direct solution-precipitation, whereby raw materials dissolve and elongated α-sialon is directly precipitated.

As the data in Figure 6.15 shows, completely replacing α-Si_3N_4 with β-Si_3N_4 had a dramatic effect of sample densification. One of the factors causing this is believed to be the increased thermodynamic stability of β-Si_3N_4 relative to α-Si_3N_4, and its effect on liquid phase generation. This is detailed in section 6.3.3. In addition to this, another factor may contribute to the hindered densification of β-Si_3N_4-based samples.

Particle rearrangement is the most prominent densification mechanism in the sintering of α-sialons (Menon and Chen 1995b). In relative terms, the rearrangement of small, equiaxed grains will proceed more easily than that of larger, needle-shaped grains. In Ca-Si-Al-O-N samples made using α-Si_3N_4, the majority of densification occurs in the

early stages of sintering, before significant grain growth has taken place. The small, equiaxed α-sialon grains and particles of partially dissolved starting powder allow for easy particle rearrangement and thus, densification proceeds rapidly.

In the case of samples made using β-Si_3N_4, this work has shown that significant α-sialon grain growth takes place in the early stages of sintering. Because this grain growth is anisotropic, the fast growing elongated grains form an interlocked network, instead of a close-packed arrangement of many fine, equiaxed grains normally observed in an α-Si_3N_4-based sample. This is clear in Figure 6.18(a). This type of microstructure would be much more difficult to densify via particle rearrangement than one made up of tiny sub-micron α-sialon nuclei, a result of the increasingly awkward α-sialon grain morphology. Furthermore, liquid phase would tend to be trapped within the network of elongated grains, preventing the liquid phase from being evenly distributed through the sample. Clearly, these rapidly developed, elongated grain morphologies could have a deleterious effect on densification.

SEM micrographs of the microstructures of 2014 and 3622 samples fabricated from the α-β Si_3N_4 mix and sintered for 4 hours at 1800°C are displayed in Figure 6.19. These microstructures appear very similar to Ca-Si-Al-O-N samples made with α-Si_3N_4, exhibiting good density and a homogeneous distribution of crystalline and amorphous phases. Clearly, the final microstructures are generally unaffected by the partial substitution of α-Si_3N_4 with β-Si_3N_4. This was consistent with the density and phase assemblage data obtained from the samples, which were also unaffected by the substitution.

SEM micrographs of the β-Si_3N_4-based samples, sintered for 4 hours at 1800°C, show that the complete substitution of α-Si_3N_4 for β-Si_3N_4 had a very significant effect on microstructural development. Figure 6.20 and 6.21 show SEM micrographs obtained from the 2014_β and 3622_β samples sintered at 1800°C, respectively. The microstructures of these two samples are considerably different from the samples fabricated with only α-Si_3N_4. The low magnification micrographs (Figures 6.20(a) and 6.21(a)) show extensive distributions of porosity in the microstructures of the samples. The pores were very large, with sizes ranging up to 30 to 50 μm. Only small regions of dense material located between pores were apparent. The extensive distributions of porosity observed

throughout the sample microstructures clearly reflect the poor densities measured for these samples (Figure 6.15). Normally, α-Si_3N_4-based Ca-Si-Al-O-N samples densify to near full density by pressureless sintering with little difficulty. Clearly, the use of β-Si_3N_4 interferes with the normal densification kinetics of the samples.

Figure 6.19. Secondary electron micrographs obtained from polished and etched samples of (a) $2014_{\alpha-\beta}$ and (b) $3622_{\alpha-\beta}$ sintered for 4 hours at 1800°C.

Higher magnification micrographs of dense regions are shown in Figures 6.20(b) and 6.21(b). In sample 3622_{β}, the distribution of phases appeared to be quite inhomogeneous. Though this is not very clear in Figure 6.21(b), observations of larger

areas of the sample found that AlN-polytypoid grains were often formed in large agglomerates, rather than being evenly distributed throughout the microstructure as is typical for Ca-Si-Al-O-N samples made with α-Si_3N_4. A group of AlN-polytypoid plates is indicated in Figure 6.21(b).

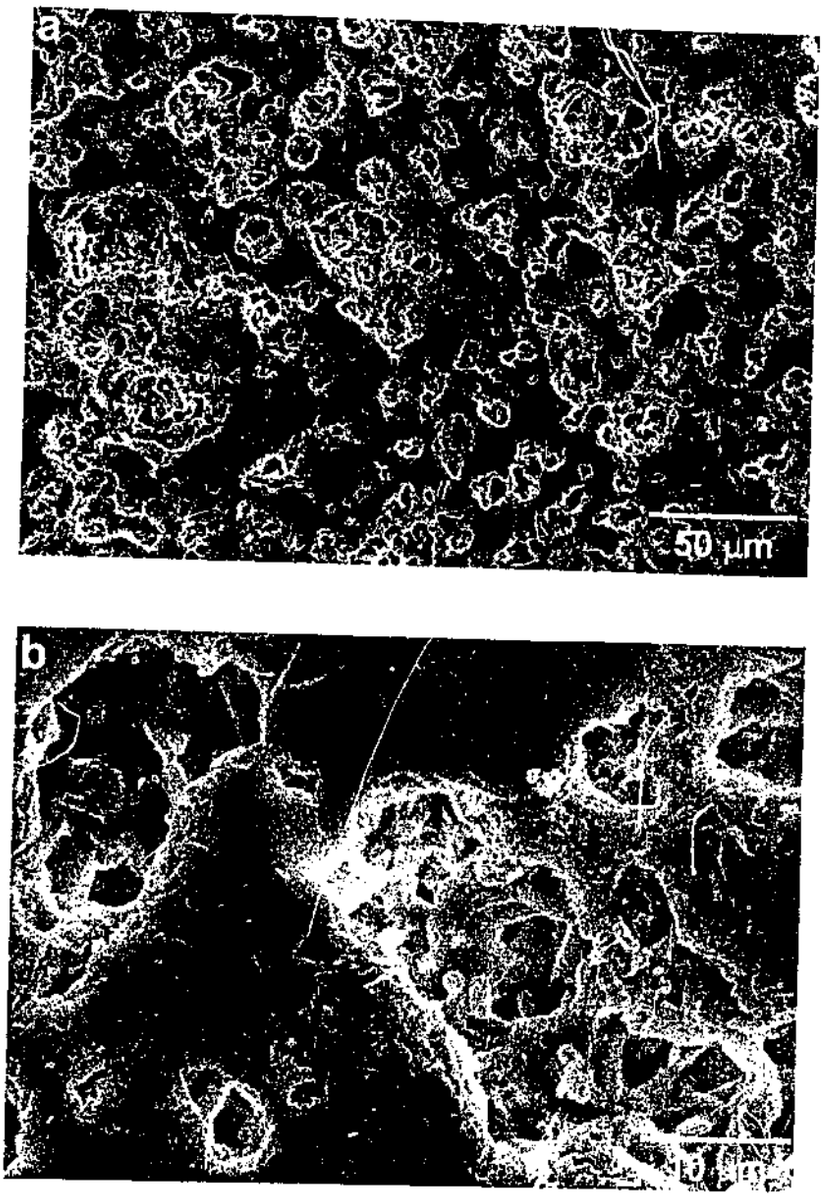

Figure 6.20. Secondary electron micrographs obtained from a polished and etched sample of 2014_β sintered for 4 hours at 1800°C.

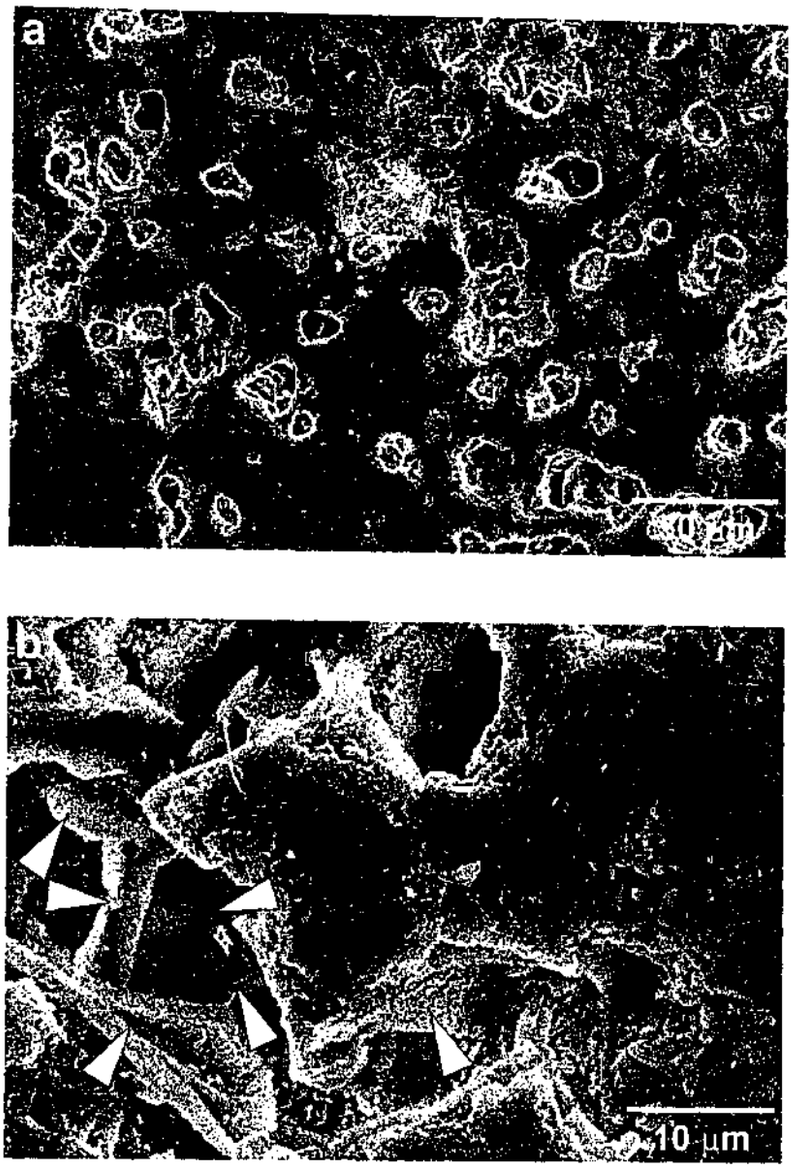

Figure 6.21. Secondary electron micrographs obtained from a polished and etched sample of 3622_β sintered for 4 hours at 1800°C. A cluster of $2H^\delta$ polytypoid plates is arrowed in (b).

The previous sub-section on densification (Section 6.3.3) described two factors that possibly contribute to the hindered densification of β-Si_3N_4-based samples. The first was the higher thermodynamic stability of β-Si_3N_4 relative to α-Si_3N_4, which reduced the volume of available liquid phase. The second was the rapid evolution of elongated α-sialon grains, which would be more difficult to densify via a particle rearrangement mechanism. These micrographs show that this combination of factors combine to prevent massive particle rearrangement from eliminating large-scale porosity in the

samples. As previously mentioned, the interlocked elongated α-sialon grains that rapidly form in β-Si_3N_4-based samples leave relatively large voids between the grains. It is possible that liquid phase becomes trapped in these voids, preventing liquid from being distributed throughout the sample. This causes only smaller pores to be removed. Even over extended sintering times, the distribution of liquid phase is such that the larger pores that originate in the green body cannot be eliminated. In a sample fabricated from α-Si_3N_4, the intergranular voids around the fine, equiaxed α-sialon grains are small. This allows liquid phase to be distributed throughout the sample when the viscosity of the liquid reduces or the volume of liquid increases with temperature, and densification proceeds rapidly.

The apparently inhomogeneous distribution of AlN-polytypoid phases in 3622_β is further evidence that the distribution of liquid phase is poor. An adequate distribution of liquid phase would allow for the dissolution of AlN and the even distribution of its components throughout the sample. The agglomerates of polytypoid phase indicate that the volume of liquid phase produced in the sample has not been adequate to properly dissolve and distribute the raw material components, leading to large clusters of AlN-polytypoid phases being observed in the microstructure.

6.3.5 Summary of the Effects of Using Different Starting Powders

The effects of substituting β-Si_3N_4 powder for α-Si_3N_4 in three Ca-Si-Al-O-N compositions were investigated in this section of work. Samples in this study were examined following sintering at temperatures of 1550°C and 1800°C.

At both temperatures, replacing α-Si_3N_4 with β-Si_3N_4 had only a minor effect on the crystalline phase assemblages of the samples. The most important feature of the phase analysis data was the detection of unreacted β-Si_3N_4 in 2014 samples sintered at 1550°C, and in a 3019_β sample sintered for 1 minute at 1800°C. For the same compositions that were formed using α-Si_3N_4, no residual α-Si_3N_4 was found at either of these sintering conditions. These results indicated that β-Si_3N_4 reacts slower than α-Si_3N_4 in equivalent Ca-Si-Al-O-N compositions. AlN was found to be more reactive in β-Si_3N_4-based

compositions than α-Si_3N_4-based compositions. This was attributed to the higher thermodynamic stability of β-Si_3N_4 relative to α-Si_3N_4.

Relative to samples made with only α-Si_3N_4, samples made with the α-β combination attained slightly lower densities when sintered at 1550°C. Densities were approximately equivalent when sintered at 1800°C. Contrasting these results, samples made with only β-Si_3N_4 powder exhibited very poor densification. When sintered at 1550°C, almost no densification took place in the β-Si_3N_4-based samples. At 1800°C, the samples were only able to attain densities in the range 77%–82% of maximum density.

Microstructural observations revealed that the poor measured densities of the β-Si_3N_4-based samples were a result of a distribution of large pores throughout the sample microstructures. This trapped porosity was believed to be attributable to two factors related to the use of β-Si_3N_4. First, using β-Si_3N_4 reduced the amount of liquid phase available for densification in the earlier stages of sintering, by virtue of its higher thermodynamic stability relative to α-Si_3N_4. Second, using β-Si_3N_4 caused accelerated grain growth of α-sialon. The rapid growth of elongated α-sialon grains made densification more difficult as the interlocked elongated grain morphology traps liquid phase in intergranular regions, and the elongated grains are more difficult to arrange during particle rearrangement. The accelerated α-sialon grain growth was attributed to the reduced number of α-sialon nucleation sites in β-Si_3N_4-based compositions.

Further evidence for the poor distribution of liquid phase in the β-Si_3N_4-based samples was observed in the 3622_β composition. In this sample, agglomerates of AlN-polytypoid grains were observed. This indicated that the volume of liquid phase was not sufficient to properly dissolve the raw AlN particles and distribute the raw material components homogeneously throughout the microstructure.

6.4 Effects of Using Different Heating Rates

6.4.1 Experimental Outline

Some recent work on elongated α-sialons has indicated that the nucleation and growth kinetics during sintering are critical to developing elongated α-sialon grains. Some workers (Chen and Rosenflanz 1997) have suggested that the number of α-Si_3N_4 nucleation sites in a composition is an important factor, and needs to be controlled.

Work presented in Chapter 4, and in the present chapter in Section 6.2, indicates that α-sialon has an optimal nucleation temperature somewhere below the optimal grain growth temperature. The conversion of raw materials to product phases in conventional Ca-Si-Al-O-N compositions made with α-Si_3N_4 is generally observed to complete at 1550°C in 4 hours or less. However, grain growth is minimal at this temperature, and does not proceed significantly until temperatures of 1700°C–1800°C are reached.

Based on this information, there exists a possibility that if the maximum nucleation rate temperature range is passed through quickly, a reduced number of α-sialon nuclei will form. By then moving to the optimal grain growth temperature, the lower density of α-sialon nuclei will allow large elongated α-sialon grains to develop with minimal hindrance from impinging on neighbouring grains. Conversely, it is possible that if the sample were held in the optimal nucleation temperature range for an extended period, a higher number of α-sialon nuclei would develop. Upon reaching the optimal grain growth temperature, the high density of α-sialon nuclei would allow only minimal anisotropic grain growth to occur, resulting in equiaxed α-sialon grains.

The time that a sample spends in the optimal nucleation temperature range can be controlled by employing a range of furnace heating rates. A fast heating rate would pass the sample through the nucleation temperature range rapidly, thus causing the sample to develop less α-sialon nuclei. Conversely, a slow heating rate would pass the sample through the nucleation temperature range slowly, allowing more extensive α-sialon nucleation to occur.

The objective of this section of work was to determine what the effects of using different furnace heating rates were on microstructural development. This work investigated a range of furnace heating rates to effectively control the amount of time a sample spent in the optimal nucleation temperature range. It will show what the effect is, if any, of slow or rapid heating rates on microstructural development. The same three Ca-Si-Al-O-N compositions examined in the previous sections of this chapter, 2014, 3019 and 3622, were used in this section of work. Samples were pressureless sintered. Initial furnace heating conditions were 30°C/min. to 1000°C. Once at 1000°C, samples were heated to the isothermal hold temperature of 1800°C at rates of 5°, 10°, 20° or 40°C per minute. They were then held at 1800°C for 4 hours. Samples were cooled in the furnace by switching the power off after sintering. Following densification, samples had their densities measured, their phase assemblages determined by XRD, and their microstructures characterised by SEM. An additional sample of Ca-Si-Al-O-N composition 3618 that had previously been sintered for 4 hours at 1600°C was refired for 4 hours at 1800°C. The microstructure of this sample was characterised by SEM.

6.4.2 Crystalline Phase Assemblages and Densification of Samples Heated at Different Rates

Phase assemblage data obtained by XRD for the 12 densified samples are displayed in Table 6.8. It is clear from the data that for the three compositions under examination, utilising different heating rates from 5°C to 40°C per minute has no detectable effect on the crystalline phases present in the densified samples.

A plot of sample density as a function of furnace heating rate is displayed in Figure 6.22. All samples attained densities within the range 93% to 99% of maximum density. Some small variations in the densities of each of the compositions were apparent. However, there was an absence of any clear overall trend in the densification data of any of the three compositions. This indicates that the different heating rates did not have a noticeable effect on sample density after 4 hours at 1800°C.

Table 6.8. Crystalline phase assemblages of the three compositions sintered for 4 hours at 1800°C, using heating rates of 5°, 10°, 20° and 40°C per minute.

Sample		Crystalline Phases			
		α-sialon	AlN	$2H^{\delta}$	33R
2014	5°/min.	vs			
	10°/min.	vs			
	20°/min.	vs			
	40°/min.	vs			
3019	5°/min.	vs		w	w
	10°/min.	vs		w	w
	20°/min.	vs		w	w
	40°/min.	vs		w	w
3622	5°/min.	vs	ms	tr	
	10°/min.	vs	ms	tr	
	20°/min.	vs	ms	tr	
	40°/min.	vs	ms	tr	

(where w = weak, m = medium, s = strong, v = very, tr = trace for XRD peak intensity)

Small variation in the density of Ca-Si-Al-O-N samples of the same composition, sintered under the same conditions, are common, especially when pressureless sintering is utilised rather than hot-pressing. These variations often arise from defects that are present within the pressed powder compacts. The fact that these samples were relatively small, with typical post-sintered masses of only 3.1 – 3.4 grams, means that a small defect or region of poor densification introduced into the green body can influence the measured density of the sample significantly. The quality of the packing powder used to surround the samples during sintering can also have an effect. Experience showed that fresh packing powder usually assisted in achieving slightly better sample densities than those achieved when previously used packing powder was utilised.

As no distinct trends are present in the densification data of any of the three compositions, it can be concluded that varying the furnace heating rate from 5°C to 40°C/min. had no measurable effect on the densification of the three pressureless sintered Ca-Si-Al-O-N compositions examined.

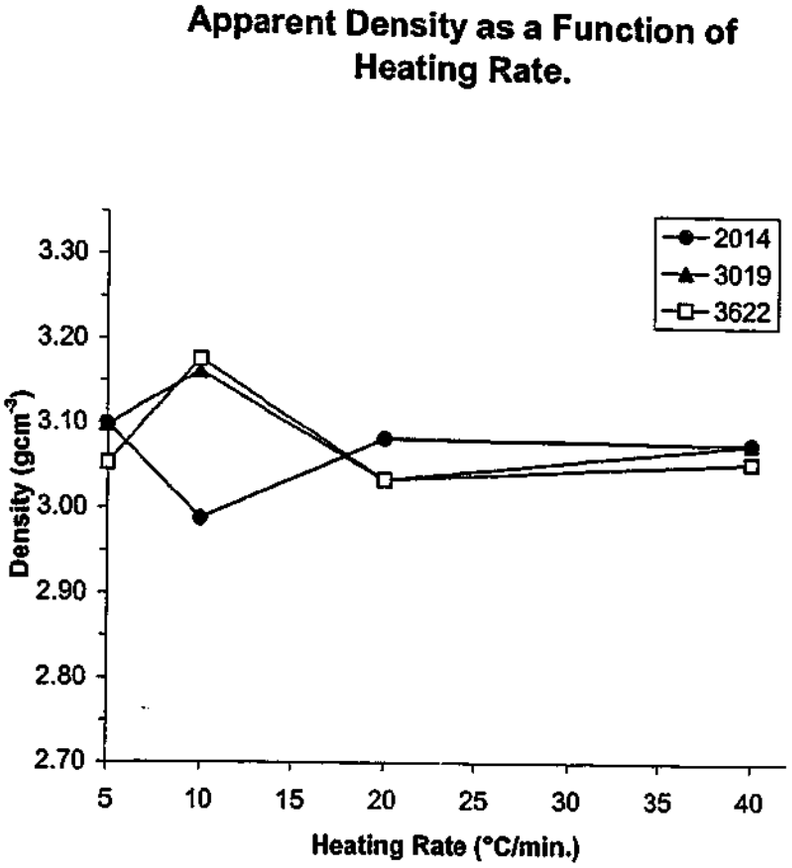

Figure 6.22. Plot of apparent density as a function of heating rate for the three compositions sintered for 4 hours at 1800°C.

6.4.3 Microstructural Characterisation of Samples Heated at Different Rates

Secondary electron micrographs were obtained from the polished and etched samples in order to examine what effect different heating rates had on microstructural development.

The different heating rates did appear to have an effect on microstructural development in some of the compositions. Figures 6.23(a-h) show secondary electron micrographs obtained from 2014 heated at 5°C, 10°C, 20°C and 40°C per minute, followed by a 4 hour isothermal hold at 1800°C. Both low and high magnification micrographs for each sample are shown. According to XRD analyses, α-sialon is the only crystalline phase

detected in these samples, though intermittent grains of AlN/AlN-polytypoid are observed in the microstructures.

Looking at the higher magnification micrographs, it is apparent that the microstructures that developed in this composition were affected by the different heating rates. In the case of the samples heated at 5°C and 10°C/min., shown in Figures 6.23(a-d), many α-sialon grains possessed an equiaxed morphology. Though some elongated grains were present in these microstructures, a significant proportion of α-sialon grains were equiaxed. Many fine, sub-micron, α-sialon grains can be seen in the sample heated at 5°C/min. (Figure 6.23(b)).

These microstructures contrasted the samples heated at 20°C and 40°C/min. (Figure 6.23(e-h)). In these samples, a much greater proportion of α-sialon grains exhibited a high aspect ratio, elongated, grain morphology. Some equiaxed α-sialon grains were still observed in these samples, though many of these would likely be elongated α-sialon grains with their growth directions oriented perpendicular to the sample surface. The equiaxed grains in the lower heating rate samples exhibited an average diameter of ~1 μm. The elongated grains in the higher heating rate samples were typically 2-3 μm in length.

A further difference observed between the 2014 samples was the distribution of intergranular glass and voids in the microstructures. Though the glass has been etched out of these samples, it can be seen that the higher heating rate samples with the elongated grains exhibit relatively large pockets of glass/voids. In contrast to this, the glass pockets/voids in the samples with the equiaxed grains are significant smaller. This observation can be explained by the fact that a microstructure composed mostly of fine equiaxed grains allows a better packing arrangement than one made up of high aspect ratio, elongated grains.

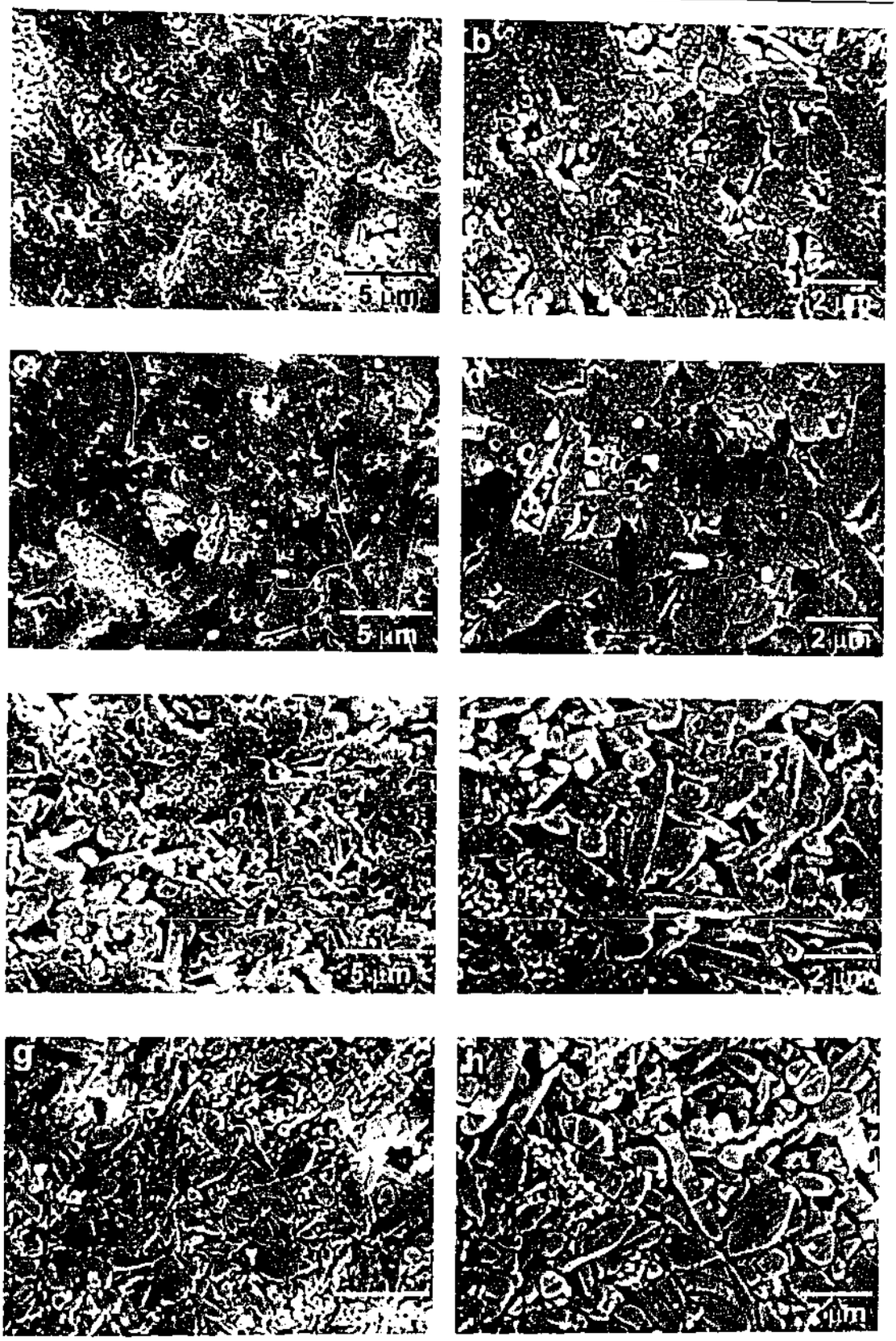

Figure 6.23. Secondary electron micrographs of composition 2014, heated at (a and b) 5°, (c and d) 10°, (e and f) 20° and (g and h) 40°C/min.

Looking at micrographs obtained from the four 3019 samples in Figures 6.24(a-h), it can be seen that the different heating rates had much less effect on microstructural development. All four samples exhibited similar microstructures, with elongated α-sialon being the dominant phase. Differences between the microstructures of the samples heated at 5, 10 and 20°C/min. were negligible. The only significant difference was observed in the sample heated at the highest rate, 40°C/min. Looking at the micrographs from this sample (Figures 6.24(g and h)), it can be seen that this sample has a slightly coarser microstructure. This appearance is mainly a result of larger regions of intergranular glass that are present in this sample.

Micrographs obtained from the 3622 samples, shown in Figures 6.25(a-h), reveal that the different heating rates had no effect on α-sialon development. Differences in α-sialon grain morphologies and the distribution of intergranular glass pockets/voids between the samples were negligible. One difference that is visible between these samples is the apparent tendency for AlN to form larger agglomerates in the rapidly heated samples. The large, equiaxed agglomerates, typically 5 to 7 μm in diameter, are easily distinguished in the micrographs of the samples heated at 20°C and 40°C per minute (Figures 6.25(e-h)). The cause of this is unknown. It is possible that rapid heating rates do not give the sample enough time to dissolve and distribute the AlN before the sample densifies. This could trap partially dissolved agglomerates of raw AlN powder that then cannot be easily removed from the microstructure. When a slower heating rate is utilised, the sample has adequate time to dissolve the AlN and distribute the components homogeneously throughout the sample. This could account for the lack of these large agglomerates in the samples sintered at 5°C and 10°C per minute (Figures 6.25(a-d)).

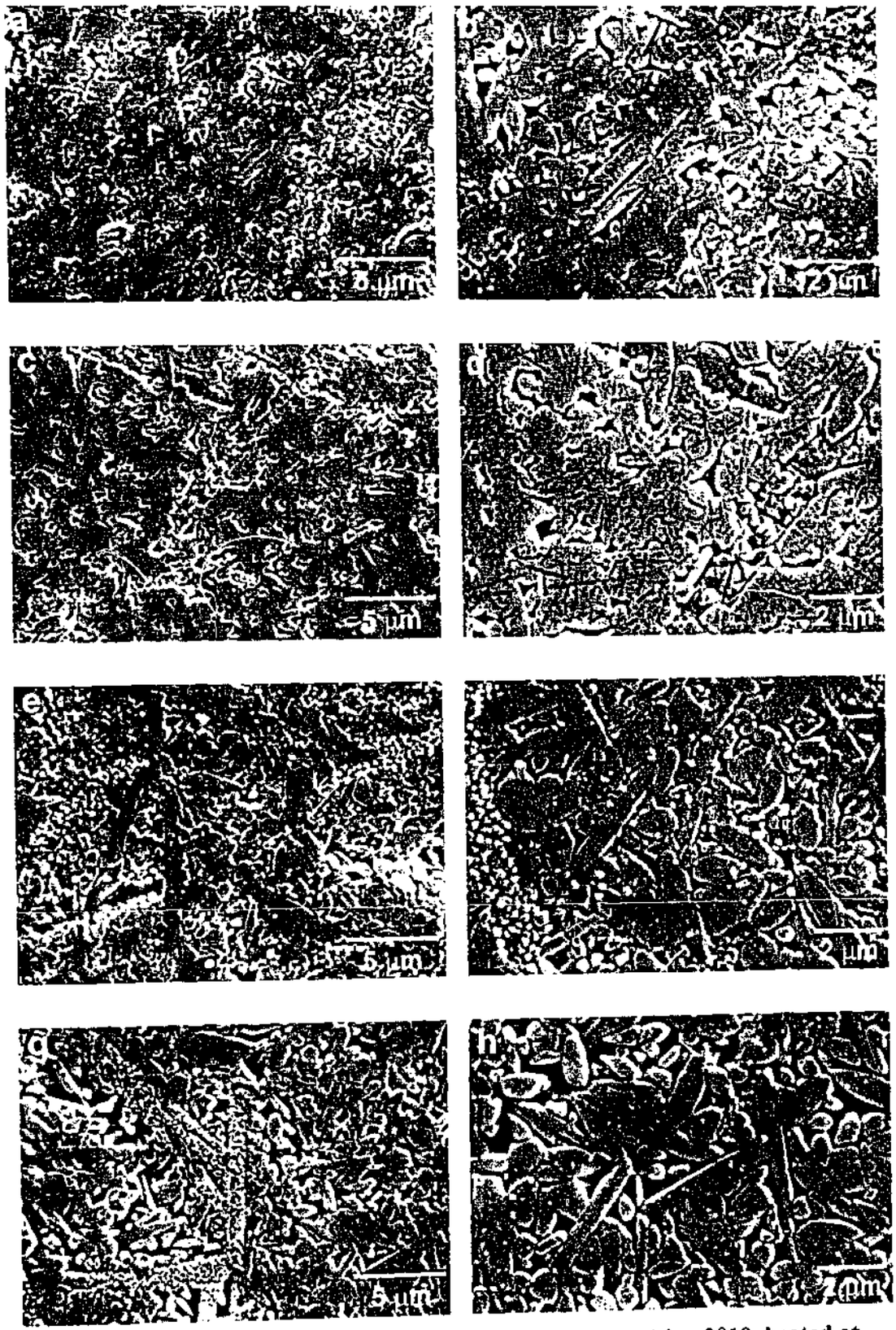

Figure 6.24. Secondary electron micrographs of composition 3019, heated at (a and b) 5°, (c and d) 10°, (e and f) 20° and (g and h) 40°C/min.

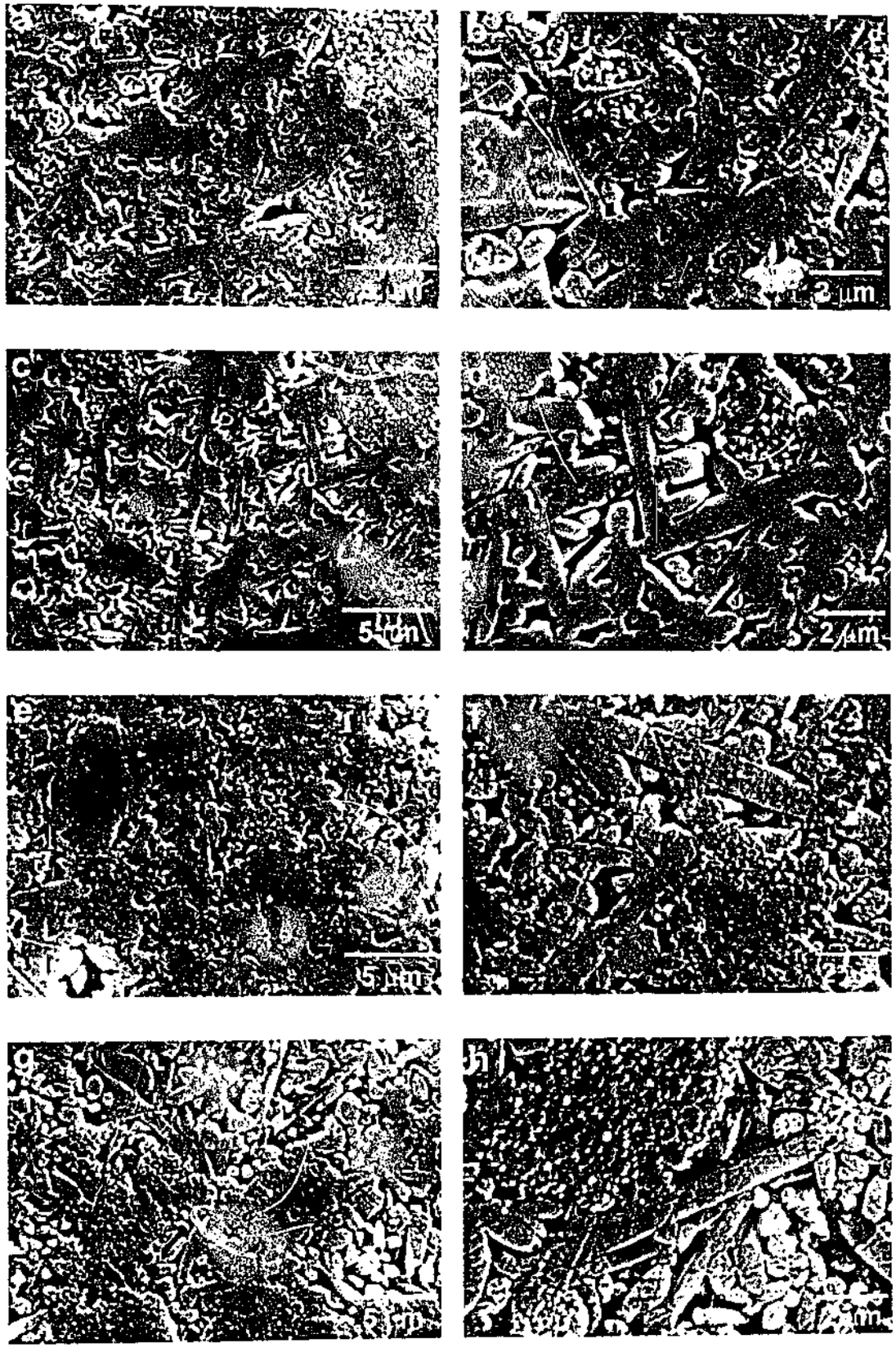

Figure 6.25. Secondary electron micrographs of composition 3622, heated at (a and b) 5°, (c and d) 10°, (e and f) 20° and (g and h) 40°C/min.

The effect that heating rate had on the microstructural development of the 2014 composition can be explained in terms of α-sialon nucleation. At very slow heating rates, the sample spends a significant amount of time in the optimal α-sialon nucleation temperature range. Most, if not all, of the α-Si_3N_4 will be converted to fine α-sialon grains. This creates a high grain density of α-sialon grains which can then yield a relatively refined microstructure of smaller, more equiaxed, grains after growth at 1800°C. At high heating rates, the optimal nucleation temperature range is passed through rapidly, and a lower density of α-sialon grains results. Upon moving into the growth temperature range, the smaller number of α-sialon nuclei grow. Because of a lower density of α-sialon nuclei, a coarser microstructure of larger α-sialon grains and larger pockets of grain boundary glass and voids results. The larger pockets of grain boundary phase are a result of the relatively poor packing arrangement of the high aspect ratio, elongated α-sialon grains.

As SEM micrographs showed, the furnace heating rate had the greatest effect on α-sialon grain morphology in the lowest m-value composition examined, 2014. Very little effect was seen in 3019, and no effect was observed in the highest m-value composition, 3622. This is believed to be related to the liquid phase in the different compositions. As earlier work in this chapter has discussed (in Sections 6.2.2.2 and 6.2.3.2), the liquid phase in Ca-Si-Al-O-N compositions is thought to facilitate anisotropic α-sialon grain growth via enhanced diffusion kinetics. The 2014 composition contains the lowest proportion of liquid phase. This liquid would also be the most viscous, given the lower Ca content of this composition. This would be likely to give the 2014 composition the poorest diffusion kinetics of the three compositions being investigated. Consequently, if equiaxed α-sialon grains were formed in a 2014 sample because of a rapid heating rate, the poorer diffusion kinetics of this composition would make further anisotropic α-sialon grain growth via Ostwald ripening progress relatively slowly. Conversely, if the more liquid-rich compositions developed equiaxed α-sialon in the early stages of sintering, their better diffusion kinetics would allow anisotropic grain growth to take place over extended sintering times. Consequently, different heating rates would not have a significant effect on the final sintered microstructure of more liquid-rich samples.

To further examine the transformation of dense microstructures of fine Ca α-sialon grains to large, elongated grains, a Ca-Si-Al-O-N sample from the work in Chapter 4 was obtained. This sample of the 3618 composition had already been sintered for 4 hours at 1600°C. The density of the sample was 94% of maximum density, and chemical reactions were essentially complete, with the sample containing only α-sialon and AlN as crystalline phases. This sample also contained a relatively high amount of intergranular glass phase. A secondary electron micrograph of this sample, shown in Figure 6.26(a), shows that the sample microstructure is composed of fine, slightly elongated α-sialon grains approximately 1 μm in diameter, and some larger equiaxed grains of AlN. This sample can be considered to have a pre-existing high density of small α-sialon grains. If the suggestion that a high density of fine α-sialon grains can evolve into larger elongated grains in the presence of adequate liquid phase is accurate, then reheating this sample to 1800°C for 4 hours should result in the evolution of a microstructure composed of large, high aspect ratio, elongated α-sialon grains.

This sample was reheated under these conditions and then examined by SEM. A secondary electron micrograph of the reheated sample in Figure 6.26(b) shows that extensive anisotropic grain growth occurred. Many α-sialon grains exceeding 5 μm can be seen in this micrograph. Indeed, the sample exhibited a very similar α-sialon grain morphology to the same composition directly fired at 1800°C for 4 hours, without a 4 hour hold at 1600°C (see Figure 4.14). This result clearly shows that in a liquid-rich Ca-Si-Al-O-N composition, a high density of fine α-sialon grains is not a barrier to the development of relatively large, high aspect ratio α-sialon grains.

The concept that increased grain boundary liquid assists elongated grain growth in sialons is not new, and is reported in the literature. However, often it is suggested that elongated grains develop because the increased proportion of liquid phase gives more freedom for grains to grow without impinging on each other (Shen et al. 1997). The present work indicates that this scenario is not the primary reason for elongated growth of Ca α-sialon. These results have shown that densely packed microstructures of small α-sialon grains that are already impinging on each other easily undergo significant anisotropic growth. As previously discussed, it is more likely that the liquid phase facilitates a type of liquid-assisted Ostwald ripening, in which larger α-sialon grains

grow at the expense of smaller grains. The liquid phase allows this process to proceed, possibly by enhancing diffusion. Where inadequate liquid phase is present, grain growth does not proceed at a significant rate. Consequently, little grain growth takes place, and equiaxed grains result.

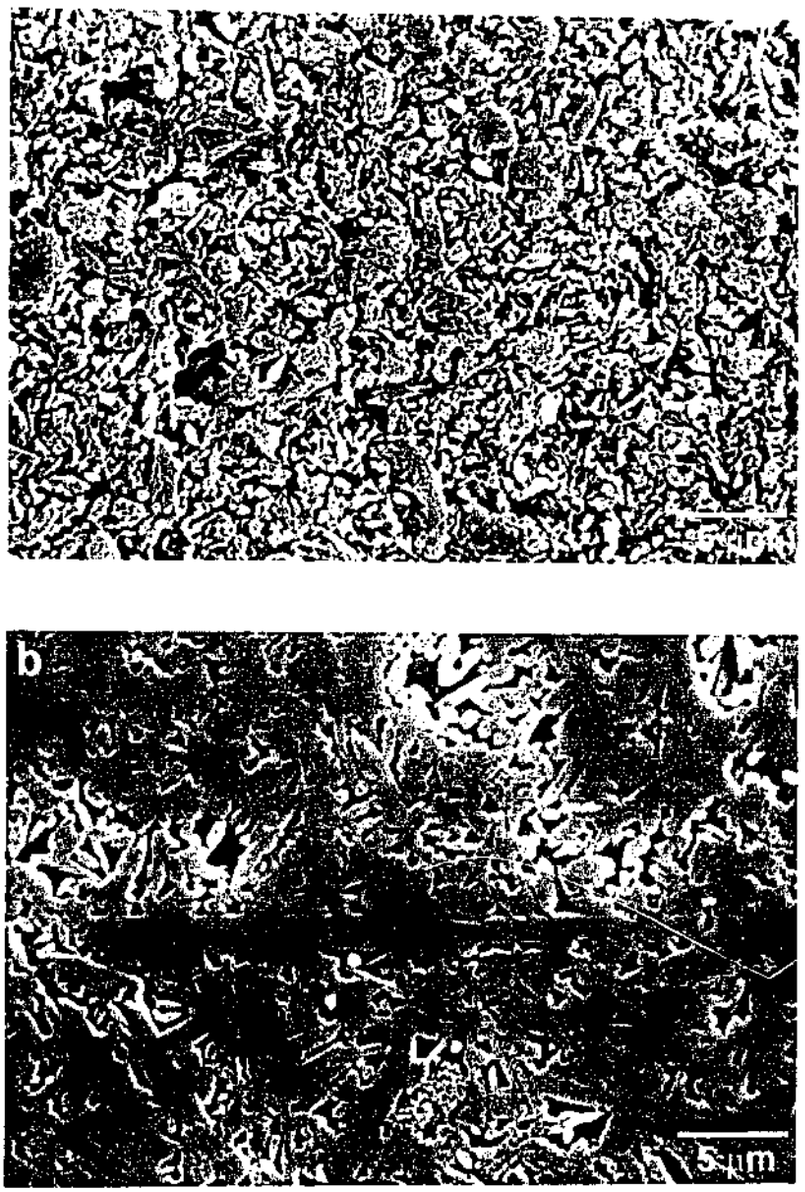

Figure 6.26. Secondary electron micrographs of polished and etched samples of (a) Ca-Si-Al-O-N composition 3618 sintered for 4 hours at 1600°C, and (b) the same sample following an additional firing of 4 hours at 1800°C.

This hypothesis could explain why Ca α-sialon typically exhibits equiaxed grain morphologies in low m-value Ca-Si-Al-O-N compositions (Hewett et al. 1998a). These samples have very little intergranular liquid phase following α-sialon precipitation, and consequently, the growth of α-sialon into elongated morphologies could be suppressed because of this.

6.4.4 Summary of the Effects of Using Different Heating Rates

This section of work examined the effects that heating rate had on the development of three Ca-Si-Al-O-N compositions. Heating rates from 5°C to 40°C/min. were examined. Different heating rates were found to have no effect on the final crystalline phase assemblages of the densified samples of a given composition. Some small variations in the sintered densities of the compositions heated at different rates were measured. However, as no clear trends were apparent in the density data, these variations were attributed to defects in green bodies.

In certain cases, the different heating rates were observed to have an effect on microstructural development. This was most apparent in the lowest m-value composition, 2014. In this composition, heating rates of 5°C and 10°C/min. were found to promote the development of a significant proportion of equiaxed α-sialon grains. Some elongated α-sialon was also present in these samples. At heating rates of 20°C and 40°C/min., mostly elongated α-sialon was observed in the samples. These samples also exhibited larger regions of intergranular glass.

The effects of heating rates on the 3019 composition were much less significant. Samples heated at 5°, 10° and 20°C/min. all developed identical microstructures dominated by elongated α-sialon. The sample heated at 40°C/min. was slightly different, in that it developed larger intergranular glass regions, and had a coarser appearance. No differences in α-sialon morphology were observed in the 3622 composition, regardless of the heating rate used. All samples developed elongated α-sialon grains. Higher heating rates appeared to cause AlN to be poorly distributed in the microstructure of 3622.

The microstructural differences were explained in terms of α-sialon nucleation. Previous work has shown that Ca α-sialon exhibits a nucleation temperature somewhere below its optimal grain growth temperature. Slow heating rates are believed to give the sample more time in the optimal α-sialon nucleation temperature range. This allows an abundance of α-sialon nuclei to precipitate. This dense packing of α-sialon nuclei then hinders anisotropic grain growth at higher temperatures, and consequently, equiaxed α-sialon grains result. At high heating rates, the optimal nucleation temperature range is passed through rapidly, and a lower density of α-sialon nuclei results. Upon moving into the growth temperature range, the smaller number of α-sialon nuclei are able to grow anisotropically with less hindrance from other grains. The larger regions of intergranular glass result from the less efficient packing arrangement of elongated grains, relative to smaller, equiaxed grains.

The greater effect of heating rate on the lower m-value 2014 composition was attributed to the lower liquid phase content of this composition. The liquid phase in the Ca-Si-Al-O-N samples is believed to assist elongated grain growth by enhancing diffusion rates. The lower liquid content and the higher viscosity of the liquid in 2014 was thought to slow the diffusion kinetics such that significant elongated grain growth did not occur if a dense microstructure of equiaxed α-sialon grains was initially developed.

Further investigation of α-sialon grain growth was carried out by examining a reheated sample of a 3618 Ca-Si-Al-O-N sample. This sample was initially reacted at 1600°C for 4 hours, and formed a dense microstructure of fine α-sialon grains. After reheating the sample at 1800°C for 4 hours, this sample exhibited high aspect ratio, elongated α-sialon grains. This offered further evidence that the presence of intergranular liquid phase facilitates the anisotropic growth of α-sialon via a type of liquid-assisted Ostwald ripening mechanism. The liquid phase is thought to enhance diffusion rates and therefore grain growth. It does not enhance grain growth by providing room for grains to grow with less hindrance, as some researchers have suggested is the case for other Me-Si-Al-O-N systems.

6.5 Conclusions for Chapter 6

The key conclusions that were reached as a result of the examination into the effects of processing parameters on the microstructures of Ca-Si-Al-O-N materials are as follows:

- Ca α-Sialon grain growth is initially more rapid in higher m-value compositions. After 1 minute at 1800°C, α-sialon grains in composition 2014 possess a sub-micron, equiaxed morphology. In composition 3019 sintered under the same conditions, many α-sialon grains are elongated and ~1 μm in length. This is attributed to enhanced diffusion kinetics that arises from higher quantities of liquid phase and calcium.

- Increased proportions of AlN in raw compositions reduces the initial densification rate of samples during pressureless sintering. This is attributed to the poorer wetting behaviour of AlN in the liquid phase. Increasing composition m-values reduces the time required to attain full density by pressureless sintering. At 1800°C samples with m = 3.0 and 3.6 attained peak density in 2 hours. The sample with m = 2.0 took 4 hours to reach peak density. This is attributable to higher quantities of liquid phase, which enhance densification. For a given composition, an optimal time exists for achieving full density. In higher m-value compositions, over-sintering leads to a loss of density. This most likely arises from mass loss from the liquid phase.

- β-Si_3N_4 reacts slower than α-Si_3N_4 in Ca-Si-Al-O-N compositions. Substituting 50 wt.% of α-Si_3N_4 with β-Si_3N_4 in Ca-Si-Al-O-N compositions has a negligible effect on densification. Completely substituting α-Si_3N_4 with β-Si_3N_4 dramatically reduces the densification rate of Ca-Si-Al-O-N compositions. This is attributable to the reduced rate of liquid phase evolution and accelerated α-sialon grain growth.

- Completely substituting α-Si_3N_4 with β-Si_3N_4 causes α-sialon grain growth to be significantly accelerated at lower temperatures. This is attributable to the reduction in the number of α-sialon nucleation sites that arises when β-Si_3N_4 replaces α-Si_3N_4.

- The liquid phase present in Ca-Si-Al-O-N compositions appears to facilitate anisotropic α-sialon grain growth. This is thought to be a result of the liquid phase enhancing diffusion kinetics such that a type of Ostwald ripening can occur, thus allowing fine α-sialon grains to grow into large, high aspect ratio grains over time. Slow heating rates can suppress anisotropic α-sialon grain growth in Ca-Si-Al-O-N compositions, provided that the composition has a low level of liquid phase. The slow heating rates can cause equiaxed α-sialon grains to develop in a sample. If a low level of liquid phase is present in the sample, the slowed diffusion kinetics can prevent elongated grains from developing via Ostwald ripening.

Chapter 7

Conclusions and Suggestions for Future Work

7.1 Conclusions

As a result of this study, a number of significant conclusions have been reached. Overall, it has been shown that the Ca-Si-Al-O-N system readily forms elongated α-sialon grains under pressureless sintering conditions. A number of methods can be used to exert a degree of control over α-sialon grain growth, thereby offering significant opportunities to further develop in-situ toughened Ca α-sialon materials.

Initial investigations into three high m-value Ca-Si-Al-O-N compositions located outside of the α-sialon forming region on the Ca α-sialon plane established that the anisotropic growth of Ca α-sialon grains occurs over a significant compositional range. Subsequent investigations into a further eight high m and n-value Ca-Si-Al-O-N compositions further established the wide range of compositions that develop elongated Ca α-sialon grains.

In addition to the development of elongated α-sialon, most of these Ca and Al-rich compositions developed significant quantities of intergranular glass phase and AlN/AlN-polytypoid phases. Compositions with higher proportions of intergranular liquid phase tended to exhibit longer α-sialon grain lengths. The exceptions to this were cases in which plate-shaped AlN-polytypoid phases formed dense networks in sample microstructures. The AlN-polytypoid phases appeared to grow significantly faster than α-sialon, which created complex networks that restricted α-sialon grain growth. A new phase compatibility region, α′ - AlN - AlN′ - liquid, was discovered on the Ca α-sialon plane. The AlN′ phase was found to be AlN containing Si in a solid solution.

The precipitation and subsequent melting/dissolution of intermediate phases were found to be critical to densification during pressureless sintering. An intermediate phase with a relatively high melting/dissolution temperature was observed in a series of 5025

samples. The densification of this composition was hindered to relatively high temperatures, and only proceeded normally once the intermediate phase melted/dissolved.

In an effort to explore ways of controlling microstructural development in Ca-Si-Al-O-N materials, a number of processing parameters were investigated. A study of furnace heating rates found that in low m-value compositions, slow heating rates could suppress anisotropic α-sialon grain growth, resulting in a significant proportion of α-sialon exhibiting an equiaxed morphology. A more rapid heating rate resulted in the development of only elongated α-sialon grains. This effect was not apparent in more liquid-rich, higher m-value samples, which tended to develop α-sialon grains with an elongated morphology over a range of heating rates. α-Sialon nucleation and growth kinetics play a role in this effect.

Experiments suggested that the intergranular liquid phase might play an important role in facilitating anisotropic α-sialon grain growth. A degree of liquid phase appeared to allow dense microstructures of fine α-sialon nuclei to transform into microstructures composed of high aspect ratio, elongated, α-sialon grains. In cases where an inadequate volume of liquid phase was present, such as in a low m-value sample, elongated growth was suppressed, and equiaxed grains resulted. It is believed that the liquid phase may act as a path for rapid diffusion, which allows anisotropic grain growth to take place via an Ostwald ripening-type mechanism. This could explain why low m-value Ca-Si-Al-O-N compositions, which exhibit very little residual grain boundary phase, develop equiaxed α-sialon grain morphologies, when much experimental evidence indicates that Ca α-sialon has an intrinsic elongated grain morphology.

The effects of substituting β-Si_3N_4 starting material in place of α-Si_3N_4 were also examined. An equal ratio α/β mix was found to have little effect on material development. However, completely substituting α-Si_3N_4 with β-Si_3N_4 had significant effects on both sample densification and α-sialon grain growth. Samples made with β-Si_3N_4 could not be densified to full density by pressureless sintering. Microstructural analyses of these samples found extensive distributions of large pores throughout the microstructures. This hindered densification was mainly attributed to the higher

thermodynamic stability of β-Si_3N_4 relative to α-Si_3N_4. The use of β-Si_3N_4 also resulted in elongated α-sialon growth occurring at abnormally low temperatures and short sintering times. This observation was attributed to the mechanism of α-sialon nucleation, and the drastic reduction in the number of α-sialon nucleation sites that occurred when α-Si_3N_4 was replaced with β-Si_3N_4.

The effectiveness of elongated α-sialon grains in toughening Ca-Si-Al-O-N materials was established by characterising the fracture behaviour of a number of Ca-Si-Al-O-N samples. These samples exhibited varying proportions of elongated α-sialon, AlN/AlN-polytypoid phases, and glass phase. Fracture surface analyses found that samples containing a large proportion of elongated α-sialon showed evidence of microstructural toughening mechanisms, such as grain debonding and grain pullout. R-curve analyses of samples indicated that the elongated α-sialon grains were effectively toughening the materials in some cases. The toughening effect was less apparent in samples containing high levels of intergranular glass phase.

From these results, it is clear that the Ca-Si-Al-O-N system possesses good potential for the further development of in-situ toughened Ca α-sialon materials.

7.2 Suggested Areas for Future Work

- It would be worthwhile applying some of the techniques studied in this work to low m-value Ca-Si-Al-O-N compositions that form single-phase Ca α-sialon. These compositions typically exhibit equiaxed grain morphologies. However, they are of more interest as engineering materials as they contain very little intergranular glass, and do not contain secondary phases such as AlN and AlN-polytypoid phases. Techniques such as rapid furnace heating rates and the partial replacement of α-Si_3N_4 with β-Si_3N_4 may make it possible to develop elongated microstructures in these compositions.

- Applying some of these techniques to yttrium and rare-earth α-sialons. These materials most often develop equiaxed grain morphologies. It would be

advantageous to investigate whether techniques studied in this work, such as rapid furnace heating rates and the partial replacement of α-Si_3N_4 with β-Si_3N_4, could promote anisotropic grain growth in these α-sialon systems.

- The use of heat treatments to devitrify the intergranular glass phase in Ca-Si-Al-O-N samples exhibiting elongated Ca α-sialon could significantly improve the fracture toughness of these materials. A study of heat treatments to establish their effectiveness in improving fracture toughness would be an interesting aspect of this research.

- Intermediate phases have been shown to play a vital role in the densification of Ca-Si-Al-O-N compositions during pressureless sintering. The identification and characterisation of the two unidentified intermediate phases detected in this study, A-phase and B-phase, would help form a more complete picture of the Ca-Si-Al-O-N system.

- The identification and characterisation of the nano-precipitates observed in some AlN grains would be a useful exercise that could have some relevance to the use of AlN as a substrate material for electronic components.

- Given that Ca α-sialon could be developed into a relatively low-cost, high hardness material with good fracture toughness properties, it would be naturally suited to a range of commercial applications. An assessment of the thermal, mechanical and chemical properties of Ca-Si-Al-O-N materials exhibiting elongated grains would help in establishing the range applications for which the material would be suited. Properties of interest include room temperature and high temperature strength, wear resistance, oxidation resistance and resistance to chemical attack.

List of Publications

Wood, C. A. and Cheng, Y.-B. (2000a). Effects of Different Starting Powders on the Microstructures of α-Sialons. In *Sintering Science and Technology*, Eds., R. M. German, G. L. Messing and R. G. Cornwall, The Pennsylvania State University: 337-42.

Wood, C. A. and Cheng, Y.-B. (2000b). Factors Influencing the Microstructural Development of Ca α-Sialon Exhibiting Elongated Grains. *J. Aust. Ceram. Soc.* **36**(1): 105-11.

Wood, C. A. and Cheng, Y.-B. (2000c). Phase Relationships and Microstructures of Ca and Al-Rich α-Sialon Ceramics. *J. Eur. Ceram. Soc.* **20**: 357-66.

Wood, C. A., Zhao, H. and Cheng, Y.-B. (1998a). Development of Elongated Ca α-Sialon Grains by Pressureless Sintering. In *Ceramic Processing Science*, Eds., G. L. Messing, F. F. Lange and S. Hirano. **83**: 533-40.

Wood, C. A., Zhao, H. and Cheng, Y.-B. (1998b). Effects of Composition on the Morphology of α-Sialon Ceramics. In *The Proceedings of The First China International Conference on High-Performance Ceramics*, Eds., D. S. Yan and Z. D. Guan: 39-41.

Wood, C. A., Zhao, H. and Cheng, Y.-B. (1998c). In-Situ Toughening of α-Sialon Ceramics. In *The Proceedings of Materials '98, The Biennial Conference of the Institute of Materials Engineering, Australasia, Ltd.*, Ed., M. Ferry: 663-8.

Wood, C. A., Zhao, H. and Cheng, Y.-B. (1998d). Phase and Microstructural Evolution of Ca α-Sialon Containing Elongated Grains. *J. Aust. Ceram. Soc* **34**(2): 54-9.

Wood, C. A., Zhao, H. and Cheng, Y.-B. (1999). Microstructural Development of Calcium α-Sialon Ceramics with Elongated Grains. *J. Am. Ceram. Soc.* **82**(2): 421-8.

Zhao, H., Wood, C. A. and Cheng, Y.-B. (2000). The Effect of Processing Conditions on the Microstructures of α-Sialon Ceramics. In *Materials Science Forum*. Switzerland, Trans Tech Publications. **325-326**: 213-8

References

Anstis, G. R., Chantikul, P., Lawn, B. R. and Marshall, D. B. (1981). A Critical Evaluation of Indentation Techniques for Measuring Fracture Toughness: I, Direct Crack Measurements. *J. Am. Ceram. Soc.* **64**(9): 533-38.

Becher, P. F., Hwang, S.-L. and Hsueh, C.-H. (1995). Using Microstructure to Attack the Brittle Nature of Silicon Nitride Ceramics. *MRS Bulletin* (February): 23-7.

Becher, P. F., Sun, E. Y., Plucknett, K. P., Alexander, K. B., Hsueh, C.-H., Waters, S. B., Westmoreland, C. G., Kang, E.-S., Hirao, K. and Brito, M. E. (1998). Microstructural Design of Silicon Nitride with Improved Fracture Toughness: I, Effects of Grain Shape and Size. *J. Am. Ceram. Soc.* **81**(11): 2821-30.

Cannard, P. J., Ekstrom, T. and Tilley, R. J. D. (1991). The Formation of Phases in the AlN-rich Corner of the Si-Al-O-N System. *J. Eur. Ceram. Soc.* **8**: 375-82.

Cao, G. Z. and Metselaar, R. (1991). α'-Sialon Ceramics: A Review. *Chem. Mater.* **3**(2): 242-52.

Chen, I.-W. and Rosenflanz, A. (1997). A Tough SiAlON Ceramic Based on α-Si_3N_4 with a Whisker-like Microstructure. *Nature* **389**: 701-4.

Deeley, G. G., Herbert, J. M. and Moore, N. C. (1961). Dense Silicon Nitride. *Powder. Metall.* **8**: 145-51.

Einarsrud, M.-A. and Mitomo, M. (1993). Grain Growth Mechanism of β-SiAlON. In *Advanced Materials '93*, Ed., N. Mizutani. Japan, Elsevier Science: 837-40.

Ekström, T. (1996). α Sialon and α-β Sialon Composites; Recent Research. In *Engineering Ceramics '96: Higher Reliability Through Processing*, Eds., G. N. Babini, M. Haviar and P. Sajgalik. Slovakia, Kluwer Academic Publications: 147-67.

Ekström, T. and Nygren, M. (1992). SiAlON Ceramics. *J. Am. Ceram. Soc.* **75**(2): 259-76.

Emoto, H., Hirotsuru, H. and Mitomo, M. (1999). Influence of Phase Transformation on Grain Growth Behaviour of Silicon Nitride Ceramics. *Key Engineering Materials* **159-60**: 215-20.

Emoto, H. and Mitomo, M. (1997). Control and Characterization of Abnormally Grown Grains in Silicon Nitride Ceramics. *J. Eur. Ceram. Soc.* **17**: 797-804.

Gauckler, L. J., Lukas, H. L. and Petzow, G. (1975). Contribution to the Phase Diagram Si_3N_4-AlN-Al_2O_3-SiO_2. *J. Am. Ceram. Soc.* **58**(7-8): 346-7.

Hampshire, S. (1991). Nitride Ceramics. In *Materials Science and Technology - A Comprehensive Treatment*, VCH. **3**: 121-71.

Hampshire, S., Park, H. K., Thompson, D. P. and Jack, K. H. (1978). α'-Sialon Ceramics. *Nature* **274**: 880-2.

Hardie, D. and Jack, K. H. (1957). Crystal Structures of Silicon Nitride. *Nature* **180**: 332-3.

Hewett, C. L. (1998). The Fabrication and Characterisation of Calcium α-SiAlON Ceramics. *Ph.D Thesis*, Department of Materials Engineering, Monash University, Melbourne, Australia.

Hewett, C. L., Cheng, Y.-B., Muddle, B. C. and Trigg, M. B. (1994a). Preparation of Fine-Grained α-Sialon. *J. Mater. Sci. Lett.* **13**: 1612-15.

Hewett, C. L., Cheng, Y.-B., Muddle, B. C. and Trigg, M. B. (1994b). Reaction Mechanism of Hot-Pressed Calcium α-Sialon. In *Austceram '94: International Ceramic Monographs*, Eds., C. C. Sorrell and A. J. Ruys: 1001-6.

Hewett, C. L., Cheng, Y.-B., Muddle, B. C. and Trigg, M. B. (1998a). Phase Relationships and Related Microstructural Observations in the Ca-Si-Al-O-N System. *J. Am. Ceram. Soc.* **81**(7): 1781-88.

Hewett, C. L., Cheng, Y.-B., Muddle, B. C. and Trigg, M. B. (1998b). Thermal Stability of Calcium α-Sialon Ceramics. *J. Eur. Ceram. Soc.* **18**: 417-27.

Hoffmann, M. J. (1994). Analysis of Microstructural Development and Mechanical Properties of Si_3N_4 Ceramics. In *Tailoring of Mechanical Properties of Si_3N_4 Ceramics*, Eds., M. J. Hoffmann and G. Petzow, Kluwer Academic Publishers: 59-72.

Hwang, S.-L. and Chen, I.-W. (1994). Nucleation and Growth of α'-Sialon on α-Si_3N_4. *J. Am. Ceram. Soc.* **77**(7): 1711-18.

Iio, S., Watanabe, M., Matsubara, M. and Matsuo, Y. (1989). Mechanical Properties of Alumina/Silicon Carbide Whisker Composites. *J. Am. Ceram. Soc.* **72**(10): 1880-84.

Jack, K. H. (1976). Review - Sialons and Related Nitrogen Ceramics. *J. Mater. Sci.* **11**: 1135-58.

Jack, K. H. (1983). The Characterisation of α-Sialons and the α–β Relationships in Sialons and Silicon Nitrides. In *Progress in Nitrogen Ceramics*, Ed., F. L. Riley. Netherlands, Martinus Nijhoff: 45-9.

Jack, K. H. (1987). Silicon Nitride, Sialons, and Related Ceramics. In *Ceramics and Civilization, Volume III, High Technology Ceramics - Past, Present and Future*, The American Ceramic Society, Inc.: 259-88.

Jack, K. H. (2000). Nitrogen Ceramics for Engine Applications. In *Materials Science Forum - Nitrides and Oxynitrides*, Eds., S. Hampshire and M. J. Pomeroy, Trans Tech Publications Ltd. **325-26:** 255-61.

Jack, K. H. and Wilson, W. I. (1972). Ceramics Based on the Si-Al-O-N and Related Systems. *Nature Physical Science* **238**: 28-9.

Kang, S.-J. L. and Han, S.-M. (1995). Grain Growth in Si_3N_4-Based Materials. *MRS Bulletin* (February): 33-7.

Kim, Y.-W., Mitomo, M., Emoto, H. and Lee, J.-G. (1998). Effect of Initial α-Phase Content on Microstructure and Mechanical Properties of Sintered Silicon Carbide. *J. Am. Ceram. Soc.* **81**(12): 3136-40.

Kim, Y. W., Mitomo, M. and Hirosaki, N. (1995). R-Curve Behaviour of Sintered Silicon Nitride. *J. Mater. Sci.* **30**: 4043-48.

Kingery, W. D., Bowen, H. K. and Uhlmann, D. R. (1976). Introduction to Ceramics. New York, Wiley.

Kitayama, M., Hirao, K., Toriyama, M. and Kanzai, S. (1998a). Modeling and Simulation of Grain Growth in Si_3N_4 - I. Anisotropic Ostwald Ripening. *Acta Mater.* **46**(18): 6541-50.

Kitayama, M., Hirao, K., Toriyama, M. and Kanzai, S. (1998b). Modeling and Simulation of Grain Growth in Si_3N_4 - II. The α–β Transformation. *Acta Mater.* **46**(18): 6551-57.

Kitayama, M., Hirao, K., Toriyama, M. and Kanzaki, S. (1998c). Anisotropic Ostwald Ripening in β-Si_3N_4 with Different Lanthanide Additives. In *Ceramic Processing Science*, Eds., G. L. Messing, F. F. Lange and S. Hirano, The American Ceramic Society. **83**.

Komeya, K., Inoue, H. and Tsuge, A. (1974). Role of Y_2O_3 and SiO_2 Additions in Sintering of AlN. *J. Am. Ceram. Soc.* **57**(9): 411-12.

Komeya, K. and Matsui, M. (1991). High Temperature Engineering Ceramics. In *Materials Science and Technology - A Comprehensive Treatment*, Eds., R. W. Cahn, P. Haasen and E. J. Kramer, VCH. **10:** 518-65.

Kramer, M., Wittmuss, D., Kuppers, H., Hoffmann, M. J. and Petzow, G. (1994). Relations Between Crystal Structure and Growth Morphology of β-Si_3N_4. *J. Crystal Growth* **140**: 157-66.

Kuang, S.-F., Huang, Z.-K., Sun, W.-Y. and Yan, D.-S. (1990). Phase Relationships in the Li_2O-Si_3N_4-AlN System and the Formation of Lithium-α'-Sialon. *J. Mater. Sci. Lett.* **9**: 72-4.

Lange, F. F. (1979). Fracture Toughness of Si_3N_4 as a Function of Initial α-Phase Content. *J. Am. Ceram. Soc.* **62**(7-8): 428.

Lee, D.-D., Kang, S.-J. L. and Yoon, D. L. (1988). Mechanism of Grain Growth and α–β' Transformation During Liquid-Phase Sintering of β-Sialon. *J. Am. Ceram. Soc.* **71**: 803-6.

Levin, E. M., Robbins, C. R., McMurdie, H. F. and Reser, M. K., Eds. (1964). Phase Diagrams for Ceramists, The American Ceramic Society, Inc.

Lewis, M. H., Fung, R. and Taplin, D. M. R. (1981). Indentation Plasticity and Fracture of Si_3N_4 Ceramic Alloys. *J. Mater. Sci.* **16**: 3437-46.

Li, H. X., Sun, W. Y., Yan, D. S. and Tien, T. Y. (1995). Mechanical Properties of Hot-Pressed 12H Ceramics. In *Proceedings of the 5th International Symposium on Ceramic Material & Components for Engines*, Ed., D. S. Yan, World Scientific: 194-97.

Lide, D. R., Ed. (1989). CRC Handbook of Chemistry and Physics. Boca Raton, FL, CRC Press.

Mandal, H. (1999). New Developments in α-SiAlON Ceramics. *J. Eur. Ceram. Soc.* **19**: 2349-57.

Mandal, H. and Thompson, D. P. (1996). CeO_2 Doped α-Sialon Ceramics. *J. Mater. Sci. Lett.* **15**: 1405.

Mandal, H. and Thompson, D. P. (1999). α to β Transformation in Calcium-containing α-Sialon Ceramics. *J. Eur. Ceram. Soc.* **19**: 543-52.

Menon, M. and Chen, L.-W. (1995a). Reaction Densification of α'-SiAlON: I, Wetting Behaviour and Acid-Base Reactions. *J. Am. Ceram. Soc.* **78**(3): 545-52.

Menon, M. and Chen, I.-W. (1995b). Reaction Densification of α'-SiAlON: II, Densification Behaviour. *J. Am. Ceram. Soc.* **78**(3): 553-59.

Mitomo, M. (1999). In-Situ Microstructural Control in Engineering Materials. *Key Engineering Materials* **161-63**: 53-8.

Nordberg, L.-O., Shen, Z., Nygren, M. and Ekstrom, T. (1997). On the Extension of the α-SiAlON Solid Solution Range and Anisotropic Grain Growth in Sm-doped α-SiAlON Ceramics. *J. Eur. Ceram. Soc.* **17**: 575-80.

Oyama, Y. and Kamigaito, O. (1971). Solid Solubility of Some Oxides in Si_3N_4. *Japan J. Appl. Phys.* **10**: 1637.

Pyzik, A. J. and Carroll, D. F. (1994). Technology of Self-Reinforced Silicon Nitride. *Annual Review of Materials Science* **24**: 189-214.

Roebuck, P. and Thompson, D. P. (1977). In *High Temperature Chemistry of Inorganic and Ceramic Materials*, Eds., F. P. Glasser and P. E. Potter. London, The Chemical Society: 222-8.

Rosenflanz, A. and Chen, I.-W. (1999). Kinetics of Phase Transformations in SiAlON Ceramics: I. Effects of Cation Size, Composition and Temperature. *J. Eur. Ceram. Soc.* **19**: 2325-35.

Scott (1986). CELSIZ. Clayton, Australia, Commonwealth Scientific and Industrial Research Organisation.

Seeber, A. and Cheng, Y.-B. (1998). The Stabilisation of α-Sialons Using Multiple Additives. *J. Aust. Ceram. Soc.* **34**(2): 72-7.

Shen, Z. J., Nordberg, L.-O., Nygren, M. and Ekstrom, T. (1997). α-SiAlON Grains with High Aspect Ratio - Utopia or Reality? In *Engineering Ceramics '96: Higher Reliability Through Processing*, Eds., G. N. Babini, M. Haviar and P. Sajgalik. Slovakia, Kluwer Academic Publications: 169-78.

Slasor, S. and Thompson, D. P. (1987). Comments on Two-Dimensional Solid Solution Formation of Y-containing α-Si_3N_4. *J. Mater. Sci. Lett.* **6**: 315-16.

Suematsu, H., Mitomo, M., Mitchell, T. E., Petrovic, J. J., Fukunaga, O. and Ohashi, N. (1997). The α–β Transformation in Silicon Nitride Single Crystals. *J. Am. Ceram. Soc.* **80**(3): 615-20.

Sun, E. Y., Becher, P. F., Plucknett, K. P., Hsueh, C.-H., Alexander, K. B., Waters, S. B., Hirao, K. and Brito, M. E. (1998). Microstructural Design of Silicon Nitride with Improved Fracture Toughness: II, Effects of Yttria and Alumina Additives. *J. Am. Ceram. Soc.* **81**(11): 2831-40.

Sun, W. Y., Yan, D. S., Gao, L., Mandal, H., Liddell, K. and Thompson, D. P. (1995). Subsolidus Phase Relationships in the Systems Ln_2O_3-Si_3N_4-AlN-Al_2O_3 (Ln = Nd, Sm). *J. Eur. Ceram. Soc.* **15**: 349-55.

Turkdogan, E. T., Bills, P. M. and Tippett, V. A. (1958). Silicon Nitrides: Some Physio-Chemical Properties. *J. Appl. Chem.* **8**: 296-302.

van Rutten, J. W. T., Hintzen, H. T. and Metselaar, R. (1996). Phase Formation of Ca-α-Sialon by Reaction Sintering. *J. Eur. Ceram. Soc.* **16**: 995-99.

van Rutten, J. W. T., Terpstra, R. A., van der Heijde, J. C. T., Hintzen, H. T. and Metselaar, R. (1995). Carbothermal Preparation and Characterisation of Ca-α-Sialon. *J. Eur. Ceram. Soc.* **15**: 599-604.

van Tendeloo, G., Faber, K. T. and Thomas, G. (1983). Characterisation of AlN Ceramics Containing Long-period Polytypes. *J. Mater. Sci.* **18**: 525-32.

Vassiliou, B. and Wilde, F. G. (1957). A Hexagonal Form of Silicon Nitride. *Nature* **179**(435-36).

Wang, C.-M., Pan, X., Ruhle, M., Riley, F. L. and Mitomo, M. (1996a). Review - Silicon Nitride Crystal Structure and Observations of Lattice Defects. *J. Mater. Sci.* **31**: 5281-98.

Wang, H., Cheng, Y.-B., Muddle, B. C., Gao, L. and Yen, T. S. (1996b). Preferred Orientation in Hot-Pressed Ca α-SiAlON. *J. Mater. Sci. Lett.* **15**(16): 1447-9.

Wang, P. L., Sun, W. Y. and Yan, D. S. (2000). Formation and Densification of 21R AlN-polytypoid. *J. Eur. Ceram. Soc.* **20**: 23-7.

Wang, P. L., Sun, W. Y. and Yen, T. S. (1994). Sintering and Formation Behaviour of R-α' Sialons (R=Nd, Sm, Gd, Dy, Er and Yb). *Euro. J. of Solid State Inorg. Chem* **31**: 93-104.

Wang, P. L., Zhang, C., Sun, W. Y. and Yan, D. S. (1999). Characteristics of Ca-α-Sialon - Phase Formation, Microstructures and Mechanical Properties. *J. Eur. Ceram. Soc.* **19**: 553-60.

Weimer, A. W., Ed. (1997). Carbide, Nitride and Boride Materials Synthesis and Processing. London, Chapman & Hall.

Xu, F., Wen, S., Nordberg, L.-O. and Ekström, T. (1997). Nucleation and Growth of the Elongated α'-SiAlON. *J. Eur. Ceram. Soc.* 17: 1631-38.

Zhao, H., Swenser, S. P. and Cheng, Y.-B. (1998). Elongated α-Sialon Grains in Pressureless Sintered Sialon Ceramics. *J. Eur. Ceram. Soc.* 18(8): 1053-57.